UNIVERSITAT POLITÈCNICA DE VALÈNCIA

Departamento de Máquinas y Motores Térmicos

DOCTORAL THESIS:

Contribution to the understanding of filtration and pressure drop phenomena in wall-flow DPFs

---

Presented by: D. EMANUELE ANGIOLINI
Supervised by: DR. D. PEDRO PIQUERAS CABRERA

in fulfillement of the requisites for the degree of

Doctor of Philosophy

Valencia, June 2017

PhD. Thesis

Contribution to the understanding of filtration and pressure drop phenomena in wall-flow DPFs

AUTHORS

Presented by: D. EMANUELE ANGIOLINI
Supervised by: DR. D. PEDRO PIQUERAS CABRERA

DEFENSE COMMITTEE

Chairman: DR. D. JOSÉ GALINDO LUCAS
Secretary: DR. D. JOSÉ RODRÍGUEZ FERNÁNDEZ
Member: DR. D. EDUARD EMIL IOJOIU

Valencia, June 2017

Contribution to the understanding of filtration and pressure drop phenomena in wall-flow DPFs

Emanuele Angiolini

Abstract

From the last decades of the 20th century, internal combustion engines have undergone a continuous improvement process aimed to the increase of their efficiency and decrease of the pollutants emissions. The reduction of the availability of fossil fuel and the increase of human-made pollution observed in the last decades is leading worldwide to more stringent emission standards that make the engine manufacturers to constantly look for fuel consumption and emission reductions while keeping engine performance.

To comply with current and incoming emission regulations, the exhaust line of internal combustion engines has been gradually complicated by the presence of aftertreatment systems. Among them, the particulate filter is the device in charge of abating the emission of soot in the atmosphere. Concerning compression ignition engines, diesel particulate filters (DPF) were first commercially utilized in significant numbers in passenger car and heavy-duty engines since the beginning of the 21st century. Euro 6 emission standards limits the emitted particulate matter from direct injection engines, thus extending the use of particulate filters also to direct injection gasoline engines.

A deep knowledge of the phenomena happening inside the DPF is required for the correct understanding of the behaviour of this system and its interaction with the engine. The precise knowledge of the filtration and pressure drop processes is mandatory for the design of the particulate filter and is also essential to wisely think up and analyse solutions aimed to limit the negative impact of the filter on the fuel consumption maintaining its capability of retaining soot particles.

Thus, the present work pretends to provide a contribution to the understanding of these phenomena in wall-flow DPFs. The problem has been faced on a computational and experimental basis. A notable part of the work was dedicated to the development and validation of a one-dimensional DPF filtration model to be coupled with the existing pressure drop model. The model was implemented in OpenWAM™, the open-source gas dynamics software for internal combustion engines and components computation developed at CMT - Motores Térmicos.

The developed computational tool was applied to the assessment of the aftertreatment (DOC&DPF) volume downsizing potential in post- and pre-turbo aftertreatment configuration. The study is completed with experimental analysis to support theoretical insights discussing how the soot deposition profile and the particulate layer properties impact on the DPF pressure drop.

Resumen

Desde las últimas décadas del siglo XX, se ha producido un proceso de mejora continua de los motores de combustión interna alternativos con el fin de aumentar su eficiencia y reducir las emisiones contaminantes. La reducción de la disponibilidad de combustibles fósiles y el incremento de la polución de origen antropogénico observados en las ultimas décadas ha provocado el progresivo endurecimiento de las normativas anticontaminación a nivel mundial obligando a los fabricantes de motores a buscar la reducción continua del consumo de combustible y emisiones, manteniendo las prestaciones del motor.

El cumplimiento de las actuales y futuras normativas anticontaminación requiere de la instalación de diversos sistemas de postratamiento de gases en la línea de escape de los motores de combustión interna alternativos, aumentando su complejidad. Entre estos sistemas, el filtro de partículas es el equipo encargado de la reducción de la emisión de hollín a la atmósfera. Con respeto a los motores de encendido por compresión, los filtros de partículas diésel se implementaron por primera vez de forma masiva en vehículos de pasajeros y vehículos pesados a principio del siglo XXI. La normativa anti contaminación Euro 6 limita las emisiones de partículas de los motores de inyección directa, extendiendo el uso de filtros de partículas a los motores de inyección directa de gasolina.

Es necesario tener un conocimiento profundo de los fenómenos que tienen lugar en el DPF para comprender el comportamiento de este sistema y su interacción con el motor. El conocimiento de los procesos de filtrado y perdida de presión es vital para el diseño del filtro de partículas y resulta esencial para encontrar y analizar soluciones que ayuden a limitar el impacto negativo del DPF sobre el consumo de combustible sin perder la capacidad de retener partículas de hollín.

En este contexto, este trabajo pretende aportar una contribucción a la comprensión de estos fenómenos en filtros de partículas de flujo de pared. Esta tarea se ha planteado desde un punto de vista computacional y experimental. Parte importante de este trabajo ha consistido en el desarrollo y validación de un modelo de filtrado unidimensional de DPF que se ha acoplado con el modelo de caida de presión ya existente. El modelo se ha implementado en OpenWAM™, el software de libre acceso para el cálculo fluidodinámico de motores de combustión interna y sus componentes desarrollado en CMT - Motores Térmicos.

La herramienta computacional desarrollada se ha aplicado a la evaluación del potencial de reducción de volumen de sistemas de postratamiento (DOC&DPF) en configuraciones post- y pre-turbo. Este estudio se ha completado con un análisis experimental para dar respaldo a los conceptos teóricos empleados discutiendo como el perfil de deposición del hollín y las propiedades de la capa de partículas afectan a la perdida de presión del DPF.

Resum

Des les últimes dècades del segle XX, s'ha produït un procés de millora contínua dels motors de combustió interna alternatius amb l'objectiu d'augmentar la seua eficiència i reduir les emissions contaminants. La reducció de la disponibilitat de combustibles fòssils i l'increment de la polució d'origen antropòlogic observats en les últimes dècades ha provocat que les normatives anticontaminació s'han fet més rígides a nivell mundial, obligant als fabricants de motors a buscar la reducció contínua del consum de combustibles i emissions, mantenint les prestacions dels motors.

El cumpliment de les normes anticontaminació actuals i futures, requereixen de l'instalació de diversos sistemes de post-tractament de gasos a l'eixida dels motors de combustió interna alternatius, llavors augmentant la complexitat. Entre aquestos sistemes, el filtre de partícules es l'equip encarregat de la reducció de les partícules de sutge a l'atmosfera. Respecte als motors d'encès per compressió, els filtres de partícules van instalar-se de manera massiva als vehicles de passatgers i vehicles pesats al principi del segle XXI. La normativa anti contaminació Euro 6 limita les emissions de partícules dels motors d'inyecció directa, estenent l'ús del filtre de partícules als motors d'injecció directa de gasolina.

És necessari tindre un coneixement dels fenòmens que tenen lloc al DPF per a comprendre el comportament del sistema i la seua interacció amb el motor. El coneixement dels processos de filtrat i la pèrdua de pressió és vital per al diseny del filtre de partícules i resulta essencial per a trobar i analitzar les solucions que ajuden a limitar l'impacte negatiu del DPF sobre el consum de combustible sense perdre la capacitat de retenir partícules de sutge.

En aquest context, el projecte pretén aportar una contribució a la comprensió d'aquestos fenòmens en els filtres de partícules de flux de paret. Aquesta feina s'ha plantejat des d'un punt de vista computacional i experimental. Part important d'aquest treball ha consistit en el desenvolupament i validació d'un model de filtrat unidimensional de DPF que s'ha acoplat a un model de pèrdua de pressió existent. El model s'ha implementat en OpenWAM™, el software de lliure accés per al cálcul fluidodinámic de motors de combustió interna i els seus components desenvolupats al CMT - Motores Térmicos.

La ferramenta computacional desenvolupada s'ha aplicat a la evaluació del potencial de reducció del volum de sistemes de post tractament (DOC&DPF) en les configuracions post- i pre-turbo. Aquest estudi s'ha completat amb una anàlisi experimental per a donar suport als concepts teòrics emprats discutint com el perfil de la disposició de sutge i les propietats de la capa de partícules que afecten a la pèrdua de pressió del DPF.

List of publications

The following papers form the basis of this thesis:

- **J. R. Serrano, C. Guardiola, P. Piqueras, E. Angiolini**. "Analysis of the aftertreatment sizing for pre-turbo DPF and DOC exhaust line configuration". In: *SAE Technical Paper 2014-01-1498*, 2014.
- **J. R. Serrano, H. Climent, P. Piqueras, E. Angiolini**. "Analysis of fluid-dynamic guidelines in diesel particulate filter sizing for fuel consumption reduction in post-turbo and pre-turbo placement". In: *Applied Energy* 132 (2014), pp. 507–523.
- **J. R. Serrano, V. Bermúdez, P. Piqueras, E. Angiolini**. "Application of Pre-DPF water injection technique for pressure drop limitation". In: *SAE Technical Paper 2015-01-0985*, 2015.
- **J. R. Serrano, H. Climent, P. Piqueras, E. Angiolini**. "Filtration modelling in wall-flow particulate filters of low soot penetration thickness". In: *Energy* 112 (2016), pp. 883–898.
- **J. R. Serrano, V. Bermúdez, P. Piqueras, E. Angiolini**. "On DPF volume downsizing and its effect on particles filtration efficiency in pre- and post-turbo placement". In: *Journal of Aerosol Science*. Submitted (2016).

Division of work between authors

These publications have been done in collaboration with other researchers, being the author signatures in order of seniority. The respondent performed the experimental measurements, results post-processing and developed the model presented here. Methodologies and results discussions were done in collaboration with his supervisor, Dr. Pedro Piqueras, as well as with the rest of co-authors.

Other publications

During the research period leading to the present work the author of this thesis has been involved in the publication detailed below. Although not directly present in this document, it has provided a deeper understanding of the behaviour of automotive engines and aftertreatment systems.

- **J. R. Serrano, P. Piqueras, E. Angiolini, C. Meano, J. De La Morena**. "On cooler and mixing condensation phenomena in the long-route exhaust gas recirculation line". In: *SAE Technical Paper 2015-24-2521*, 2015.

Acknowledgements

It is not easy to express my acknowledgement to everyone in a few lines on a paper, I will try to do my best but in case I forget about someone, please forgive me. This part is written in different languages in order to make it understandable to everyone I name here, I am sure I owe it to all of them.

First of all, my most sincere acknowledgement to the whole CMT - Motores Térmicos team for giving me the opportunity of being part of it. Dr. Alberto Broatch and Dr. Antonio Torregrosa deserve a special mention for believing in me and inviting me to join the PhD program of the department. All the administration staff, in particular Teresa, Habi and Amparo, who helped me during these 4 years. All the technicians, researchers and professors who have always been happy to support and share their ideas and knowledge with me.

Last, my most sincere thanks to my thesis supervisor, Dr. Pedro Piqueras, for being patient and attentive in directing my job.

A mio padre, per esser sempre dove serve, capace di dire sempre quel che serve e soprattutto tacere quando le parole non servono.

A mia madre, che di donne cosi non ne fanno più e meriterebbe infinite più attenzioni di quelle che sono capace di darle.

A zia Elena, che nonostante tutto continua ad essere il collante di questa sgangherata famiglia e a mio fratello Daniele, che della famiglia è forse la parte piu sgangherata.

Alla mia seconda famiglia, Angelo, Grenkio, Gianfranco, Vincenza, il Ciotto, Paola, Mirchetto, Lupo, Ezio e Itala che mi hanno accolto e trattato sempre come un fratello e un figlio... quelli che ci sono stati, ci sono e ci saranno sempre. Al piccolo Riccardino, che quando mi chiama "Zio Lele" mi riempie il cuore... che la vita ti sorrida sempre. E per ultimo Altea, che tra ingegneri ci si capisce sempre, e quando non ci si capisce si apre una bottiglia ed è tutto più facile.

A Dario e Diego, compagni di mille avventure e diecimila dis-avventure, e a Chiara e Adriana che delle mille avventure sanno tutto e delle diecimila dis-avventure ancor di più.

A Ciccio, Fabio, Bobo, Chiara, Giulietta e Matteo perchè è bello pensare che ci siamo conosciuti poco più che bambini e siamo ancora qua.

A Valencia, mi Valencia querida que me ha visto rodeado de miles de amigos o completamente solo con la tristeza que solo quien se ha ido lejos de su país puede conocer. A Valencia que me ha amado en todas mis formas y que me ha acogido como un hijo y me ha dado la posibilidad de encontrar personas estupendas que me han honrado con su amistad. Alvarin, Dani, Richie, Javi y Lukas, compañeros maravillosos en el trabajo e inigualables en la barra. A Oscar el flaco, maestro extraordinario y compañero de cervezas y barbacoas, por las discusiones en voz baja sobre el diagrama h-s. A todos los demás compañeros del CMT que poco a poco se han vuelto en amigos: Vicente el cubano, Jose el

torner, Miguel el yayo, Antonio, Bernardo, Figo, Fito, Juanan, Valentin, Vicente, Dani el negro, Omarin, Ricardo, Enrique y Maria José... no todo el mundo ha tenido la suerte que he tenido yo de poder compartir el trabajo y la bodegueta con personas así. No puedo olvidarme de todos los proyectandos que han trabajado conmigo, ya que todos han contribuido directamente a la realización de este trabajo: Paloma, Sara, Celia, Eduardo, Jesús, Salvador.

A los que en Valencia encontré primero y de los que a pesar de la distancia nunca más me he separado: Andrea por las maravillosas pizzas y las interminables noches, Carmen por ser mamma Carmen, Sergetto por "Grande figlio di puttana" de los Stadio, Shirish por aquel "This is my friend Lele...he knows what life is about", Alan por ser mucho más que un compañero de piso y Anna por las conversaciones sobre nuestro señor de camino a Alcoy a las once de la mañana. A Enrico y Claudia, que a Valencia llegaron después y en breve se convirtieron en unos amigos como no es fácil encontrar hoy en día.

A Shirley, por haber sido capaz de entender que soy "un oso, pero con un gran corazón" y más aún por haber sido capaz de lidiar con ello.

A la pequeña Joana, porque una niña en diez minutos de paseo para ir al cole te puede enseñar lo que no aprenderás en ningún libro jamás.

A Javi, su hermano José, Andrei y todos los compañeros del boxeo y a Calo y los compañeros de buceo, que en la vida no todo es trabajo y con ellos he podido disfrutarlo al máximo.

En fin, a todos los que de una manera u de otra han contribuido a hacer de mi lo que soy hoy: gracias!

"Nella mia vita non ho mai avuto fame
e non ricordo sete di acqua o di vino
ho sempre corso libero, felice come un cane"
F. De Gregori, Due zingari. 1978.

Contents

List of Figures

List of Tables

Nomenclature

$\bar{E}_f$	In-cycle averaged filtration efficiency
$\dot{m}_w$	Mass flow through the porous wall
$\dot{V}_g$	Exhaust volume flow
A_f	Filtration area
A_{fr}	Monolith cross-section
A_{open}	Open monolith cross-section area
ATDC	After top death centre
bmep	Brake mean effective pressure
bsfc	Brake specific fuel consumption
BTDC	Before top death centre
cad	Crank angle degree
D	Monolith diameter
$d_{c,w}$	Porous wall collector unit diameter
d_{cell}	Cell unit diameter
D_{part}	Particle diffusion coefficient
d_{part}	Particle diameter
d_p	Mean pore diameter
DOC	Diesel oxidation catalyst
DPF	Diesel particulate filter
E_D	Dense material modulus of elasticity
E_w	Porous wall modulus of elasticity
e_0	Specific stagnation internal energy
ECU	Electronic control unit
ED	Ejector diluter
EGR	Exhaust gas recirculation
F	Minimum load carrying capacity
F_w	Momentum transfer coefficient for square channels
f_w	Porous wall thickness fraction penetrated by soot
h_0	Specific stagnation enthalpy
HEPA	High-efficiency particulate arrestance
HTP	Bulk heat transfer parameter

K	Kuwabara's hydrodynamic factor
k_w	Porous wall permeability
k_B	Boltzman constant
k_{pl}	Particulate layer permeability
$k_{w,e}$	Effective porous wall permeability
k_{w_0}	Clean porous wall permeability
Kn	Knudsen number
L	Monolith length
L_e	Monolith effective length
L_{plug}	Plug length
LNT	Lean NO_x trap
LOF	Light-off factor
LOL	Lift-off length
m_{pl}	Particulate layer soot mass
$m_{s_{cell}}$	Cell unit soot mass
m_{sp}	Soot mass in the porous wall control volume
MIF	Mechanical integrity factor
MOR_z	Modulus of rupture
N	Channels number
N_R	Interception parameter
n_{cell}	Cell units number
N_{in}	Inlet channels number
NEDC	New European driving cycle
NO_x	Nitrogen oxides
Nu	Nusselt number
OFA	Open frontal area
p	Gas pressure
Pe	Peclet number
PF	Particulate filter
PM	Particulate matter
PSD	Particle size distribution
PTD	Porous tube diluter
q	Heat per unit of time and mass
RDE	Real driving emission
S_c	Sticking coefficient
S_l	Limit saturation coefficient
SCF	Stokes-Cunningham factor
SCR	Selective catalytic reduction
SFA	Specific filtration area
SGA	Specific geometric area
SMPS	Scanning mobility particle sizer
SoI	Start of injection
ST	Strain tolerance
St	Stokes number
STP	Strain tolerance parameter
T	Gas temperature

t_c Engine cycle duration

TIF Thermal integrity factor

u_w Filtration velocity

$u_{i,w}$ Interstitial velocity

V_e Effective monolith volume

$V_{DOC,g}$ DOC volume occupied by exhaust gas

V_{sp} Soot penetration volume

VGT Variable geometry turbine

w_w Porous wall thickness

w_{pl} Particulate layer thickness

WHTC World harmonized transient cycle

Greek Symbols

α Cell width

χ Shape factor

Δp Pressure drop

Δp_{DPF} DPF pressure drop

Δt Time-step

Δx Control volume length

ϵ_w Porous wall porosity

η_{DRI} Single sphere global collection efficiency

η_D Single sphere diffusion collection efficiency

η_I Single sphere inertial collection efficiency

η_R Single sphere interception collection efficiency

λ Gas mean free path

μ Dynamic viscosity

ϕ Porous wall saturation coefficient

Φ_{ρ_s} Soot density factor

ψ Percolation factor

$\rho_{s,w}$ Soot density inside the porous wall

ρ Gas density

ρ_{pl} Particulate layer density

σ Cell density

σ_D Dense material tensile strength

σ_w Porous wall tensile strength

τ Dwell time

ς_{ic} Inlet channel pressure drop coefficient

ς_{mon} Monolith pressure drop coefficient

ς_{oc} Outlet channel pressure drop coefficient

ξ Surface correcting factor

Vectors and matrices

$\boldsymbol{C_w}$ Porous wall source term vector

$\boldsymbol{C}$ Friction and heat transfer source term vector

$\boldsymbol{F}$ Flow terms vector

$\boldsymbol{S}$	Particle size diameter percentage vector
$\boldsymbol{W}$	Solution vector
$\boldsymbol{Y}$	Chemical species mass fraction vector

Overbar and others

$\bar{}$	Mean value

Subscripts

CV	Control volume
opt	Optimum value
pl	Particulate layer
w	Porous wall

CHAPTER 1

Introduction

Contents

Figures

1.1 Background

INTERNAL combustion engines are nowadays by far the most common power source for land and water vehicles, including automobiles, motorcycles, ships and, to a lesser extent, locomotives. The spark ignition internal combustion engine was invented in 1876 by Nicolaus Otto. In 1892 Rudolf Diesel invented another kind of internal combustion engine in which ignition is due to compression [1]. Focusing on this last version, usually named Diesel engine, it has undergone a continuous improvement aimed to reduce its noise and vibrations and increase its reliability and performance. Also, strong efforts have been done, especially in the last decades, to reduce exhaust emissions.

Recently, climate change due to global warming has been recognized as a major social problem. An increase in the amount of carbon dioxide emitted from vehicles has been highlighted as one of the factors responsible for global warming [2]. Due to their higher efficiency, Diesel engines are characterized by lower CO_2 emissions compared with gasoline ones. On the negative side however, compression ignition engines are source of other pollutants, first and foremost nitrogen oxides (NO_x) and particulate matter (PM). In particular, particulate matter plays an important role in Earth's climate [3] and its negative effects on human health [4] and environment [5] are well-known. Hybrid electric vehicles show great potential as new alternative means of transportation [6] and heavy machinery [7]. Most of the auto companies in the world are developing mild and full hybrid-electric vehicles using internal combustion engines as the prime energy converter with gasoline or diesel as the fuel [8]. Anyway, despite the strong effort, these solutions are still not widely used at the present time.

Thus, to preserve human and environmental health, exhaust gas emissions from internal combustion engines are regulated throughout the world by emission regulations like, for example, the Euro 6 currently in force in Europe for passenger car and light commercial engines [9]. Such regulations impose air quality standards that require the use of aftertreatment systems to be met. In the case of Diesel engines these systems comprise Diesel oxidation catalysts (DOC), Diesel particulate filters (DPF), lean NO_x trap (LNT) and selective catalyst reduction devices (SCR). These systems have an impact on the engine performance. In the case of the DPF, the device in charge of limiting particulate emissions, its impact strongly varies with the soot and/or ash mass collected inside the filter. The presence [10], spatial distribution [11] [12] and characteristics [13] [14], i.e. density and permeability, of these particles inside the filter strongly affect the generated back-pressure, hence the engine performance. Contrarily to ash, soot can be removed by burning it during the normal operation of the DPF, i.e. soot removal does not need special maintenance operation like ash does, if the required thermal level is achieved. Oxidation of soot is normally referred to as regeneration. Regeneration process can be passive or active. In

the first case the soot oxidation temperature is lowered to a level allowing for auto-regeneration during regular vehicle operation, a task commonly achieved by introducing an oxidation catalyst to the system. The catalyst can promote oxidation of carbon through oxygen or NO_2. Active regeneration is achieved by raising the temperature of soot trapped in the filter through the use of an outside energy source, normally fuel. The energy from fuel combustion can be used to increase exhaust gas temperature by either in-cylinder engine management methods, i.e. late injection of additional fuel quantities, or injection and combustion of fuel in the exhaust gas. If exhaust gas combustion is used, fuel can be burned in a fuel burner or else oxidized over an oxidation catalyst, e.g. the DOC, in a catalytic combustion process. The active regeneration approach implies an additional fuel consumption penalization to be added to the one generated by the filter back-pressure.

The importance of achieving high temperature at the DPF inlet gave raise, already in the 80's, to the idea of placing this device upstream of the turbine [15] [16]. The poor thermo-mechanical properties of the monolith together with the lack of precise knowledge of the regeneration phenomena in this era resulted in monolith failure due to the high temperature peaks achieved during the regeneration process. The detached ceramic fragments passed through the turbine damaging its blades. The increasing understanding of the phenomena happening inside the filter and the increasing thermo-mechanical properties of the monolith materials is bringing back the interest in the pre-turbo aftertreatment configuration.

The research institute CMT - Motores Térmicos, in which the respondent has done the work leading to this dissertation, has a strong experience in engines and aftertreatment systems research and one-dimensional ICE code development. Focusing on the DPF, Moya [17] applied the 1D model developed within his thesis to predict the acoustic response of wall-flow particulate filters. Later, Piqueras [18] developed a 1D model to calculate the heat transfer and back-pressure of the DPF. The possibility of taking into account unsteady, compressible and non-homentropic flow makes the model suitable to study the pre-turbo DPF placement. The model was further improved by García Afonso [19] who also performed a comprehensive computational and experimental study of the pre-turbo DPF configuration.

The other aftertreatment systems would also benefit of the pre-turbo placement as they all require a high thermal level to perform their function in optimal conditions. The pre-turbo positioning of the DOC was studied in detail by Reizig *et al.* [20] and Carberry *et al.* [21] among others and a pre-turbo placed SCR has been proposed by Johnson Matthey for a Diesel electric power generator [22]. The needed high thermal level cannot be achieved in many engine operating points in case the aftertreatment is placed downstream of the turbine. Moreover, incoming certification cycles provide for very low temperatures and altitude

effects to be taken into account for engine approval, further increasing this problem.

Back on the DPF subject, CMT - Motores Térmicos proposed and characterized the pre-DPF water injection as a technique aimed to reduce and control the pressure drop generated by a soot and/or ash loaded DPF. This technique was patented by the research institute in 2013 [23]. The capacity of the pre-DPF water injection to reduce the back-pressure of a soot loaded DPF was proven by Bermúdez *et al.* [24] who also characterized the effect of the technique on pollutants emission [25]. Anyway, the physical reason at the basis of the experimentally observed pressure drop and filtration efficiency behaviour after a pre-DPF water injection are still unknown.

1.2 Motivation of the study

It is clear that the presence of aftertreatment systems in the exhaust line of an internal combustion engine is mandatory to comply with emissions legislation. In particular, the particulate filter is in charge of reducing soot emission to the atmosphere. The back-pressure generated by this system, increasing as soot and/or ash is accumulated in its interior, has a strong effect on the engine fuel consumption.

A deep knowledge of the heat transfer, filtration and regeneration phenomena happening inside the DPF is required for the correct understanding of the behaviour of this system and its interaction with the engine and the turbocharger. Figure 1.1 schematizes the interaction between the different phenomena happening inside a DPF and how a DPF model should face them. The porous wall characteristics, i.e. mean pore diameter and porosity, on one hand define the back-pressure and heat transfer behaviour of the filter. Thus, the pressure drop & heat transfer model has to provide to the filtration model the fluid dynamic field at the DPF inlet. This, together with the porous wall characteristics, define the filter capability of collecting particles, hence the retained soot mass. This mass determines the porous wall saturation coefficient ϕ, i.e. the parameter governing the transition from deep bed to cake filtration regime. During the former phase the collected soot mass affects the porous wall characteristics leading to a mean pore diameter and porosity reduction. During the cake filtration phase it defines the particulate layer thickness. As a consequence the back-pressure and filtration efficiency are affected. On the other hand, the fluid dynamic field affects the DPF regeneration behaviour. Thus, the oxidation rate is responsible of the porous wall characteristics variation while the heat released during the soot oxidation affects the fluid dynamic field. A correct DPF model should be able to keep into account all the above listed contributions.

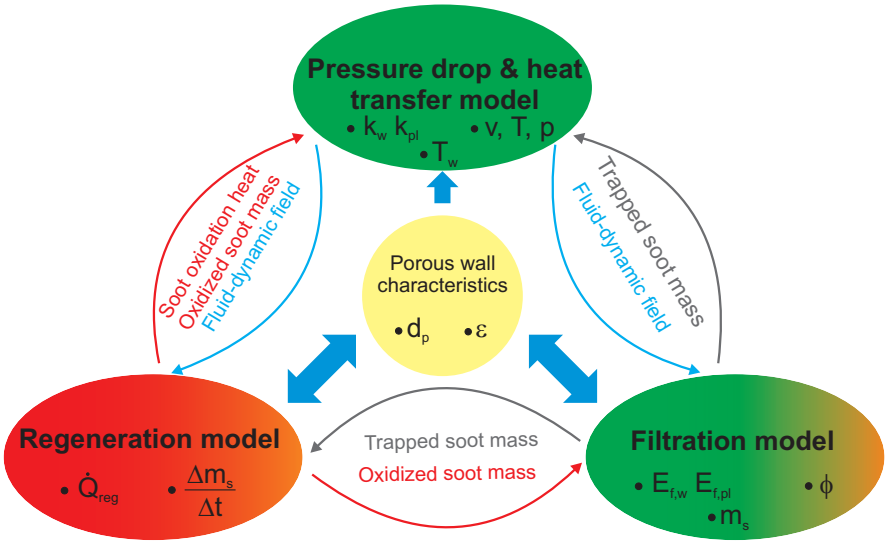

Figure 1.1: Scheme of a complete DPF model and interactions between the different phenomena happening in its interior.

On the other hand, the deep knowledge of all these phenomena is very useful in the design and calibration of the particulate filter and is also essential to wisely think up and analyse solutions aimed to limit the negative impact of the DPF on the fuel consumption maintaining its capability of retaining soot particles.

The present work is focused on the understanding of filtration and pressure drop phenomena in wall-flow DPFs. Highlight that a PhD thesis on the regeneration phenomena is currently under development at the research institute CMT - Motores Térmicos.

1.3 Objectives

Objective of this work is to provide a contribution to the understanding of the filtration and pressure drop phenomena happening in wall-flow DPFs. To achieve it, a list of partial objectives is presented in the following.

- First of all it is important to get an overview of the current situation. Thus, a bibliographic review of the filtration process and the approach of state-of-the-art DPF models to it has been performed. The current DPF design guidelines and the pre-turbo aftertreatment configuration is also analysed together with the effect of the pre-DPF water injection technique.

- Development and experimental validation of a DPF filtration model to be coupled with the current 1D pressure drop model. The model has to be able to predict the filtration efficiency of the filter as a function of the flow field and the porous wall micro-structure. Also, the effect of the collected soot mass on the porous wall micro-structure and, as a consequence, on the flow field has to be accurately predicted.
- Analysis of the potential of aftertreatment (DOC&DPF) volume downsizing considering the conventional post-turbo positioning, i.e. aftertreatment downstream of the turbine, and pre-turbo positioning. i.e. aftertreatment upstream of the turbine. To achieve it the developed model has been used.
- Analysis of the effect of the inlet DPF Peclet number variation on the filter back-pressure and filtration efficiency. The DPF volume downsizing and pre-turbo positioning lead to a modification of the inlet filter flow field, i.e. Peclet number.
- Analysis of the pre-DPF water injection as a technique to reduce the filter back-pressure and/or avoid the risk of channels clogging in downsized volume filters in post-turbo DPF placement.

1.4 Methodology

To achieve the proposed objectives it is essential to define and follow a correct work methodology. The one followed in the present work is sketched in Figure 1.2.

Following the scheme in Figure 1.2, Chapter 1 is dedicated to the definition of the problem and the objectives to be achieved. Once this has been done, Chapter 2 presents a detailed bibliographic review focused on the filtration process and how state-of-the-art DPF models face it. On the other hand the current criteria for DPF design are analysed together with the pre-turbo aftertreatment configuration. Last, the pre-DPF water injection as a technique to limit the pressure drop of soot and/or ash loaded DPF is considered in the bibliographic review.

Given an overview of the current DPF filtration models in the literature, Chapter 3 is dedicated to the development and validation of a 1D DPF filtration model. The model considers the porous media as a packed bed of spherical particles. Main assumption of the proposed model is the experimentally well-known low soot penetration inside the porous wall. Because of the interest in the pre-turbo DPF configuration, the model is able to deal with the pulsating flow typical of this configuration.

In Chapter 4 the developed model is applied to the evaluation of the potential of the aftertreatment (DOC&DPF) volume downsizing. The DOC and DPF

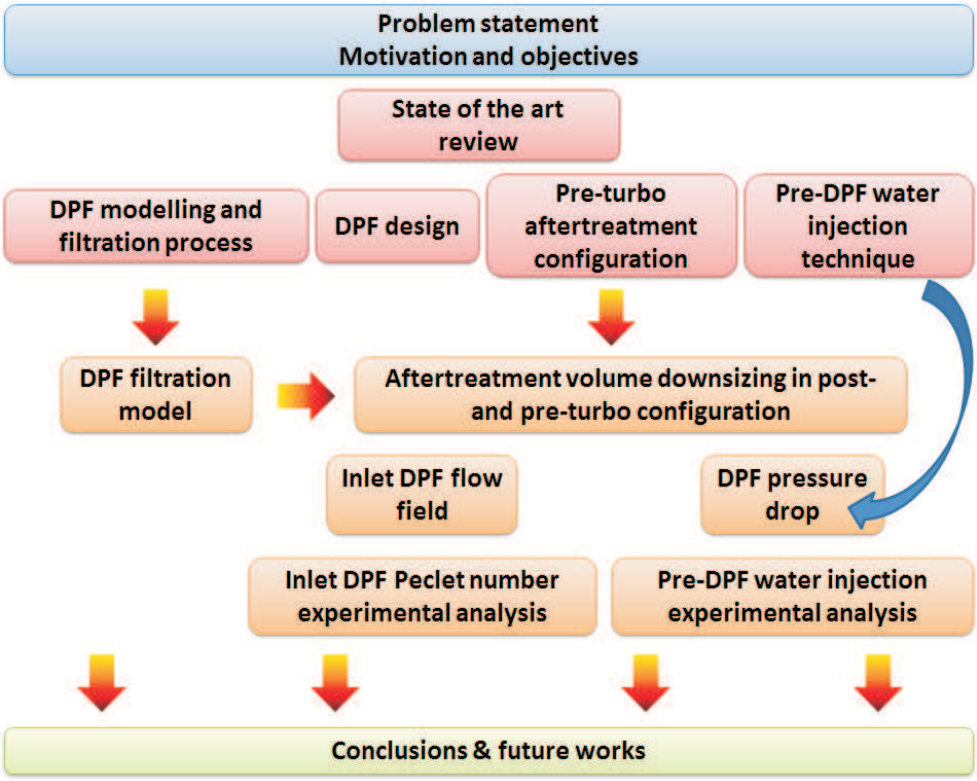

Figure 1.2: Scheme of the methodology followed in the present work.

volume reduction influence on DOC dwell time, DPF back-pressure, hence engine fuel consumption, and filtration efficiency are presented and compared between post- and pre-turbo aftertreatment positioning. The aftertreatment volume reduction impact on the final engine price and on the engine response under transient operation is also analysed.

Last, Chapter 5 is devoted to the experimental characterization of the inlet DPF Peclet number variation and of the pre-DPF water injection technique. The interest in the former is related to the inlet flow field variation related to the DPF volume downsizing and pre-turbo DPF positioning. On the other hand, the pre-DPF water injection is a recently patented technique proposed by CMT - Motores Térmicos [23] aimed to reduce and control the DPF pressure drop under soot loading conditions [24]. In the mark of the present thesis, the interest in this technique is related to its capability of reducing or avoiding the risk of channels clogging.

The main conclusions of the work are summarized in Chapter 6 in which proposals for future works are also listed.

1.5 References

[1] F. Payri and J. Desantes. *Motores de combustión interna alternativos*. Ed. by E. Reverté. 2015 (cit. on p. 3).

[2] N. Okui and M. Kobayashi. "A study on hybrid control method for improvement of fuel economy and exhaust-gas emission of hybrid trucks". In: *SAE Technical Paper 2015-01-1780*. 2015 (cit. on p. 3).

[3] T. C. Bond, S. J. Doherty, D. W. Fahey, P. M. Forster, and et al. "Bounding the role of black carbon in the climate system: A scientific assessment". In: *Journal of Geophysical Research: Atmospheres* 118(11) (2013), pp. 5380–5552 (cit. on p. 3).

[4] G. Oberdster and M. J. Utell. "Ultrafine particles in the urban air: to the respiratory track and beyond". In: *Environmental Health Perspectives* 110(8) (2002), A440–A441 (cit. on p. 3).

[5] C. A. Pope and D. W. Dockery. "Health effects of fine particulate air pollution: lines that connect". In: *Journal of the Air and Waste Management Association* 56(6) (2006), pp. 709–742 (cit. on p. 3).

[6] A. Gupta, V. Kartik, and C. Ramanarayanan. "Experimental study on performance of a parallel Diesel hybrid vehicle retrofitted with a single planetary gear train as an add-onn transmission". In: *SAE Technical Paper 2016-28-0154*. 2016 (cit. on p. 3).

[7] A. Lajunen. "Energy efficiency of conventional, hybrid electric, and fuel cell hybrid powertrains in heavy machinery". In: *SAE Technical Paper 2015-01-2829*. 2015 (cit. on p. 3).

[8] A. Burke. "Saving petroleum with cost-effective hybrids". In: *SAE Technical Paper 2003-01-3279*. 2003 (cit. on p. 3).

[9] *Regulation (EC) No 715/2007 of the European Parliament and of the Council of 20 June 2007 on type approval of motor vehicles with respect to emissions from light passenger and commercial vehicles (Euro 5 and Euro 6) and on access to vehicle repair and maintenance information*. Official Journal of the European Union. 2007 (cit. on pp. 3, 62).

[10] J. R. Serrano, F. J. Arnau, P. Piqueras, and O. García-Afonso. "Packed bed of spherical particles approach for pressure drop prediction in wall-flow DPFs (diesel particulate filters) under soot loading conditions". In: *Energy* 58 (2013), pp. 644–54 (cit. on pp. 3, 15, 17, 19, 63, 71, 73, 82, 87, 167).

[11] S. Nishina, K. Takeuchi, M. Shinohara, M. Imamura, M. Shibata, Y. Hashimoto, and F. Watanabe. “Novel nondestructive imaging analysis for catalyst washcoat loading and DPF soot distribution using terahertz wave computed tomography”. In: *SAE International Journal of Fuels and Lubricants* 5(1) (2011), pp. 343–351 (cit. on pp. 3, 189).

[12] Y. Liu, C. Su, A. Clerc J.and Harinath, and L. Rogoski. “Experimental and modeling study of ash impact on DPF backpressure and regeneration behaviors”. In: *SAE International Journal of Engines* 8(3) (2015), pp. 1313–1321. (Cit. on pp. 3, 189, 249).

[13] A. G. Konstandopoulos, E. Skaperdas, and M. Masoudi. “Microstructural properties of soot deposits in Diesel particulate traps”. In: *SAE Technical Paper 2002-01-1015*. 2002 (cit. on pp. 3, 27, 189, 206, 227).

[14] J. Liu, J. J. Swanson, D. B. Kittelson, D. Y. H. Pui, and J. Wang. “Microstructural and loading characteristics of diesel aggregate cakes”. In: *Powder Technology* 241 (2013), pp. 244–251 (cit. on pp. 3, 189, 206, 214, 227).

[15] H. Hiereth. “Daimler-Benz AG car test with a free-running pressure-wave charger - A study for an advanced supercharging system”. In: *SAE Technical Paper 890453*. 1989 (cit. on pp. 4, 40).

[16] E. Jenny, J. Hansel, and A. Mayer. “The transient behaviour of supercharged passenger car diesel engines fitted with particulate traps”. In: *SAE Technical Paper 890453*. 1989 (cit. on pp. 4, 40).

[17] D. Moya. “Contribución a la predición del ruido pulsante de admisión y escape en motores de combustión interna alternativos”. PhD thesis. Universitat Politécnica de Valéncia, 2005 (cit. on p. 4).

[18] P. Piqueras. “Contribution to thermo-and fluid dynamic modelling of wall-flow Diesel particulate filters (text in spanish)”. PhD thesis. Universitat Politécnica de Valéncia, 2010 (cit. on pp. 4, 16).

[19] O. García-Afonso. “Analisis teorico-experimental de la arquitectura pre-turbo de sistemas de post-tratamiento en MCIA”. PhD thesis. Universitat Politécnica de Valéncia, 2013 (cit. on pp. 4, 42).

[20] M. Reizig, R. Brück, R. Konieczny, and P. Treiber. “New Approaches to Catalyst Substrate Application for Diesel Engines”. In: *SAE Technical Paper 2001-01-0189*. 2001 (cit. on p. 4).

[21] B. Carberry, G. Grasi, S. Guerin, F. Jayat, and R. Konieczny. “Pre-turbocharger Catalyst - Fast catalyst light-off evaluation”. In: *SAE Technical Paper 2005-01-2142*. 2005 (cit. on pp. 4, 121).

[22] *SCR system for 2-Stroke MAN Diesel Engines*. Johnson Matthey webpage: www.jmcatalysts.com. 2009 (cit. on p. 4).

[23] J. M. Desantes, F. Payri, P. Piqueras, and J. R. Serrano. *Sistema de filtro*. Spanish Patent ES2408243(B1). 2013 (cit. on pp. 5, 8, 16, 43).

[24] V. Bermúdez, J. R. Serrano, P. Piqueras, and O. García-Afonso. "Pre-DPF water injection technique for loaded DPF pressure drop reduction and control". In: *Applied Energy* 140 (2015), pp. 234–245 (cit. on pp. 5, 8, 43, 44, 48, 80, 203).

[25] V. Bermúdez, J. R. Serrano, P. Piqueras, and D. Campos. "Analysis of the influence of pre-DPF water injection technique on pollutants emission". In: *Energy* 89 (2015), pp. 778–792 (cit. on pp. 5, 45–47, 65, 216, 233).

CHAPTER 2

Background and state of the art

Contents

Figures

2.1 Introduction

AFTERTREATMENT systems have become essential in the last decades in both spark and compression ignition engines due to the always more stringent emission legislations [26]. Their correct operation in terms of pollutants conversion efficiency as well as the consequences of their implantation in the exhaust line on the engine and the turbocharger performance need to be evaluated.

Due to the high cost and complexity of the experimental tests for this purpose the use of aftertreatment simulation software has grown in parallel with the application of such these systems. Engine manufacturers and research centres make an intensive use of 1D codes as they provide accurate results while keeping their computational cost low enough to be used during intensive and broad simulation campaigns.

In the specific case of the DPF it is of great importance the correct definition of the filter size and micro- and meso-structure because of their impact on the filter performance and on the engine behaviour.

In this section the actual DPF model implemented in OpenWAM™ is described. Particular attention will be dedicated to the pressure drop sub-model (Section 2.2.2) because of its deep connection with the developed filtration model. Highlight that the existing DPF model was already able to keep into account the effect of the presence of soot in the filter on the generated pressure drop [10]. Nevertheless before the implementation of the proposed filtration model only discrete soot loads with homogeneous soot distribution could be taken into account. Therefore only the presence of a given fixed soot mass could be simulated, there was no possibility of simulating, for example, a soot loading process in a stationary engine point nor the particles accumulation inside the filter during a certification cycle like the NEDC or WLTC. In the specific, the presence of soot inside the DPF affects the filter, the turbocharger and the engine behaviour in terms of filtration efficiency, pressure drop, VGT position and bsfc respectively. Obviously in order to get reliable results all these parameters need to be precisely evaluated.

The most relevant DPF filtration models from the literature will be then presented together with the current state of the art in DPF design. Parameters such as substrate material, porous media micro-structure, monolith sizing and meso-structure deeply influence the filter thermo-mechanical, filtration and regeneration performance. Thus it is useful to define the relation between these parameters and the filter behaviour.

In the mark of the optimization of the filter behaviour two strategies are presented: the pre-turbo aftertreatment configuration and the pre-DPF water injection technique. The benefits related to the former have been explored since the early 80's. The latter is a new technique developed by CMT - Motores Térmicos aimed to the reduction of the back-pressure generated by soot and/or

ash loaded DPFs [23]. This technique has showed to be effective for the control and limitation of the filter pressure drop with no negative effects on the filtration efficiency and the regeneration behaviour.

2.2 Wall-flow DPF modelling in OpenWAM™

OpenWAM™ is a 1D, open-source gas dynamics software for internal combustion engines and components computation developed at CMT - Motores Térmicos [27] [28]. It includes a wall-flow DPF model that assumes one-dimensional, unsteady, compressible and non-homentropic flow solving the governing equations in the inlet and outlet channels. As detailed by Piqueras in [18], the model provides the possibility of a radial axisymmetric discretization of the filter in various channels' beams. The possibility of describing the thermo- and fluid-dynamic behaviour of a channel as a function of its radial positioning is of great interest when considering a non-uniform mass flow and/or temperature distribution at the filter inlet as both these cases strongly affect the heat transfer, filtration and regeneration performance [29]. Only one couple of inlet-outlet channels is solved for every considered channels beam, as proposed by Bisset [30]; the inlet-outlet channels flow field is coupled by the source terms related to the porous substrate [29].

2.2.1 Governing equations

The solved equations are the mass, momentum and energy conservation. In the following subscript j identifies the type of monolith channel and takes into account the existence of particulate layer. It takes value 0 to represent the governing equations of the outlet channels and 1 in the case of inlet channels.

- Mass conservation

$$\frac{\partial\left(\rho_j F_j\right)}{\partial t}+\frac{\partial\left(\rho_j u_j F_j\right)}{\partial x}=(-1)^j 4\left(\alpha-2w_{pl}j\right)\rho_j u_{w_j} \tag{2.1}$$

- Momentum conservation

$$\frac{\partial\left(\rho_j u_j F_j\right)}{\partial t}+\frac{\partial\left(\rho_j u_j^2 F_j+p_j F_j\right)}{\partial x}-p_j\frac{dF_j}{dx}=-F_w\mu_j u_j \tag{2.2}$$

- Energy conservation

$$\frac{\partial\left(e_{0j}\rho_j F_j\right)}{\partial t}+\frac{\partial\left(h_{0j}\rho_j u_j F_j\right)}{\partial x}= q_j\rho_j F_j+(-1)^j 4\left(\alpha-2w_{pl}j\right)h_{0w}\rho_j u_{w_j} \tag{2.3}$$

The system of governing equations is closed with the ideal gas state equation applied to the inlet and outlet channels and by the equation governing the pressure drop in the porous medium. This is based in the Darcy's law applied across the porous wall and the particulate layer [29]. Therefore, assuming incompressible unsteady flow across the porous media, the filtration velocity in the inlet channel is calculated as:

$$u_{w_1}=\frac{p_1-p_0}{\frac{\mu_1 w_w}{k_w}\frac{\rho_1(\alpha-2w_{pl})}{\rho_0\alpha}+\frac{\mu_1(\alpha-2w_{pl})}{2k_{pl}}\ln\left(\frac{\alpha}{\alpha-2w_{pl}}\right)} \tag{2.4}$$

The filtration velocity corresponding to the outlet channel is then calculated based on the continuity equation applied to the porous medium:

$$u_{w_0}=\frac{u_{w_1}\rho_1\left(\alpha-2w_{pl}\right)}{\rho_0\alpha} \tag{2.5}$$

2.2.2 Pressure drop sub-model

As indicated in eq. 2.4, the fluid-dynamic field is a function of the permeability of the porous substrate (k_w) and the particulate layer (k_{pl}). In turn, the permeability depends on microstructure properties, such as the porosity (ε) and the mean pore diameter (d_p) [31], as well as the slip-flow effect (SCF) [32]. Therefore, the permeability of every porous medium is determined according to eq. (2.6) [10]:

$$k=\frac{2}{9(1-\varepsilon)}Kd_c^2 SCF \tag{2.6}$$

Here K is the Kuwabara's hydrodynamic factor [33] and is computed as:

$$K=2-\varepsilon_w-\frac{9}{5}(1-\varepsilon_w)^{\frac{1}{3}}-\frac{1}{5}(1-\varepsilon_w)^2 \tag{2.7}$$

In the case of the porous wall the effective permeability is computed applying eq. 2.8.

$$k_{w,e}=\frac{k_w k_{w_0}}{f_w k_{w_0}+(1-f_w)k_w} \tag{2.8}$$

This expression accounts for the existence of one layer with soot deposition, thus varying its microstructure as a function of the soot loading, followed by a porous wall layer that is kept clean. The thickness of the former layer f_w is of critical importance for the correct modelling of the filter performance and their

evolution as soot is collected. A correlation for its estimation has been developed within this PhD thesis and will be detailed in Section 3.8.

In the following it will be showed how the model calculates the porous wall permeability in clean conditions from given microstructure properties and the variation they suffer as a consequence of particles deposition.

Basic assumption of the model is that the porous medium behaves like a packed bed of spherical particles. That is, the porous wall is assumed to be formed by partially void spheres occupied in the centre by a collector unit, as sketched in Figure 2.1.

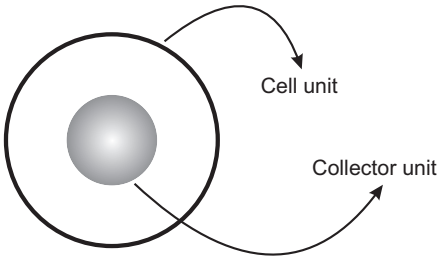

Figure 2.1: Sketch of a cell unit forming the packed bed of spherical particles.

The diameters of the clean collector (d_{c,w_0}) and cell unit ($d_{cell,w}$) depend on the microstructure of the porous medium, i.e. porosity (ε_{w_0}) and mean pore diameter (d_{p,w_0}), and are respectively calculated as:

$$d_{c,w_0} = 1.5\frac{\left(1-\varepsilon_{w_0}\right)}{\varepsilon_{w_0}} d_{p,w_0} \tag{2.9}$$

$$d_{cell,w} = \frac{d_{c,w_0}}{\left(1-\varepsilon_{w_0}\right)^{\frac{1}{3}}} \tag{2.10}$$

The characteristics of the clean porous wall (ε_{w_0} and d_{p,w_0}) are either given by the porous media supplier or obtained following the experimental-theoretical procedure proposed by Payri *et al.* [32]. Known these parameters it is possible to calculate the clean porous medium permeability by applying eq. 2.6. Additionally the cell unit diameter permits calculating its volume and from it the total number of cell units of the porous wall affected by soot deposition.

$$n_{cell} = \frac{4\alpha L_e w f_w N_{ic}}{\pi \frac{d_{cell,w}^3}{6}} \tag{2.11}$$

Looking at eq. 2.11 it is possible to note that the number of cell units depends on the porous medium microstructure by means of $d_{cell,w}$ and on the

filter geometry by means of the effective length L_e, the inlet channels number N_{ic}, the cell width α and the wall thickness w_w. It is worth to highlight here that only the portion of porous wall thickness affected by soot penetration f_w is considered in the computation of the total cells number. The importance of this parameter will result clear later on in the analysis of the soot loading processes carried out in Chapter 3.

As soot is collected inside the porous wall particles stick on the collector unit until the cell unit is saturated. As showed in Figure 2.2 the model considers that particles are deposited around the collector unit in an irregular way [10].

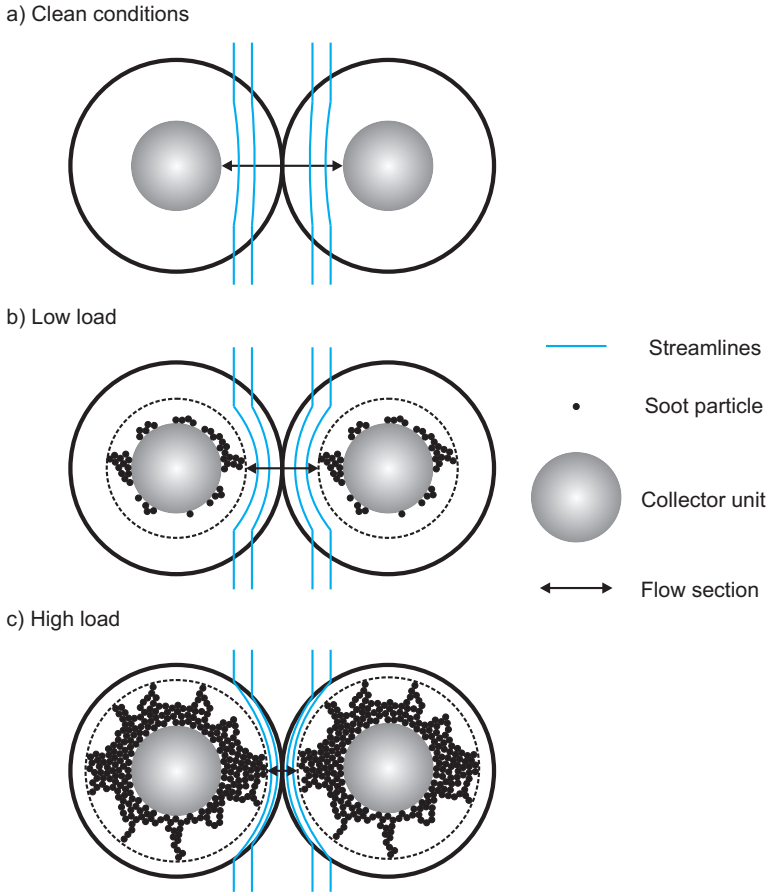

Figure 2.2: Sketch of the irregular particles deposition around the collector unit.

In order to mathematically take into account this irregularity, the collector unit growth is modelled as in eq. 2.12. Here the apparent soot density inside the cell unit is obtained multiplying ρ_{s_w} by a shape factor χ. Nominal value for

ρ_{s_w} is assumed to be 345 kg/m^3, which is the density of soot aggregates with medium fractal dimension and medium number of primary particles obtained by Lapuerta *et al.* [34] assuming the carbon density to be 2000 kg/m^3 as proposed in the late eighties by Heywood [35] and more recently by Dobbins [36] and Kondo *et al.* [37].

$$d_{c,w} = 2\left(\frac{d_{c,w_0}^3}{8} + \frac{3m_{s_{cell}}}{4\pi\chi\rho_{s_w}}\right)^{\frac{1}{3}} \tag{2.12}$$

The shape factor takes into account the irregular deposition of aggregates around the collector unit. Its value increases as the soot loading does, being 1 the value corresponding to a perfect spherical growth of the collector unit. The shape factor obeys an expression of the type

$$\chi = a\left(\Phi_{\rho_s}\right)^b + c \tag{2.13}$$

where Φ_{ρ_s} is the soot density factor. It is defined as the ratio between the soot packing density inside the porous wall and the soot mass to soot penetration volume ratio, i.e. it is the ratio between the real and the virtual soot density inside the porous wall. It is calculated at every time-step and calculation node of the 1D discretization as:

$$\Phi_{\rho_s} = \frac{\rho_{s,w}}{m_{s,w}/V_p} \tag{2.14}$$

Since the cell unit diameter is constant, as the collector unit diameter increases the porosity and mean pore diameter decrease as in eq. 2.15 and eq. 2.16 respectively.

$$\varepsilon_w = 1 - \left(\frac{d_{c,w}}{d_{c,w_0}}\right)^3 \left(1 - \varepsilon_{w_0}\right) \tag{2.15}$$

$$d_{p,w} = \frac{2}{3}\frac{\varepsilon_w}{(1-\varepsilon_w)} d_{c,w} \tag{2.16}$$

Consequently the porous wall permeability decreases leading to the pressure drop increase as soot is accumulated in the filter. In parallel, also the capability of collecting particles increases. The cell unit has a finite soot storage capacity so that this process has a limit. The saturation mass of a cell unit is proportional to the void volume of the cell, i.e. the difference between the cell unit and the clean collector unit volumes. It is calculated as:

$$m_{sat_{cell}} = \frac{4}{3}\pi\rho_{s,w}\left(\left(\psi\frac{d_{cell,w}}{2}\right)^3 - \left(\frac{d_{c,w_0}}{2}\right)^3\right) \tag{2.17}$$

The degree of saturation of the cell unit is computed by mean of a porous wall saturation coefficient ϕ:

$$\phi = \frac{d_{c,w}^3 - d_{c,w_0}^3}{\left(\psi d_{cell,w}\right)^3 - d_{c,w_0}^3} \tag{2.18}$$

where ψ is a dimensionless percolation factor whose value, usually close to 0.9 [38], has to be estimated from experimental data.

The upper limit of ϕ is 1, once this extreme value is reached the cell unit is said to be saturated, i.e. no further soot can be collected inside it. The saturation mass of the whole filter m_{sat} is obtained multiplying the cell unit saturation mass $m_{sat_{cell}}$ for the number of unit cells in the porous wall where soot is deposited (n_{cell}). This value sets the border between the deep bed and the cake filtration phases. Its correct estimation is of great importance for the precise simulation of the filter performance, i.e. pressure drop and filtration efficiency. As stated above in eq. 2.11, n_{cell} depends on one hand on the micro- and macrostructure of the filter and on the other hand on the soot penetration inside the porous wall. As the first parameters are given the importance of the soot penetration thickness (f_w) results evident.

Once the porous wall gets saturated the additional collected soot is deposited above the porous wall developing a particle layer. For every inlet channel finite volume of length Δx_k (Figure 2.3) the influence of the layer on the flow field is related with its thickness w_{pl_k} and permeability k_{pl_k} (eq. 2.4). The former parameter is calculated as:

$$\alpha^2 - \left(\alpha - 2w_{pl_k}\right)^2 = \frac{m_{pl_k}}{\rho_{s,pl}\Delta x_k} \Rightarrow w_{pl_k} = \frac{\alpha - \left(\alpha^2 - \frac{m_{pl_k}}{\rho_{s,pl}\Delta x_k}\right)^{\frac{1}{2}}}{2} \tag{2.19}$$

where m_{pl_k} is the soot mass in the particle layer referred to the control volume k. The cake layer density $\rho_{s,pl}$ is calculated from the supposed cake layer porosity assuming the carbon density ρ_C to be 2000 kg/m^3.

$$\rho_{s,pl} = (1 - \varepsilon_{s,pl})\rho_C \tag{2.20}$$

On the other hand, the particulate layer permeability is calculated applying eq. 2.6.

Apart from the above detailed contributions of the porous wall and the particulate layer to the pressure drop, the model takes into account inertial pressure losses. Figure 2.4 helps understanding how the model considers these contributions to the global canned DPF pressure drop. The inlet and outlet connection cones of the DPF are modelled as 0D elements (volumes #1 and #2 in Figure 2.4). In any of these volumes two boundary conditions connecting 0D and 1D elements (ducts or monolith channels) are identified. So boundary conditions

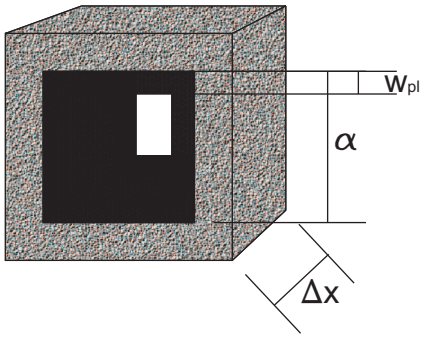

Figure 2.3: Scheme of an inlet channel finite volume with particle layer

#1 and #2 in Figure 2.4 are used to model the expansion in the inlet cone and the contraction in the outlet one. Boundary conditions #3 and #4 represent the pressure drops related with the flow contraction/expansion due to the sudden variation of the cross section area at the channel inlet/outlet respectively. The definition of the discharge coefficients in this kind of boundaries, whose detailed solution can be consulted in [28] [39], allows calculating the pressure drop at the inlet and outlet of every volume.

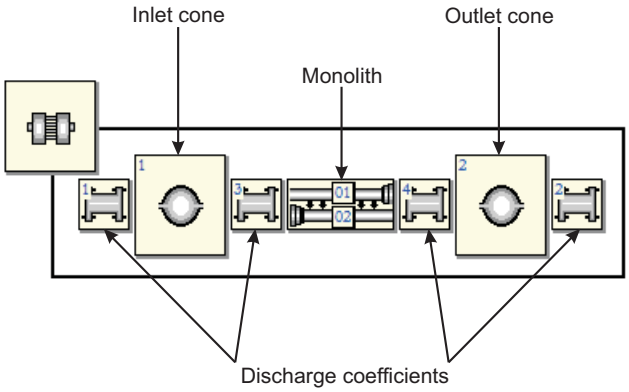

Figure 2.4: DPF model scheme in OpenWAM™.

2.2.3 Heat transfer sub-model

The heat transfer sub-model is based on the bidimensional discretization of the porous medium between the inlet and the outlet channels of the monolith [40]. The nodal scheme is represented in Figure 2.5. Additionally, the monolith

can be discretised in the radial direction by means of concentric channel beams where all the pairs of inlet and outlet channels are assumed to behave the same. The model also considers the coupling between the concentric beams in order to account for the conductive heat transfer in the radial direction.

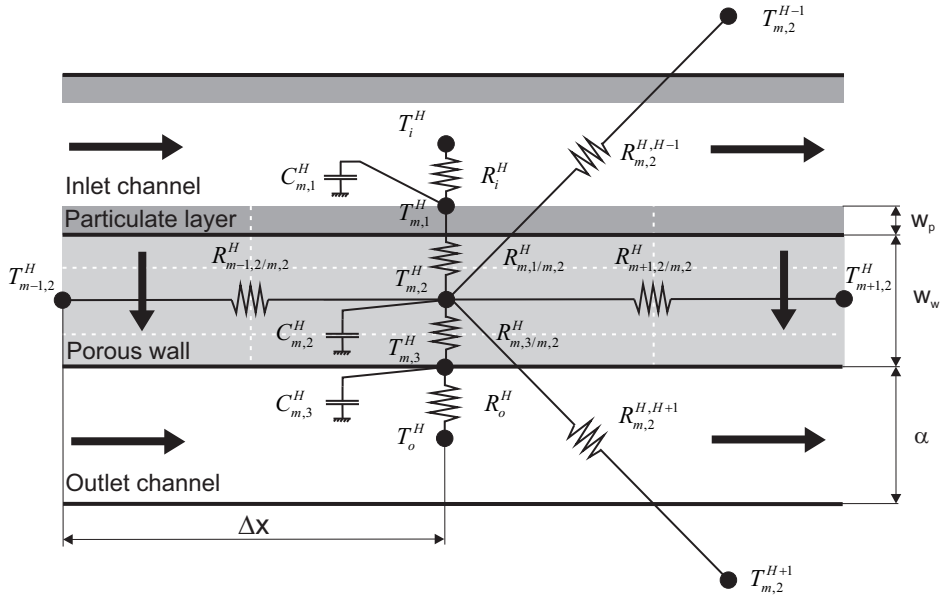

Figure 2.5: Nodal scheme of the heat transfer sub-model in the porous substrate [40].

As shown in Figure 2.5 in every axial section 5 nodes are considered:

- in the inlet/outlet channel for the gas phase T_i^H and T_o^H;
- in the interface between the porous medium (porous wall or particulate layer) and the gas phase of the inlet channel $T_{m,1}^H$;
- in the middle of the porous wall $T_{m,2}^H$;
- in the interface between the porous wall and the gas phase of the outlet channel $T_{m,3}^H$.

The existence of the particulate layer is taken into account in order to properly model its effect on the effective tangential conductivity.

The outer monolith beam is connected with the DPF canister, where a specific bi-dimensional discretization, depicted in Figure 2.6, is also proposed. It allows

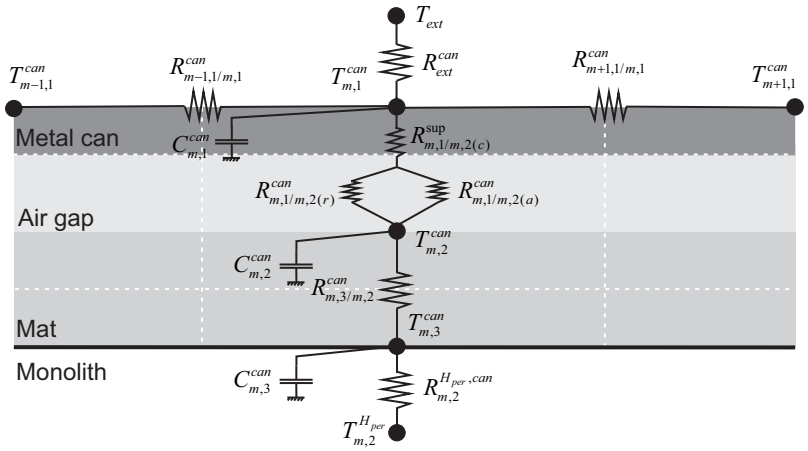

Figure 2.6: Nodal scheme of the heat transfer sub-model in the external canister [40].

providing the wall and gas temperature field in the DPF, assuming axisymmetric behaviour and including both the monolith and the canister [40].

As a last contribution the model considers the heat transfer due to conduction between the inlet and outlet ducts to the respective cones, and from these to the canister, to properly represent the wall temperature field [40].

2.3 Filtration models

In order to correctly model the filtration process the characteristics of the dispersed particles, the carrying fluid and the porous media need to be well known as any of these parameters influences the process. Fuchs [41] and Friedlander [42] proposed filtration theories based on aerosol collection by an isolated sphere making use of the Stokes [43] and Tomotika and Aoi [44] solutions for the flow field respectively. However these flow fields are inadequate for filtration theories of packed spheres as they do not take into account the mutual interference effects of neighbouring spheres on the flow field [45]. Kuwabara [33] and Happel [46] proposed similar solutions for the flow field both considering $v=0$ at the sphere surface and zero vorticity or vanishing shearing stress at the outer boundary respectively. In spite of the similarity, Kuwabara's solution resulted to be a better approximation of the flow field in packed beds as stated by Lee *et al.* [47], Kirsh [48] and Yeh [49] and has been used by Lee and Gieseke [45] to obtain a formula for the collection efficiency of a packed bed. In the last years various models based on the single collector sphere approach have been

proposed to calculate the filtration efficiency of a DPF and its evolution with soot loading.

Konstandopoulos *et al.* [38] introduced the porous wall discretization in the direction perpendicular to the axial flow. As sketched in Figure 2.7, the porous wall is divided into slabs whose efficiency is calculated considering Brownian and interception collection mechanisms of the single sphere.

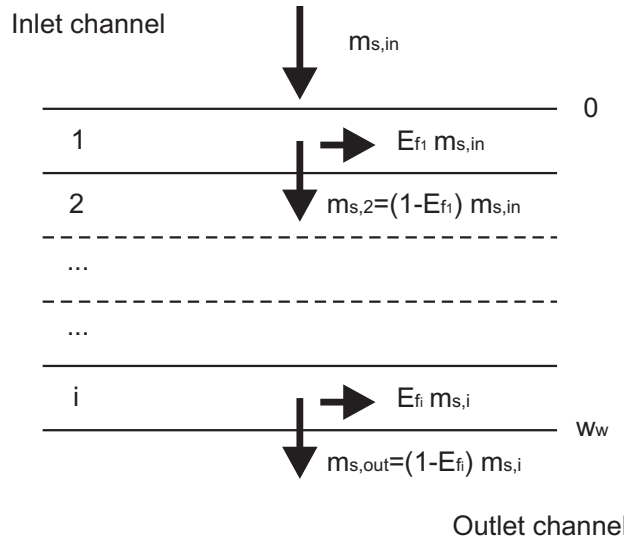

Figure 2.7: Scheme of the porous wall discretization proposed by Konstandopoulos *et al.*. Adapted from [38].

The single spherical collector efficiency for Brownian diffusion is given by:

$$\eta_D = 3.5 g(\varepsilon) Pe^{-\frac{2}{3}} \tag{2.21}$$

where the Peclet number is defined as:

$$Pe = \frac{u_w d_c}{\varepsilon D_{part}} \tag{2.22}$$

and $g(\varepsilon)$ is the geometric function for the Kuwabara unit cell:

$$g(\varepsilon) = \left[\frac{\varepsilon}{2 - \varepsilon - \frac{9}{5}(1-\varepsilon)^{\frac{1}{3}} - \frac{1}{5}(1-\varepsilon)^2} \right]^{\frac{1}{3}} \tag{2.23}$$

In eq. 2.22 D_{part} represents the diffusion coefficient of the particles in the porous substrate. It is calculated as:

$$D_{part} = \frac{Tk_B SCF}{3\pi\mu d_p} \tag{2.24}$$

where k_B is the Boltzmann constant. The diffusion coefficient is inversely proportional to the particle diameter, smaller particles diffuse more inside the porous wall. The temperature has an opposite effect: a higher temperature promotes diffusion. Both these contributions make the diffusion mechanism more important than the advection one leading to an increase in the Brownian efficiency. For the same reason a lower velocity results in higher Brownian efficiency.

The second filtration mechanism considered by Konstandopolous is the one due to interception. Once again the model calculates the single sphere collection efficiency due to interception according to eq. 2.25:

$$\eta_R = 1.5 N_R^2 \frac{[g(\varepsilon)]^3}{(1+N_R)^s} \tag{2.25}$$

Here N_R is the interception parameter computed as:

$$N_R = \frac{d_p}{d_c} \tag{2.26}$$

and the exponent s is a function of the porosity:

$$s = \frac{3-2\varepsilon}{3\varepsilon} \tag{2.27}$$

Looking at eq. 2.26 and eq. 2.27 it results clear that the efficiency related to the interception mechanism is dependent on the relative dimension of the particle and the collector unit. Thus this contribution to the filtration efficiency increases as the particle diameter does.

Once the efficiency of the two mechanisms has been calculated as in eq. 2.21 and eq. 2.25 it is necessary to calculate the mutual effect they have on each other. Making use of the independence rule the resulting combined efficiency can be expressed as:

$$\eta_{DR} = \eta_D + \eta_R - \eta_D \eta_R \tag{2.28}$$

Knowing the collection efficiency of a single sphere it is possible to calculate the overall efficiency of the considered slab i. The single collector filtration efficiency is then related to the filtration efficiency of one slab through a mass

balance that, for a packed bed filter composed of uniform spheres, results in [45] [50]:

$$E_f(i) = 1 - \mathrm{e}^{\left[-\frac{3\eta_{DR}(i)(1-\varepsilon(i))(z_{i+1}-z_i)}{2\varepsilon(i)d_{cu}(i)}\right]} \tag{2.29}$$

where $(z_{i+1} - z_i)$ defines the thickness of the considered slab.

Every slab forming the porous wall has a finite soot accumulation capacity. In the case of the first slab the fraction of soot mass that forms the cake layer is determined making use of a partition coefficient, ranging from 0 to 1, whose definition is given by:

$$\Phi = \left(\frac{d_{cu}^2 - d_{cu,0}^2}{\left(\psi d_{cell}^2\right) - d_{cu,0}^2} \right) \tag{2.30}$$

Comparing Φ with ϕ (eq. 2.18) it is immediate to note that the first is calculated basing on 2D considerations, i.e. it defines the blocked area of the single cell unit, while the second is based on 3D considerations, i.e. it evaluates the available volume for soot storage in the cell.

Based on Konstandopoulos model, Johnson *et al.* [51] developed a parametric model to simulate the filtration by the particulate layer based on eq. 2.31. It can be noted that the structure of the equation is similar to eq. 2.29, used for the evaluation of the porous wall efficiency. In eq. 2.31 the collector unit diameter in the cake is assumed to be the diameter of the soot aggregates, usually in the range of 100-250 nm [13] [52]. Additionally two empirical parameters are considered: A_η to avoid E_f of the cake being 100% and η_c to represent the collection efficiency of a single particle. Both these parameters need to be calibrated to fit pressure drop and filtration efficiency data.

$$\eta_{pl} = A_\eta \left(1 - \mathrm{e}^{\eta_c \frac{w_{pl}}{d_{c,pl}}} \right) \tag{2.31}$$

Eq. 2.31 states that cake layer thickness (w_{pl}) is of great importance in the calculation of the cake efficiency. In contrast to the porous wall case, the cake layer filtration model assumes no variations of the cake microstructure (porosity and collector unit diameter) while the particles are deposited. The only effect of the deposition is the increase of the layer thickness. As a consequence it is important to precisely calculate the growth/reduction of the cake thickness related with particles deposition/oxidation respectively. To achieve the needed precision the particulate layer is divided into 2 layers in order to properly represent the effect of the catalyst on the oxidation of soot during the regeneration process. With this approach, also used by Huinh *et al.* [53], a precise characterization of the soot mass burned in the regeneration can be obtained. As a result an exact calculation of the variation of the cake layer thickness related to this process is obtained.

The transition from porous wall to cake layer filtration is modelled making use of a partition coefficient calculated as proposed by Konstandopoulos *et al.* (eq. 2.30). Particles are collected inside the porous wall until the partition coefficient is higher than the cake efficiency value. Once the two values are equal the model considers that the particle layer is filtering with an efficiency given by eq. 2.31. In this way a smooth transition from deep bed to cake filtration regime is obtained.

Last, the model proposed by Johnson *et al.* introduced the possibility of taking into account the particle size distribution in the evaluation of the filtration efficiency. As a result both the soot mass and the particle size distribution (PSD) can be evaluated at the filter outlet.

In the past years Tandon *et al.* [54] introduced the inertial contribution in the evaluation of the single sphere collection efficiency making use of the formula proposed by Langmuir [55]. The dynamic of the filtration efficiency evolution is modelled considering two distinct regimes separated by a transition permeability. Until the porous wall permeability is higher than the transition one the rapid increase of E_f is due to the reduction of wall porosity and increase of the collector unit diameter. Once the critical value of the permeability is reached, the additional soot deposition results in the reduction of the number of collectors due to the blocking of some of the pores. As a consequence the E_f increase is more gradual. Once the number of collectors has dropped to a critical value the cake layer starts its formation and growth.

Another relevant contribution is the one proposed by Bollerhoff *et al.* [56]. This model is implemented in Axitrap, the wall-through filters model of the package Axisuite [57], and is able to account for multiple layers inside or above the wall structure with variable geometrical/filtration properties. PSD at the entrance of the filter can be considered. Also in this model the filtration efficiency is evaluated for a single sphere considering the Brownian diffusion and interception deposition mechanism separately. However, as shown in eq. 2.32, in this case the combined single grain efficiency is calculated as a simple sum of the two filtration efficiencies. As the product is not subtracted according to the independence rule (eq. 2.28) the obtained values are slightly higher.

$$\eta_{DR,0} = \eta_{D,0} + \eta_{R,0} \tag{2.32}$$

The considerable difference with respect to other models is the computation of the E_f evolution by means of an empirical correlation. The correlation is based on a wall saturation index (eq. 2.33) to consider the effect of the soot deposition inside the porous media.

$$W_{cap} = \frac{\varepsilon_{w,0} - \varepsilon_w}{\varepsilon_{w,0}} \tag{2.33}$$

W_{cap} is then used to estimate the loaded grain efficiency by means of eq. 2.34.

$$\eta_{DR} = \eta_{DR,0} + \left(1 - \eta_{DR,0}\right) f\left(W_{cap}\right) \tag{2.34}$$

As W_{cap} ranges from 0 in clean conditions to 1 when the porosity is equal to 0, the loaded grain efficiency tends to 100% as particles are collected. Finally the filtration efficiency of every layer is evaluated as:

$$E_{f,w} = 1 - e^{-\eta_R \left(\frac{3\left(1-\varepsilon_{w,0}\right)}{2\varepsilon_{w,0}} \frac{\Delta w}{d_{c,0}} \right)} \tag{2.35}$$

Also the model proposed by Bollerhoff *et al.* considers a transition from wall to cake filtration. In this model however it is a slow process resulting from the overlapping of two cake filtration mechanisms. The first one represents the initial formation of the first cake layer on a clean wall surface due to wall saturation. This is expressed mathematically by a linear function of the cake filtration efficiency as a function of the wall porosity. Cake filtration starts after wall porosity has reduced beyond a critical limit. The second mechanism represents the final steps of cake formation from a sparse collection of particles to a dense particle structure. In this case the cake filtration efficiency is no more expressed as a function of wall porosity but as a linear function of cake mass. When no cake is existing, mechanism 2 does not contribute to soot filtration. As the cake is formed, the particles, accumulated on the surface, start to contribute to filtration. Finally a dense structure of particles is formed, which succeeds in full filtration of the incoming particles. As said before, there is some time of overlap of the two mechanisms during which the total cake filtration is evaluated as:

$$E_{pl,tot} = E_{mech1} + E_{mech2} - E_{mech1} E_{mech2} \tag{2.36}$$

Recently Gong and Rutland [58] proposed a filtration model that combines the classical filtration theory with the statistical theory to keep into account the heterogeneity in the porous medium microstructure. In this work the authors developed a probability density function (PDF) based heterogeneous multiscale filtration (HMF) model to predict filtration efficiency of clean particulate filters. The well-known influence of the pore structure on the filter performance reported by Fukushima and Ohno [59], Mizuno *et al.* [60] and Ogyu *et al.* [61] is taken into account by defining a PDF-based pore size distribution. As the collector unit diameter depends on the pore diameter it results

$$d_{c,w_i} = \frac{3(1-\varepsilon)}{2\varepsilon} d_{p,w_i}, \tag{2.37}$$

which defines the probability density function of the collector unit diameter as

$$PDF_{d_{c,w_i}} = \frac{2\varepsilon}{3(1-\varepsilon)} PDF_{d_{p,w_i}} \tag{2.38}$$

In previous equations i defines the pore diameter considered in the PDF. The authors make use of an analytical solution of the Stokes flow in a system of randomly packed spheres derived by Kuwabara [33]. Assuming the drag force exerted by the flow on an isolated sphere as

$$F_D = 3\pi\mu d_{c,w}\bar{U}, \tag{2.39}$$

in case of a system of spheres with a packing density $(1-\varepsilon)$ it turns into:

$$F_D = \frac{3\pi\mu d_{c,w}\bar{U}}{K(\varepsilon)} \tag{2.40}$$

In eq. 2.40 $\bar{U}$ is the mean superficial velocity far away from the sphere with diameter d_c and $K(\varepsilon)$ is the Kuwabara's hydrodynamic factor defined as:

$$K(\varepsilon) = 2 - \varepsilon_w - \frac{9}{5}(1-\varepsilon_w)^{\frac{1}{3}} - \frac{1}{5}(1-\varepsilon_w)^2 \tag{2.41}$$

Performing a linear momentum balance on the fluid in the control volume in steady state and assuming the pressure drop across the porous wall with thickness h is a simple summation of all the drag force around each sphere, it results:

$$A_f \Delta P = N_s F_D \tag{2.42}$$

The number of spheres N_s can be calculated as:

$$N_s = \frac{A_f h(1-\varepsilon_w)}{\frac{1}{6}\pi d_{c,w}^3} \tag{2.43}$$

Thus combining eq. 2.40 with eq. 2.42 and eq. 2.43 and resolving for $\bar{U}$ it results

$$U_i = \frac{K(\varepsilon)}{18\mu(1-\varepsilon)} \frac{\Delta P}{w_w} d_{c,w_i}^2 \tag{2.44}$$

in which the presence of spheres with different diameter d_{c,w_i} has already been taken into account.

Once U_i is calculated, the Brownian diffusion, interception and inertial deposition mechanisms are considered. The collection capability of the single sphere is calculated for any deposition mechanism as a function of the pore size, thus of the related collector diameter d_{c,w_i} (eq. 2.37) and flow velocity U_i

(eq. 2.44). So, for example, the Peclet number used in the evaluation of the first mechanism is defined as:

$$Pe_i = \frac{U_i d_{c,w_i}}{D_{part}} \tag{2.45}$$

Again the global filtration efficiency of the single sphere (η_{DRI}) is calculated with the independence rule and from there the efficiency of the porous wall with thickness w_w is given by:

$$E_{f,w}\left(d_{c,w_i}, d_{part}\right) = 1 - e^{-\frac{3(1-\varepsilon)w_w}{2\varepsilon}\frac{\eta_{DRI}\left(d_{c,w_i}, d_{part}\right)}{d_{c,w_i}}} \tag{2.46}$$

In eq. 2.46 the dependence of the filtration efficiency on the pore size and the particle size is explicitly expressed. The dependence on the pore size is eliminated by summing all the contributions from all the collectors with different sizes. Summing the fitted PDF weighted contributions from all of the collectors the filtration efficiency is finally obtained as:

$$E_{f,w}\left(d_{part}\right) = \frac{\int U_i E_{f,w}\left(d_{c,w_i}, d_{part}\right) PDF_{d_{c,w_i}} d\left(d_{c,w_i}\right)}{\int U_i PDF_{d_{c,w_i}} d\left(d_{c,w_i}\right)} \tag{2.47}$$

2.4 DPF design criteria

The main characteristics required when designing a wall-flow DPF typically are high filtration efficiency, low pressure drop, high maximum operating temperature, low thermal expansion, resistance to thermal and mechanical stress and chemical resistance to metal oxides [62]. Another important parameter in the definition of the DPF design is the filter maximum soot load (MSL). It is defined as the maximum amount of soot tolerated by the filter without degradation during severe regeneration [63]. From a structural point of view this parameter defines the interval between two regenerations. It is desirable that this magnitude is as great as possible in order to limit oil dilution and fuel consumption increase related to active regenerations. On the other hand, the pressure drop point of view has to be taken into account. The engine calibration requires that the back-pressure does not exceed a given value so that the lower soot load between the one defined by the MSL and the one defined by the filter pressure drop is taken as limit.

As a consequence a high filter MSL and a pressure drop as low as possible are required in order to keep long regeneration intervals. To maximize the useful life of the system also high mechanical resistance is required as well as a high filtration efficiency in order to fulfil emission legislations.

Ash accumulation inside the filter also needs to be carefully taken into account [64] [65]. Ash is incombustible particulate matter derived from lubricant oil, engine wear, fuel additives etc. It cannot be cleaned from DPF without mechanical ash removal process [66]. Its presence gradually increases the back-pressure of a DPF without soot loading. In contrast, when the simultaneous presence of soot and ash in the filter is considered the back-pressure is seen to firstly reduce with low ash loading and then rise again with further ash accumulation [67] [68].

Many efforts have been done since the implementation of the DPF in the engine exhaust line to optimize the above listed characteristics leading the DPFs to a continuous optimization and cost reduction process [69]. All of them have a dependence on the selected material and on the micro-, meso- and macro-structure of the filter. For the sake of clarity in the following the description will be separated for any of the above listed items.

2.4.1 Material

The selected material defines the thermo-mechanical characteristics of the dense substrate, in the following indicated with the "D" subscript. In the specific, thermal conductivity (λ), coefficient of thermal expansion (CTE), Young's modulus (E_z) and strength (σ) are key parameters in the substrate material selection [70].

Limiting the analysis to wall-flow filters, silicon carbide (SiC), cordierite (Cd) and aluminum titanate (AT) [71] are usual substrate materials for DPFs [72]. The firsts two are recognized as the most prevalent DPF materials since the 2000's [73]. SiC is mostly used in passenger car applications and is currently expanding into larger sizes for light-duty trucks applications [74]. Despite its high soot mass limit capability, high thermal conductivity and high material strength, DPFs made of this material tend to crack in case of high internal temperature distribution, e.g. under uncontrolled regeneration conditions, due to the relatively high coefficient of thermal expansion. In order to moderate the thermo-mechanical stress SiC DPFs are normally designed with small square segments bonded together with cement.

On the other hand cordierite has been the cost-effective material of choice for diesel particulate filters for heavy duty vehicles [75]. Its lower CTE indeed makes this material adequate for use in larger monolith structures.

Concerning aluminum titanate, filters made of this material have been firstly introduced in 2005 and have found broad commercial application in light-duty applications since this date [76]. By tightening the pore size distribution and reducing the porosity these kind of filters achieved either a 2-3 g/l increase in soot mass limit or a 20-25% back-pressure reduction, depending on cell geometry [77].

Also the use of advanced ceramic material like the acicular mullite has been considered for high performance Diesel engine applications. A DPF made of this porous material was developed in 2004 by Li *et al.* [78] and has been successfully applied to the Audi R10 TDI race car [79]. Despite the high filtration efficiency and low pressure drop related with the peculiar shape of the mullite grain (Figure 2.8(c)), this material is not widely used at the present days. It is interesting to highlight that although this mullite DPF was especially designed for the Le Mans race track the authors state that by optimizing this system design a size reduction up to 40% without impact on performance could be achieved [79].

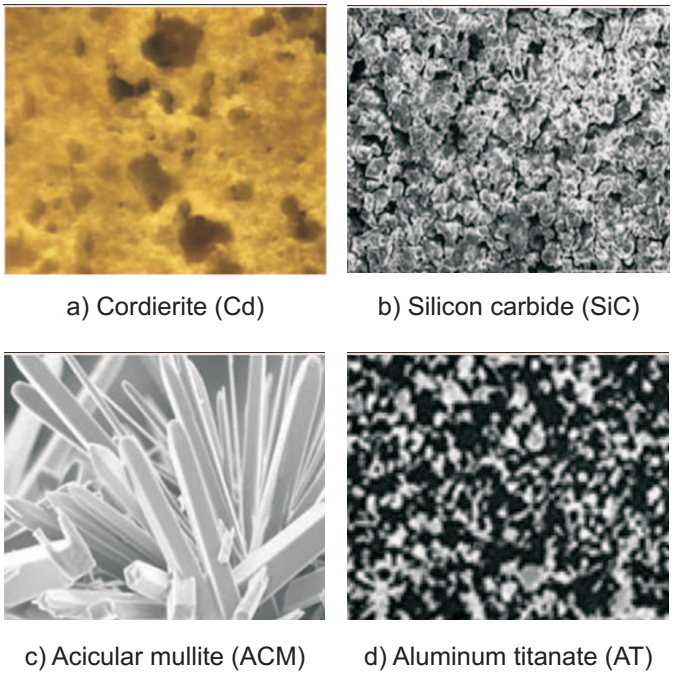

Figure 2.8: SEM images of different DPF substrate materials. Adapted from [62].

2.4.2 Micro-structure

The porosity and the mean pore diameter are the main parameters defining the substrate micro-structure [31]. On one hand these magnitudes affect the mechanical behaviour of the monolith, on the other hand they have a deep impact on the permeability, hence pressure drop, and filtration efficiency of the porous substrate.

The porosity assumes great importance because of its effect on the tensile strength and the modulus of elasticity of the wall [80]. The relation between the dense and the porous material as a function of the porosity is described in eqs. 2.48 [81] and 2.49 [82] respectively:

$$\sigma_w = \sigma_D e^{(-4.9\varepsilon_w)} \tag{2.48}$$

$$E_w = E_D \left(\frac{1-\varepsilon_w}{1+4\varepsilon_w} \right) \tag{2.49}$$

From a modelling point of view, the effect of porosity and mean pore diameter variation on the porous wall permeability and collection efficiency is taken into account making use of the equations detailed in Section 2.2.2 and Section 2.3 respectively.

The equations listed in Section 2.2.2 state that the porosity has a second-order effect on the clean filter's pressure drop. On the contrary, in soot loaded conditions a lower porosity substrate exhibits higher pressure drop. This trend has been experimentally confirmed in the tests run by Dimou *et al.* [73]. In contrast to porosity, the mean pore size (MPS) and pore size distribution have a stronger impact on both filtration efficiency and permeability [62] [83]. Typical mean pore sizes are about 10-30 μm [84] [85]. In [73] Dimou *et al.* reported not significant difference in soot loaded DPF back pressure response below 6 g/l soot loading. Above this limit a 15 μm MPS and 60% porosity SiC DPF exhibited slightly higher pressure drop compared to a substrate with same porosity and MPS of 25 μm. Merkel *et al.* [75] considered several cordierite DPF samples with a median pore size ranging from 3.9 to 30.6 μm. The authors state that the soot-loaded pressure drop is largely controlled by the median pore diameter of the substrate. Considering 5 and 10 g/l soot loading the authors found the minimum pressure drop for median pore diameters between 14 and 19 μm. A similar result was observed by Murtagh *et al.* [86] who studied 4 cordierite filters with a median pore diameter ranging from 12.5 to 34.1 μm. In case of a soot load of 50 g the measured pressure drop increased for mean pore sizes greater than 20 μm.

Concerning the micro-structure effect on the filtration efficiency, small mean pore diameter and porosity generally lead to higher filtration efficiency values. Howitt and Montierth [87] reported the average pore size of the filter wall to be the major factor influencing the filtration efficiency. Wall thickness and porosity affect filtration to a lesser extent, primarily with the large pore (>15 μm) filter materials. This trend is also expressed by the two correlations proposed by Fukushima *et al.* [59], which developed a relation between the substrate porosity and mean pore diameter and the DPF filtration efficiency (evaluated on a number basis by using a Scanning Mobility Particle Sizer (SMPS)). Nevertheless

in this study both the porosity and mean pore diameter of the considered samples were changing at the same time so that these correlations have to be carefully evaluated as they do not distinguish the effect of every parameter separately. The wide filtration efficiency range for clean substrates is strongly reduced in presence of a particulate layer. This is indeed normally associated with high filtration efficiencies (>90%) independently of the filter characteristics, i.e. MPS, porosity, material, cell shape etc. [86] [88].

To conclude this section, the growing interest in integrated SCR/DPF systems [89] [90] [91] and in catalysed DPFs [83] to favour the passive regeneration deserve to be mentioned. The necessity to coat a large amount of catalyst without clogging the pores requires large pores with accurate size uniformity. Regarding the coating, the interest in the concept of a coating filtration layer on the inlet channel walls is growing [88] [92]. Research proved computationally and experimentally that the use of this technique implies high clean filtration efficiency, high PM oxidation efficiency and low pressure drop without affecting the thermo-mechanical response of the monolith.

2.4.3 Meso-structure

This field refers to the cell shape, the cell width (α) and the porous wall thickness (w_w) effect on the DPF performance. These parameters influence the monolith pressure drop and filtration efficiency because of their effect on the filtration area and on the inertial losses. On the other hand the filter meso-structure has a strong influence on the thermo-mechanical response of the monolith.

In the following a list of equations that relate the cell width α and the wall thickness w_w with parameters used to characterize the thermal and mechanical behaviour of the filter are given. For the sake of brevity the particular case of symmetric square cell monoliths is considered in the presented equations as this is the most common cell shape at the present day and is the type of all the filters studied in this PhD thesis. Equations for different cell shapes can be consulted in [80] and [93].

The filtration area is an important parameter as it directly affects the wall velocity, hence pressure drop and filtration efficiency. It also influences the soot and ash accumulation capability and the regeneration rate since it directly affects the catalyst surface and loading, gas to solid contact surface and dwell time across the wall. It is defined as the product of the specific filtration area and the effective monolith volume, which in turn depends on the monolith diameter and the effective channel length:

$$A_f = SFA \frac{\pi D^2}{4} L_e, \tag{2.50}$$

being the effective channel length:

$$L_e = L - L_{plug} \tag{2.51}$$

The specific filtration area is defined as the area per unit volume over which the flow goes from the inlet to the outlet channels. Therefore, it coincides with half the geometric surface area (GSA) of the monolith because only computes the inlet channels [93]. The higher the SFA for a given volume the better regeneration dynamics and the lower the pressure drop in soot loaded DPFs. Contrarily to the filtration area the change in SFA is only dependent on the cell unit geometry through the honeycomb cell size and the porous wall thickness. In the case of symmetric square cell, SFA is obtained as:

$$SFA = \frac{2\alpha}{(\alpha + w_w)^2} \tag{2.52}$$

Other cell unit parameters can be related to the specific filtration area because of the common dependence on the monolith meso-structure. It is the case of the cell density (σ), which is defined as:

$$\sigma = \frac{1}{(\alpha + w_w)^2} = \frac{SFA}{2\alpha} \tag{2.53}$$

The open frontal area (OFA) is a geometric monolith parameter also accounting for the effect of the pressure drop. It is related to the inertial contributions due to local flow contraction and expansion at the monolith inlet and outlet respectively [29]. For a wall-flow monolith, OFA is defined as the ratio of the open monolith cross-section area, which is calculated as the cell cross-section area times the number of inlet channels, and the total monolith cross-section area:

$$OFA = \frac{A_{open}}{A_{fr}} = \frac{\alpha^2 N_{ic}}{A_{fr}} = \frac{\alpha^2 \sigma}{2} = \frac{\alpha^2}{2(\alpha + w_w)^2} = \frac{\alpha SFA}{4} \tag{2.54}$$

Within the parameters related to the thermal and mechanical response of the filter, LOF is accounting for the light-off performance of the monolith [94]. From the LOF definition for a flow-through honeycomb monolith, eq. 2.55 [93],

$$LOF_{flow-through} = \frac{1}{4}\left(\frac{GSA}{OFA} - GSA\right) \tag{2.55}$$

LOF is defined according to eq. 2.56 in the case of a wall-flow honeycomb structure of square channels. Considering that SFA is half the GSA and OFA half the open frontal area of a completely open monolith it is found:

$$LOF = \frac{1}{4}\left(\frac{SFA}{OFA} - 2SFA\right) = \frac{(\alpha + w_w)^2 - \alpha^2}{\alpha(\alpha + w_w)^2} \tag{2.56}$$

In DPF application, LOF is representative of the substrate thermal response under transient operation. During steady-state conditions, the heat transfer is related to the bulk heat transfer parameter (HTP). Taking into account the definition of HTP for a honeycomb monolith, eq. 2.57 [93],

$$HTP_{flow-through} = \frac{1}{4} Nu \frac{GSA^2}{OFA} \tag{2.57}$$

and the SFA and OFA definitions in wall-flow monoliths, HTP in a wall-flow honeycomb structure is given by:

$$HTP = \frac{1}{2} Nu \frac{SFA^2}{OFA} = 4Nu \frac{1}{(\alpha + w_w)^2} = 4Nu\sigma \tag{2.58}$$

These parameters indicate that the higher the SFA the faster wall temperature increase under transient operation but the higher the gas heat losses for the same OFA.

Finally, it is useful to define others parameters such as the thermal integrity factor (TIF), the mechanical integrity factor (MIF) and the strain tolerance parameter (STP):

$$TIF = \frac{\alpha + w_w}{w_w} \tag{2.59}$$

$$MIF = \frac{w_w^2}{(\alpha + w_w)\alpha} \tag{2.60}$$

$$STP = TIF(1 - 2OFA) \tag{2.61}$$

The TIF is proportional to the maximum temperature gradient that the monolith can withstand when is subjected to thermal cycles [93]. MIF and STP are parameters representing the geometric contribution to the mechanical resistance of the substrate. The MIF is defining the load carrying limit of a cell unit, which is given by the diagonal of the cell [93]. From its value it is possible to obtain the load carrying capability accounting for the tensile strength of the wall (σ_w), which is constant if the porosity wall is not modified (eq. 2.48):

$$F = \frac{2}{3} \sigma_w MIF \tag{2.62}$$

The STP is an indicator of the thermal durability. In this specific case, i.e. DPF with symmetric square cell geometry, it can be derived from the definition of the strain tolerance (ST) [95] to consider only the cellular geometry influence on this parameter. Therefore the ST definition [95]

$$ST = \frac{MOR_z}{E_z} = \frac{\frac{3}{5}\sigma_w(1 - 2OFA)}{\frac{2E_o}{TIF}\left(\frac{1-\varepsilon}{1+4\varepsilon}\right)} \tag{2.63}$$

turns into

$$STP = TIF(1 - 2OFA) \tag{2.64}$$

in the case that σ_w and E_o are constant, i.e. for a given material and substrate porosity.

Konstandopoulos *et al.* calculated the α value that minimises the DPF pressure drop in clean [96] and soot loaded [97] symmetric square cell monoliths. However these studies are based on honeycomb cell size optimisation keeping constant the porous wall thickness and do not take into account the thermal response [98] or mechanical resistance of the filter [80].

With respect to the cell shape, in recent times is increasing the interest in non-symmetric cell filters as a way to reduce the pressure drop [99] [100] and comply with the lifetime pressure drop requirements with the accumulation of ash over time in the filter [101]. These kind of filters have larger inlet and smaller outlet channels. Examples are the Corning Asymmetric Cell Technology (ACT) with standard square cells [64] or the Saint-Gobain "wavy" cell geometry derived from the standard square geometry by adding a sinusoidal undulation of the honeycombs walls as detailed in Figure 2.9 [102]. The use of these geometries leads to higher available volume for ash storage and filtration area without affecting the filter bulk heat capacity and mechanical integrity [62].

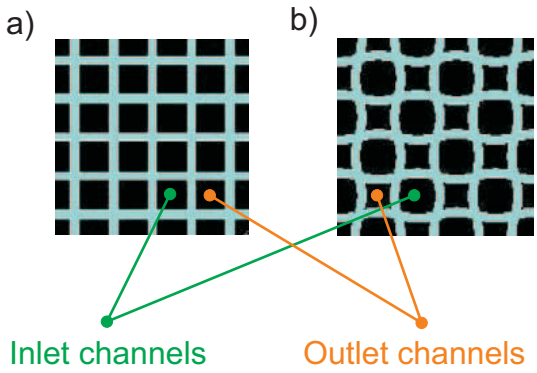

Figure 2.9: Standard symmetric square (a) versus wavy cell (b) geometry of honeycomb structures. Adapted from [102].

2.4.4 Macro-structure

Once the meso-structure has been fixed, the filter volume is a key parameter, together with the filter maximum soot load (MSL), in the definition of the regeneration intervals. Also, it has a strong influence on the ash accumulation

capability. As stated before, it is desirable that both the regeneration interval and the ash accumulation capability are as high as possible. For this reason in real-world applications large volume DPFs have been used in order to get high soot and ash mass capability and achieve better fuel consumption. In addition, at same specific filtration area, i.e. wall thickness and cell density, larger volumes lead to higher filtration area which result in lower filtration velocity, hence low Darcy's pressure drop and high filtration efficiency.

Early literature refers a DPF volume almost equal to the engine displacement and an aspect ratio, i.e. L/D, on the order of 1 [50]. More recent data in [103] report DPFs volumes for heavy-duty applications typically ranging between 1.5 and 2.5 times the engine displacement for cordierite filters. In case of light and medium-duty vehicles, Blanchard *et al.* [104] and Kai *et al.* [105] indicate a DPF volume for SiC monoliths up to 2 times the engine displacement (Figure 2.10). Since DPFs are mainly mounted in under-floor positions on the vehicle the cross-section area tends to be small and high L/D designs, i.e. long and narrow shapes, have been usually applied [74]. Currently the monolith aspect ratio is around 1.5 in the majority of the cases.

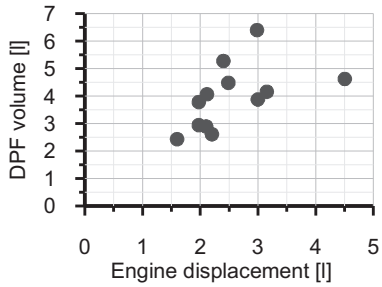

Figure 2.10: Engine displacement vs DPF volume for SiC monolith.

2.5 Pre-turbo aftertreatment placement

Some of the benefits related to the positioning of the aftertreatment systems upstream of the turbine were identified since the early 80's. In this period the company Daimler-Benz introduced in its 300 SD-Turbodiesel a ceramic filter located upstream of the turbine [106]. The idea was abandoned due to the turbine blades damaging related to the detachment of ceramic fragments from the filter. The high temperature peaks during the regeneration process indeed led to the monolith break.

Also the Brown Boveri Company proposed an exhaust line with a pre-turbo DPF for its Comprex supercharger. The transient response of the system was

very slow because of the high thermal inertia of the monolith despite its reduced size [15] [16]. The use of a metal filter led to acceptable performance during transient conditions ensuring at the same time safe turbine operation [107]. As a counterpart the filtration efficiency of this system was quite low.

In the early 90's Mayer *et al.* [108] realized an experimental test campaign to evaluate the potential of the pre-turbo positioning with a metal filter. The authors found out that this configuration permitted passive regeneration starting from an engine load of 30% and reduced the bsfc penalization comparing with the post-turbo DPF placement.

More recently, Subramanian *et al.* [109] quantified by means of 1D modelling the reduction in bsfc penalization related with the pre-turbo positioning of the DOC and DPF. Authors calculated a reduction up to 3% in case of a notable particle accumulation in the filter. According to the authors and to some previous studies [108] [110] the calculated bsfc reduction is related on one hand to the lower flow velocity upstream of the turbine and on the other hand to the pressure drop positioning. As it is located upstream of the turbine it is not multiplied for the turbine expansion ratio resulting in a lower engine back-pressure. On the negative side in case of a transient from 2 to 16 bars BMEP the engine response was very slow. The high thermal inertia of the aftertreatment system accumulated most of the energy notably reducing the available turbine inlet energy.

Brustle *et al.* [111] analysed by means of 1D modelling the impact on performance, sizing and cost of a pre-turbo aftertreatment composed by DOC, DPF and SCR for the case of a 35 litres Diesel engine. The aftertreatment systems for this kind of engines has a significant cost. The aftertreatment volume could be reduced up to a 40% with the consequent weight and cost reduction. Concerning the bsfc the authors calculated a reduction between 0.03% and 0.68% at low and high engine regime respectively, raising to 0.04% to 0.76% in case of a soot mass of 4 g/l in the DPF. Such small bsfc reduction would lead to important fuel and CO_2 emission saving for a 35 litres engine.

The possibility of reducing the aftertreatment cost by volume reduction in pre-turbo positioning boosted the investigation on this placement for this kind of engines earlier [112]. Blanchet *et al.* [113] found that the high turbulence upstream of the turbine permits important DOC and SCR volume reduction because of its positive effect on the mass transfer coefficient.

In more recent years a great deal of effort has been put into the study of the aftertreatment pre-turbo positioning by the researchers of CMT - Motores Térmicos. In the case of a turbocharged Diesel engine for passenger car in steady-state operation, Lujan *et al.* [114] found that at the low engine load and speed operating region the pre-turbo positioning leads to closer VGT positions resulting in a slight damage in fuel consumption. Such a damage is reduced as the engine load increases. Indeed at medium-high load operating points the

high aftertreatment pressure drop reduction lead to a bsfc reduction between 3% and 6%. The position of the DOC with respect to the DPF has been found not to affect the engine operation in pre-turbo placement. Independently of the relative position with respect to the DPF, the DOC showed an increase of the CO and HC conversion efficiency at very low load due to the significant increase of the thermal level across the aftertreatment systems. Increased NO to NO_2 conversion ratio was also observed [115]. Concerning particles measurement, smaller size nucleation particle emission is reduced at the DPF inlet in the case of the pre-turbo aftertreatment configuration [115]. Nevertheless, in presence of a soot load inside the filter, the overall DPF filtration efficiency is not affected by the DPF placement. Highlight that the filtration efficiency of the clean DPF placed upstream of the turbine was not experimentally measured. No evidences of experimental or computational studies about it have been found in the literature, what clearly points out the need to evaluate the effect of the pre-turbo positioning on the DPF filtration efficiency in case of clean substrate. On the other hand its passive regeneration capability showed a noticeable improvement in comparison to the post-turbo DPF placement. The experimental analysis of the engine behaviour with a pre-turbo aftertreatment positioning in transient operation [116] revealed that this configuration is able to follow the driving conditions imposed by the NEDC driving cycle in spite of the cold start conditions. Nevertheless a bsfc penalization between 4% and 8% was found due to the increase of the VGT closing and the increase of the pedal demand during the last acceleration of the EUDC phase. In case of transient tests at constant engine speed the monolith wall temperature was found to be the controlling parameter. Thus, in case of hot wall operation, the monolith heats the gases from the exhaust manifold to the VGT inlet during the low load phase. As a result the turbocharger speed and the boost pressure are kept almost constant so that the subsequent tip-in process is not suffering turbocharger lag. On the contrary, under cold wall operation the thermal inertia of the aftertreatment negatively affects the abilitiy of the engine to provide the expected driveability. Similar results were obtained in the computational study of a heavy-duty Diesel engine performed by Bermudez *et al.* [117]. In this study three load transient processes at constant engine speed, representative of those taking place in the world harmonized transient cycle (WHTC) [118], have been modelled considering cold monolith wall. Results pointed out that the engine driveability can be preserved with a pre-turbo aftertreatment configuration without high influence on the specific fuel consumption by means of proper management of the boost and EGR control, i.e. allowing transient equivalence ratios equal or even higher than stoichiometric conditions and applying suitable settings for the EGR valve opening. To complete the analysis the effect of the soot accumulation inside the filter has to be taken into account. The soot loading increase leads to higher pressure drop across the DPF. In case of post-turbo placement this results in

an important increase of exhaust back-pressure which affects both the engine operation range (EGR and AFR limits) and bsfc penalty. When the DPF is moved upstream of the turbine the back-pressure increase is strongly mitigated on one hand because of the higher flow density, hence lower flow velocity. On the other hand this lower aftertreatment pressure drop is not multiplied for the turbine expansion rate, what plays an important role in the back-pressure reduction of the pre-turbo positioning [119] [120]. Finally, the aforementioned research has been further documented in the PhD thesis of Dr. García-Afonso [19].

In the last decade a notable number of patents related to the pre-turbo aftertreatment positioning proposing different solutions for it have been deposited. At the beginning of the 2000's Watanabe *et al.* [121] suggested to place the filter monolith directly into the exhaust pipes in order to reduce the DPF volume. The inventors included ducts that communicate adjacent cylinders' exhaust pipes regulated by a valve system aimed to the reduction of the back-pressure. A similar configuration was proposed by the company Elring Klinger [122]. More recently Winsor and Baumgard [123] proposed to split the DPF monolith in two parts, each of them receiving the exhaust flow of one half of the cylinders. The flow is then directed to a twin turbine as shown in Figure 2.11.

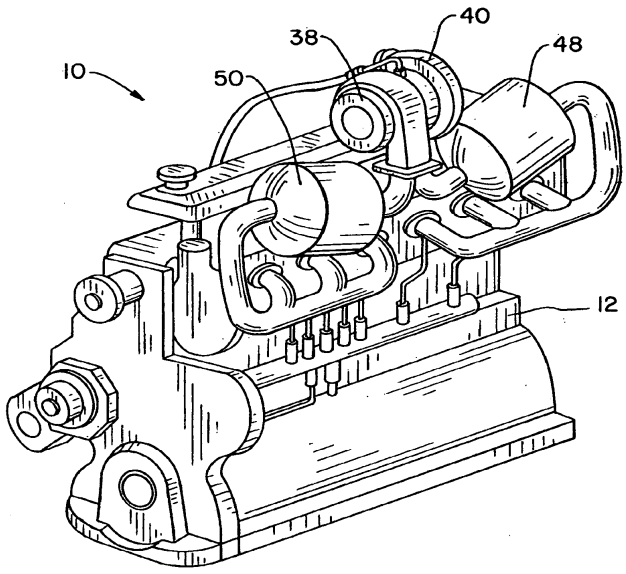

Figure 2.11: Scheme of the pre-turbo aftertreatment configuration patented by Winsor and Baumgard [123].

Toshihisa *et al.* [124] proposed a patent to take advantage of the clean high-pressure EGR brought by the pre-turbo placement. The lack of particles deposition in the EGR line avoids the decrease of this system reported by Sludder *et al.* [125]. Takashi *et al.* [126] went further beyond, in the configuration they patented the EGR was made to flow through a lining all around the exhaust manifold and the aftertreatment system as a way to insulate it. Researchers from CMT - Motores Térmicos also own two patents related with the pre-turbo aftertreatment positioning. In the first one, showed in Figure 2.12, Payri *et al.* [127] proposed a design for the exhaust manifold which integrates the DPF monolith and an insulating lining which take advantage of the EGR flow to keep the monolith at high temperature.

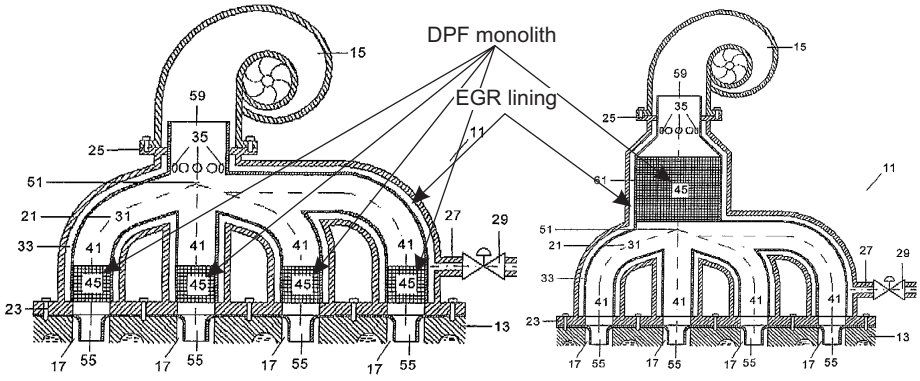

Figure 2.12: Scheme of the patent proposed by Payri *et al.* [127].

Later, Desantes *et al.* [128] patented a multifunctional exhaust manifold that integrates tubular metallic pre-DOC inside the exhaust pipes followed by the DPF monolith and the metallic DOC which acts as a protection for the turbine in case the DPF monolith would suffer damages. The whole structure, showed in Figure 2.13, is thermally insulated with the EGR flow.

2.6 Pre-DPF water injection technique

The water injection at the DPF inlet as a way to reduce the generated pressure drop is a relatively new technique patented by CMT - Motores Térmicos [23]. Aim of this technique is to reduce and control the DPF pressure drop under soot loading conditions [24]. As a consequence, the engine fuel consumption and CO_2 emission decrease. Additionally, the possibility of controlling the back-pressure generated by a loaded filter brings advantages concerning the

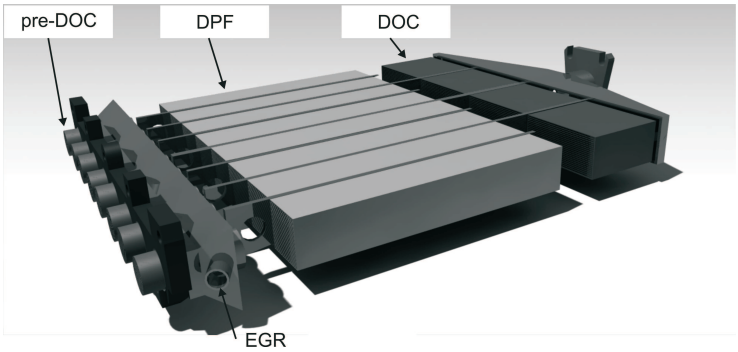

Figure 2.13: Scheme of the multifunctional exhaust manifold patented by Desantes *et al.* [128].

regeneration management or the maintenance related to ash presence [24]. In the former case the active regeneration dependence on pressure drop would disappear resulting in a particulate oxidation strategy dependent on other constraints such as critical soot mass for safe regeneration. On the other hand the maintenance related to ash accumulation in the filter could be delayed [24].

A specific test campaign was carried out in the experimental facilities of CMT - Motores Térmicos in order to prove the effectiveness of this technique and the lack of any negative effect related to it. Two DPF soot loading processes were performed: the first up to a soot mass of 60 grams (~22 g/l) with injections of 500 ml of water and the second up to 32 grams (~11 g/l) injecting 200 ml of water at a time. Every test was repeated twice to compare the engine and DPF performance with and without the application of the pre-DPF water injection. Results are summarized in Figure 2.14.

In both the loading tests the water tank, hence injection pressure, was set to 1.5 bar and the nozzle diameter was 4 mm, what provided an injection rate of 66 g/s. It results evident from the analysis of Figure 2.14 that by the application of several injections it is possible to keep the DPF pressure drop at a certain target value. The authors found out that the minimum effective quantity of injected water mass in every event was 200 g. In these conditions the authors estimated that it is required about 1 kg of injected water every 13.25 NEDCs, what corresponds to an average water consumption of 0.23 kg/h. It was also proven that the pressure drop reduction is not related to soot release. Its magnitude was experimentally measured pointing out that it is negligible in comparison to the soot loading and, more important, it does not affect the capability to fulfil emission standards. In terms of bsfc improvement the authors calculated that the pressure drop reduction leads to a potential for fuel consumption reduction slightly higher than 1% [24].

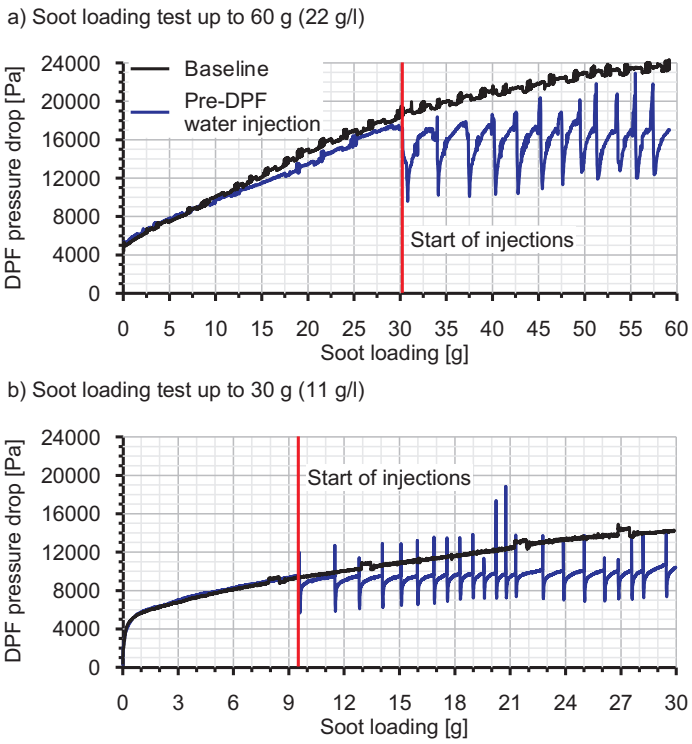

Figure 2.14: Pre-DPF water injection effect on pressure drop during the soot loading tests.

Concerning the DPF filtration efficiency, Bermúdez *et al.* [25] found out that the pre-DPF water injection technique does not affect it, neither during the DPF loading test (Figure 2.15) nor under steady-state operating conditions (Figure 2.16). In both cases the values are similar between the baseline and the water injection test.

Also, Figure 2.16 clearly shows that the engine particles emissions, i.e. upstream of the DPF, are not affected by the discussed technique. Only during every injection event the water causes a dilution effect in the analysed pollutants (CO_2, CO, HC and NO_x) related to the increase of the exhaust mass flow. As the water concentration comes back to the nominal value the nominal concentration of the analysed pollutants is also recovered, without any influence of the proposed technique.

Figure 2.17 shows that the regeneration rate of the baseline and the water injection test shows the same trend and dynamics. It confirms that the regeneration process is unaffected by the application of pre-DPF water injection technique.

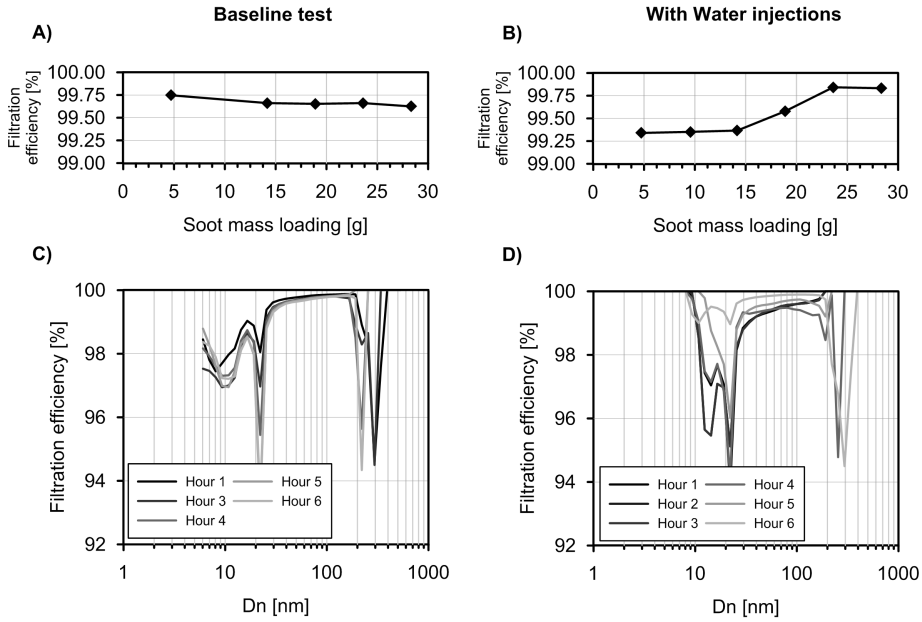

Figure 2.15: Pre-DPF water injection effect on filtration efficiency during the soot loading tests [25].

2.7 Summary

The present chapter is focused on the description of the current state of the art in DPF modelling and design. Additionally, two techniques aimed to increase the DPF performance were introduced: the pre-turbo positioning and the pre-DPF water injection technique.

First of all the original computational model for wall-flow particulate filters implemented in OpenWAM™ has been described. After detailing the governing equations the attention was focused on the pressure drop and heat transfer sub-models. Particular emphasis has been put on the former because of its deep relation with the filtration sub-model developed in this thesis.

Next, a review of the main DPF filtration models described in the literature has been presented. Early model by Konstandopoulos *et al.* was considered first to end with the probability density function based heterogeneous multiscale filtration model proposed in more recent times by Gong and Rutland.

To conclude, the criteria considered in the design of wall-flow DPFs have been discussed. The attention was focused on the most commonly used materials, sizing as well as micro- and meso-structure parameters defining the monolith.

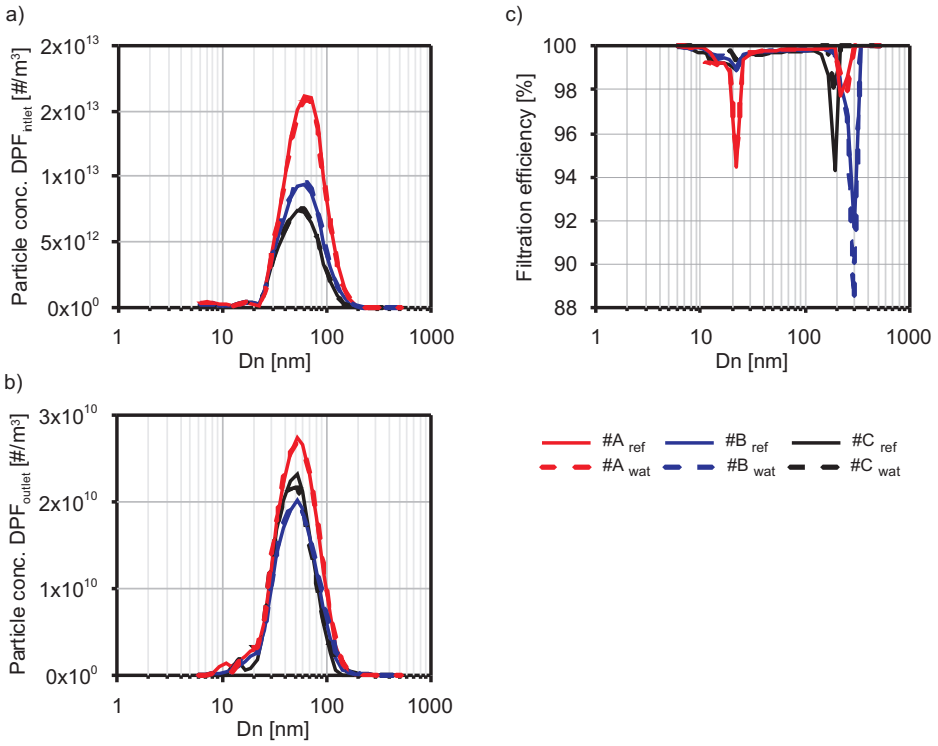

Figure 2.16: Pre-DPF water injection effect on filtration efficiency under steady-state operating conditions [25].

The relation between the above listed parameters and the filter performance have been listed.

The last part has been dedicated to the discussion of two strategies aimed to increase the DPF performance: the pre-turbo positioning and the pre-DPF water injection technique. The former has been demonstrated to have a positive impact on the engine bsfc and passive regeneration but penalizes the response during transient operation. The second is a recently patented technique from CMT - Motores Térmicos aimed to limit the pressure drop generated by soot and/or ash loaded filters, thus reducing its impact on the fuel consumption and simplifying regeneration and maintenance management.

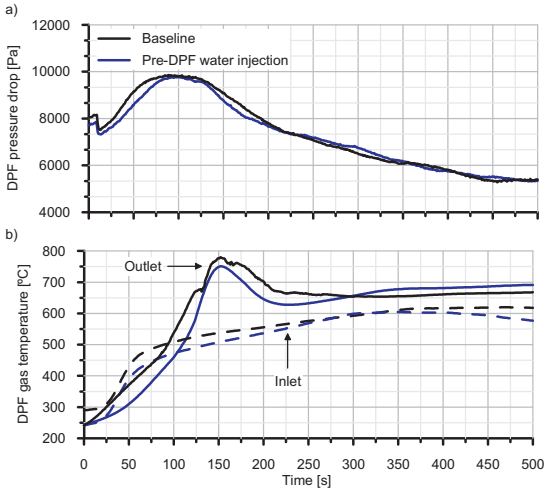

Figure 2.17: Comparison of the DPF response under active regeneration conditions between the baseline and the water injection test [24].

2.8 References

[10] J. R. Serrano, F. J. Arnau, P. Piqueras, and O. García-Afonso. “Packed bed of spherical particles approach for pressure drop prediction in wall-flow DPFs (diesel particulate filters) under soot loading conditions”. In: *Energy* 58 (2013), pp. 644–54 (cit. on pp. 3, 15, 17, 19, 63, 71, 73, 82, 87, 167).

[13] A. G. Konstandopoulos, E. Skaperdas, and M. Masoudi. “Microstructural properties of soot deposits in Diesel particulate traps”. In: *SAE Technical Paper 2002-01-1015*. 2002 (cit. on pp. 3, 27, 189, 206, 227).

[15] H. Hiereth. “Daimler-Benz AG car test with a free-running pressure-wave charger - A study for an advanced supercharging system”. In: *SAE Technical Paper 890453*. 1989 (cit. on pp. 4, 40).

[16] E. Jenny, J. Hansel, and A. Mayer. “The transient behaviour of super-charged passenger car diesel engines fitted with particulate traps”. In: *SAE Technical Paper 890453*. 1989 (cit. on pp. 4, 40).

[18] P. Piqueras. “Contribution to thermo-and fluid dynamic modelling of wall-flow Diesel particulate filters (text in spanish)”. PhD thesis. Universitat Politécnica de Valéncia, 2010 (cit. on pp. 4, 16).

[19] O. García-Afonso. “Analisis teorico-experimental de la arquitectura pre-turbo de sistemas de post-tratamiento en MCIA”. PhD thesis. Universitat Politécnica de Valéncia, 2013 (cit. on pp. 4, 42).

[23] J. M. Desantes, F. Payri, P. Piqueras, and J. R. Serrano. *Sistema de filtro*. Spanish Patent ES2408243(B1). 2013 (cit. on pp. 5, 8, 16, 43).

[24] V. Bermúdez, J. R. Serrano, P. Piqueras, and O. García-Afonso. “Pre-DPF water injection technique for loaded DPF pressure drop reduction and control”. In: *Applied Energy* 140 (2015), pp. 234–245 (cit. on pp. 5, 8, 43, 44, 48, 80, 203).

[25] V. Bermúdez, J. R. Serrano, P. Piqueras, and D. Campos. “Analysis of the influence of pre-DPF water injection technique on pollutants emission”. In: *Energy* 89 (2015), pp. 778–792 (cit. on pp. 5, 45–47, 65, 216, 233).

[26] T. Johnson. “Review of Vehicular Emissions Trends”. In: *SAE International Journal of Engines* 8(3):2015 (2015), pp. 1152–1167 (cit. on p. 15).

[27] *OpenWAM website, CMT - Motores Térmicos (Universitat Politécnica de Valéncia)*. www.openwam.org. 2016 (cit. on pp. 16, 112).

[28] J. Galindo, J. R. Serrano, F. J. Arnau, and P. Piqueras. “Description and analysis of a one-dimensional gas-dynamic model with Independent Time Discretization”. In: *Proceedings of the ASME Internal Combustion Engine Division 2008 Spring Technical Conference ICES2008*. 2008 (cit. on pp. 16, 22, 67, 112).

[29] A. J. Torregrosa, J. R. Serrano, F. J. Arnau, and P. Piqueras. “A fluid dynamic model for unsteady compressible flow in wall-flow Diesel particulate filters”. In: *Energy* 36 (2011), pp. 671–684 (cit. on pp. 16, 17, 36, 62, 63, 72, 81, 158).

[30] E. J. Bisset. “Mathematical model of the thermal regeneration of a wall-flow monolith Diesel particulate filter”. In: *Chemical Engineering Science* 39.7-8 (1984), pp. 1233–1244 (cit. on p. 16).

[31] F. Dullien. *Porous Media. Fluid Transport and Pore Structure*. Academic Press, New York, 1992 (cit. on pp. 17, 33, 75).

[32] F. Payri, A. Broatch, J. R. Serrano, and P. Piqueras. “Experimental-theoretical methodology for determination of inertial pressure drop distribution and pore structure properties in wall-flow diesel particulate filters (DPFs)”. In: *Energy* 36 (2011), pp. 6731–6744 (cit. on pp. 17, 18, 78, 125, 198).

[33] S. Kuwabara. “The forces experienced by randomly distributed parallel circular cylinders or spheres in a viscous fluid at small Reynolds numbers”. In: *Journal of the Physical Society of Japan* 14 (1959), pp. 527–532 (cit. on pp. 17, 24, 30, 63).

[34] M. Lapuerta, R. Ballesteros, and F. Martos. “A method to determine the fractal dimension of diesel soot agglomerates”. In: *Journal of Colloid and Interface Science* 303 (2006), pp. 149–158 (cit. on pp. 20, 226).

[35] J. B. Heywood. *Internal Combustion Engine Fundamentals*. McGraw-Hill, 1988 (cit. on p. 20).

[36] R. A. Dobbins. “Soot inception temperature and the carbonization rate of precursor particles”. In: *Combustion and Flame* 130(3) (2002), pp. 204–214 (cit. on p. 20).

[37] K. Kondo, T. Aizawa, S. Kook, and L. Pickett. “Uncertainty in Sampling and TEM Analysis of Soot Particles in Diesel Spray Flame”. In: *SAE Technical Paper 2013-01-0908*. 2013 (cit. on p. 20).

[38] A. G. Konstandopoulos, M. Kostuglou, E. Skaperdas, E. Papaioannou, D. Zarvalis, and E. Kladopoulou. “Fundamental studies of Diesel particulate filters: transient loading, regeneration and aging”. In: *SAE Technical Paper 2000-01-1016*. 2000 (cit. on pp. 21, 25).

[39] D. Winterbone and R. Pearson. *Theory of engine manifold design: wave action methods for IC engines*. Professional Engineering Publishing, 2000 (cit. on pp. 22, 67).

[40] J. Galindo, J. R. Serrano, P. Piqueras, and O. García-Afonso. “Heat transfer modelling in honeycomb wall-flow diesel particulate filters”. In: *Energy* 43 (2012), pp. 201–213 (cit. on pp. 22–24).

[41] N. A. Fuchs. *The mechanics of aerosols*. Ed. by C. N. Davies. Pergamon press, 1964 (cit. on pp. 24, 70).

[42] S. K. Friedlander. “Mass and heat transfer to single spheres and cylinders at low Reynolds numbers”. In: *AIChE Journal* 3(1) (1957), pp. 43–48 (cit. on p. 24).

[43] G. G. Stokes. “On the effect of the internal friction of fluids on the motion of a pendulum”. In: *Transactions of the Cambridge Philosophical Society* 9 Part 2 (1851), pp. 8–106 (cit. on p. 24).

[44] S Tomotika and T Aoi. “The steady flow of viscous fluid past a sphere and circular cylinder at small Reynolds numbers”. In: *Quarterly Journal of Mechanics and Applied Mathematics* 3 (1950), pp. 140–161 (cit. on p. 24).

[45] K. Lee and J. Gieseke. “Collection of aerosol particles by packed beds”. In: *Environmental Science and Technology* 13.4 (1979), pp. 466–470 (cit. on pp. 24, 27, 68, 70).

[46] J. Happel. “Viscous flow in multiparticle systems: Slow motion of fluids relative to beds of spherical particles”. In: *American Institute of Chemical Engineers Journal* 4 (1958), pp. 197–201 (cit. on p. 24).

[47] K. W. Lee, L. D. Reed, and J. A. Gieseke. “Pressure drop across packed beds in the low Knudsen number regime”. In: *Journal of Aerosol Science* 9 (1978), pp. 557–565 (cit. on p. 24).

[48] A. A. Kirsh and N. A. Fuchs. “Studies on fibrous aerosols filters - II. Pressure drop in systems of parallel cylinders”. In: *Annals of Occupational Hygiene* 10 (1967), pp. 23–30 (cit. on p. 24).

[49] H. Yeh and B. Liu. “Aerosol filtration by fibrous filtersI. Theoretical”. In: *Journal of Aerosol Science* 5 (1974), pp. 191–204 (cit. on p. 24).

[50] A. G. Konstandopoulos and J. H. Johnson. “Wall-flow Diesel particulate filters - Their pressure drop and collection efficiency”. In: *SAE Technical Paper 890405*. 1989 (cit. on pp. 27, 39, 63).

[51] H. Mohammed, A. P. Triana, S. L. Yang, and J. H. Johnson. “An advanced 1D 2-layer catalized Diesel particulate filter model to simulate: filtration by the wall and particulate cake, oxidation in the wall and particulate cake by NO2 and O2 and regeneration by heat addition”. In: *SAE Technical Paper 2006-01-0467*. 2006 (cit. on p. 27).

[52] B. Stanmore, J. Brilhac, and P. Gilot. “The oxidation of soot: a review of experiments, mechanisms and models”. In: *Carbon* 39 (2001), pp. 2247–2268 (cit. on p. 27).

[53] T. C. Huinh, J. H. Johnson, S. L. Yang, S. T. Bagley, and J. R. Warner. “A one dimensional computational model for studying the filtration and regeneration characteristics of a catalyzed wall flow Diesel particulate filter”. In: *SAE Technical Paper 2003-01-0841*. 2003 (cit. on p. 27).

[54] P. Tandon, A. Heibel, J. Whitmore, N. Kekre, and K. Chithapragada. “Measurement and prediction of filtration efficiency evolution of soot loaded diesel particulate filters”. In: *Chemical Engineering Science* 65 (2010), pp. 4751–4760 (cit. on pp. 28, 65, 70).

[55] I. Langmuir. “The production of rain by a chain reaction in Cumulus clouds of temperatures above freezing”. In: *Journal of the Atmospheric Sciences* 5 (1948), pp. 175–192 (cit. on p. 28).

[56] T. Bollerhoff, I. Markomanolakis, and G. Koltsakis. “Filtration and regeneration modeling for particulate filters with inhomogeneous wall structure”. In: *Catalysis Today* 188 (2012), pp. 24–31 (cit. on pp. 28, 138).

[57] *Axisuite user’s manual*. www.exothermia.com. Exothermia S.A. 2010 (cit. on p. 28).

[58] J. Gong and C. J. Rutland. “PDF-based heterogeneous multiscale filtration model”. In: *Environmental Science and Technology* 49(8) (2015), pp. 4963–4970 (cit. on pp. 29, 96, 97).

[59] S. Fukushima and K. Ohno. “New approach for pore structure and filtration efficiency characterization”. In: *SAE Technical Paper 2007-01-1918*. 2007 (cit. on pp. 29, 34).

[60] Y. Mizuno, Y. Miyairi, F. Katsube, E. Ohara, A. Takahashi, M. Makino, T. Mizutani, K. Yuki, and H. Kurachi. “Study on wall pore structure for next generation diesel particulate filter”. In: *SAE Technical Paper 2008-01-0618*. 2008 (cit. on p. 29).

[61] K. Ogyu, T. Ogasawara, H. Sato, K. Yamada, and K. Ohno. “Development of high porosity SiC-DPF which is compatible with high robustness and catalyst coating capability for SCR coated DPF application”. In: *SAE Technical Paper 2013-01-0840*. 2013 (cit. on p. 29).

[62] B. Guan, R. Zhan, H. Lin, and Z. Huang. “Review of the state-of-the-art of particulate filter technology”. In: *Journal of Environmental Management* 154 (2015), pp. 225–258 (cit. on pp. 31, 33, 34, 38, 95).

[63] A. Briot, F. Carranza, P. Girot, and S. Bardon. “Minimizing filter volume by design optimization”. In: *SAE Technical Paper 2007-01-0657*. 2007 (cit. on p. 31).

[64] K. Aravelli and A. Heibel. “Improved lifetime pressure drop management for Robust Cordierite (RC) filters with Asymmetric Cell Technology (ACT)”. In: *SAE Technical Paper 2007-01-0920*. 2007 (cit. on pp. 32, 38).

[65] A. Sappok, Y. Wang, R. Wang, C. Kamp, and V. Wong. “Theoretical and experimental analysis of ash accumulation and mobility in ceramic exhaust particulate filters and potential for improved ash management”. In: *SAE International Journal of Fuels and Lubricants* 7(2) (2014), pp. 511–524 (cit. on pp. 32, 249).

[66] S. Fujii and T. Asako. “Design optimization of non-catalyzed DPF from viewpoint of back pressure in ash loading state”. In: *SAE Technical Paper 2011-01-2091*. 2011 (cit. on p. 32).

[67] S. Fujii and T. Asako. “Development of artificial ash accelerated accumulation test method”. In: *SAE Technical Paper 2010-01-2171*. 2010 (cit. on p. 32).

[68] A. Sappok, I. Govani, C. Kamp, Y. Wang, and V. Wong. “In-situ optical analysis of ash formation and transport in Diesel Particulate Filters during active and passive DPF regeneration processes”. In: *SAE International Journal of Fuels and Lubricants* 6(2) (2013), pp. 336–349 (cit. on p. 32).

[69] T. Johnson. “Diesel emission control in review”. In: *International Journal of Engine Research* 10 (2009), pp. 275–285 (cit. on p. 32).

[70] C. Benaqqa, M. Gomina, A. Beurotte, M. Boussuge, B. Delattre, K. Pajot, E. Pawlak, and F. Rodrigues. “Morphology, physical, thermal and mechanical properties of the constitutive materials of Diesel Particulate Filters”. In: *Applied Thermal Engineering* 62 (2014), pp. 599–606 (cit. on p. 32).

[71] R. S. Ogunwumi, Q. Dong, T. A. Murrin, R. Y. Bhargava, J. L. Warkins, and A. K. Heibel. “Performance evaluations of aluminum titanate Diesel Particulate Filters”. In: *SAE Technical Paper 2007-01-0656*. 2007 (cit. on p. 32).

[72] J. Li and R. Mital. “Effect of DPF design parameters on fuel economy and thermal durability”. In: *SAE Technical Paper 2012-01-0847*. 2012 (cit. on p. 32).

[73] I. Dimou, A. Sappok, V. Wong, S. Fujii, H. Sakamoto, K. Yuuki, and C. Vogt. “Influence of material properties and pore design parameters on non-catalyzed Diesel Particulate Filter performance with ash accumulation”. In: *SAE Technical Paper 2012-01-1728*. 2012 (cit. on pp. 32, 34).

[74] T. Mizutani et al. “The study for structural design of the segmented SiC-DPF”. In: *SAE Technical Paper 2006-01-1527*. 2006 (cit. on pp. 32, 39).

[75] G. Merkel, D. Beall, H. D.L., and V. M. J. “Effects of microstructure and cell geometry on performance of cordierite Diesel Particulate Filters”. In: *SAE Technical Paper 2001-01-0193*. 2001 (cit. on pp. 32, 34, 121, 124).

[76] T. Boger, J. Jamison, J. Warkins, N. Golomb, W. C., and A. Heibel. “Next generation Aluminum Titanate filter for light-duty Diesel applications”. In: *SAE Technical Paper 2011-01-0816*. 2011 (cit. on p. 32).

[77] T. V. Johnson. “Vehicular emissions in review”. In: *SAE International Journal of Engines* 5 (2012), pp. 216–234 (cit. on p. 32).

[78] C. Li, F. Mao, S. Swartzmiller, S. Wallin, and R. Ziebarth. “Properties and performance of Diesel Particulate Filters of an advanced ceramic material”. In: *SAE Technical Paper 2004-01-0955*. 2004 (cit. on p. 33).

[79] C. Li, H. Koelman, R. Ramanathan, U. Baretzky, G. Forbriger, and T. Meunier. “Particulate Filter design for high performance Diesel engine application”. In: *SAE Technical Paper 2008-01-1747*. 2008 (cit. on p. 33).

[80] C. D. Depcik and A. J. Hausmann. “Review and a methodology to investigate the effects of monolithic channel geometry”. In: *Journal of Engineering for Gas Turbine and Power* 135 (2013), pp. 032301 1–16 (cit. on pp. 34, 35, 38, 128).

[81] R. H. Heck, J. Wei, and J. R. Katzer. “Mathematical modeling of monolithic catalysts”. In: *Aiche journal* 22(3) (1976), pp. 477–484 (cit. on pp. 34, 248).

[82] G. Groppi, A. Belloli, E. Tronconi, and P. Forzatti. “A comparison of lumped and distributed models of monolith catalytic combustors”. In: *Chemical Engineering Science* 50(17) (1995), pp. 2705–2715 (cit. on pp. 34, 248).

[83] K. Yuuki, T. Ito, H. Sakamoto, R. Matsubara, S. Hashimoto, and T. Hamanaka. “The effect of SiC properties on the performance of catalyzed Diesel particulate filter (DPF)”. In: *SAE Technical Paper 2003-01-0383*. 2003 (cit. on pp. 34, 35).

[84] M. Khair. “A review of Diesel particulate filter technologies”. In: *SAE Technical Paper 2003-01-2303*. 2003 (cit. on p. 34).

[85] D. Rose, J. Jamison, T. Boger, and R. Kataria. “Light duty Diesel exhaust gas after treatment challenges and technologies for post BS-IV regulations”. In: *SAE Technical Paper 2013-26-0051*. 2013 (cit. on p. 34).

[86] M. Murtagh, D. Sherwood, and L. Socha. “Development of a diesel particulate filter composition and its effect on thermal durability and filtration performance”. In: *SAE Technical Paper 940235*. 1994 (cit. on pp. 34, 35, 63, 78, 84).

[87] J. Howitt and M. Montierth. “Cellular ceramic Diesel particulate filter”. In: *SAE Technical Paper 81104*. 1981 (cit. on p. 34).

[88] K. Ogyu, T. Oya, K. Ohno, and A. G. Konstandopoulos. “Improving of the filtration and regeneration performance by the Sic-DPF with the layer coating of PM oxidation catalyst”. In: *SAE Technical Paper 2008-01-0621*. 2008 (cit. on p. 35).

[89] G. Cavataio, J. Girard, and C. Lambert. “Cu/Zeolite SCR on high porosity filters: laboratory and engine performance evaluations”. In: *SAE Technical Paper 2009-01-0897*. 2009 (cit. on p. 35).

[90] J. Tan, C. Solbrig, and S. Schmieg. “The development of advanced 2-Way SCR/DPF systems to meet future Heavy-duty Diesel emissions”. In: *SAE Technical Paper 2011-01-1140*. 2011 (cit. on p. 35).

[91] A. Kawakami, T. Mizutani, Y. Shibagaki, K. Yuuki, H. Sakamoto, C. Vogt, T. Tatsuyuki Kuki, W. Heuss, P. Kattouah, and M. Makino. “High porosity DPF design for integrated SCR functions”. In: *SAE Technical Paper 2012-01-0843*. 2012 (cit. on p. 35).

[92] K. Nakamura, N. Vlachos, A. Konstandopoulos, H. Iwata, and O. Kazushige. “Performance Improvement of Diesel Particulate Filter by Layer Coating”. In: *SAE Technical Paper 2012-01-0842*. 2012 (cit. on p. 35).

[93] S. Gulati. “Cell design for ceramic monoliths for catalytic converter application”. In: *SAE Technical Paper 881685*. 1988 (cit. on pp. 35–37, 169).

[94] R. Heck, J. Robert, and S. T. Gulati. *Catalytic air pollution control. Commercial Technology.* Wiley, New York, 2009 (cit. on p. 36).

[95] S. Gulati. “Performance parameters for advanced ceramic catalyst supports”. In: *SAE Technical Paper 1999-01-0269*. 1999 (cit. on p. 37).

[96] A. G. Konstandopoulos, E. Skaperdas, J. Warren, and R. Allansson. “Optimized filter design and selection criteria for continuously regenerating Diesel particulate traps”. In: *SAE Technical Paper 1999-01-0468*. 1999 (cit. on pp. 38, 128).

[97] A. G. Konstandopoulos and E. Kladopoulou. “The optimum cell density for wall-flow monolithic filters: effects of filter permeability, soot cake structure and ash loading”. In: *SAE Technical Paper 2004-01-1133*. 2004 (cit. on pp. 38, 128).

[98] S. J. Lee, S. J. Jeong, and W. S. Kim. “Numerical design of the diesel particulate filter for optimum thermal performances during regeneration”. In: *Applied Energy* 86 (2009), pp. 1124–1135 (cit. on pp. 38, 128).

[99] A. Konstandopoulos and M. Kostoglou. “Analysis of asymmetric and variable cell geometry wall-flow particulate filters.” In: *SAE Technical Paper 2014-01-1510*. 2014 (cit. on p. 38).

[100] K. Nakamura, A. Konstandopoulos, M. Kostoglou, T. Shibata, and Y. Hashizume. “New asymmetric plugging layout of Diesel Particulate Filters for the pressure drop reduction”. In: *SAE Technical Paper 2014-01-1512*. 2014 (cit. on p. 38).

[101] A. Heibel and R. Bhargava. “Advanced Diesel Particulate Filter design for lifetime pressure drop solution in light duty applications”. In: *SAE Technical Paper 2007-01-0042*. 2007 (cit. on p. 38).

[102] S. Bardon, B. Bouteiller, N. Bonnail, P. Girot, V. Gleize, L. Oxarango, P. Higelin, J. Michelin, S. Schuerholz, and F. Terres. “Asymmetrical channels to increase DPF lifetime”. In: *SAE Technical Paper 2004-01-950*. 2004 (cit. on pp. 38, 138).

[103] *U.S. Environmental Protection Agency (EPA), regulatory impact analysis: control of emissions of air pollution from highway Heavy-Duty engines, 2000, U.S. Environmental Protection Agency - Office of Transportation and Air Quality.* 2000 (cit. on p. 39).

[104] G. Blanchard, C. Colignon, C. Griard, C. Rigaudeau, O. Salvat, and T. Seguelong. “Passenger car series application of a new Diesel Particulate Filter system using a new Ceria-based fuel-borne catalyst: from the engine test bench to european vehicle certification”. In: *SAE Technical Paper 2002-01-2781*. 2002 (cit. on p. 39).

[105] R. Kai, T. Sekiya, M. Ogawa, K. Saiki, R. Matsubara, H. Kurachi, M. Brayer, E. Warner, S. Fujii, and S. Ren. “Thermal-mechanical durability of DOC and DPF aftertreatment system for light heavy pickup truck application”. In: *SAE Technical Paper 2009-01-2707*. 2009 (cit. on p. 39).

[106] H. D. Schuster. “Verminderung der Partikelemission amb PKW-Motor”. In: *VDI-Bericht* 559 (1985) (cit. on p. 39).

[107] A. Mayer, A. Buck, and H. Bressler. “The knitted Particulate Trap: field experience and development progress”. In: *SAE Technical Paper 930362*. 1993 (cit. on p. 40).

[108] A. Mayer, R. M. Schmidt, H. Sudmanns, P. Mattes, and A. Buck. “Pre-turbo application of the knitted fiber diesel particulate trap”. In: *SAE Technical Paper 940459*. 1994 (cit. on p. 40).

[109] M. N. Subramaniam, V. Joergl, P. Keller, O. Weber, T. Toyoshima, and C. D. Vogt. “Feasibility assessment of a pre-turbo after-treatment system with a 1D modeling approach”. In: *SAE Technical Paper 2009-01-1276*. 2009 (cit. on pp. 40, 176).

[110] V. Joergl, P. Keller, O. Weber, K. Mueller-Hass, and R. Konieczny. “Influence of pre turbo catalyst design on diesel engine performance, emissions and fuel economy”. In: *SAE Technical Paper 2008-01-0071*. 2008 (cit. on pp. 40, 121).

[111] C. Brüstle, M. Downey, M. N. Subramaniam, A. Birckett, and D. Tomazic. “Aftertreatment in a pre-turbo position: size and fuel consumption advantage for Tier 4 large-bore Diesel engines”. In: *Aachen Colloquium Automobile and Engine Technology 2011*. 2011 (cit. on p. 40).

[112] D. T. Osborne, S. G. Fritz, and M. Iden. “Exhaust emissions from a 2,850 kW EMD SD60M locomotive equipped with a Diesel Oxidation Catalyst”. In: *ASME/IEEE Joint Rail Conference and Internal Combustion Engine Division Spring Technical Conference*. 2007 (cit. on p. 40).

[113] S. Blanchet, R. Richmond, and G. Vaneman. “Implementation of the effectiveness-Ntu methodology for catalytic converter design”. In: *SAE Technical Paper 980673*. 1998 (cit. on p. 40).

[114] J. M. Lújan, V. Bermúdez, P. Piqueras, and O. García-Afonso. “Experimental assessment of pre-turbo aftertreatment configurations in a single stage turbocharged Diesel engine. Part 1: Steady-state operation”. In: *Energy* 80 (2015), pp. 599–613 (cit. on pp. 40, 113, 133, 135, 141, 156).

[115] V. Bermúdez, J. M. Lujan, P. Piqueras, and D. Campos. “Pollutants emission and particle behavior in a pre-turbo aftertreatment light-duty diesel engine”. In: *Energy* 66 (2014), pp. 509–522 (cit. on p. 41).

[116] J. M. Lújan, J. R. Serrano, P. Piqueras, and O. García-Afonso. “Experimental assessment of a pre-turbo aftertreatment configuration in a single stage turbocharged Diesel engine. Part 2: Transient operation”. In: *Energy* 80 (2015), pp. 614–627 (cit. on pp. 41, 113).

[117] V. Bermúdez, J. R. Serrano, P. Piqueras, and O. García-Afonso. “Analysis of heavy-duty turbocharged diesel engine response under cold transient operation with a pre-turbo aftertreatment exhaust manifold configuration”. In: *International Journal of Engine Research* 14.4 (2013), pp. 341–353 (cit. on pp. 41, 127, 173).

[118] *WHTC emission test cycles*. https://dieselnet.com/standards/cycles/whtc.php. 2016 (cit. on p. 41).

[119] F. Payri, J. R. Serrano, P. Piqueras, and O. García-Afonso. "Performance Analysis of a Turbocharged Heavy Duty Diesel Engine with a Pre-turbo Diesel Particulate Filter Configuration". In: *SAE Technical Paper 2011-37-0004*. 2011 (cit. on p. 42).

[120] V. Bermúdez, J. R. Serrano, P. Piqueras, and O. García-Afonso. "Influence of DPF soot loading on engine performance with a pre-turbo aftertreatment exhaust line". In: *SAE Technical Paper 2012-01-0362*. 2012 (cit. on pp. 42, 136, 141).

[121] Y. Watanabe, Y. Araki, K. Kobashi, and Y. Henda. *An exhaust gas purification device for a compression-ignition combustion engines*. Patent Application EP 0823545 (B1). 2002 (cit. on p. 42).

[122] ElringKlinger. *Seal for combustion engine has catalysis element or particulate filter element connected to the seal with sealing plate whereby sealing plate has exhasut gas passage through which exhaust gas of combustion engine ows*. Patent Application DE 202006004489 (U1). 2006 (cit. on p. 42).

[123] R. Winsor and K. Baumgard. *Internal combustion engine with a dual particulate traps ahead of turbocharger*. Patent Application US/2009 0151328 (A1). 2009 (cit. on p. 42).

[124] S. Toshihisa, Y. Hiromichi, H. Yoshimitsu, Y. Yoshio, and K. Zenichiro. *Exhaust emission control device*. Patent Application JP2002364335 (A). 2005 (cit. on p. 43).

[125] C. Sludder, J. Storey, S. Lewis, D. Styles, J. Giulano, and J. Hoard. "Hydrocarbons and particulate matter in EGR cooler deposits: Effects of gas flow rate, coolant temperature and oxidation catalyst". In: *SAE Technical Paper 2008-01-2467*. 2008 (cit. on p. 43).

[126] M. Takashi, N. Hideo, I. Toshio, O. Kazuya, and I. Seiji. *Exhaust gas recirculating system*. Patent Application JP2005232996 (A). 2005 (cit. on p. 43).

[127] F. Payri, J. M. Desantes, J. Galindo, and J. R. Serrano. *Exhaust manifold of a turbo-supercharged reciprocating engine*. Patent WO2010092201A1. Priority date 13/02/2009. European Patent Office. 2010 (cit. on p. 43).

[128] J. M. Desantes, F. Payri, J. R. Serrano, and P. Piqueras. *Device for treating exhaust gases from diesel turbo-supercharged reciprocating internal combustion engines (RICE)*. Patent WO 2013/041747 A1. Priority date 23/09/2011. European Patent Office. 2013 (cit. on pp. 43, 44, 113).

CHAPTER 3

Wall-flow PF filtration model

Contents

Figures

Tables

3.1 Introduction

THE emissions legislations are getting day by day more stringent all over the world. In the case of the European Community the current regulation fixes for the emitted particulate matter a maximum value of:

- 0.005 g/km & $6x10^{11}$ #/km for passenger cars and light commercial vehicles DI engines (Euro 6) [9];
- 0.01 g/kWh & $8x10^{11}$ #/km for HD Diesel engines in steady state testing (Euro VI) [129];
- 0.01 g/kWh & $6x10^{11}$ #/km for HD Diesel and gas engines in transient testing (Euro VI) [129].

Additionally the upcoming Euro 6d Emission Regulation will implement Real Driving Emissions (RDE) as an additional type approval requirement for passenger cars in the 2017-2020 time frame. The 28th of October of 2015 the Technical Committee of Motor Vehicles (TCMV) voted on the second package of measures on the regulatory not-to-exceed (NTE) emission limits applicable in RDE testing, which needs to enter into force so that RDE testing has implications on the conformity certificate issued by the national type-approval authority (TAA) [130]. The high cost and uncertainty of the real driving on-road certification is resulting in a growing interest for virtual test benches.

Given the above described picture of the current situation, i.e. the low and continuously decreasing PM limits in both mass and number, applying to Diesel and direct injection gasoline engines, and the introduction of the RDE testing, the need of precise models for particulate filters is evident. The correct simulation of the dynamic behaviour of the engine and the aftertreatment requires that the mutual interaction between these two systems is kept into account. In the specific, concerning the PF, it is required a model capable of a precise calculation of the flow field and the particulate matter mass trapped or oxidized at any time-step. This in turn results in porous medium microstructure modification that finally leads to flow field variations. These are the key parameters as directly affect both the capacity of collecting particles and the generated pressure drop. On the other hand this latter magnitude affects the engine and the VGT behaviour hence modifying again the flow field. Based on this, achieving a correct simulation of the PF and engine performance requires a robust PF model that includes pressure drop, filtration, regeneration and heat-transfer sub-models interacting continuously with each other.

In the present chapter the PF filtration model developed within the framework of this PhD thesis is presented and discussed. The proposed filtration submodel is implemented as a part of the fluid-dynamic model of wall-flow particulate filters [29] integrated in OpenWAM™. The model solves non-homentropic,

1D, unsteady, compressible flow along every pair of inlet and outlet channels. The filtration computation is coupled with the pressure drop model in order to provide a complete, dynamic description of the filter performance evolution from clean [29] to soot loaded conditions [10]. The objective is to finally get a tool able to continuously calculate the modification of the PF filtration efficiency and pressure drop related with the variations of the flow field, e.g. engine operating point changes, and/or of the porous medium properties, e.g. soot accumulation. Highlight that a second PhD thesis is currently being carried on by the same research group to include a regeneration sub-model in the PF model. Once the regeneration sub-model will also be implemented in OpenWAM™ the software will be able to precisely simulate dynamic driving cycles as it will be able to consider all the processes taking place in a PF and their effect on the VGT and engine performance.

The main assumption of the proposed model is the experimentally well-known low soot penetration inside the porous wall. Its value will be shown to linearly increase with the mean filter Peclet number. Its precise estimation is of critical importance for the correct modelling of the filtration efficiency and pressure drop evolution as soot is collected inside the porous wall. The porous medium is modelled as a packed bed of spherical particles [50]. The Kuwabara's flow field around the collector unit [33] is applied. Soot penetration into the porous wall is restricted to be partial in order to agree with experimental evidences, which point out a very fast formation of the soot cake on the surface of the porous wall [131]. This result was already obtained at the early developments of wall-flow DPFs by Murtagh *et al.* [86]. Recent works focused on the influence of filtration velocity and particulate matter characteristics on soot loading characteristics [132] and the development of experimental techniques applied to the analysis of loaded DPFs [133] have also addressed this result. Similarly, soot and ash characterization at the catalyst-substrate interface performed by Kamp *et al.* [134] indicates that soot penetration is very reduced. These experimental insights have been corroborated by different computational studies applying the Lattice-Boltzmann method to the microscale analysis of the pressure drop [135] and soot accumulation [136] processes.

According to the proposed approach, in the developed model the porous wall is divided into two layers. The one facing the inlet channel is affected by soot deposition, the remaining part of the porous wall is simplified to be kept completely clean. Concerning the particulate layer, a model based on porous wall saturation is proposed to control a smooth increase of the particulate layer filtration efficiency during the transition from deep bed to cake filtration regime. This process is also governed by the change in effective filtration area. It controls the initial growth rate of the particulate layer thickness, as experimentally described by Choi and Lee [137].

In the following, after a detailed description, the model is validated against experimental data obtained during several soot loading tests, both in-house and from the literature, in different wall-flow PFs. The ability of the model to account for the particle size distribution effect on the filtration efficiency is also assessed.

3.2 Species transport equation

In order to describe the evolution of the porous wall microstructure and the formation of the particle layer the model needs two basic information: the filtration efficiency, whose calculation by the filtration sub-model will be detailed in Section 3.3, and the inlet DPF soot mass. This last parameter is given to the code defining the inlet system flow composition hence specifying, among all the other gas components, the soot mass fraction. Soot particles are modelled as solid carbon transported by the carrying flow by convection along the system ducts and inside the monolith channels. CFD calculations runned by Foster *et al.* [138] demonstrated that the particles Stokes number inside the monolith channels is very reduced, convective transport is the dominant one inside the monolith channels, i.e. particles follow the streamlines. The fraction of soot mass corresponding to the calculated filtration efficiency is retained inside the filter, the remaining part keeps flowing in the exhaust gas. To keep it into account the chemical species conservation equation has to be added to the system of equations described in Section 2.2.1:

- Chemical species conservation

$$\frac{\partial\left(\rho_j \mathbf{Y}_j F_j\right)}{\partial t} + \frac{\partial\left(\rho_j \mathbf{Y}_j u_j F_j\right)}{\partial x} = (-1)^j 4\left(\alpha - 2w_{pl}\right)\rho_j u_{w_j} \mathbf{Y}_{w_j} \tag{3.1}$$

As for the conservation equations described in Section 2.2, subscript j identifies the type of monolith channel and considers the presence of a particulate layer. Value 0 is referred to the outlet channels and value 1 to the inlet channels. $\mathbf{Y}$ is the vector defining the mass fraction of all the considered chemical species in the monolith channels. Because of the filtration process the species responsible for the flow composition variation is the soot by means of the term $\mathbf{Y}_{w_j}$. Indeed in the case of the inlet channel, i.e. $j = 1$, the soot mass fraction entering the porous wall corresponds to the one of the inlet channel:

$$Y_{soot_{w_1}} = Y_{soot_1} \tag{3.2}$$

while in the case of the outlet channel the wall outlet soot mass fraction is affected by the filtration efficiency:

$$Y_{soot_{w_0}} = Y_{soot_{w_1}} \left(1 - E_f\right) \tag{3.3}$$

On the other hand, it has to be kept into account that the mass fraction variation of every species, due to the filtration or regeneration process inside the porous wall ($\mathbf{Y}_{w_j}$), affects the channel mass fraction of all the remaining species $\mathbf{Y}_j$. The model keeps it into account by calculating the total mass fraction variation and using it to re-normalize the "new" mass fraction vector in the outlet channel.

Focusing back on the soot, the model allows the definition of the inlet Particle Size Distribution (PSD) as an additional virtual species. The vector $\mathbf{S}$ is used to define the percentage of the inlet soot concentration corresponding to any considered particle diameter. The soot fraction corresponding to any given particle size is then treated mathematically exactly in the same way as the chemical species, i.e. it is transported along the monolith channels according to eq. 3.4:

- PSD conservation

$$\frac{\partial\left(\rho_j \mathbf{S}_j Y_{soot} F_j\right)}{\partial t} + \frac{\partial\left(\rho_j \mathbf{S}_j Y_{soot} u_j F_j\right)}{\partial x} = (-1)^j 4\left(\alpha - 2w_{pl}\right)\rho_j u_{wj} \mathbf{S}_{w_j} Y_{soot} \tag{3.4}$$

As detailed in Section 3.3 the model is able to evaluate the collection efficiency as a function of the particle size. As in the case of eq. 3.1 the difference between the inlet and outlet channel PSD is governed by the filtration efficiency by means of the term $\mathbf{S}_{w_j}$. Again the PSD entering the porous wall corresponds to the one of the inlet channel:

$$S_{w_1} = S_1 \tag{3.5}$$

The wall outlet PSD corresponding to the outlet channel is determined by the filtration efficiency corresponding to every considered particle size i:

$$S_{w_0} = S_{w_1}\left(1 - E_{f_i}\right) \tag{3.6}$$

As a consequence the PSD variation downstream of the DPF related with the experimentally observed dependence of the filtration efficiency on the particles diameter [25] [54] can be calculated.

It is important to note that eq. 3.1 is of great importance also in the modelling of the regeneration process. The strong dependence of this process on the O_2 and NO_2 concentration requires an accurate calculation of the flow composition. Last, in case of a SCR system downstream of the DPF the filter outlet Y_{NO_2}

has to be precisely calculated because of their influence on the NO_x conversion efficiency.

The system obtained adding eqs. 3.1 and 3.4 to the conservation equations listed in Section 2.2 is solved by means of shock capturing finite-difference schemes. In the specific the two-steps Lax&Wendroff method was adapted to take into account the source term related with the porous wall, i.e. perpendicular mass flow across the porous media [139]. As a result the governing equations are expressed in the vector form as

$$\frac{\partial \mathbf{W}_j}{\partial t} + \frac{\partial \mathbf{F}_j}{\partial x} + \mathbf{C}_j + \mathbf{C}_{w_j} = 0, \tag{3.7}$$

where $\mathbf{W}_j$ is the solution vector, $\mathbf{F}_j$ the flux vector and $\mathbf{C}_j$ and $\mathbf{C}_{w_j}$ are the source terms. The former is related to friction and heat transfer contributions, the latter refers to the perpendicular mass flow across the porous wall. Again subscript j identifies the inlet or outlet channel. The two steps of the Lax&Wendroff method are formulated as in eq. 3.8 and eq. 3.9 respectively:

- 1st step

$$\mathbf{W}^{n+\frac{1}{2}}_{j,k+\frac{1}{2}} = \frac{\mathbf{W}^n_{j,k} + \mathbf{W}^n_{j,k+1}}{2} - \frac{\Delta t}{2\Delta x}\left(\mathbf{F}^n_{j,k+1} - \mathbf{F}^n_{j,k}\right) + \\ - \frac{\Delta t}{4}\left(\mathbf{C}^n_{j,k} + \mathbf{C}^n_{j,k+1}\right) - \frac{\Delta t}{4}\left(\mathbf{C}^n_{w_j,k} + \mathbf{C}^n_{w_j,k+1}\right) \tag{3.8}$$

- 2nd step

$$\mathbf{W}^{n+1}_{j,k} = \mathbf{W}^n_{j,k} - \frac{\Delta t}{\Delta x}\left(\mathbf{F}^{n+\frac{1}{2}}_{j,k+\frac{1}{2}} - \mathbf{F}^{n+\frac{1}{2}}_{j,k-\frac{1}{2}}\right) + \\ - \frac{\Delta t}{2}\left(\mathbf{C}^{n+\frac{1}{2}}_{j,k-\frac{1}{2}} + \mathbf{C}^{n+\frac{1}{2}}_{j,k+\frac{1}{2}}\right) - \frac{\Delta t}{2}\left(\mathbf{C}^{n+\frac{1}{2}}_{w_j,k-\frac{1}{2}} + \mathbf{C}^{n+\frac{1}{2}}_{w_j,k+\frac{1}{2}}\right) \tag{3.9}$$

where subscript n indicates the time-step and subscript k indicates the node position. Figure 3.1 helps understanding the formulation of the method expressed by the above equations. The first step is dedicated to the solution in halfway time-step $n+\frac{1}{2}$ and position $k \pm \frac{1}{2}$. In this step the flow entering or exiting the control volume is calculated considering the flow properties of the previous time-step n at close positions $k \pm 1$, taking into account the porous wall contribution. The intermediate flow properties calculated in first step are used in second step to finally calculate the flow properties at position k and time-step $n+1$.

The two-steps Lax&Wendroff method is coupled with a Flux-Corrected Transport (FCT) technique to avoid spurious oscillations close to discontinuities typical

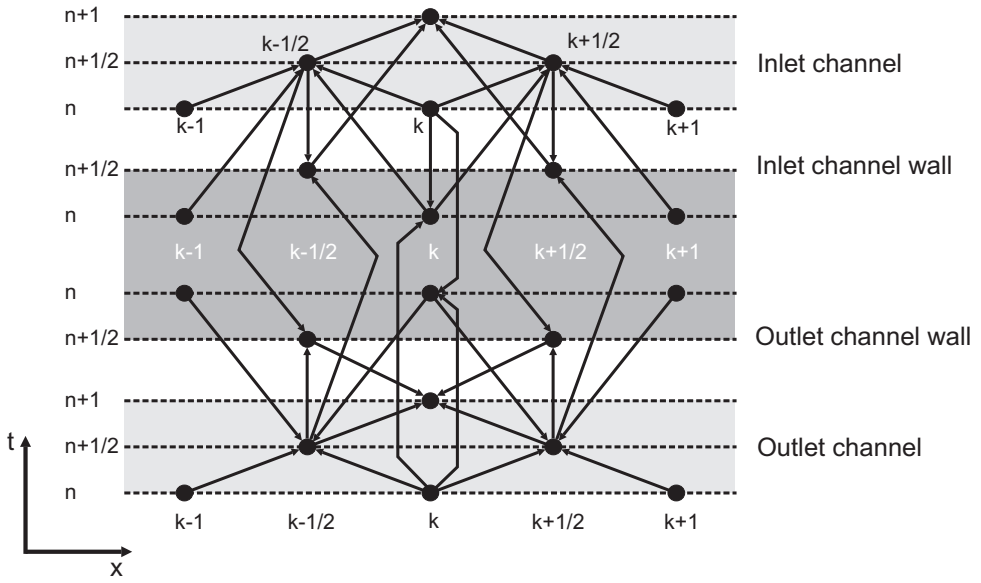

Figure 3.1: Computational grid of the two-steps Lax&Wendroff method [139].

of second-order symmetric schemes [139]. The FCT algorithm consists of three stages:

- transport stage, i.e. the application of the two-steps Lax&Wendroff method to calculate the flow properties at time-step $n+1$;
- diffusion stage in which the non-physical overshoots are removed by applying an artificial smoothing operator to the solution of the two-steps Lax&Wendroff method;
- anti-diffusion stage in which the second-order accuracy in the regions where the two-steps Lax&Wendroff solution was smoothed is recovered by applying a non-linear operator.

The boundary conditions are solved making use of the Method of Characteristics as commonly done in gas dynamic codes [28] [39]. In this particular case of the wall-flow monolith channels the method has been specifically formulated in order to be able to take into account influence of the flow through the porous wall on the values of the Riemann variables (λ and β) and the entropy level (A_A) as detailed in [140].

3.3 Filtration Mechanisms

As stated in Section 3.1 the model assumes the porous medium as a packed bed of spherical particles. Therefore the filtration efficiency of the porous substrate depends on the collection efficiency of a single sphere. The mechanisms responsible of the particles sticking on the surface of a collector unit are considered to be: Brownian diffusion, interception and inertial deposition. The three mechanisms are sketched in Figure 3.2.

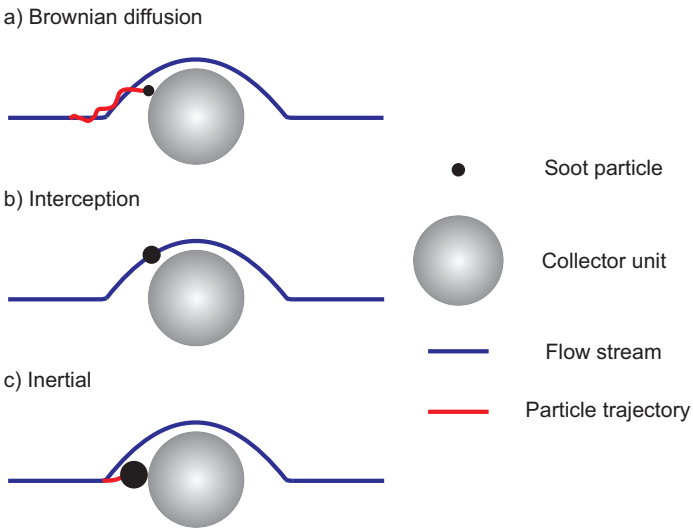

Figure 3.2: Deposition mechanisms of a particle on the collector unit.

3.3.1 Brownian diffusion deposition

Brownian diffusion deposition is the main collection mechanism of particles whose diameter is vanishingly small [45] at low flow velocities. The Brownian motion that aerosol particles undergo gradually affects them as their size decreases. Consequently, small particles leave the streamlines diffusing away and being finally deposited on the collector unit, as sketched in Figure 3.2(a). The filtration efficiency of a single sphere due to Brownian diffusion mechanism depends on the Peclet number, which relates the diffusion and advection processes. The Peclet number is defined as the ratio of the rate at which particles diffuse to the sphere surface to that at which particles approach toward the sphere surface within its cross-sectional area [45]. It is calculated for particle of diameter i as

$$Pe_{w_i} = \frac{u_{i,w} d_{c,w}}{D_{part_i}}, \tag{3.10}$$

so that it is a function of the interstitial or pore velocity ($u_{i,w}$), i.e. the ratio between filtration velocity and substrate porosity. The flow field also affects the Peclet number by means of the particle diffusion coefficient (D_{part_i}), which is calculated as:

$$D_{part_i} = \frac{T k_B SCF_w}{3\pi\mu d_{part_i}} \tag{3.11}$$

This parameter is a function of the particle diameter (d_{part_i}), the gas temperature (T) and the dynamic viscosity (μ) as well as the slip-flow effect, which is computed as a function of the Stokes-Cunningham factor:

$$SCF_w = 1 + Kn_w \left(1.257 + 0.4e^{\frac{1.1}{Kn_w}}\right) \tag{3.12}$$

$$Kn_w = \frac{2\lambda}{d_{p,w}} \tag{3.13}$$

being the mean-free path defined as:

$$\lambda = \nu\sqrt{\frac{\pi}{2RT}} \tag{3.14}$$

Finally, the microgeometry of the porous wall determines the Peclet number as a function of the collector unit diameter ($d_{c,w}$), whose formula, already defined in Section 2.2.2, is repeated here for the sake of clarity.

$$d_{c,w} = 2\left(\frac{d_{c,w_0}^3}{8} + \frac{3m_{s_{cell}}}{4\pi\chi\rho_{s_w}}\right)^{\frac{1}{3}} \tag{3.15}$$

Here d_{c,w_0} is the diameter of the clean collector unit in the porous substrate already defined in eq. 2.8. According to eq. 3.15, the collector diameter in a soot loaded cell is obtained considering the influence of three parameters:

- the clean collector unit diameter, i.e. the diameter of the collector unit when the porous wall is completely free of soot and ash;
- the soot mass inside the cell unit ($m_{s_{cell}}$), calculated at any time step by the developed filtration sub-model;
- the collector unit shape factor χ, function of the cell unit soot mass as detailed in Section 2.2.2.

Known the Peclet number of an aerosol particle approaching a single collector unit and accounting for Kuwabara's hydrodynamic factor (K), the filtration

efficiency of the single sphere due to Brownian diffusion is computed according to eq. 3.16 [45]:

$$\eta_{D_i} = 3.5\left(\frac{\varepsilon_w}{K}\right)^{\frac{1}{3}} Pe_{w_i}^{-\frac{2}{3}} \tag{3.16}$$

$$K = 2 - \varepsilon_w - \frac{9}{5}(1-\varepsilon_w)^{\frac{1}{3}} - \frac{1}{5}(1-\varepsilon_w)^2 \tag{3.17}$$

3.3.2 Interception deposition

Particles of higher diameter whose trajectory does not deviate from the streamline can be collected by single collectors due to interception mechanism. Figure 3.2(b) shows that the particles can get stuck on the collector unit in the case the streamline brings the particle surface within the radius of the collector surface. The magnitude of the filtration efficiency due to this mechanism depends on the relative dimensions of the soot particle and the collector unit. Tandon *et al.* [54] stated that this mechanism becomes relevant for particles greater than 300 nm. Nevertheless, its gradual increase as the particle size grows requires its consideration in order to evaluate the filtration efficiency in the range of the typical particle size distribution of Diesel and gasoline engines.

The interception filtration efficiency of a collector unit in the porous wall is obtained applying eq. 3.18:

$$\eta_{R_i} = 1.5\frac{N_{R_i}^2}{1+N_{R_i}^{\frac{3-2\varepsilon_w}{3\varepsilon_w}}}\frac{\varepsilon_w}{K} \tag{3.18}$$

It depends on the porous wall porosity and the interception parameter [45], which represents the particle diameter to collector unit diameter ratio:

$$N_{R_i} = \frac{d_{part_i}}{d_{c,w}} \tag{3.19}$$

3.3.3 Inertial deposition

The inertial deposition is related to the inability of a particle of changing its trajectory when the streamline is close to the collector unit. Figure 3.2(c) shows how this mechanism works: large particles, i.e. high inertia, leave the streamline and are finally collected on the surface of the collector unit by impaction. This filtration mechanism is the most important in particles of great diameter but it is also governed by the velocity. Thus, the inertial filtration efficiency of a single sphere is a function of the Stokes number [41]:

$$\eta_{I_i} = \frac{St_i^2}{(St_i + 0.25)^2} \tag{3.20}$$

$$St_i = \frac{SCF_w \rho_{s,w} u_{i,w} d_{part_i}^2}{9\mu d_{c,w}} \tag{3.21}$$

3.3.4 Overall filtration efficiency

The filtration efficiency of a single sphere is calculated considering that any deposition mechanism acts independently of the others. Therefore, the combined filtration efficiency is obtained applying the independence rule [141]:

$$\eta_{DRI_i} = \left(\eta_{D_i} + \eta_{R_i} + \eta_{I_i}\right) - \left(\eta_{D_i}\eta_{R_i} + \eta_{R_i}\eta_{I_i} + \eta_{D_i}\eta_{I_i}\right) + \eta_{D_i}\eta_{R_i}\eta_{I_i} \tag{3.22}$$

Finally, the filtration efficiency of the whole porous wall thickness is defined for every control volume CV and particle diameter i as:

$$E_{f_{w,CV_i}} = 1 - e^{-\frac{3\eta_{DRI_i}(1-\varepsilon_w)w_w f_w S_c}{2\varepsilon_w d_{c,w}}} \tag{3.23}$$

This expression is obtained taking into account the mass balance of particles through the packed bed control volume using the pore velocity as characteristic velocity for the particles due to the proximity among collectors [142].

According to Logan *et al.* [142], the term S_c represents the sticking coefficient, which is defined as the ratio of rate particles stick to collector to rate they strike it. It is an empirically derived parameter used to correct the collection efficiency of the single sphere. As forward shown in Section 3.7, the filtration efficiency in clean conditions is very sensitive to this parameter. However it has no influence on the filtration efficiency variation with soot loading and on its maximum value.

The dynamics of the filtration efficiency as the soot loading varies is directly determined by the soot penetration into the porous substrate, which is known to be very superficial [133]. Therefore, the model is simplified to accumulate the collected soot in a small portion of the porous wall thickness. It is defined by the term f_w, which represents the fraction of the porous wall thickness that is penetrated by soot.

Due to this approach, the model is not able to reproduce the gradient of soot concentration. Therefore, it is expected the prediction of a value of soot penetration slightly lower than the real one. The remaining thickness of the porous wall is assumed to be kept completely clean. Although in the real case a small amount of soot mass gets trapped in it, the dilution into a great volume allows considering it to be negligible in terms of substrate properties variation. This assumption has been already successfully checked in the prediction of the pressure drop increase as a function of a fixed, discrete soot loading [10]. In this work, the pressure drop was a function of the shape factor once imposed the soot

penetration thickness. The use of the soot aggregates properties as parameters controlling the packing density of soot into the porous wall demonstrated that the soot penetration is superficial. In following sections, the discussion is to be focused on the coupled modelling of filtration efficiency and pressure drop. The inclusion of the filtration efficiency computation makes possible to evaluate the influence of the soot penetration on its dynamics as well as on the pressure drop change as a function of the soot loading and time.

3.4 Filtration regimes

The filtration process comprises two different loading regimes as well as a transition phase where both of them are contemporaneously taking place:

- Deep bed filtration regime. In the first phase of the soot loading process all the collected soot is trapped inside a small portion of the porous wall thickness. The filtration efficiency is determined by the three collection mechanisms previously described. Both the pressure drop and the filtration efficiency suffer a steep increase during this filtration regime. This is due to the irregular deposition of soot around the collector units. The growth of the collector unit diameter is governed by the shape factor. It mainly sets the pressure drop to soot loading ratio. The filtration efficiency dynamics is controlled by the soot penetration, which in turn determines the variation of the pressure drop along the time.

- Transition regime. This phase of the filtration process is characterised by a gradual reduction of the pressure drop increasing rate as a consequence of three different phenomena. On one hand, there is a transition phase affecting the macroscale of the monolith. The flow field along the inlet channel determines differences in filtration velocity. As a result, the soot mass trapped is not uniformly distributed in the axial direction but conditioned by the flow field characteristics. The higher filtration velocity is usually located at the rear end of the inlet channel because of the flow accumulation as well as the pressure decrease in this region of the outlet channel [29]. Therefore, the saturation is firstly reached at the rear end region. This process is self-regulatory because the lower permeability in the saturated porous wall causes the air flow through the remaining region. Consequently the porous wall is progressively saturated all along the channel length.

  On the other hand there is a transition phase governed by the variation of the microgeometry of the porous wall. The model considers the deposition of a fraction of the incoming soot on the surface of the porous wall before the saturation. This process is controlled by the limit saturation coefficient

(S_l). This parameter defines the maximum local soot loading before the particulate layer formation. In turn, the local soot loading is defined by means of a geometric saturation coefficient of the porous wall (ϕ) [10], whose definition was already given in eq. 2.18 and is repeated here for the sake of clarity:

$$\phi = \frac{d_{c,w}^3 - d_{c,w_0}^3}{\left(\psi d_{cell,w}\right)^3 - d_{c,w_0}^3} \tag{3.24}$$

The particulate layer is assumed to have filtration efficiency proportional to that of the porous wall. Eq. 3.25 defines the filtration efficiency of the particulate layer, whose growth is linearly proportional to the geometric saturation coefficient conditioned by the limit saturation coefficient:

$$E_{f,pl} = E_{f,w}\left(\frac{\phi - S_l}{1 - S_l}\right) \tag{3.25}$$

As shown in Figure 3.3, that represents the particular case in which $S_l = 0.5$, the filtration efficiency of the particulate layer increases as the soot loading of the porous wall does. Both are finally equal once the porous wall reaches the saturation ($\phi = 1$).

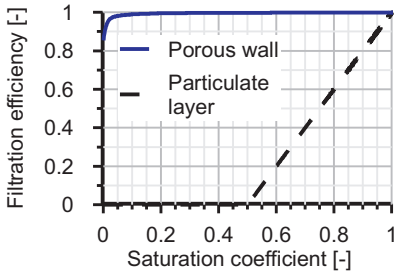

Figure 3.3: Particulate layer filtration efficiency versus porous wall saturation coefficient. $S_l = 0.5$.

The third phenomena governing the transition phase is also related to the microscale of the porous wall. It concerns the rate of particle layer thickness growth. As the air carrying the soot particles flows through the pores of the porous wall, the deposition is assumed to be initially taking place in their border region, thus generating hills-like structures. This approach is based on the experimental findings of Choi and Lee [137], which are obtained from the analysis of the soot dynamic deposition using optical techniques, and in the 3D computational results obtained by Rief *et*

al. [143]. Figure 3.4(a) shows schematically the growing dynamics around the external pores from a local particulate layer of reduced length up to cover the whole surface of the porous wall.

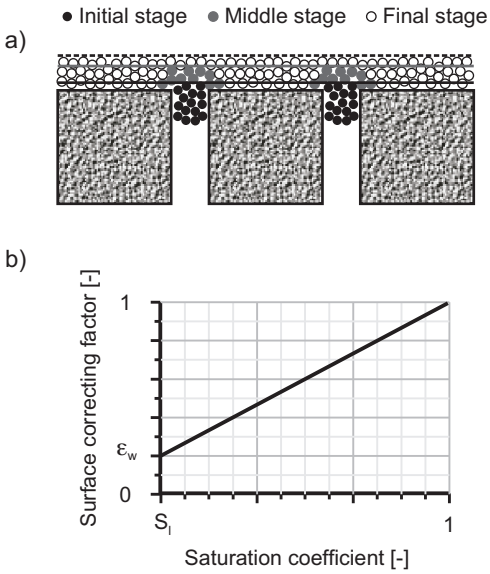

Figure 3.4: Particulate layer growth during the transition phase: a) sketch of the soot deposition onto the porous wall around the border region of a superficial pore; b) surface correcting factor function.

To take into account this phenomenon the model assumes that the particulate layer is initially formed over an effective filtration area equal to the geometric filtration area multiplied by a surface correcting factor (ξ). Thus the cake layer thickness is calculated for every node k as:

$$\alpha^2 - \left(\alpha - 2w_{pl_k}\right)^2 = \frac{m_{pl_k}}{\rho_{s,pl}\Delta x_k \xi} \Rightarrow w_{pl_k} = \frac{\alpha^2 - \left(\alpha - \frac{m_{pl_k}}{\rho_{s,pl}\Delta x_k \xi}\right)^{\frac{1}{2}}}{2} \tag{3.26}$$

which differs from eq. 2.19 for the presence of the term ξ:

$$\xi = \varepsilon_w + \left(m_{s_{cell}} - m_{s_{k|\varphi=S_l}}\right) \frac{(1-\varepsilon_w)}{\left(m_{sat_{cell}} - m_{s_{k|\varphi=S_l}}\right)} \tag{3.27}$$

From the analysis of eq. 3.26 it is possible to note that the surface corrector factor is applied to the considered finite volume length Δx_k. It implies

assuming that the 2D porosity is equal to the 3D one, what has been to be a good assumption for porous media with random structure [31].

As shown in Figure 3.4(b), the initial value of surface correcting factor is equal to the wall porosity at the onset of the particulate layer formation. The value increases linearly converging to 1, i.e. it finally meets the geometric filtration area because of the more homogeneous distribution of the streamlines. Since the available surface for soot deposition increases with time, in case of constant soot rate deposition the particulate layer thickness and pressure drop rate of growth would decrease.

- Cake filtration regime. Once the porous wall is completely saturated its properties remain constant. The particulate layer acts as a barrier filter and all the collected soot is assumed to be deposited above it. Therefore, the filtration efficiency of the particulate layer during this phase is that of the saturated porous wall. The collected soot varies the particulate layer thickness and thus governs the pressure drop.

3.5 Pulsating flow effect

As one of the focal points of this PhD thesis is the pre-turbo aftertreatment placement it is worth to clarify what are the characteristics of the flow typical of this DPF positioning, their effect on the filtration efficiency and how the model faces it.

The placement of the DPF upstream of the turbine results in inlet DPF unsteady flow, i.e. pulsating, instead of the quasi-steady flow observed downstream of the turbine. Figure 3.5 shows a comparison between the instantaneous DPF inlet pressure and temperature as well as the filtration velocity in the axial position $L_e/2$ in pre- and post-turbine configuration. Figure 3.5(a), which plots the instantaneous inlet pressure, clearly states the different nature of the flow across the DPF as a function of its placement. The Peclet number is the main parameter controlling the change in filtration efficiency in a particular DPF because of the Brownian diffusion. It is dependent on the gas temperature and filtration velocity, represented in Figures 3.5(b) and (c) respectively. The relevant variations in the fluid dynamic field result in the instantaneous filtration efficiency in pre-turbine placement depicted in Figure 3.5(c). The showed efficiency variations, over 50% during in-cycle assessment, are governed by the inverse relation between filtration efficiency and filtration velocity, whose percentage variation is more intense than instantaneous gas temperature. This result contrasts with the profile of instantaneous filtration efficiency in post-turbine DPF configuration. Although the influence of filtration velocity is still noticed,

the small variation of this variable along the cycle leads to almost constant filtration efficiency.

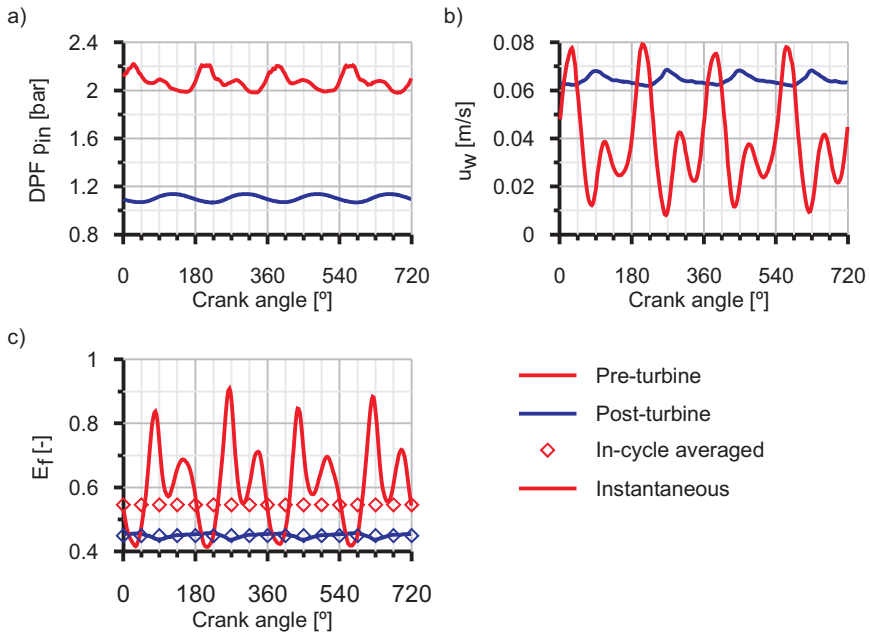

Figure 3.5: Pre- versus post-turbo DPF instantaneous inlet pressure, wall velocity and filtration efficiency throughout an engine cycle.

The showed inlet pressure peaks are associated with air mass flow, hence velocity, peaks particularly marked in pre-turbo case. The Peclet number is the main parameter controlling the filtration efficiency of a particular DPF because of the Brownian diffusion. The dependence of this parameter on the filtration velocity and gas temperature has been shown in Section 3.3.1. Eqs. 3.10 and 3.16 state that the filtration efficiency has an inverse relation with the wall velocity that leads to considerable efficiency variations along an engine cycle, i.e. up to 50% in pre-turbo placement. In contrast the profile of instantaneous filtration efficiency in post-turbo DPF configuration is showed to be very smooth. In both cases the influence of gas temperature variations is negligible compared with flow velocity variations.

Such a filtration efficiency dependence on instantaneous flow field leads to the need to properly define its averaged value during the engine cycle. A direct averaging of the instantaneous filtration efficiency throughout the engine cycle would lead to great errors, especially in the case of the pre-turbo aftertreatment positioning. In fact this procedure would involve assigning the same weight to

the highest in-cycle filtration efficiency instants, i.e. smallest mass flow and filtration velocity, that to the lowest ones. However this last value is more relevant on the amount of soot that is collected because it is related to the maximum mass flow across the porous medium. As a solution in the model the instantaneous filtration efficiency corresponding to every particle size i is weighted with the mass flow at every time-step for every control volume k as showed in eq. 3.28.

$$\bar{E}_{f_{k_i}} = \frac{\sum^{t_c} E_{f_{k_i}} \dot{m}_{w_k} \Delta t}{\sum^{t_c} \dot{m}_{w_k} \Delta t} \tag{3.28}$$

$$\dot{m}_{w_k} = \rho u_{w_k} A_{f_k} \tag{3.29}$$

In this way the precise mass-weighted average value of the filtration efficiency in an engine cycle is obtained for all the considered particle diameters i.

3.6 Soot distribution for water injection modelling

As anticipated in Section 2.6 the CMT - Motores Térmicos owns a patent related to the pre-DPF water injection technique as a way to limit the pressure drop generated by soot loaded DPFs. Part of this PhD thesis is dedicated to the experimental characterization of the water injection effect as a technique to optimize the filter performance. Having the possibility of simulating the effect of the water flow through the filter is of great interest but requires the availability of a tool that makes it possible.

The previous CMT model was coded as to automatically distribute in a uniform way the possible presence of soot mass inside the filter at the simulation beginning. That is, in case of the simulation of a loading process starting with a given soot mass the model distributes it uniformly to every computation node resulting in a constant particle layer thickness along the axial direction calculated making use of eq. 2.19.

This is exactly the case of a water injection event in normal engine operation conditions: in presence of a given soot mass the water injector is opened to reduce the pressure drop generated by the loaded DPF. However the water flow is supposed to influence the layer distribution and characteristics. On one hand it is believed to push the particle layer towards the inlet channels rear part and/or to make the soot penetrate deeper inside the porous wall. On the other hand the momentum of the water jet could be high enough to affect the particle layer density. Meanwhile the engine is still emitting particles with the original

characteristics that will be deposited above the particle layer modified in shape and characteristics by the water injection. Consequently a "new" particle layer with the original characteristics would grow above the "perturbed" one.

In this context, in the filtration model developed in the mark of this PhD thesis has been implemented a feature that gives the possibility of simulating the water injection process. The model provides on one hand the possibility of manually distributing the soot mass along the monolith length as depicted in Figure 3.6.

On the other hand the user has the possibility of defining two different sets of characteristics for the incoming soot particles and the already deposited particles, i.e. the layer subjected to the water injection. As stated above it is indeed plausible that the pressure actuated by the water jet on the particle modifies its characteristics, i.e. porosity, density, permeability. The result is the superposition of two layers with different thickness and permeability. The model faces it by calculating at every time step the total thickness as the sum of the two layers and the equivalent permeability as:

$$k_{pl,e} = \frac{w_{pl} k_{pl,wat} k_{pl,in}}{w_{pl,wat} k_{pl,in} + w_{pl,in} k_{pl,wat}} \tag{3.30}$$

3.7 Loading processes

This section is devoted to the assessment of the filtration model by means of the analysis of modelling results obtained from different particulate filters. In order to demonstrate the robustness of the proposed model both in-house and literature experimental filtration data are considered. Table 3.1 summarises the main geometrical characteristics of the modelled particulate filters.

Table 3.1: Characteristics of modelled DPFs.

		#A [32]	#B [86]	#C [86]	#D [86]	#E [86]
D	[mm]	132	267	267	267	267
L	[mm]	200	305	305	305	305
α	[mm]	1.48	2.11	2.11	2.11	2.11
w_w	[mm]	0.31	0.43	0.43	0.43	0.43
σ	[cpsi]	200	100	100	100	100
ε_0	[-]	0.41	0.48	0.5	0.5	0.5
d_{p_0}	[μm]	12.1	12.5	13.4	24.4	34.1
k_{w_0}	[$x10^{-13}$m^2]	2.49	3	3.44	11.6	22.54

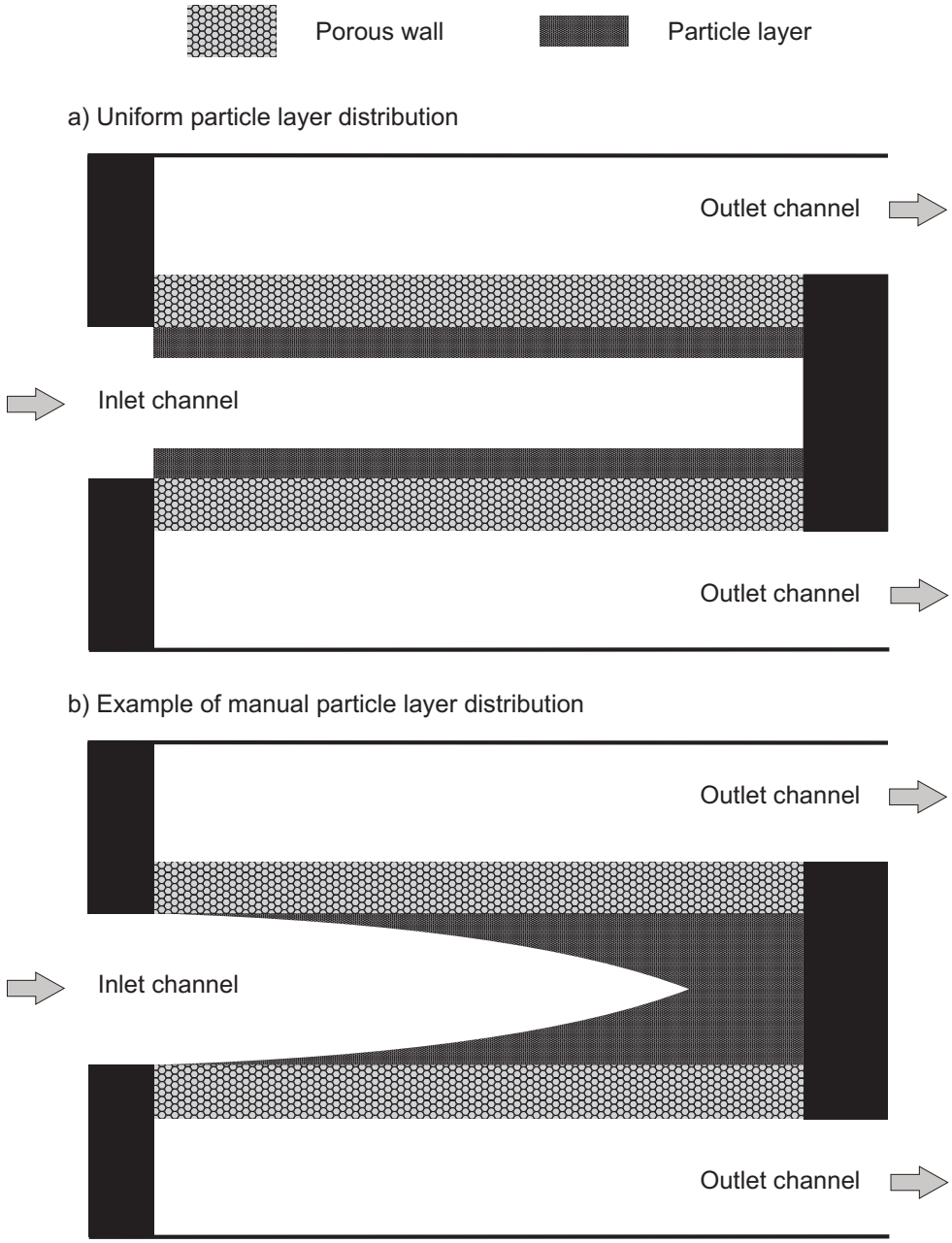

Figure 3.6: Schematic representation of the soot layer distribution: a) Uniform; b) Manual.

3.7.1 Soot penetration thickness

As a baseline, pressure drop and filtration efficiency of DPF #A were experimentally characterized during a soot loading process. The DPF was installed in the exhaust line of a 2.0 l Diesel engine in a test bench. The engine, whose characteristics are reported in Table 3.2, was fueled with a commercial light Diesel and run under steady-state operating conditions at 2500 rpm and 80 Nm.

Table 3.2: Engine #1 specifications.

Type		HSDI Diesel engine
Emission standard		Euro IV
Injection system		Common rail
Turbocharger		VGT
Displacement	[cc]	1997
Cylinders number	[-]	4 in line
Valves number	[-]	4 per cylinder
Bore	[mm]	85
Stroke	[mm]	88
Compression ratio	[-]	1:18
Maximum power	[kW]	100 @ 4000 rpm
Maximum torque	[Nm]	320 @ 1750 rpm

In these conditions, exhaust gas flow and temperature at the DPF inlet are 0.04 kg/s and 300°C. The particle concentration and size distribution upstream and downstream of the filter were measured by using a TSI Engine Exhaust Particle Sampler (EEPS) following the methodology proposed by Desantes *et al.* [144]. The DPF pressure drop was measured by means of two piezorresistive transducers placed at the inlet and outlet cones of the device. Similarly, gas temperature was also monitored by means of K-type thermocouples placed at the inlet cone and next to the outlet duct junction. The filter was free of soot at the beginning of the test since it was firstly regenerated and the exhaust flow was bled to a secondary exhaust line using a by-pass valve during the engine stabilisation, as explained in [24].

Before starting the analysis of the soot penetration thickness on the generated pressure drop and filtration efficiency, for the sake of completeness, Figure 3.7 shows the velocity and pressure field in the inlet and outlet channels as a function of the axial position.

Solid lines refer to clean substrate, while dashed lines refer to the case of 6 grams of soot inside the DPF. In both cases the red line is related to the conditions in the inlet channel and the black line to the conditions in the outlet channel. The velocities and pressure trends are similar to the ones shown by Depcik and Assanis in [145] and Liu *et al.* in [146]. Figure 3.7(a) shows the filtration velocity in the inlet and outlet channel. As shown in the works of

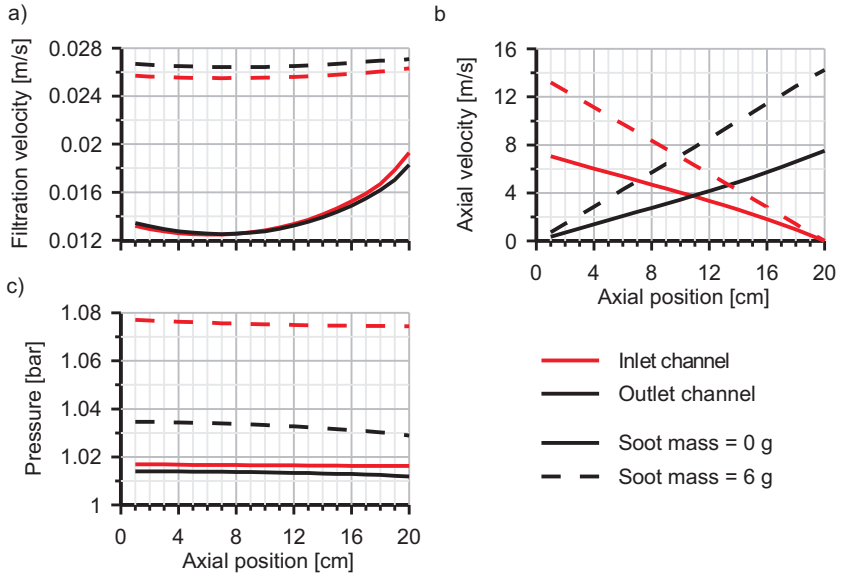

Figure 3.7: Velocity and pressure field in the inlet and outlet channels in clean and 6 grams soot loaded conditions. a) filtration velocity b) axial velocity c) pressure.

Depcik and Assanis [145] and Liu *et al.* [146] the filtration velocity owns a parabolic profile with the maximum value in the rear end part of the channels. Torregrosa *et al.* [29] showed that the parabolic shape of the filtration velocity changes to a monotonously increasing filtration velocity along the channel length at high inlet DPF Reynolds number, i.e. around 150000. The reason lies in the mass flow accumulation capacity of the inlet channel because of the plug end, which dominates over the friction effects as Re increases. The axial velocity, presented in Figure Figure 3.7(b), displays an opposite trend between inlet and outlet channel as expected, approaching to 0 moving towards the respective channel plug. Regarding pressure, Figure 3.7(c) shows that friction and flow loss, related to gas flowing from the inlet to the outlet channel, make the pressure in the inlet channel gradually decrease along the channel length. As soot is accumulated inside the filter, both the filtration and the axial velocities increase. The main reason is the notable temperature difference, around 300°C, between the beginning of the soot loading process and the time at which 6 grams of soot are accumulated inside the filter. The filtration velocity shows a flatter profile and a much more marked velocity difference between inlet and outlet channel. The outlet channel velocity is higher than the inlet one because of the notable pressure difference between inlet and outlet. As the temperature difference

between inlet and outlet channel is negligible, this pressure difference leads to a density difference of the same percentage magnitude of the velocity difference.

Figure 3.8 shows the comparison between the experimental and modelled pressure drop and filtration efficiency corresponding to the soot loading test of DPF #A. All the results showed in this section have been calculated assuming that the mode of the particle size distribution governs the soot loading process, as concluded by Serrano *et al.* [10] from pressure drop modelling. In this work also the filtration process is referred to the mode of the particle size distribution. Its value is 69 nm in case of DPF #A. The modelling has been performed imposing 2% and 10% in soot penetration fraction inside the porous wall in order to demonstrate the dependence of pressure drop and filtration efficiency on this parameter.

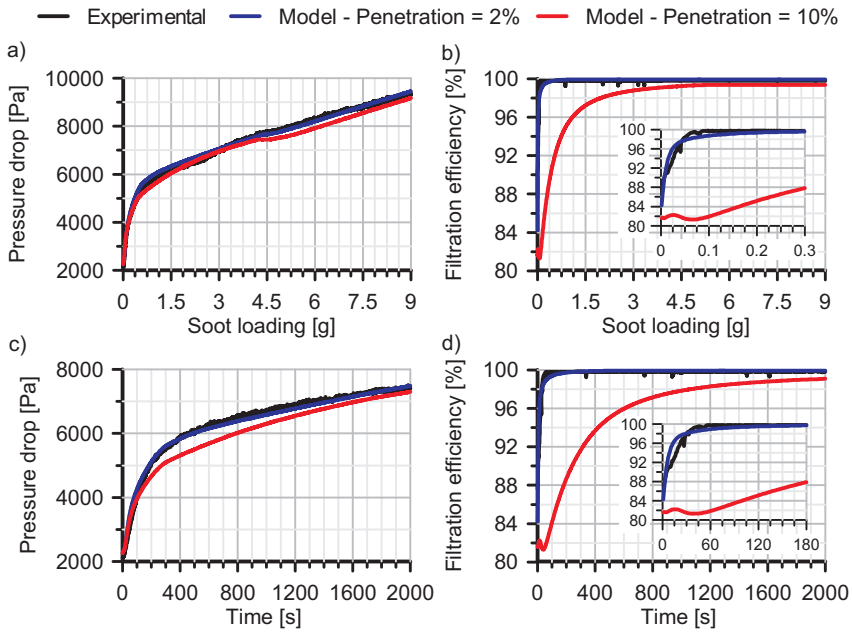

Figure 3.8: Experimental versus modelled pressure drop and filtration efficiency in DPF #A. Soot penetration influence.

The analysis of Figure 3.8(a) points out that the pressure drop can be reproduced as a function of the soot loading within a great range of soot penetration thickness. This is possible by acting on the shape factor. The change in shape factor value makes the apparent soot packing density inside the porous wall vary. As the soot penetration is increased, the permeability of the substrate also varies at a particular soot loading. Consequently, the shape factor correlation

must be modified to obtain again the effective porous wall permeability that reproduces the experimental pressure drop.

The uncertainty provided by the model because of possible multiple mathematical setups able to reproduce the pressure drop as a function of the soot mass loading for different soot penetrations is removed when the calculation of the filtration efficiency is coupled. Figure 3.8(b) clearly shows that the filtration efficiency is correctly modelled only in the case of 2% of penetrated fraction of porous wall thickness. This means that the pressure drop dynamics as a function of the time can be only attained when filtration efficiency is properly captured. This is only obtained with 2% of soot penetration thickness, as confirmed in plots (c) and (d) of Figure 3.8.

The impossibility to get the filtration efficiency with high soot penetration is explained based on the change suffered by the substrate microstructure. This is plotted in Figure 3.9, which shows the main magnitudes governing pressure drop and filtration phenomena at the middle of the inlet channel (0.1 m).

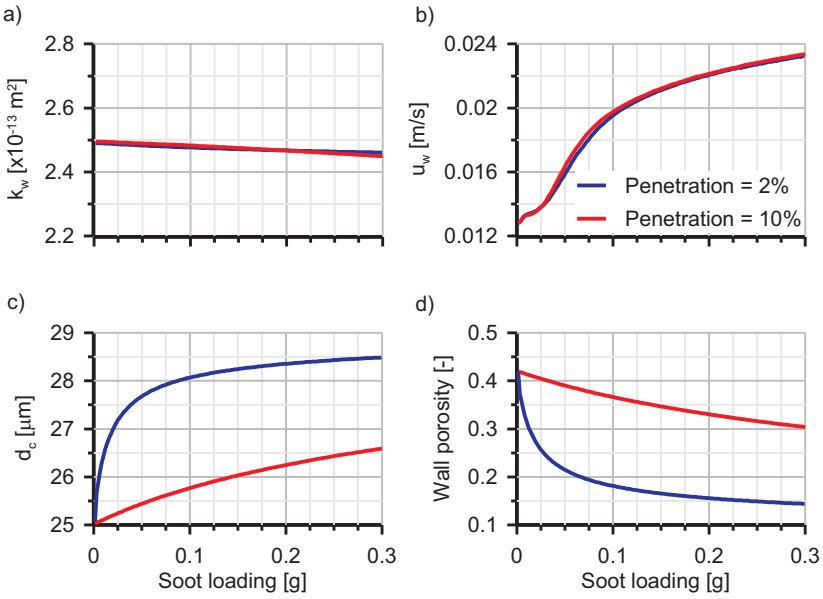

Figure 3.9: Soot penetration effect on porous wall microstructure properties.

Plot (a) in Figure 3.9 represents the effective porous wall permeability. It is clearly noticed that the differences between the two modelled cases are negligible, since the difference in soot penetration is offset by the change in the setup of the shape factor, as previously explained. The equality in effective porous wall permeability leads to similar filtration velocity variation as the soot

load increases, as shown in Figure 3.9(b). This result also points out that the differences in filtration efficiency (Figure 3.8(b)) are not due to the fluid-dynamic field, which is not varied. Therefore, the cause of this difference is to be found in the porous wall microstructure. Thus, plots (c) and (d) in Figure 3.9 represent the variation of the collector unit diameter and porosity as a function of the soot mass loading and the soot penetration fraction into the porous wall. As the penetration increases, the diameter of the collector unit decreases for the same soot loading (Figure 3.9(c)) despite the decrease of the shape factor (decrease in apparent soot packing density), which is set to reproduce the effective porous wall permeability based on Eqs. 2.6-2.7. As a result the increase of the soot penetration leads to an increase of the porosity for the same soot loading, as shown in Figure 3.9(d), because of the greater volume available for soot storage.

The smaller collector unit diameter in 10% penetration case has a positive effect on the Brownian diffusion efficiency. This is due to the Peclet number decrease against the same fluid-dynamic field. However, the filtration efficiency gets more damaged by the porosity increase because of the higher value of the Kuwabara's hydrodynamic factor K. This trend leads to a slight decrease of collected soot mass at any time-step. Consequently, a snowball effect is produced and the filtration efficiency increases much more slowly than experimentally when the penetration is overestimated.

The influence of the sticking coefficient (eq. 3.23), i.e. the remainder filtration model parameter, is analysed in Figure 3.10. The evolution of the filtration efficiency is represented during the initial phase of the loading process. The results depicted by the dashed red series correspond to an increase of the sticking coefficient value in the case of soot penetration fraction equal to 10%. It can be noted how the sticking coefficient increase leads to higher clean filtration efficiency but it has no effect on its dynamics during the soot loading process. This result certifies that the soot penetration is the only geometric parameter governing the univocal relation between pressure drop and filtration efficiency. It is determined during the first phase of the deep bed filtration regime, since almost maximum filtration efficiency is reached before the change in pressure drop slope, which indicates the change to cake filtration regime (~0.1 g against ~1 g of collected soot). Therefore a coupled modelling of these phenomena allows providing a confident prediction of the soot penetration as a function of the porous medium properties and the fluid-dynamic conditions.

The variations of pressure drop and filtration efficiency in DPFs #B to #E during soot loading processes have been modelled according to this approach. The experimental data corresponding to these particulate filters have been obtained from the work of Murtagh *et al.* [86]. As described in [86], the tests were conducted under steady state operating conditions being mass flow 0.285 kg/s and gas temperature 260°C at the DPF inlet.

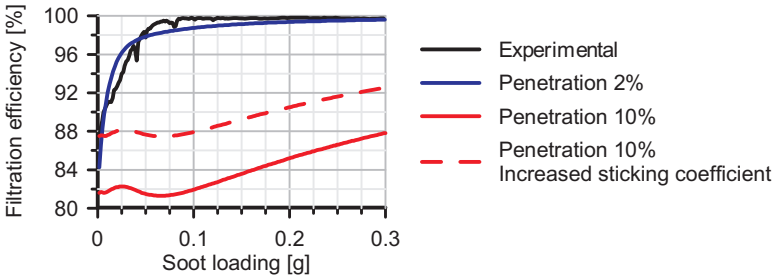

Figure 3.10: Experimental versus modelled filtration efficiency in DPF #A. Sticking coefficient influence.

Figure 3.11 shows the comparison between experimental and modelled pressure drop and filtration efficiency in DPFs #B to #E during the soot loading tests. The accurate modelling of both phenomena indicates the ability of the model to describe variations in porous medium properties and flow field as soot is collected.

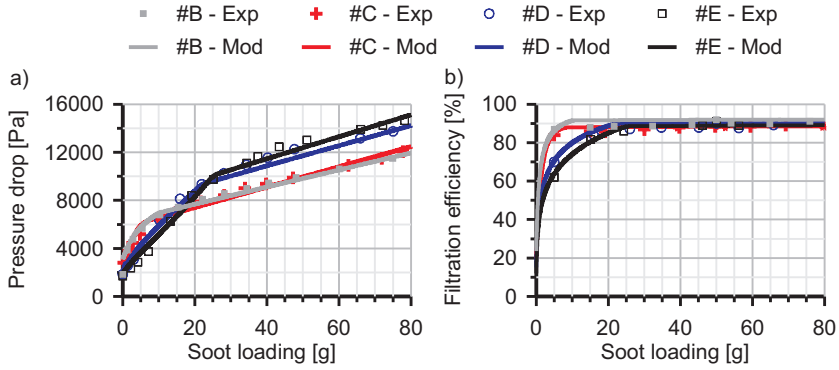

Figure 3.11: Experimental versus modelled pressure drop and filtration efficiency in DPFs #B to #E.

3.7.2 Transition filtration regime

Although usually transition from deep bed to cake filtration regime is described based on local effects, the differences in the axial direction of the inlet channel are much more important because of the relation with the fluid-dynamic field, hence with the pressure drop dynamics. The modelling of the soot loading test corresponding to DPF #A with a fraction of porous wall thickness penetrated by

soot equal to 2% indicates that the quantity of soot able to be collected inside the porous wall before its saturation is 1.05 g. Nevertheless, the parabolic profile of the filtration velocity along the inlet channel makes that some regions of the porous wall get saturated before others, thus contributing to an irregular particulate layer formation.

Figure 3.12 shows the main variables explaining the trend of the filtration efficiency as a function of the channel length and soot mass loading, which is shown in plot (a). The saturation coefficient of the porous wall is plotted in Figure 3.12(b). The porous wall in the rear end of the inlet channel gets saturated once the collected soot mass reaches 0.89 g. Despite this is not the region with the highest filtration efficiency, which is located in the middle of the inlet channel, the difference is almost negligible. Consequently, the rear end region is the first to be saturated because it is subjected to the highest filtration velocity, i.e. to the highest soot mass rate, as shown in Figure 3.12(c). As the soot mass increases, the saturation region of the porous wall gradually propagates towards the inlet section. The porous wall is completely saturated when 1.11 g of soot have been collected. This process defines a transition window from deep bed to cake filtration regime equivalent to 0.22 g of soot accumulation. As shown in Figure 3.8(a), the pressure drop slope varies along it from the maximum value during deep bed filtration regime to the minimum one once the whole porous wall is saturated.

As shown in Figure 3.12, once the whole porous wall is saturated (1.11 g), i.e. its microstructure is constant along the channel length, the parabolic profile of the filtration efficiency is only conditioned by the fluid-dynamic field. This mainly concerns the influence of the filtration velocity, although second order effects may appear related to temperature and pressure gradients impact on the diffusion coefficient.

On the contrary, the filtration efficiency profile before saturation is determined by both the flow field and the local properties of the porous wall microstructure. Plots (d) and (e) in Figure 3.12 represent the variation in collector unit diameter and porosity respectively. Even though values of the saturation coefficient over 0.8 mean almost maximum filtration efficiency, it can be noted its gradual increase up to saturation conditions. Given the negligible change in filtration velocity as the collected soot increases, this phase is governed by the local collector unit diameter increase and the subsequent porosity reduction. This process makes that only when the whole porous wall is saturated the maximum filtration efficiency is located in the region of minimum filtration velocity. Otherwise it is moved towards the inlet channel rear end, where the porosity is low, despite the slight increase in filtration velocity.

Once the particulate layer is completely formed, the increase of the soot loading leads to the progressive decrease of the filtration velocity. It is a consequence of the notable pressure drop increase which leads to a higher inlet pressure,

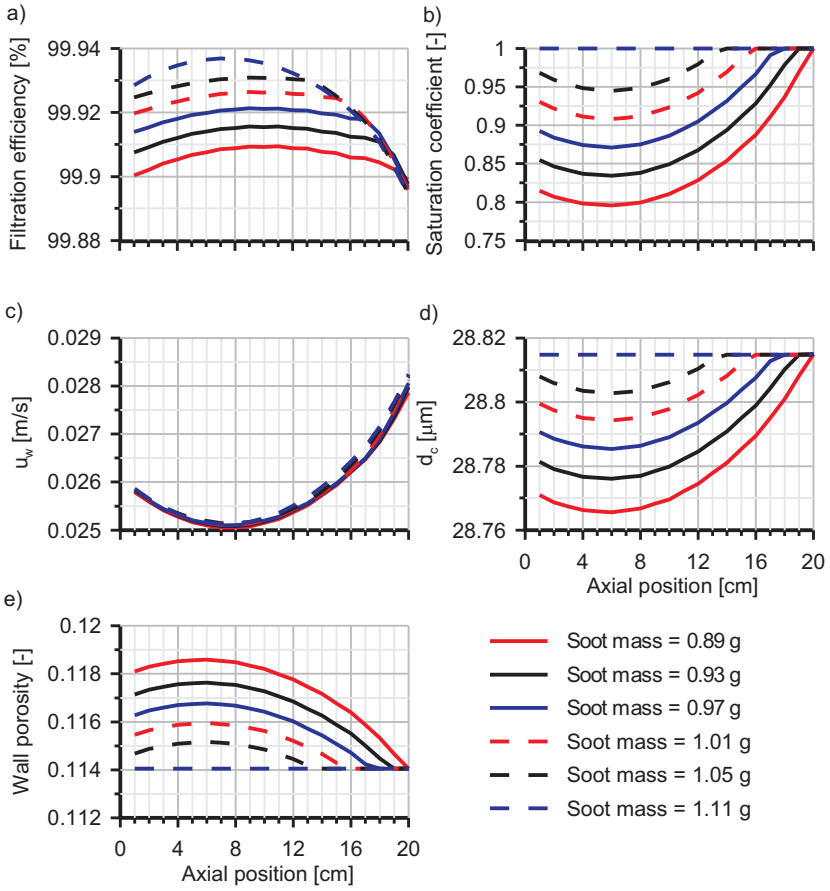

Figure 3.12: Axial distribution of the flow and porous wall properties along the inlet channel of DPF #A as a function of the soot mass loading during transition filtration regime.

hence higher flow density. According to the results shown in Figure 3.13 and comparing with plot (a) in Figure 3.12, it is noticed how the parabolic profile of the filtration velocity, with maximum velocity at the rear end of the inlet channels, moves towards a flatter axial distribution. This gradual change is due to the higher accumulation of soot in the rear region caused by the higher soot mass rate, which eventually compensates the slightly lower filtration efficiency. In turn, the change in filtration velocity gives rise to the complementary variation of the filtration efficiency. It is also strictly depending on the fluid-dynamic field since the particulate layer microstructure properties can be assumed to be constant [10].

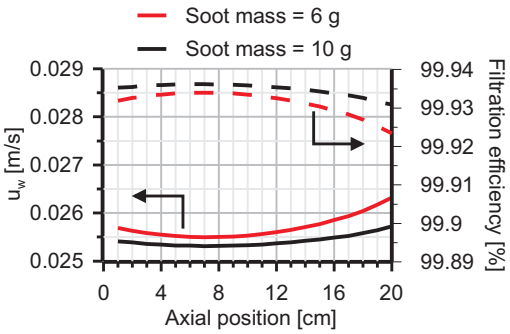

Figure 3.13: Axial distribution of the filtration velocity and efficiency along the inlet channel of DPF #A during the cake filtration regime.

In comparison to macroscale transition from deep bed to cake filtration, local transition is a process that cannot be directly described by 1D modelling assuming lumped and quasi-steady behaviour of the porous substrate. As described in Section 3.4, the approach to deal with local transition is then based on the combination of two concepts. These involve saturation limit of the porous wall before the onset of the particulate layer formation and local growth of the particulate layer around the saturated pores. This modelling requires the experimental characterisation of the critical soot loading inside the porous wall and the rate of the particulate layer growth around the pore. Although the complexity of this setup brings to uncertainty, its influence on pressure drop and overall filtration efficiency is demonstrated to be completely negligible in comparison to macroscale transition. On this concern, Figure 3.14 shows a comparison between experimental and modelled results for pressure drop and filtration efficiency in DPF #A. The modelling of the loading process has been performed with two different values of the limit saturation coefficient (1 and 0.5). Note that the effective filtration area for particulate layer formation is depending on the limit saturation coefficient according to eq. 3.26. It has effects on the filtration efficiency of the particulate layer (eq. 3.25) and hence on the amount of soot contributing to increase the layer thickness. Nevertheless, the evolution of the DPF response is reproduced with great accuracy whatever the limit saturation coefficient.

Red series in Figure 3.14 represents the case of limit saturation coefficient set to 0.5. When the saturation coefficient of the node reaches this value the model imposes a filtration efficiency for the particulate layer according to eq. 3.25. Thus, the incoming soot starts depositing on the top of the porous wall and forming the particulate layer. Initially its efficiency is very low thus driving to a progressive growth in parallel to deep bed filtration.

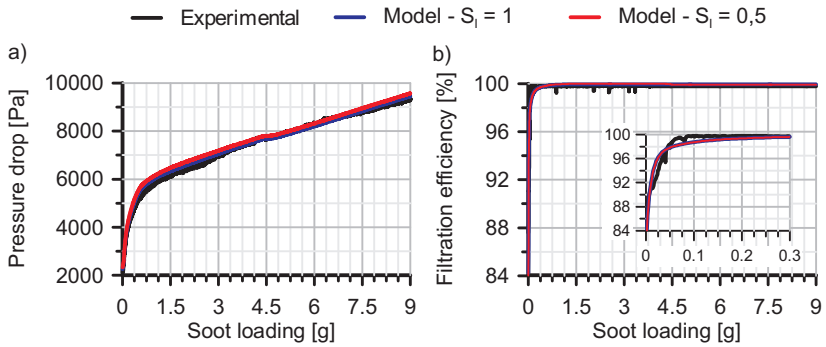

Figure 3.14: Experimental versus modelled pressure drop and filtration efficiency in DPF #A. Limit saturation coefficient influence.

Against lack of local transition between filtration regimes, the benefit of using a limit saturation coefficient is a smooth variation of the porous media properties as a function of the soot loading. This is shown in Figure 3.15, in which different porous medium properties are represented during the local transition phase as example. The value of these parameters has been taken at 0.1 m from the monolith inlet cross-section. The increasing rate of the saturation coefficient, which is represented in Figure 3.15(a), gets reduced when it reaches the limit value. This kind of approach avoids the appearance of the non-physical discontinuities affecting all porous medium properties when the local transition phase is not considered, i.e. limit saturation coefficient equal to 1.

The inclusion of the local transition phase leads to higher duration of the deep bed filtration regime. Consequently the particulate layer thickness undergoes a slow growth, as represented in Figure 3.15(b), up to converge to the same rate of increase that the case of lack of local transition. Nevertheless, the slow particulate layer thickness variation has minor effect on filtration efficiency and pressure drop. On one hand, during the deep bed filtration regime, the filtration efficiency has almost reached its maximum value, at the expense of asymptotic convergence as shown in Figures 3.12 and 3.13. On the other hand, results in Figure 3.14(a) demonstrate the slight variation in pressure drop. The sooner onset of the particulate layer formation might suggest an increase of the pressure drop. However this process is in trade-off with the porous wall contribution to pressure drop. As shown in plot (c) of Figure 3.15, the deposition of soot to form the particulate layer causes a slowdown of the collector unit diameter growth inside the porous wall. Hence, the permeability, which is shown in Figure 3.15(d), is kept higher than in modelling in which the local transition phase is not considered.

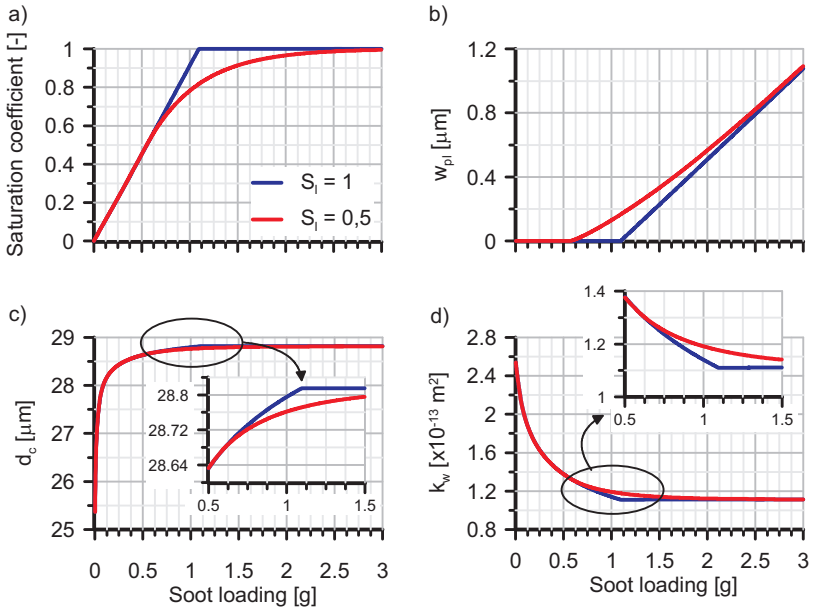

Figure 3.15: Limit saturation coefficient effect on substrate properties.

3.8 Peclet number - soot penetration correlation

As previously discussed on DPF #A results, the main parameter governing the coupling between pressure drop and filtration efficiency is the degree of soot penetration into the porous wall. This has been set in every DPF up to reproduce the dynamics of both variables. As represented in Figure 3.16(a), which summarises penetration results for DPF #A to #E, the result is a linear increase of the soot penetration inside the porous wall with the mean Peclet number. Note that this latter parameter is evaluated for clean filter conditions and mode value of the particle size distribution. Eq. 3.31 shows the correlation obtained from the modelled DPFs:

$$w_{sp} = 0.0019 Pe_{w_0} \tag{3.31}$$

This result is congruent with the decrease of Brownian diffusion efficiency as the convective transport takes importance since this mechanism is the main one contributing to the combined filtration efficiency. The dependence of the filtration efficiency on the Peclet number, which is depicted in Figure 3.16(b) in terms of soot penetration, allows also concluding that the higher the filtration efficiency in clean conditions the lower the penetration thickness. Indeed, as the Brownian mechanism is the most important one, high efficiencies are

related with highly disordered particles motion. As the particles do not follow the streamlines it is easy that they get stuck on a collector unit immediately after penetrating the porous wall. In the specific case of DPFs #B to #E, it is interesting to note that the operating conditions are the same for all of them as well as their volume and filtration area. Therefore, the filtration velocity is also coincident. According to eq. 3.10, the differences in Peclet number are exclusively due to microstructure variations. Since the clean porosity is also identical or very similar between all these DPFs, the differences found in penetration and filtration efficiency are strictly sensitive to the variation of the clean mean pore diameter, which ranges from 12.1 μm to 34.1 μm. It is interesting to note that in a visualization study of soot loaded DPF samples by means of a SEM the authors came to the same conclusion stating that the maximum soot penetration thickness, as well as its mean value, presents a strong dependence on the porous media mean pore diameter [147].

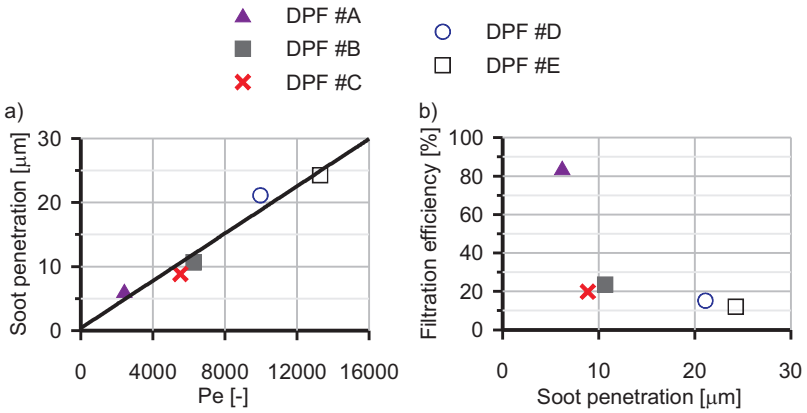

Figure 3.16: Soot penetration and filtration efficiency in clean conditions as a function of the clean porous wall Peclet number.

In order to further prove the robustness of the developed correlation, it has been applied to the soot loading processes analysed by Sanui and Hanamura in [148] and by Karin in [147]. In both these studies the authors used a scanning electron microscope (SEM) to dynamically visualize the soot deposition process in different SiC DPF samples. Table 5.1 resumes the characteristics of the tested samples.

In [148] a fuel burner was used to simulate soot emitted from a diesel engine. Two dilution systems were used to ensure a constant filtration velocity of 0.1 m/s. In these conditions, applying the correlation proposed in this work (eq. 3.31), the calculated maximum soot penetration inside the porous wall, corresponding to

Table 3.3: Characteristics of optically analysed DPF samples.

		#F [148]	#G [147]	#H [147]
d_{p,w_0}	[μm]	15	15	40
w_w	[mm]	0.4	0.4	0.38
σ	[cpsi]	200	200	300
ε	[-]	0.5	0.58	0.6

the biggest observed particles (400 nm), is 115 μm. Figure 3.17 shows that this order of magnitude definitely agrees with the depth observed with the SEM and marked with the dotted black circle below which no presence of soot is detected.

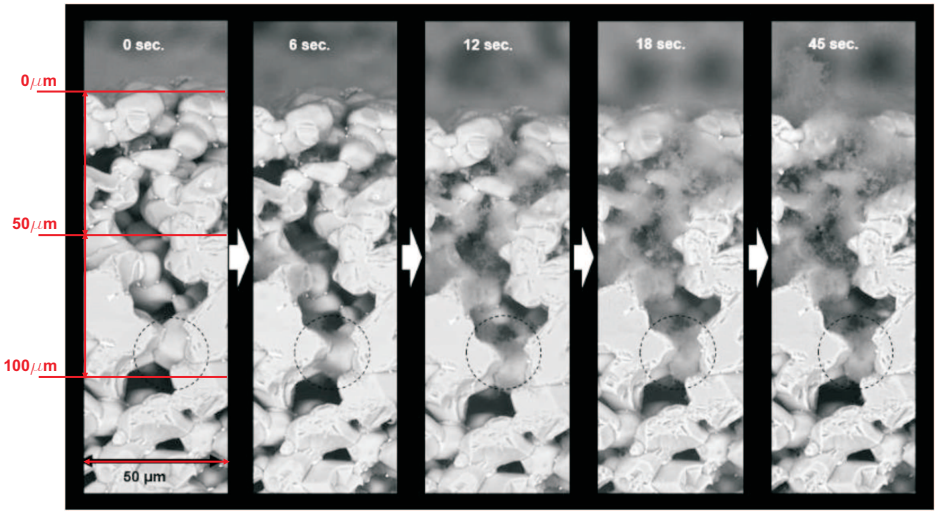

Figure 3.17: SEM image of soot penetration in sample #F. Adapted from [148].

The SEM technique was also used in [147] on two different SiC DPF samples. In this case the soot source for the loading process was a Diesel engine whose main characteristics are resumed in Table 3.4.

The operating point was 2.1 kW load and 3000 rpm speed with a fuel injection pressure of approximately 50 MPa. A fraction of the exhaust gas was introduced into the DPF sample through a bypass line maintained at a constant temperature of approximately 200°C. The filtration velocity was approximately 2.31 cm/s for sample #G and 3.47 cm/s for sample #H. Such velocities are similar to that of a DPF under representative real driving conditions. SEM images of the emitted particles revealed an agglomeration soot size from sub-micron order to around 1 μm being the size of primary particles between 20 and 60 nm

Table 3.4: Engine #2 specifications.

Type	Four strokes Diesel engine
Displacement	230 cm^3
Bore	70 mm
Stroke	60 mm
Number of cylinders	1
Compression ratio	1:21
Maximun power	3.3 kW at 3000 rpm
Maximun torque	10.8 Nm at 2300 rpm
Fuel	Commercial light Diesel

and agglomerated size about 100 to 300 nm [149]. The normalized particle size distribution is showed in Figure 3.18.

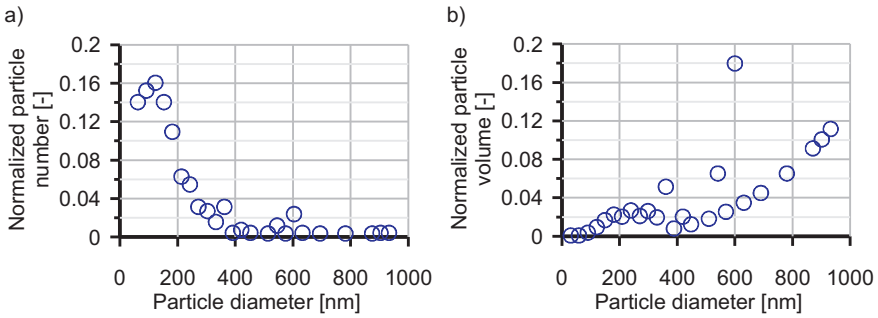

Figure 3.18: Normalized particle size distribution using SEM images. Adapted from [149].

Figure 3.19 shows the PM distribution into the transversal section of the porous wall for DPF sample #G. It can be seen that the majority of the particles are collected at a depth smaller than 20 μm. A lower soot presence is detected up to around 40 μm. According to eqs. 3.10 and 3.11 the Peclet value is influenced by the particle diameter by means of the diffusion coefficient so that the bigger the particles the higher the Peclet number, thus increasing the penetration thickness. Therefore the proposed correlation provides a soot penetration value of 15 μm (red line) for agglomerated particles, i.e. up to 300 nm, and a maximum penetration of 45 μm (blue line) for the largest observed particles, i.e. around 1 μm.

In case of DPF sample #H, Figure 3.20 shows that the majority of the soot is collected between the surface and a depth of around 70 μm. Sparse presence of

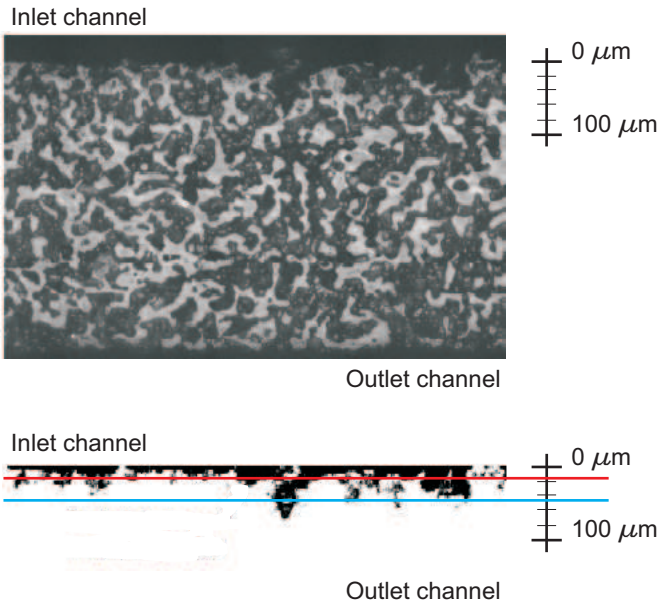

Figure 3.19: SEM image of PM distribution into the transversal section of the porous wall for sample #G. Adapted from [147].

soot particles is detected up to 300 μm. Again, applying the proposed correlation, the result is a soot penetration value of 60 μm(red line) for agglomerated particles, i.e. up to 300 nm, and a maximum penetration of 205 μm (blue line) for the largest observed particles, i.e. around 1 μm.

The developed correlation to calculate the soot penetration thickness inside the porous wall of a PF has been demonstrated to be consistent with experimental evidences in all the considered cases. It was showed that the use of the aggregates particles size for the Pe number calculation results in soot penetration values (red lines in Figure 3.19 and Figure 3.20) that cover the particulates trapped in the surface pores, i.e. the overwhelming majority of the collected soot mass. The difference between the experimentally observed and the calculated soot penetration thickness is in the range 5-10 μm. Concerning the greatest particle size, its use provides penetration thickness that comprises also the reduced amount of particulates trapped inside the inner pores.

3.9 Particle size effect on filtration efficiency

Previous results have proved the usefulness of the mode of the particle size distribution as representative of the overall PF performance in terms of pressure

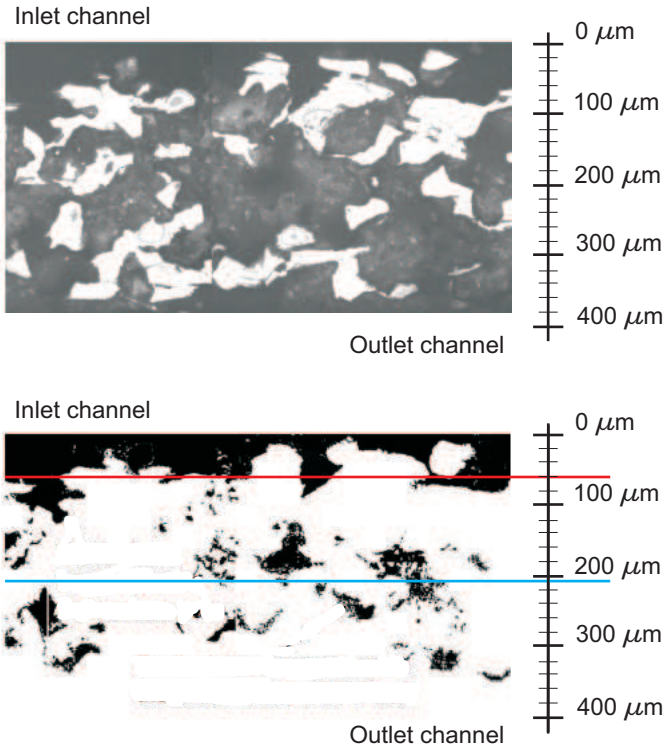

Figure 3.20: SEM image of PM distribution into the transversal section of the porous wall for sample #H. Adapted from [147].

drop and filtration efficiency. However, current emission standards already require to account for the particle number emission [62]. Therefore, filtration models must also assess their ability to predict the filtration efficiency as a function of the particle size and to track the change in PSD across the PF.

Experimental data of two DPFs and one HEPA ceramic membrane filter from the literature have been used to prove the ability of the developed model to deal with the influence of the particle diameter on the filtration efficiency. The characteristics of the considered filters are reported in Table 3.5.

Figure 3.21 represents the comparative between experimental and modelled filtration efficiency as a function of the particle size corresponding to PF #I in clean conditions. This particulate filter is a HEPA ceramic membrane filter whose geometrical characteristics and experimental data have been obtained from the work of Marre *et al.* [150]. The measured filtration efficiency corresponds to four different cases defined by filtration velocity ranging from 0.01 to 0.04 m/s.

Table 3.5: Characteristics of modelled PFs.

		#I [150]	#L [58]	#M [58]
D	[mm]	-	25.4	25.4
L	[mm]	-	76.2	76.2
α	[mm]	-	1.48	1.16
w_w	[mm]	1.65	0.31	0.31
σ	[cpsi]	-	200	300
ε_0	[-]	0.45	0.558	0.65
d_{p_0}	[μm]	10.8	18	23.5

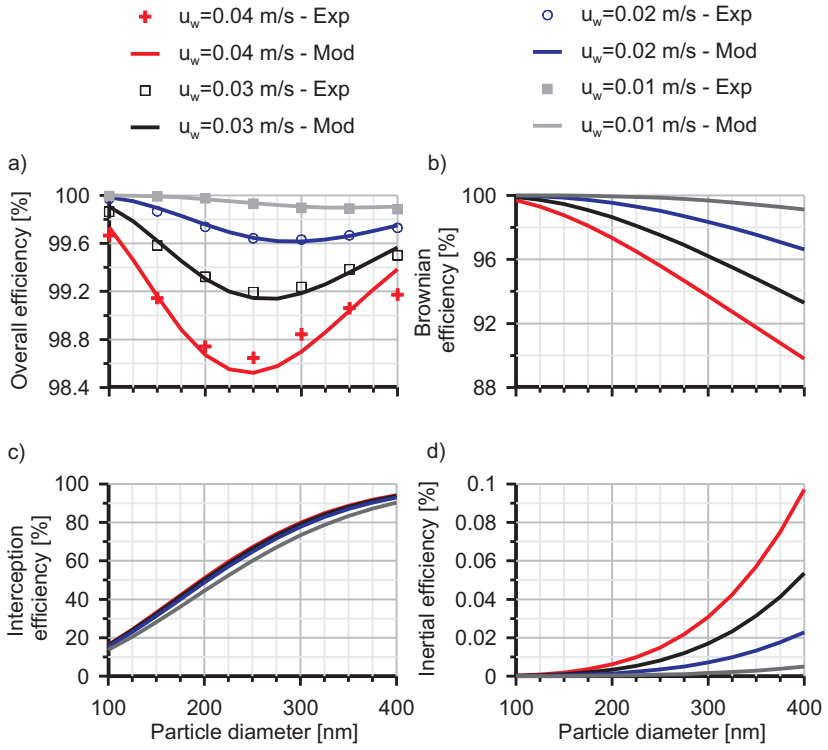

Figure 3.21: Experimental versus modelled filtration efficiency in clean conditions of filter #I as a function of particles size and filtration velocity.

The soot penetration thickness into the porous wall has been estimated according to the correlation obtained in the modelling of filters #A to #E detailed in Section 3.8. Figure 3.22 plots the variation of the penetration as a function of

the Peclet number whose values are set, in this specific case, by the filtration velocity variation from test to test.

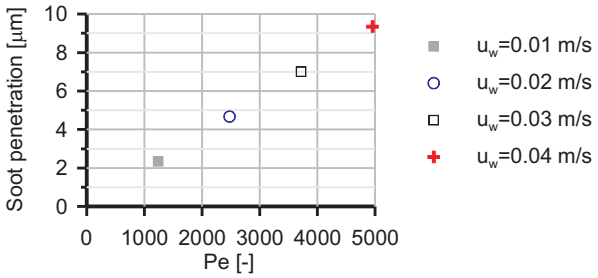

Figure 3.22: Estimated penetration of soot into the porous wall of filter #I as a function of the Peclet number.

According to the results shown in Figure 3.21(a), the model is able to predict the overall filtration efficiency as a function of the particle size within a broad range from 100 to 400 nm. This range would correspond to the aggregate particles emitted by internal combustion engines. It covers the most penetrating particle size, whose value decreases as the filtration velocity increases from 350 nm to 250 nm accompanied by a relevant decrease of the filtration efficiency.

In addition, the filtration efficiency corresponding to every deposition mechanism is represented. Plots (b), (c) and (d) in Figure 3.21 show the Brownian, interception and inertial filtration efficiency respectively. It is clearly shown how the Brownian diffusion mechanism is the dominant one despite its decrease as the particle size and filtration velocity increase. In fact, its contribution is of the same order of magnitude that the one provided by interception mechanism at 400 nm even under the highest tested filtration velocity conditions. Interception mechanism, which gradually increases its efficiency as the diameter does, is relevant to meet the overall filtration in the range of aggregate particles size. This behaviour balances the decrease in filtration efficiency related to the Brownian diffusion mechanism and allows reaching high filtration efficiency in the whole PSD range. Contrarily, the inertial efficiency is completely negligible because of the low flow velocity due to the great filtration area and the small size of the particles.

The validation of the model capability to predict filtration efficiency against particles of different size has been completed with the analysis of filtration efficiency in wall-flow DPFs #L and #M. These DPF samples were subjected to flow containing aerosolized salt particles [58]. The spatial-averaged filtration velocity during tests was 0.0168 m/s in DPF #L and 0.0155 m/s in the case of DPF #M. Again the particles penetration into the porous wall has been estimated

from the Peclet number correlation given by eq. 3.31. Thus, the thickness of penetrated porous wall has been imposed equal to 3.53 μm and 2.50 μm for DPFs #L and #M respectively.

Figure 3.23 shows the comparison between the experimental and modelled overall filtration efficiency in clean conditions of DPFs #L and #M as a function of the particle size. Results are very accurate over 25 nm. The decreasing value of the overall filtration efficiency as the particle size increases is accurately predicted in both filters, which show similar performance. The model only shows deviations with respect to the experimental data at very low particle diameter. In this range the model seems to overestimate the filtration efficiency. That is, the Brownian diffusion contribution, which theoretically tends to 100% as the particle size decreases, is overestimated.

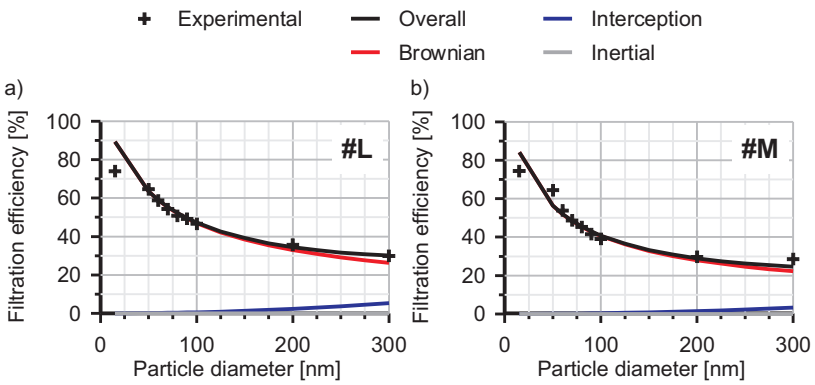

Figure 3.23: Experimental versus modelled filtration efficiency in clean conditions of filters #L and #M as a function of particles size.

Figure 3.24 and Figure 3.25 show the evolution of the overall filtration efficiency as a function of the particle size as soot is collected inside the filter #L and #M respectively. In none of the modelled cases the porous wall has reached the saturation. The variation of the microstructure derived from soot accumulation inside the porous media affects in both cases the value of the most penetrating particle size. Indeed in clean and very low soot loading conditions the filtration efficiency continuously decreases as the particle size increases. As soot is collected the filtration efficiency grows in the whole particle size range, being this growth more marked for the bigger particles. This effect is related to the interception contribution, which tends to retain higher size particles and rapidly increases as the collector unit diameter increases and the porosity decreases. Differences in microstructure, marked by the clean porous media characteristics reported in Table 3.5, between the two DPFs are responsible of

the different most penetrating particle size value at the end of the simulation, i.e. around 0.3 collected soot grams. Therefore sample #L presents a value around 150 nm while in case of sample #M, characterized by higher porosity and mean pore diameter, the most penetrating particle size takes a slightly higher value, i.e. around 200 nm.

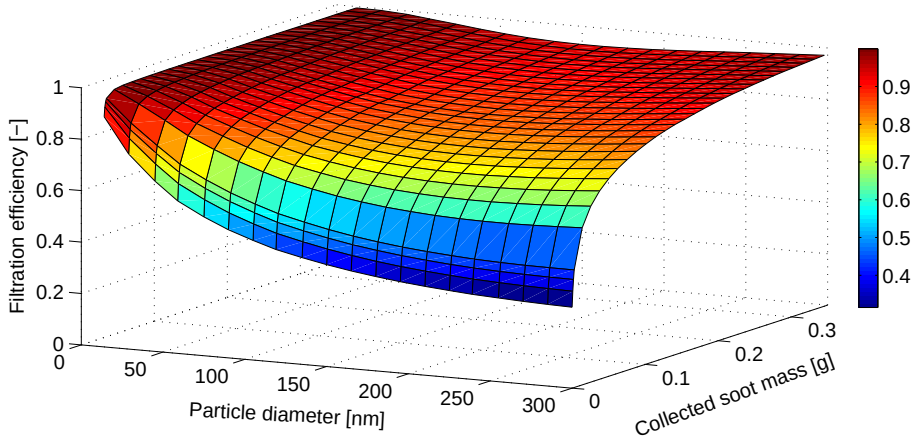

Figure 3.24: Evolution of filtration efficiency with collected soot mass as a function of particles size. Filter #L.

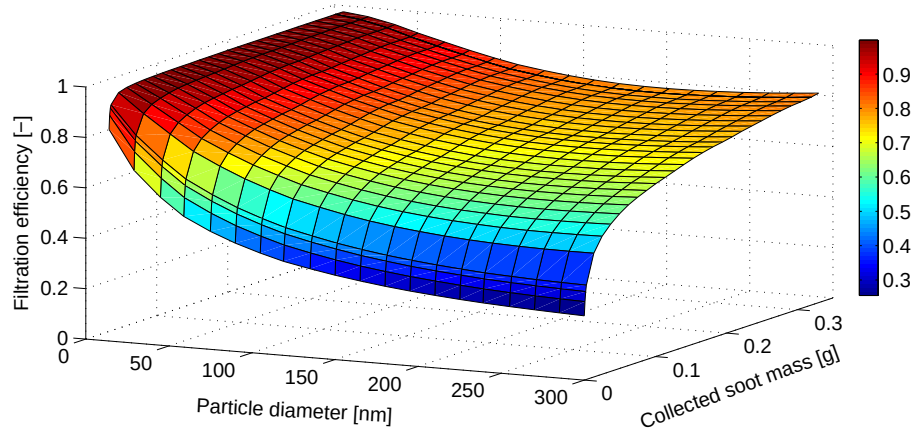

Figure 3.25: Evolution of filtration efficiency with collected soot mass as a function of particles size. Filter #M.

3.10 Summary

In the present chapter the filtration model developed within the framework of this PhD thesis has been presented and discussed. The model has been implemented in OpenWAM™. It is based on the packed bed of spherical particles approach to describe the properties of the porous medium. As a consequence the filtration efficiency of the porous substrate can be referred to the response of a single collector unit. To assess it the Brownian diffusion, interception and inertial deposition mechanisms are considered. According to experimental and computational evidences the main hypothesis of the model is the partial soot penetration into the porous wall. Therefore, the porous wall is divided into two layers: an inner one, i.e. facing the inlet channel, and an outer one, i.e. facing the outlet channel. The former is assumed to be the only one in which soot deposition takes place. Its microstructure is modified because of the soot accumulation in its interior. The outer slab is considered to be kept always clean, i.e. it is not subjected to particles accumulation.

The model includes a sticking coefficient in the filtration efficiency calculation. Such a parameter has to be included in order to properly predict the filtration efficiency in clean conditions but does not affect its evolution as soot is collected. The filtration efficiency and pressure drop dynamics have been shown to be governed by the soot penetration inside the porous wall. Their correct modelling relies on the proper estimate of the porous wall fraction affected by particles deposition. That is, soot penetration is the geometrical parameter that governs the unequivocal relation between pressure drop and filtration efficiency.

A correlation for the estimation of soot penetration thickness inside the porous wall has been obtained. Soot penetration has been shown to be linearly proportional to the mean Peclet number referred to the collector unit diameter of the clean porous wall. The proposed correlation has been applied to the modelling of 8 PFs and to the optical analysis of 3 DPFs samples. In the former case the mode value of the emitted PSD has been used to calculate the soot penetration thickness. It resulted in the precise modelling of both the filtration efficiency and the pressure drop evolution as soot is collected considering both changes in the porous media microstructure and in the operating conditions. Also, in 3 of the 8 PFs considered cases, it has been proved the ability of the model to deal with the effect of the particle size on the filtration efficiency. Concerning optical analysis, the comparison of the calculated penetration thickness with SEM images of 3 different soot loaded DPFs samples has showed that the use of the representative aggregate particles diameter provides soot penetration values that comprise the overwhelming majority of the collected soot mass.

As one of the focal points of this PhD thesis is the pre-turbo aftertreatment placement, the model needs to be able to deal with the pulsating flow typical of this configuration. The flow field fluctuations upstream of the turbine result in

considerable filtration efficiency variations along an engine cycle. In order to provide reliable results, in the model the instantaneous (corresponding to every crank angle degree) filtration efficiency is weighted with the instantaneous mass flow at every time-step and for every control volume. Thus the precise mass-weighted average value of the filtration efficiency is calculated at any engine cycle.

Also, because of the interest in the possibility of modelling the effect of the water injection at the DPF inlet, the developed model has been provided with a feature aimed to it. The model is able to consider on one hand the redistribution of the particle layer and the variation of its characteristics related with the water droplets flow through the channels. On the other hand the model is able to face with the formation of a new particle layer above an old one with different characteristics, i.e. modified by the water injection for example. Apart from opening the possibility of modelling the water injection at the DPF inlet and its effect on the pressure drop and filtration efficiency the above described feature makes possible to model the simultaneous presence of soot and ash by defining the right characteristics for the ash layer. It also makes possible to evaluate by means of simulation campaigns the effect of the ash distribution along the filter length on the pressure drop as well as the evolution of the filtration efficiency and pressure drop during a soot loading process in presence of ash. An example of this last case could be the simulation of a certification cycle with an aged filter loaded with ash.

Although the filtration efficiency gets almost its maximum value during the deep bed filtration regime, the pressure drop shows a slow transition phase up to cake filtration regime. The analysis of the modelled results indicates that such a transition depends on the flow field prediction, which causes the saturation of the porous wall along the inlet channel length. Therefore, transition in pressure drop, i.e. the reduction of its increasing rate up to be governed by the particulate layer properties, is essentially dependent on macroscale properties. Consequently 1D modelling is required for its correct prediction in order to avoid mismatch in the evolution of microscale properties such as porosity or mean pore diameter change. The capability to model the local transition, which depends on microgeometry properties of the loaded porous wall, is very limited in lumped quasi-steady porous medium models. It is based on criteria related to cell loading and effective filtration area for particulate layer initial growth. Nevertheless, the influence of these phenomena on the filter response has been shown to be of second order. The interest for these approaches lies in the need to avoid non-physical discontinuities thus providing a smooth variation of the involved porous media properties.

The set of different particulate filters used in the experimental validation has allowed proving that the change in overall filtration efficiency is governed, like the pressure drop, by the mode diameter of the particle size distribution.

As additional feature of the model, very good accuracy to predict the filtration efficiency as a function of the particle size has been also obtained. It has been computed within the range of aerosol size in internal combustion engines, i.e. covering from primary to aggregate particles, which is mainly depending on the right modelling of the Brownian diffusion and interception deposition mechanisms.

3.11 References

[9] *Regulation (EC) No 715/2007 of the European Parliament and of the Council of 20 June 2007 on type approval of motor vehicles with respect to emissions from light passenger and commercial vehicles (Euro 5 and Euro 6) and on access to vehicle repair and maintenance information*. Official Journal of the European Union. 2007 (cit. on pp. 3, 62).

[10] J. R. Serrano, F. J. Arnau, P. Piqueras, and O. García-Afonso. "Packed bed of spherical particles approach for pressure drop prediction in wall-flow DPFs (diesel particulate filters) under soot loading conditions". In: *Energy* 58 (2013), pp. 644–54 (cit. on pp. 3, 15, 17, 19, 63, 71, 73, 82, 87, 167).

[24] V. Bermúdez, J. R. Serrano, P. Piqueras, and O. García-Afonso. "Pre-DPF water injection technique for loaded DPF pressure drop reduction and control". In: *Applied Energy* 140 (2015), pp. 234–245 (cit. on pp. 5, 8, 43, 44, 48, 80, 203).

[25] V. Bermúdez, J. R. Serrano, P. Piqueras, and D. Campos. "Analysis of the influence of pre-DPF water injection technique on pollutants emission". In: *Energy* 89 (2015), pp. 778–792 (cit. on pp. 5, 45–47, 65, 216, 233).

[28] J. Galindo, J. R. Serrano, F. J. Arnau, and P. Piqueras. "Description and analysis of a one-dimensional gas-dynamic model with Independent Time Discretization". In: *Proceedings of the ASME Internal Combustion Engine Division 2008 Spring Technical Conference ICES2008*. 2008 (cit. on pp. 16, 22, 67, 112).

[29] A. J. Torregrosa, J. R. Serrano, F. J. Arnau, and P. Piqueras. "A fluid dynamic model for unsteady compressible flow in wall-flow Diesel particulate filters". In: *Energy* 36 (2011), pp. 671–684 (cit. on pp. 16, 17, 36, 62, 63, 72, 81, 158).

[31] F. Dullien. *Porous Media. Fluid Transport and Pore Structure*. Academic Press, New York, 1992 (cit. on pp. 17, 33, 75).

[32] F. Payri, A. Broatch, J. R. Serrano, and P. Piqueras. "Experimental-theoretical methodology for determination of inertial pressure drop distribution and pore structure properties in wall-flow diesel particulate filters (DPFs)". In: *Energy* 36 (2011), pp. 6731–6744 (cit. on pp. 17, 18, 78, 125, 198).

[33] S. Kuwabara. "The forces experienced by randomly distributed parallel circular cylinders or spheres in a viscous fluid at small Reynolds numbers". In: *Journal of the Physical Society of Japan* 14 (1959), pp. 527–532 (cit. on pp. 17, 24, 30, 63).

[39] D. Winterbone and R. Pearson. *Theory of engine manifold design: wave action methods for IC engines*. Professional Engineering Publishing, 2000 (cit. on pp. 22, 67).

[41] N. A. Fuchs. *The mechanics of aerosols*. Ed. by C. N. Davies. Pergamon press, 1964 (cit. on pp. 24, 70).

[45] K. Lee and J. Gieseke. "Collection of aerosol particles by packed beds". In: *Environmental Science and Technology* 13.4 (1979), pp. 466–470 (cit. on pp. 24, 27, 68, 70).

[50] A. G. Konstandopoulos and J. H. Johnson. "Wall-flow Diesel particulate filters - Their pressure drop and collection efficiency". In: *SAE Technical Paper 890405*. 1989 (cit. on pp. 27, 39, 63).

[54] P. Tandon, A. Heibel, J. Whitmore, N. Kekre, and K. Chithapragada. "Measurement and prediction of filtration efficiency evolution of soot loaded diesel particulate filters". In: *Chemical Engineering Science* 65 (2010), pp. 4751–4760 (cit. on pp. 28, 65, 70).

[58] J. Gong and C. J. Rutland. "PDF-based heterogeneous multiscale filtration model". In: *Environmental Science and Technology* 49(8) (2015), pp. 4963–4970 (cit. on pp. 29, 96, 97).

[62] B. Guan, R. Zhan, H. Lin, and Z. Huang. "Review of the state-of-the-art of particulate filter technology". In: *Journal of Environmental Management* 154 (2015), pp. 225–258 (cit. on pp. 31, 33, 34, 38, 95).

[86] M. Murtagh, D. Sherwood, and L. Socha. "Development of a diesel particulate filter composition and its effect on thermal durability and filtration performance". In: *SAE Technical Paper 940235*. 1994 (cit. on pp. 34, 35, 63, 78, 84).

[129] *Regulation (EC) No 595/2009 of the European Parliament and of the Council of 18 June 2009 on type-approval of motor vehicles and engines with respect to emissions from heavy duty vehicles (Euro VI) and on access to vehicle repair and maintenance information and amending Regulation (EC) No 715/2007 and Directive 2007/46/EC and repealing Directives 80/1269/EEC, 2005/55/EC and 2005/78/EC*. Official Journal of the European Union. 2009 (cit. on p. 62).

[130] *Official website of the European Union*. 2015 (cit. on p. 62).

[131] S. Somiya, J. Adler, U. Petasch, and et al. *Handbook of Advanced Ceramics: Materials, Applications, Processing, and Properties. Chapter 8.1*. Academic Press, 2013 (cit. on p. 63).

[132] R. Yapaulo, E. Wirojsakunchai, T. Orita, D. Foster, M. Akard, L. Walker, and M. Lance. “Impact of filtration velocities and particulate matter characteristics on diesel particulate filter wall loading”. In: *International Journal of Engine Research* 10.5 (2009), pp. 287–304 (cit. on p. 63).

[133] D. Fino, N. Russo, F. Millo, D. Vezza, F. Ferrero, and A. Chianale. “New tool for experimental analysis of diesel particulate filter loading”. In: *Top Catalysis* 52 (2009), pp. 13–20 (cit. on pp. 63, 71).

[134] C. Kamp, A. Sappok, and V. Wong. “Soot and ash deposition characteristics at the catalyst-substrate interface and intra-layer interactions in aged diesel particulate filters illustrated using Focused Ion Beam (FIB) milling”. In: *SAE Technical Paper 2012-01-0836*. 2012 (cit. on p. 63).

[135] M. Stewart, T. Gallant, D. Kim, G. Maupin, and A. Zelenyuk. “Fuel efficient diesel particulate filter (DPF) modeling and development”. In: *Pacific Northwest National Laboratory, PNNL-19476*. 2010 (cit. on p. 63).

[136] K. Yamamoto, A. Oohori, H. Yamashita, and S. Daido. “Simulation on soot deposition and combustion in diesel particulate filter”. In: *Proceedings of the Combustion Institute* 32 (2009), pp. 1965–1972 (cit. on p. 63).

[137] S. Choi and K. Lee. “Detailed Investigation of Soot Deposition and Oxidation Characteristics in a Diesel Particulate Filter Using Optical Visualization”. In: *SAE Technical Paper 2013-01-0528*. 2013 (cit. on pp. 63, 73).

[138] F. Piscaglia, C. Rutland, and D. Foster. “Development of a CFD model to study the hydrodynamic characteristics and the soot deposition mechanism on the porous wall of a Diesel particulate filter”. In: *SAE Technical Paper 2005-01-0963*. 2005 (cit. on p. 64).

[139] J. R. Serrano, F. J. Arnau, P. Piqueras, and O. García-Afonso. “Application of the two-step Lax&Wendroff-FCT and the CE-SE method to flow transport in wall-flow monoliths”. In: *International Journal of Computer Mathematics* 91(1) (2014), pp. 71–84 (cit. on pp. 66, 67).

[140] J. M. Desantes, J. R. Serrano, F. J. Arnau, and P. Piqueras. “Derivation of the method of characteristics for the fluid dynamic solution of flow advection along porous wall channels”. In: *Applied Mathematical Modelling* 36 (2012), pp. 3144–3152 (cit. on p. 67).

[141] W. Ferrel. *An Introduction to Probability Theory and Its Applications*. Wiley, New York, 1971 (cit. on p. 71).

[142] B. E. Logan, D. G. Jewett, R. G. Arnold, J. Bouwer E., and C. R. O’Melia. “Clarification of clean-bed filtration models”. In: *Journal of Environmental Engineering* 121 (1995), pp. 869–873 (cit. on p. 71).

[143] S. Rief, D. Kehrwald, K. Schmidt, and A. Wiegmann. “Simulation of ceramic DPF media, soot deposition filtration efficiency and pressure drop evolution”. In: *Proceedings of the 10th World Filtration Congress 2008;3:318-22*. 2008 (cit. on p. 74).

[144] J. M. Desantes, V. Bermúdez, S. Molina, and W. G. Linares. “Methodology for measuring exhaust aerosol size distributions using an engine test under transient operating conditions”. In: *Measurement Science and Technology* 22(11) (2011), p. 115101 (cit. on pp. 80, 194).

[145] C. D. Depcik and D. Assanis. “Simulating area conservation and the gas-wall interface for one-Dimensional based Diesel particulate filter models”. In: *Journal of Engineering for Gas Turbines and Power* 130(6) (2008), p. 062807 (cit. on pp. 80, 81, 204).

[146] Y. Liu, J. Gong, J. Fu, H. Cai, and G. Long. “Nanoparticle motion trajectories and deposition in an inlet channel of wall-flow diesel particulate filter”. In: *Journal of Aerosol Science* 40 (2009), pp. 307–323 (cit. on pp. 80, 81).

[147] P. Karin, L. Cui, P. Rubio, T. Tsuruta, and K. Hanamura. “Microscopic visualization of PM trapping and regeneration in micro-structural pores of a DPF wall”. In: *SAE International Journal of Fuels and Lubricants* 2(1) (2009), pp. 661–669 (cit. on pp. 91, 92, 94, 95).

[148] R. Sanui and K. Hanamura. “Scanning Electron Microscopic visualization of transition from surface pore filtration to cake filtration inside Diesel Particulate Filter walls”. In: *SAE Technical Paper 2015-01-1018*. 2015 (cit. on pp. 91, 92).

[149] P. Karin. “Microscopic visualization and characterization of particulate matter trapping and oxidation in diesel particulate filters and membrane filters”. PhD thesis. Tokyo Institute of Technology, 2010 (cit. on p. 93).

[150] S. Marre, J. Palmeri, A. Larbot, and M. Bertrand. “Modeling of submicrometer aerosol penetration through sintered granular membrane filters”. In: *J. Colloid Interface Sci.* 274 (2004), pp. 167–182 (cit. on pp. 95, 96).

CHAPTER 4

Aftertreatment volume downsizing in pre- and post-turbo configuration

Contents

Figures

Tables

4.1 Introduction

THE intensive, mandatory use of aftertreatment systems in the exhaust line of internal combustion engines, especially in compression ignition ones, results in a notable cost increase. Considering different control emission technologies covering active and passive solutions, Posada *et al.* stated that the cost to fulfill Euro 6 is around 1600$ in a 4 cylinder 2.0 l engine, 50% of which directly coming from aftertreatment systems [151]. The most important contribution comes from the NO_x emission reduction system (LNT in the study of Posada *et al.*) with a 50% followed by the DPF and the DOC with a 40% and 10% respectively. Other studies, such as the reports from EPA/NHTS [152] and NAS [153], provide aftertreatment systems cost even higher. From these data, and assuming that the whole aftertreatment system to fulfil Euro 6 is estimated to reach circa 30% of the engine cost, the DOC and DPF are representing around 15% of it.

The DOC and DPF monolith volume directly affects on one hand the system cost and on the other hand its performance. That is, its reduction would result in cheaper systems but the eventuality of any negative effect on the system efficiency should be carefully evaluated. On the other hand the monolith size decrease might result in lower thermal inertia, what would be of particular interest in the case of pre-turbo positioning, as detailed in Section 2.5.

The present chapter is devoted to the analysis of the effect of the DPF and DOC volume downsizing on both the engine and aftertreatment systems performance. The problem has been approached by means of a wide computational campaign using the in-house 1D OpenWAM™ software. Particular attention has been paid to the DPF, being it the main focus of this PhD thesis. The developed filtration model described in Chapter 3 has been applied in this study.

4.2 Modelling methodology

The results obtained in this study are based on the gas dynamic modelling of the same turbocharged 2 litres diesel engine, whose main characteristics have been given in Table 3.2. As anticipated in Section 4.1 the computational study has been performed using the in-house 1D software OpenWAM™ [27] [28], already introduced in Chapter 2.

As first step of the study, the engine model was tuned up from experimental data obtained in engine test bench. Reference tests were performed under steady-state operating conditions for both post- and pre-turbo aftertreatment configurations. The considered engine operating points were 90% load at 1500 rpm, 80% load at 2000 and 2500 rpm and 70% load at 3000 rpm. The choice of these points for the model setup is based on the fact that operating points of

medium to high engine load make possible to analyse with high sensitivity all the phenomena explaining the engine response with pre-turbo aftertreatment architecture [114]. The response of the engine in transient operation from 0% to 80% load at 2000 rpm constant speed was also modelled from experimental data in both aftertreatment placements.

A scheme of the exhaust line configuration in post- and pre-turbo case is shown in Figure 4.1. The post-turbo configuration comprises a close-coupled DOC next to the VGT, an underfloor DOC and a DPF. The pre-turbo aftertreatment architecture is simplified by removing the close-coupled DOC, the DPF is directly placed upstream of the turbine followed by the DOC. The relative DPF and DOC placement in pre-turbo configuration has no relevance on sizing since its effect on the pressure drop is negligible [114]. The selection of this kind of pre-turbo aftertreatment architecture is justified by the need to improve the aftertreatment warm-up [116] and as a solution to protect the VGT from ceramic debris coming from an eventual DPF fault by making use of a metallic DOC [128]. Table 4.1 shows the main characteristics of the reference DPF and DOC.

Table 4.1: Characteristics of the reference DOC and DPF.

		DPF	**DOC**
D	[mm]	135	145
L	[mm]	170	105
L_{plug}	[mm]	5	-
V	[l]	2.43	1.73
Cellular geometry	[-]	Square	Square
$alpha$	[mm]	1.47	0.94
w_w	[mm]	0.32	0.33
σ	[cpsi]	200	400
ε_0	[-]	0.46	-
d_{p_0}	[μm]	14.4	-
k_{w_0}	[$x10^{-13}$m^2]	3.85	-
N	[−]	4470	10240
A_f	[m^2]	2.17	-
SFA	[1/m]	917.6	-
SGA	[1/m]	1835.2	2331.2
MIF	[−]	0.0389	0.0912
TIF	[−]	5.59	3.85
OFA	[−]	0.34	0.54

Figure 4.2 shows the comparison between experimental data and modelled results for the variables of interest in this study.

The model shows good accuracy and sensitivity to predict the engine performance and the DPF pressure drop independently of the aftertreatment placement and operating point. Engine torque and bsfc are always accurately pre-

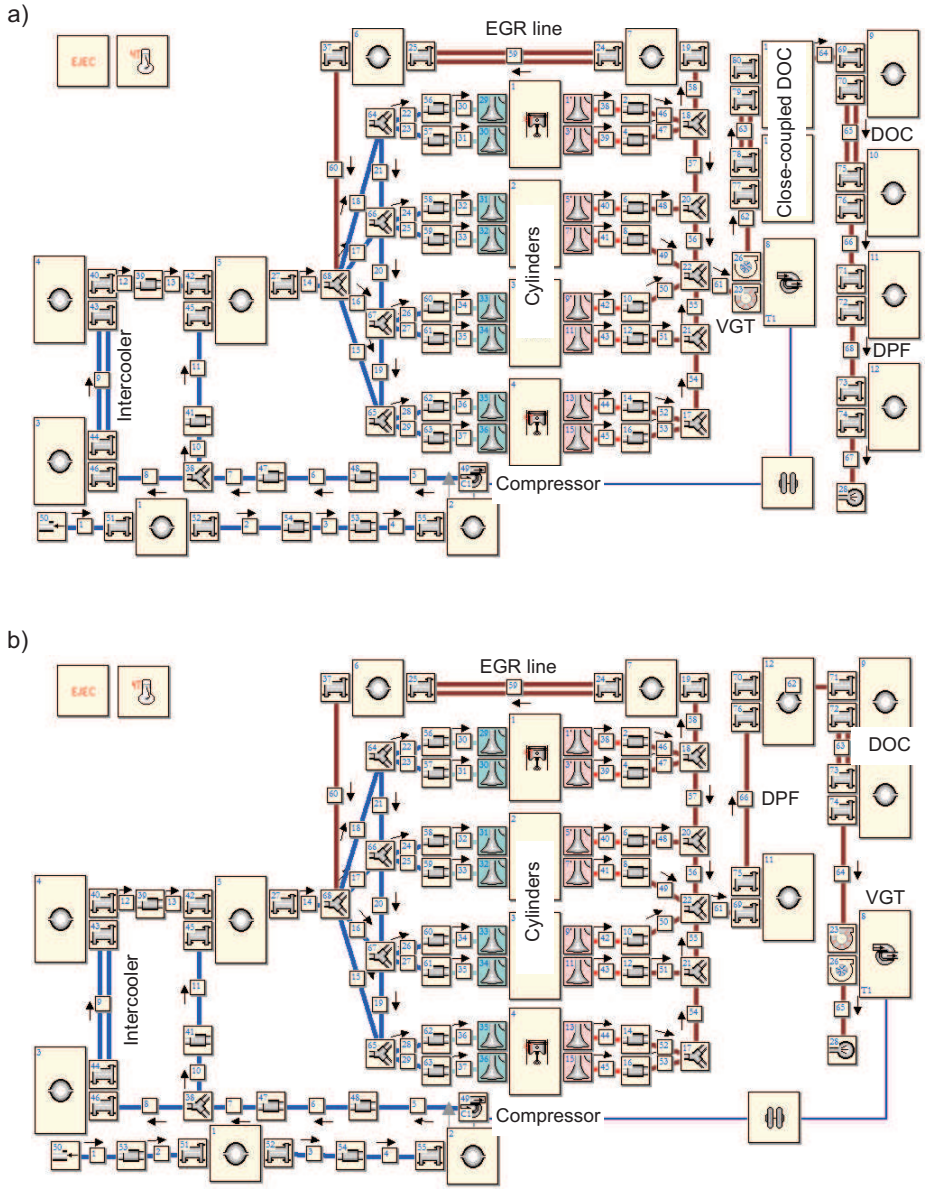

Figure 4.1: Engine scheme in OpenWAM's interface: a) Post-turbo DOC and DPF configuration, b) Pre-turbo DPF and DOC configuration.

dicted by the model being the maximum error within ±2%. Air mass flow is also well modelled, the major percentage error is occurring at low flow points but is still below 4%. The modelled DPF pressure drop shows some dispersion around

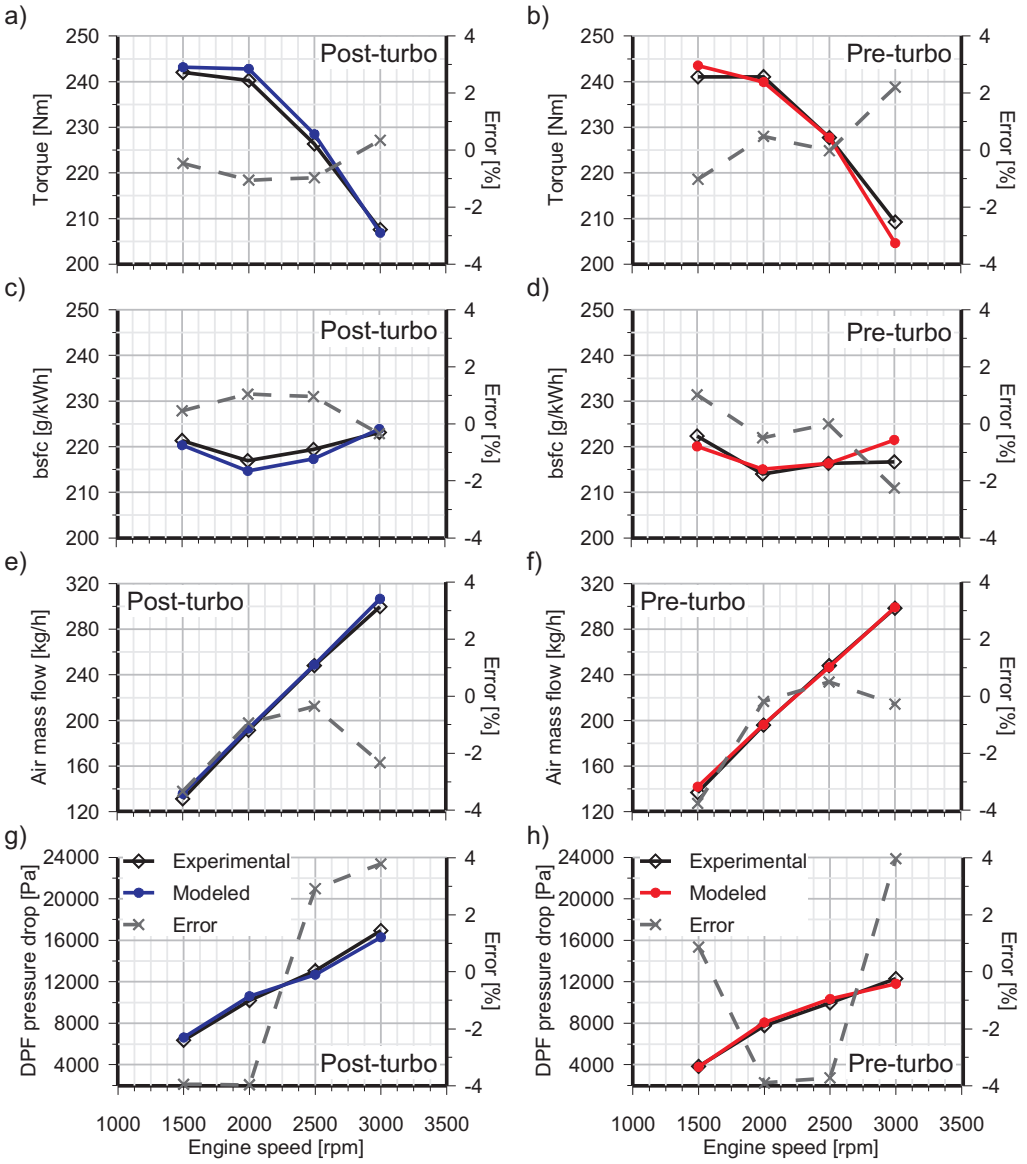

Figure 4.2: Experimental data vs modelled results for post-turbo and pre-turbo aftertreatment configurations.

the experimental value. Nevertheless, the absolute error is always kept in a maximum of ±1000 Pa. Therefore it is possible to state that the model provides high consistency and reliability in the prediction of all the aspects describing the engine operation and makes it suitable to be applied to parametric studies.

The operating point selected for the study is 80% load at 2500 rpm. It has been selected because is the one with the smallest global error between the experimental data and the modelled results providing the best baseline for comparing simulation results between pre- and post-turbo aftertreatment configurations. In fact, the bsfc and DPF pressure drop are underestimated in post-turbo aftertreatment configuration while in pre-turbo the model is accurate in bsfc but slightly overestimates the DPF pressure drop. It ensures a margin of error placed in the security side for all the subsequent analysis and conclusions regarding the fuel economy and DPF response in pre-turbo placement. Moreover the selected engine operating point is representative of the minimum bsfc making more interesting the analysis of the potential of the pre-turbo aftertreatment placement to improve the engine efficiency in this operating range.

It is worth to underline that the chemical reactions both in the DOC and DPF have not been taken into account in the computational study. As a consequence, it is only accounting for the effect of the monolith geometry on the pressure drop and heat transfer phenomena, hence on the engine performance. Consequently, there is not quantitative prediction on the changes in conversion efficiency and DPF passive regeneration being the discussion and conclusions on these topics only related to literature insights. Additionally, the corresponding heat release due to chemical reactions is neglected when predicting the turbine inlet temperature in the case of pre-turbo aftertreatment placement. This assumption slightly affects the energy recovered in the turbine but anyway ensures being again in the security side when discussing the engine performance with pre-turbo aftertreatment configuration.

For all the simulations the ambient conditions have been set to 1.025 bar and 27°C both for pre-turbo and post-turbo aftertreatment configurations. The injected fuel mass and the equivalence ratio are also kept constant in the study and equal to the experimental values obtained with pre-turbo aftertreatment configuration. The VGT position is changed as the aftertreatment geometry is modified (different pressure drop) in order to keep constant the air mass flow and hence the equivalence ratio.

4.3 Diesel Oxidation Catalyst

The influence of the monolith volume on the DOC and engine performance has been addressed considering a population of geometries in which diameter and length have been varied. The selection of diameters and lengths has been performed so that five volumes are included and repeated with different L/D ratios. The cellular geometry of the monolith, i.e. cell width and wall thickness, has been kept constant in the study. Table 4.2 shows the set of computed DOC geometries. The reference length of the DOC is reduced from 105 mm to 66

mm, whereas the diameter ranges from the reference 145 mm to 125 mm. Four lengths and three diameters are considered providing a minimum volume of 0.81 litres, which represents a 53% reduction with respect to the reference volume (1.73 l).

Table 4.2: Modelled DOC geometries.

Volume [l]					
		Length [mm]			
		66	79	92	105
Diameter [mm]	125	0.81	0.97	1.13	1.29
	135	0.94	1.13	1.32	1.5
	145	1.09	1.3	1.52	**1.73**

4.3.1 Pressure drop analysis

Figure 4.3 represents the engine bsfc and DOC pressure drop in order to assess the influence of the DOC macro-geometry.

Plot (a) in Figure 4.3 shows the bsfc for every DOC geometry and placement; the results for the post-turbo aftertreatment placement are represented in blue squares whereas red circles are used to identify the pre-turbo aftertreatment configuration. The reference geometry is marked in black for every configuration. As also concluded from the comparison between plot (c) and (d) in Figure 4.2, the bsfc of the pre-turbo aftertreatment placement is lower than the obtained with the traditional post-turbo configuration. In both cases, it is proved that the DOC macro-geometry is only slightly affecting the engine fuel economy. Although the influence is always higher in the case of the post-turbo aftertreatment configuration, the bsfc reaches a maximum variation of circa 0.06% with respect to the reference DOC geometry, marked with a black square for the post-turbo aftertreatment configuration. It is because of the low differences in pressure drop with respect to the reference geometry.

In Figure 4.3(b) it is shown that, as expected, the DOC pressure drop is reduced as the diameter increases for any length (increase of diameter to length ratio). It leads to a reduction of the inertial pressure drop and friction due to the gas velocity decrease. Regarding the length, the trend in pressure drop shows an increase as the length does because of the additional friction losses. In the case of the post-turbo aftertreatment location, the maximum pressure drop reached is 1097 Pa higher than the value for the reference DOC volume, what represents an increase of 34.4%. The maximum reduction is close to 760 Pa (23.7%). With the same geometry constraints, the DOC pressure drop is less sensitive to geometry variation in the case of the pre-turbo aftertreatment configuration. It provides a

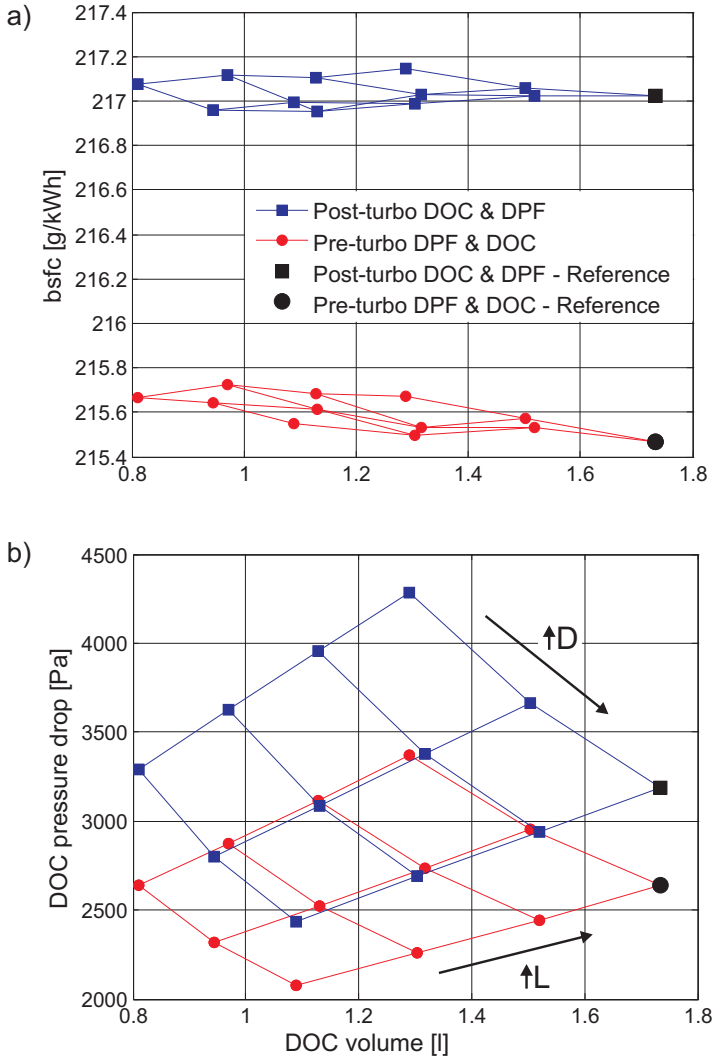

Figure 4.3: Comparison between pre- and post-turbo aftertreatment placement at 2500 rpm and 80% engine load as a function of the DOC macro-geometry: a) engine bsfc, b) DOC pressure drop.

range of DOC pressure drop variation within [730,-570] Pa with respect to the reference geometry value.

The pressure drop variation in the DOC is very low, especially in comparison with that of the DPF, as it will be shown in Section 4.4.1. It justifies the negligible influence on fuel economy. However, the results clearly show how the trend in pressure drop between post-turbo and pre-turbo placement is governed by the

increase of density and decrease of velocity for the same inlet cross section and mass flow at the inlet of the aftertreatment when it is placed upstream of the turbine. The square dependence on the velocity but linear on gas density makes the pressure drop less dependent on geometry changes for this exhaust line architecture.

4.3.2 Dwell time analysis

The space velocity combined with the inlet gas temperature [154] is a usual parameter applied to refer the HC and CO conversion efficiency provided that other DOC characteristics like cell density or catalyst concentration are unvaried. Although it is the case of this study, the direct application of the space velocity is not appropriated to qualitatively discuss the effect on conversion efficiency when comparing pre-turbo against post-turbo DOC placement. The reason yields in the fact that it is defined as a function of the standard exhaust volume flow [155]. As an alternative it is proposed the calculation of the gas dwell time referred to the local exhaust volume flow at the DOC inlet both for its post- and pre-turbo placement:

$$\tau = \frac{V_{DOC,g}}{\dot{V}_g} \tag{4.1}$$

In equation 4.1, τ represents the dwell time, $V_{DOC,g}$ is the DOC volume occupied by the exhaust gas and $\dot{V}_g$ is the exhaust volume flow. According to this definition, the dwell time has been analysed for the different DOC geometries and operating conditions shown in Table 4.3.

Table 4.3: Operating conditions for DOC dwell time analysis.

Point	Engine speed [rpm]	Engine load [%]	EGR rate [%]	DOC inlet temperature [°C]		DOC inlet pressure [bar]	
A	2500	80	0	*604*	494	*1.97*	1.13
B	1960	5	33.5	*215*	159	*1.15*	1.06
C	1660	30	14.2	*480*	362	*1.24*	1.08

Both post-turbo and pre-turbo aftertreatment locations have been considered. Italics and red colour numbers refer to the pre-turbo DPF and DOC configuration while blue colour numbers to the post-turbo DOC and DPF configuration. Point A is representing high load operating conditions in contrast to low load operating conditions B and C, selected from the NEDC. In this way it is possible to analyse in a representative range the influence on dwell time of the DOC location, which is governed by changes in temperature and pressure.

Table 4.4 resumes the calculated dwell time for operating point A. Comparing the dwell time between the exhaust line configurations it can be observed that the one of the reference DOC geometry (D = 145 mm, L = 105 mm) with post-turbo placement can be reproduced with a pre-turbo placement but reducing the length (D = 145 mm, L = 66 mm). These results show that the DOC monolith volume may be reduced around 40% providing minimum pressure drop, without negative conversion efficiency effects. In fact, the pressure drop is lower than that provided by the reference DOC geometry in post-turbo location. Additionally, the higher temperature and flow turbulence because of the pressure pulses will further contribute to raise conversion efficiency both for CO and HC [156]. Further reduction of length would mean the decrease of dwell time unless it is accompanied with a diameter increase.

Table 4.4: DOC dwell time at engine point A.

Dwell time [ms]									
		Length [mm]							
		66		79		92		105	
Diameter [mm]	125	*4.9*	3.1	*5.9*	3.7	*6.9*	4.4	*7.8*	5.0
	135	*5.7*	3.6	*6.9*	4.3	*8.0*	5.1	*9.1*	5.8
	145	*6.6*	4.2	*7.9*	5.0	*9.2*	5.8	*10.5*	6.7

However, when the engine operates at low load, the benefit in dwell time of the pre-turbo aftertreatment location disappears, as shown in Table 4.5 for point B. It is due to the fact that at the inlet of the DOC the gas temperature increases with respect to post-turbo location but the turbine expansion ratio is very low so that pressure does not raise enough. It leads to lower gas density at the DOC inlet in pre-turbo configuration for this engine operating region.

Table 4.5: DOC dwell time at engine point B.

Dwell time [ms]									
		Length [mm]							
		66		79		92		105	
Diameter [mm]	125	*21.3*	21.9	*25.5*	26.3	*29.8*	30.6	*34.0*	34.9
	135	*24.9*	25.6	*29.8*	30.6	*34.7*	35.7	*39.6*	40.7
	145	*28.7*	29.5	*34.4*	35.4	*40.0*	41.2	*45.7*	47.0

Although there is no advantage in dwell time, low load operating conditions are mainly limited by gas temperature in post-turbo DOC location. Table 4.3 shows that in point B (only 5% in engine load) temperature is above 200°C with pre-turbo aftertreatment configuration, ensuring light-off; when engine load increases to 30% (point C in Table 4.3) temperature is very close to 500°C.

Experimental results present in the literature indicate that by previous reasons the volume reduction would be still attainable with pre-turbo DOC location; i.e. flow conditions, mainly temperature, are ensuring the required high conversion efficiency with Euro 5 DOCs around 1 l in monolith volume [21] [110]. Besides the temperature advantage in pre-turbo DOC placement, since the reduction of the monolith cross section has low penalty in pressure drop, as shown in Figure 4.3(b), higher benefits in conversion efficiency may be explored through monolith cell density increase. Other aspects such as catalyst loading and composition may be also optimized for pre-turbo applications in order to take maximum advantage of the DOC size reduction potential.

4.4 Diesel Particulate Filter

Besides the influence of the positioning (pre- and post-turbo) and the volume as in the case of the DOC, the DPF parametric study comprises changes in cell density, TIF and soot mass loading.

The cell density has been swept from 100 to 500 cpsi with steps of 50 cpsi. Higher values of cell density have been avoided because of soot plugging issues [75]. As pointed out in Section 2.4.3 by eq. 2.53, the change in cell density has two degrees of freedom, i.e. α and w_w. To prevent arbitrary cellular geometry changes, the cell density variation has been performed imposing constant TIF. This involves keeping constant the α to w_w ratio when changing the cell density:

$$TIF = \frac{\alpha + w_w}{w_w} \rightarrow \frac{\alpha}{w_w} = TIF - 1 \tag{4.2}$$

The study comprises three TIF values in order to account for the effect of its change on the engine and DPF response.

Regarding the soot mass loading, the case of clean DPF (soot and ash free substrate) and 5 g of soot mass loading, i.e. ≈ 2 g/l in reference volume, have been considered. Such a soot mass loading seems to be a low value but its choice is based on test results. After the steady-state tests of operating points shown in Figure 4.2 a soot mass loading of 5 g was weighted in post-turbo location while less than 0.5 g were found in pre-turbo placement. Therefore, 5 g was selected to avoid the modelling of the DPF loading too far from real operation and to keep the reliability of the study.

4.4.1 Pressure drop analysis

4.4.1.1 Clean substrate

As a first step of the study, the differences between acting on the monolith diameter or effective length to achieve the desired volume reduction have been

evaluated. Therefore reductions in both dimensions up to reach a minimum volume of 0.85 l, i.e. a maximum reduction of ~65%, have been modelled. The resulting range is [135, 94.5] mm in monolith diameter and [165, 115.5] mm in effective length. In this preliminary study the monolith cellular geometry, i.e. cell size and porous wall thickness, has been kept constant to the reference value (Table 4.1). It means that MIF, TIF, OFA and SFA also remain constant, at the expense of the filtration area, which reduces as volume does (eq. 2.50). The filtration area is reduced linearly as a function of the volume and ranges between 2.17 m^2 and 0.74 m^2. Table 4.6 details the DPF macro-geometry defining this preliminary study.

Table 4.6: DPF geometries modelled in the preliminary study.

Volume [l]					
		Effective length [mm]			
		115.5	132	148.5	165
Diameter [mm]	94.5	0.85	0.96	1.08	1.19
	108	1.10	1.26	1.41	1.56
	121.55	1.40	1.59	1.78	1.97
	135	1.72	1.96	2.20	**2.43**

Figure 4.4 represents in plot (a) the change in bsfc as the monolith volume is reduced from the reference geometry. It is clearly observed the high sensitivity of bsfc to the diameter decrease with a post-turbo DPF location. A maximum bsfc increase of 1.5% is found with respect to the reference DPF geometry with this configuration. In pre-turbo aftertreatment configuration the bsfc is practically insensitive to the DPF volume reduction; maximum bsfc increase is less than 0.4% when the DPF volume is reduced from 2.43 l to 0.85 l. This result shows the high potential for volume reduction without effect on engine performance. In both configurations the effect of the length is much less relevant. Contrarily to the DOC, the increase of length in the DPF monolith provides a slight decrease in bsfc because of the reduction in pressure drop, as shown in Figure 4.4(b). Despite the higher length at constant diameter, friction losses are not dominant in the DPF. The filtration area increases as the length does so that the axial velocity profile is smoothed and the filtration velocity reduced. As a consequence, the porous wall pressure drop decreases according to the Darcy's law as shown in eq. 4.3. Here Δp_w represents the pressure drop across the porous wall, μ is the gas dynamic viscosity, u_w is the filtration velocity, w_w is the porous wall thickness and k_w represents the porous wall permeability.

$$\Delta p_w = \frac{\mu u_w w_w}{k_w} \tag{4.3}$$

That is, as the monolith length is increased at constant diameter the Darcy's pressure drop reduction counterbalances the friction pressure drop increase and the overall pressure drop, hence the bsfc, is only slightly affected.

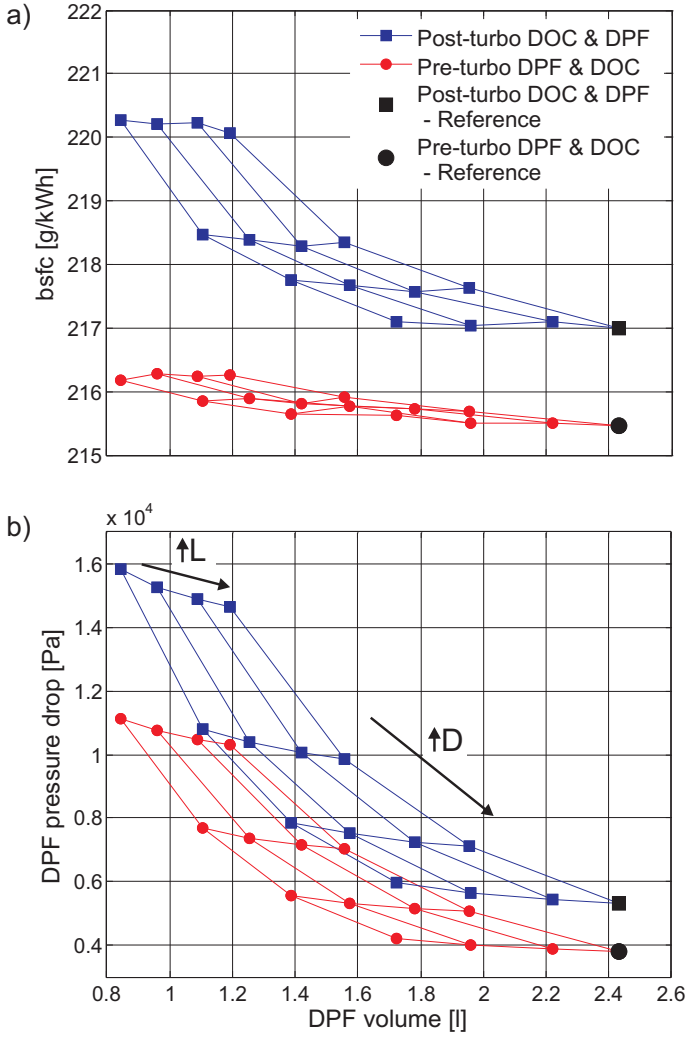

Figure 4.4: Comparison between pre- and post-turbo aftertreatment placement at 2500 rpm and 80% load as a function of the DPF macro-geometry for clean substrate and reference cellular geometry: a) engine bsfc; b) DPF pressure drop.

In case the cellular geometry is also modified the pressure drop behaviour gets more complex because of this additional degree of freedom. However the monolith length reduction is still less penalizing compared to diameter reduction. Figures 4.5(a) and (c) show the DPF pressure drop variation related with the

length reduction in pre- and post-turbo placement while Figures 4.5(b) and (d) refer to the case of diameter reduction. The coordinates of the computed cases are pointed out by black circles in both plots. White colour lines on the pressure drop contour are identifying filtration area iso-lines. The minimum volume modelled in this study is 1.57 litres. This volume provides the same filtration area of the baseline geometry with a cell density of 500 cpsi, i.e. the maximum value considered to avoid channels plugging issues [75]. Acting on the monolith length leads to a lower pressure drop increase comparing with the case of diameter reduction, as resulted already clear from the analysis of Figure 4.4(b). In addition, the pre-turbo positioning presents lower pressure drop values in all the volume and cell density range comparing with post-turbo.

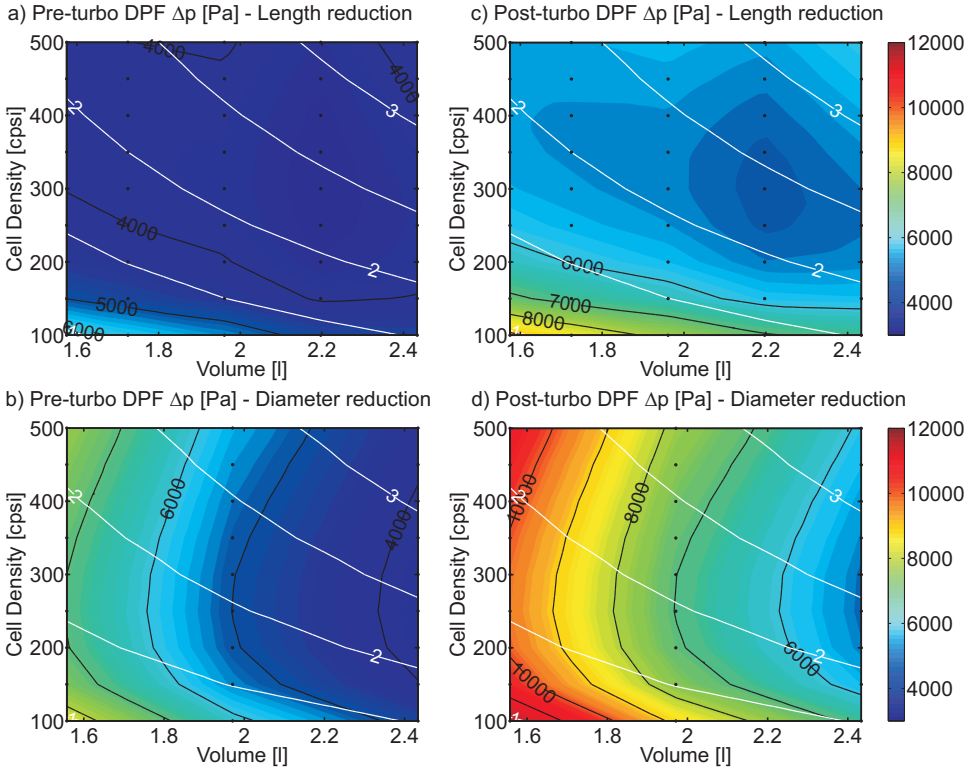

Figure 4.5: DPF pressure drop as a function of monolith volume and cell density for reference TIF and clean DPF substrate.

In order to understand the differences in the pressure drop behaviour it is worth to analyse the contributions to the pressure drop and their dependence on monolith length and diameter. To do it the pressure drop of a symmetric channels DPF monolith can be estimated by means of a lumped model based on

incompressible flow approach as proposed in [32]. Assuming the DPF to be free of particulate matter:

$$\Delta p_{DPF} = \frac{\mu Q}{2V_e}(\alpha + w_w)^2 \left[\frac{w_w}{\alpha k_w} + \frac{4F_w L_e^2}{3}\left(\frac{1}{\alpha^4}\right)\right] + \\ + \frac{2\rho Q^2}{V_e^2 \alpha^2}(\alpha + w_w)^4 \left[(\varsigma_{mon} + \varsigma_{ic} + \varsigma_{oc})\left(\frac{L_e}{\alpha}\right)^2 \right] \tag{4.4}$$

First part of eq. 4.4 is related to the Darcy and friction contributions to the pressure drop while the second part expresses the contribution of the flow contraction/expansion at the channel inlet/outlet respectively. Considering that constant TIF value has been imposed in the current study, it results $\frac{\alpha}{w_w} = const$ (eq. 4.2). Moreover assuming constant flow properties the Darcy and friction contributions to the pressure drop only depend on the cell width α and the monolith dimensions, i.e. diameter and length. In the case the volume reduction is obtained by length decrease it results:

$$\Delta p_{Darcy}\big|_{D=cst} \propto \frac{\alpha^2}{V_e} \Rightarrow \frac{\alpha^2}{L_e} \tag{4.5}$$

$$\Delta p_{fric}\big|_{D=cst} \propto \frac{L_e^2}{V_e \alpha^2} \Rightarrow \frac{L_e}{\alpha^2} \tag{4.6}$$

The analysis of eqs. 4.5 and 4.6 reveals that a reduction of the length keeping constant the monolith diameter has a negative effect, i.e. increase, on the Darcy's contribution, but a positive one, i.e. decrease, on the friction contribution to the pressure drop. The first effect is related to the filtration area decrease due to the length reduction that leads to higher filtration velocity for the same mass flow. The second effect is related to the lower contact surface between the porous wall and the flow in the inlet and outlet channels, which results in lower friction losses. With respect to mesostructure variations, i.e. cell width α, it's necessary to emphasize that they have exactly the same effect in case of diameter or length variation, hence they cannot be considered responsible of the differences between the two volume reduction strategies showed in Figure 4.5. As a general rule α diminishes with increasing cell density and so does w_w as $TIF = const$. It results in the decrease of the Darcy's contribution and the increase of the friction one when moving towards high cell density values.

Regarding the inertial pressure drop eq. 4.7 states that this contribution is insensitive to length variations at constant monolith diameter:

$$\Delta p_{iner}\big|_{D=cst} \propto \frac{L_e^2}{V_e^2} \Rightarrow const \tag{4.7}$$

On the other hand when the dependence of the same contributions on the monolith diameter keeping constant the length is analysed one gets for the Darcy and friction pressure drop:

$$\Delta p_{Darcy}|_{L=cst} \propto \frac{\alpha^2}{V_e} \Rightarrow \frac{\alpha^2}{D^2} \tag{4.8}$$

$$\Delta p_{fric}|_{L=cst} \propto \frac{1}{V_e \alpha^2} \Rightarrow \frac{1}{D^2 \alpha^2} \tag{4.9}$$

Comparing eq. 4.8 with eq. 4.5 it results evident that the diameter reduction at constant length affects in a stronger way the Darcy pressure drop comparing with the case of length reduction at constant diameter. In the first case the pressure drop dependence is quadratic while in the second case the dependence is linear. On the other hand the friction pressure drop has an opposite behaviour: the positive effect related with the length reduction turns into a negative one (friction pressure drop increase) when the diameter is reduced (eq. 4.9 vs eq. 4.5). For the inertial pressure drop it results:

$$\Delta p_{iner}|_{L=cst} \propto \frac{1}{V_e^2} \Rightarrow \frac{1}{D^4} \tag{4.10}$$

The inertial contribution, that is not affected by length variation, is inversely proportional to the diameter, i.e. it raises when the monolith volume decreases because of a diameter reduction.

According to eqs. 4.5 - 4.10 the monolith diameter reduction leads necessarily to a more marked DPF pressure drop increase comparing with the case of length reduction (Figure 4.5). This effect is even more evident in case the post-turbo aftertreatment positioning is considered.

Figure 4.6(a) and (b) clearly show that the pressure drop behaviour is not reflected in significant bsfc differences in case of pre-turbo positioning. Indeed, even if there is an evident change in the specific consumption trend with minimum values corresponding to the lower pressure drop zone, the variation in its value is negligible. On the contrary when the post-turbo configuration is considered (Figure 4.6(c) and (d)) the difference in bsfc value is more marked.

Based on these results, in the following a detailed analysis of the effect of volume downsizing and cell density variation will be performed in the case of acting on the monolith diameter. In this way the difference between the two aftertreatment placements will result more evident.

Figure 4.7 represents the DPF pressure drop variation as a function of monolith volume and cell density for the reference TIF under clean DPF conditions. Plots (a) and (b) are referred to pre-turbo and post-turbo DPF placement respectively. The pressure drop trend is mainly dependent on the monolith volume

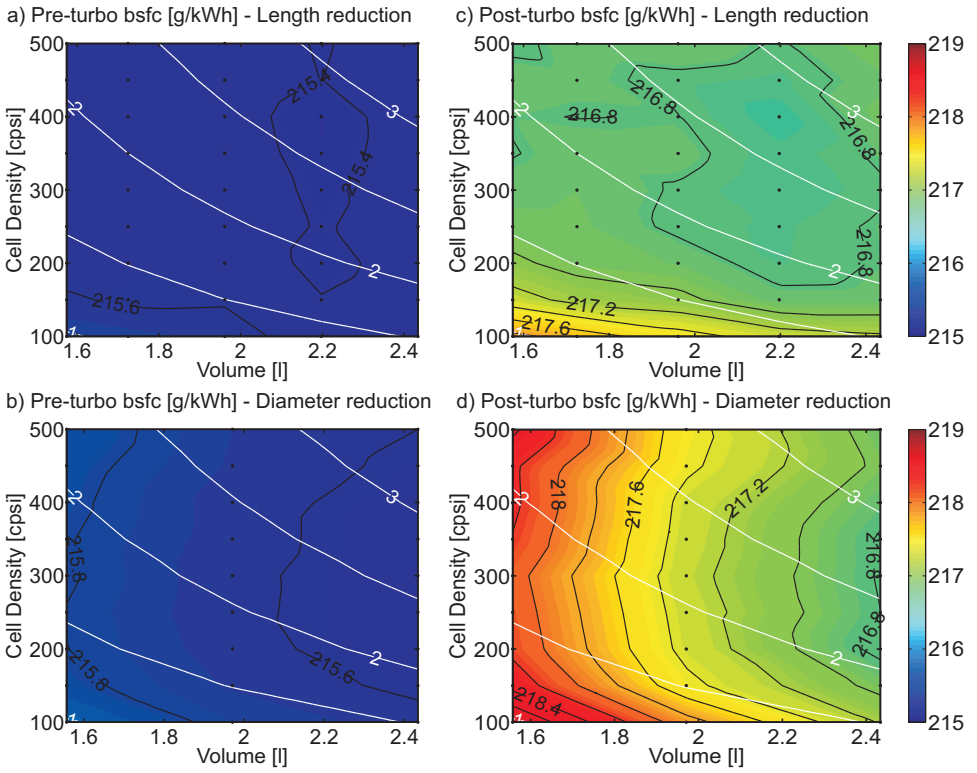

Figure 4.6: bsfc as a function of monolith volume and cell density for reference TIF and clean DPF substrate.

with weaker dependence on the cell density. The comparison between both DPF placements confirms the pressure drop reduction related to the pre-turbo DPF configuration. It is due to the higher gas density and lower velocity for the same geometry what reduces the pressure drop [117].

It can be noted how the difference in pressure drop with respect to the post-turbo DPF configuration increases as volume reduces in both absolute and percentage terms (Figure 4.8). A volume reduction from 2.4 l to ~1 l results in a pressure drop multiplied approximately by 3.5 in pre-turbo placement and by 5 in post-turbo case. Under clean operating conditions, this behaviour is due to the increase of the channel velocity and filtration velocity as volume reduces at constant cell density.

An analysis at constant volume reveals that there is an optimum cell density for either DPF placement. Such an optimum cell density is located between 225 and 250 cpsi under clean DPF conditions and TIF=5.59 (reference value) independently of the monolith volume. Nevertheless, the cell density influence

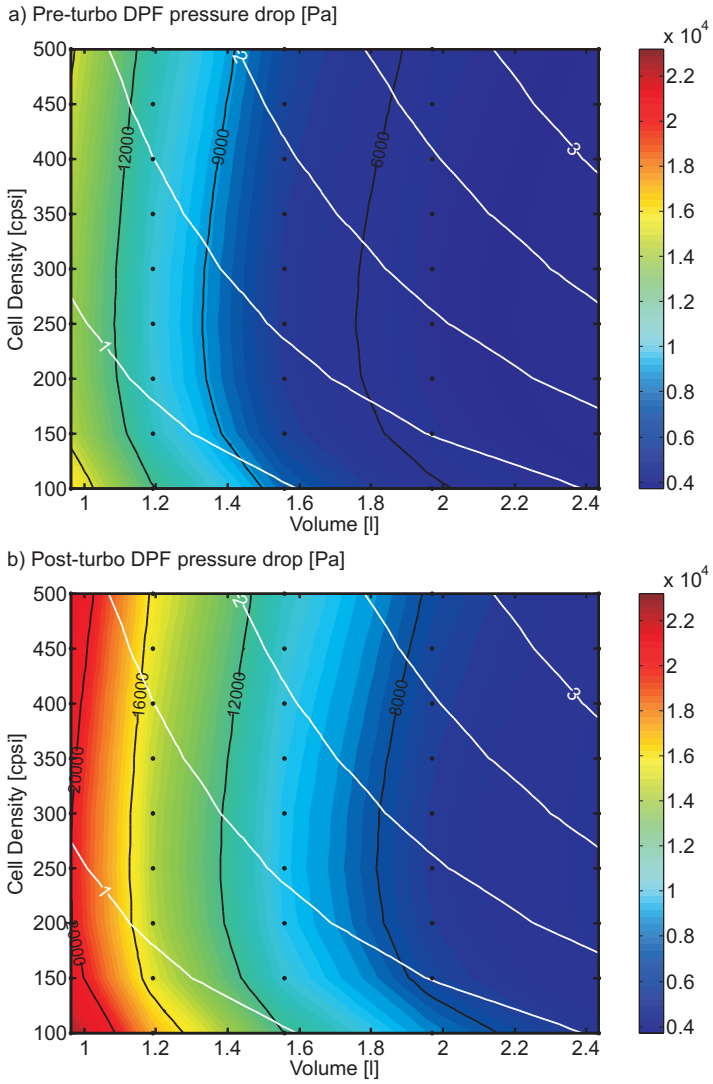

Figure 4.7: DPF pressure drop as a function of DPF placement, monolith volume and cell density for reference TIF and clean DPF substrate.

on the pressure drop is negligible inside the range from 200 to 300 cpsi. As anticipated in Section 2.4, Konstandopoulos *et al.* calculated the α value that minimise the DPF pressure drop in clean [96] and soot loaded [97] symmetric square cell monoliths. However these studies are based on honeycomb cell size optimisation keeping constant the porous wall thickness and do not take into account the thermal response and mechanical resistance of the filter [80] [98]. To

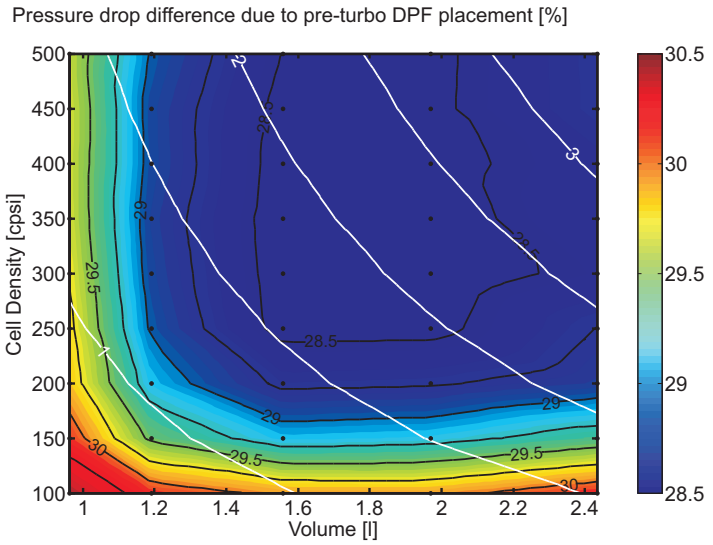

Figure 4.8: Percentage pressure drop difference between pre- and post-turbo DPF placement for reference TIF and clean DPF substrate.

extend the analysis of the optimum cell density under the constraint of constant TIF, the pressure drop of a canned DPF device can be estimated according to eq. 4.4, including the effect of soot presence as:

$$\begin{aligned}\Delta p_{DPF} = &\frac{\mu Q}{2V_e}(\alpha + w_w)^2 \left[\frac{w_w}{\alpha k_w} + \frac{1}{2k_{pl}} \ln\left(\frac{\alpha}{\alpha - 2w_{pl}}\right)\right. \\ &\left. + \frac{4F_w L_e^2}{3}\left(\frac{1}{(\alpha - 2w_{pl})^4} + \frac{1}{\alpha^4}\right)\right] \\ &+ \frac{2\rho Q^2}{V_e^2 \alpha^2}(\alpha + w_w)^4 (\varsigma_{mon} + \varsigma_{ic} + \varsigma_{oc})\left(\frac{L_e}{\alpha}\right)^2 \end{aligned} \tag{4.11}$$

Combining eq. 4.11 and eq. 4.2, the DPF pressure drop can be expressed as a function of TIF. Firstly, the term depending on the particulate layer thickness is expressed as a function of this parameter:

$$w_{pl} = \frac{\alpha - \sqrt{\alpha^2 - \frac{m_{pl}}{N_{in} L_e \rho_{pl}}}}{2} \tag{4.12}$$

$$\alpha - 2w_{pl} = \sqrt{\alpha^2 - \frac{m_{pl}}{N_{in} L_e \rho_{pl}}} = \sqrt{\alpha^2 - \frac{2m_{pl}}{A_{fr} \sigma L_e \rho_{pl}}}$$
$$= \alpha \sqrt{1 - \frac{2m_{pl} TIF^2}{A_{fr} (TIF-1)^2 L_e \rho_{pl}}} = \alpha \Upsilon \tag{4.13}$$

Taking into account that TIF is kept constant while the cell geometry is changed, the variable Υ is also a constant magnitude for a given DPF soot loading. Therefore, the pressure drop can be written as:

$$\Delta p_{DPF} = \frac{\mu Q}{2V_e} \frac{TIF^2}{(TIF-1)^3} \frac{\alpha^2}{k_w} + \frac{\mu Q}{2V_e} \left(\frac{TIF}{TIF-1} \right)^2 \alpha^2 \frac{1}{2k_{pl}} \ln\left(\frac{1}{\Upsilon}\right)$$
$$+ \frac{\mu Q}{2V_e} \left(\frac{TIF}{TIF-1} \right)^2 \frac{4F_w L_e^2}{3} \frac{1}{\alpha^2} \left(1 + \frac{1}{\Upsilon^4}\right)$$
$$+ \frac{2\rho Q^2}{V_e^2 \alpha^2} \left(\frac{TIF}{TIF-1} \right)^4 \alpha^4 (\varsigma_{mon} + \varsigma_{ie} + \varsigma_{oc}) \left(\frac{L_e}{\alpha} \right)^2 \tag{4.14}$$

Considering again that TIF is imposed to be constant and deriving eq. 4.14 with respect to α, it is possible to obtain the optimum value of the honeycomb cell size as:

$$\alpha_{opt} = \sqrt[4]{\frac{\frac{8F_w L_e^2}{3}\left(\frac{1}{\Upsilon} + 1\right)}{\frac{2}{k_w}\frac{1}{TIF-1} + \frac{1}{k_{pl}} \ln\left(\frac{1}{\Upsilon}\right)}}, \tag{4.15}$$

and hence the optimum porous wall thickness and cell density:

$$w_{w_{opt}} = (TIF - 1)\, \alpha_{opt} \tag{4.16}$$

$$\sigma_{opt} = \frac{1}{\left(\alpha_{opt} + w_{w_{opt}}\right)^2} \tag{4.17}$$

Figure 4.9 shows the optimum cell density value as a function of TIF, porous wall permeability (plot (a)) and channel length (plot (b)) for a clean DPF. For the reference TIF, porous wall permeability and effective length, the application of the lumped parameter model provides an optimum cell density equal to 227, i.e. similar to the results shown in Figure 4.7 and obtained applying the one-dimensional compressible unsteady flow DPF model. Nevertheless, the analysis of the results in Figure 4.9(a) reveals that the optimum cell density is very sensitive to the porous wall permeability. As the porous wall permeability

increases the optimum cell density value is reduced. This means not only advantages in lower pressure drop but also a significant reduction of plugging issues risk. Concerning TIF and channel length, the increase of these two parameters provides lower values for optimum cell density but its influence is lower than that of the porous wall permeability.

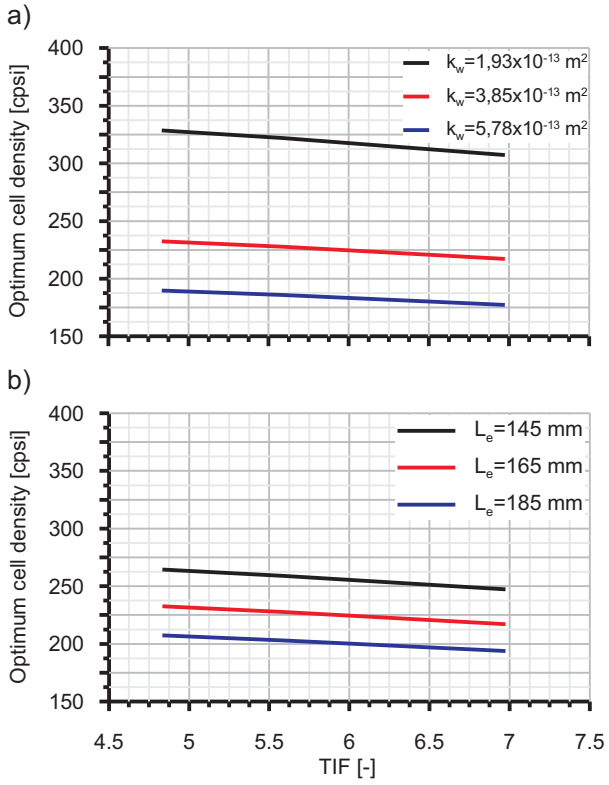

Figure 4.9: Optimum cell density dependence on TIF, clean porous wall permeability and channel length.

The pressure drop behaviour around the optimum cell density range shown in Figure 4.7 is also manifested in specific fuel consumption, which is represented in Figure 4.10. Plot (a) refers to pre-turbo DPF configuration and plot (b) shows the results corresponding to post-turbo DPF configuration. Although keeping the same trend than the DPF pressure drop, the bsfc magnitude scarcely varies with pre-turbo DPF placement. However, it shows high sensitivity to macro-geometry variation in post-turbo DPF configuration.

The use of pre-turbo DPF configuration is bringing almost absolute independence of the DPF sizing on fuel economy what is added to the already known

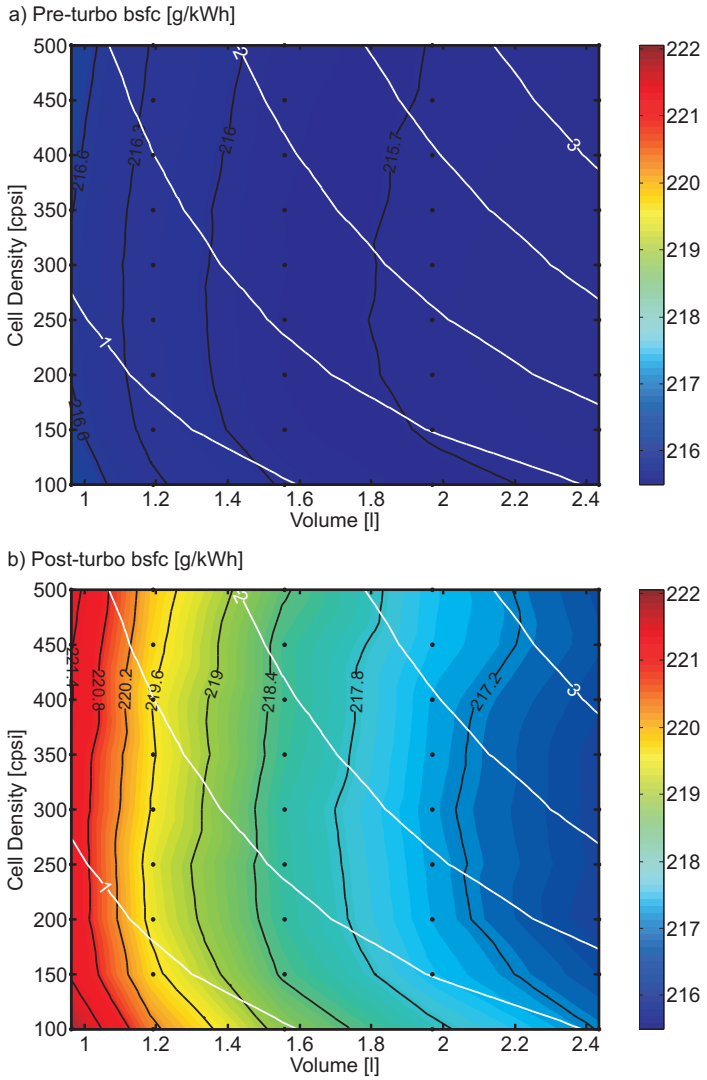

Figure 4.10: Brake specific fuel consumption as a function of monolith volume and cell density for reference TIF and clean DPF substrate.

effect of soot loading [157]. A volume reduction from 2.4 l to ~1 l (-58%) produces a bsfc change of less than 0.5%.

However, the bsfc suffers an important increase as the monolith volume decreases in the case of post-turbo DPF placement. A volume reduction up to 1.6 l (-33%) involves a bsfc increase of 0.8%. This raises up to 2.1% when the volume gets to 1 l (-58%). Given that these results are obtained in the most favourable

conditions, i.e. clean DPF, the trend in bsfc precludes any possibility for volume reduction in post-turbo location and confirms the empirical rule imposing a DPF volume higher than the engine displacement [151].

The reason justifying the low sensitivity of the pre-turbo aftertreatment configuration to the DPF pressure drop change, in this study evidenced by changing the monolith volume, is found in the interaction with the turbine [114]. Such an interaction is setting the engine back-pressure. As schematised in Figure 4.11, in post-turbo aftertreatment configuration the engine back-pressure is given by the turbine pressure ratio times the sum of the ambient pressure and the aftertreatment pressure drop. When pre-turbo aftertreatment configuration is used, the engine back-pressure is given by the sum of the aftertreatment pressure drop and the product of the turbine pressure ratio and the ambient pressure. Besides the lower aftertreatment pressure drop, this means that the pre-turbo aftertreatment placement prevents the DPF pressure drop from being multiplied by the turbine pressure ratio. Consequently the damage on pumping work of the aftertreatment elements is highly reduced. This is the main effect explaining the change in engine performance with a pre-turbo aftertreatment placement. According to the discussion given in [114] based on experimental data, this phenomenon is able to compensate the losses in pulsating energy and heat transfer at VGT inlet when a pre-turbo aftertreatment placement is used.

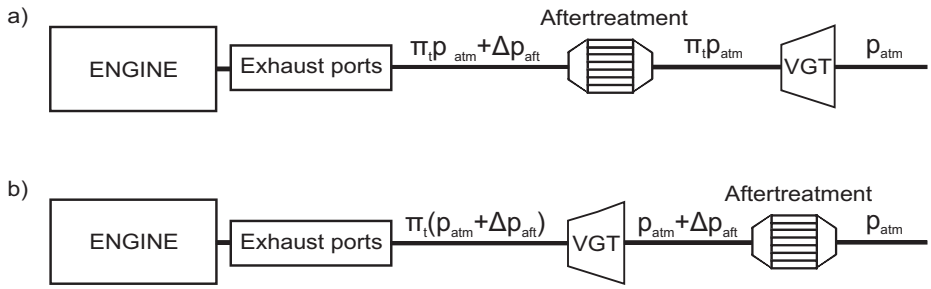

Figure 4.11: Scheme of the engine back-pressure as a function of the aftertreatment placement.

One of the consequences of this behaviour is also related to the control of the VGT. Figure 4.12(a) shows that the VGT position remains constant with pre-turbo DPF placement under clean DPF conditions. However, the VGT must close as the DPF pressure drop increases in post-turbo aftertreatment placement in order to recover the required expansion ratio. It leads to further pumping work and bsfc penalty. Figure 4.12(b) shows how the VGT position is completely governed by the DPF pressure drop as concluded from comparing with Figure 4.7(b). As discussed in [114], for a clean DPF this behaviour is

a consequence of the new conditions at the VGT inlet because of the filter placement. The control must act on the VGT to obtain the target operating conditions (air mass flow in this study).

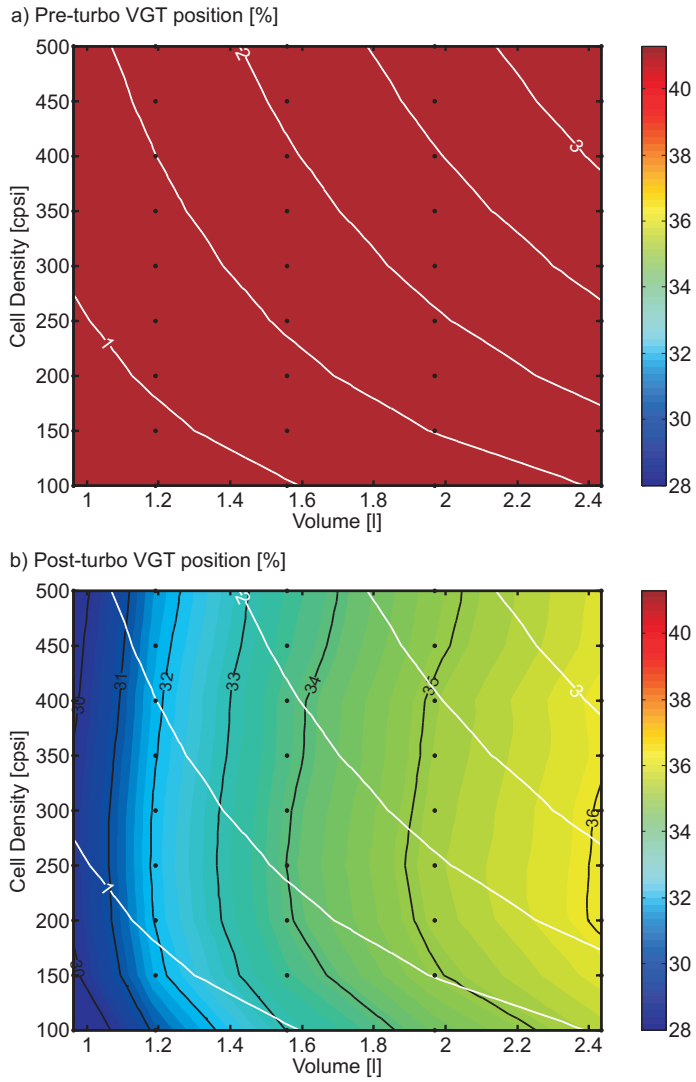

Figure 4.12: VGT position as a function of DPF placement, monolith volume and cell density for reference TIF and clean DPF substrate.

The VGT position affects in turn the turbine efficiency which is also affected by the flow characteristics (constant against pulsating turbocharging pressure when changing to pre-turbo aftertreatment placement). Plots (a) and (b) in

Figure 4.13 show the VGT efficiency for pre-turbo and post-turbo aftertreatment configurations respectively. The constant VGT position in pre-turbo aftertreatment placement avoids efficiency change. Additionally, this efficiency is higher than that obtained for post-turbo aftertreatment placement. The reasons are the greater VGT opening but also the quasi-constant instantaneous VGT efficiency in contrast to the important instantaneous change that suffers under pulsating pressure operation [114].

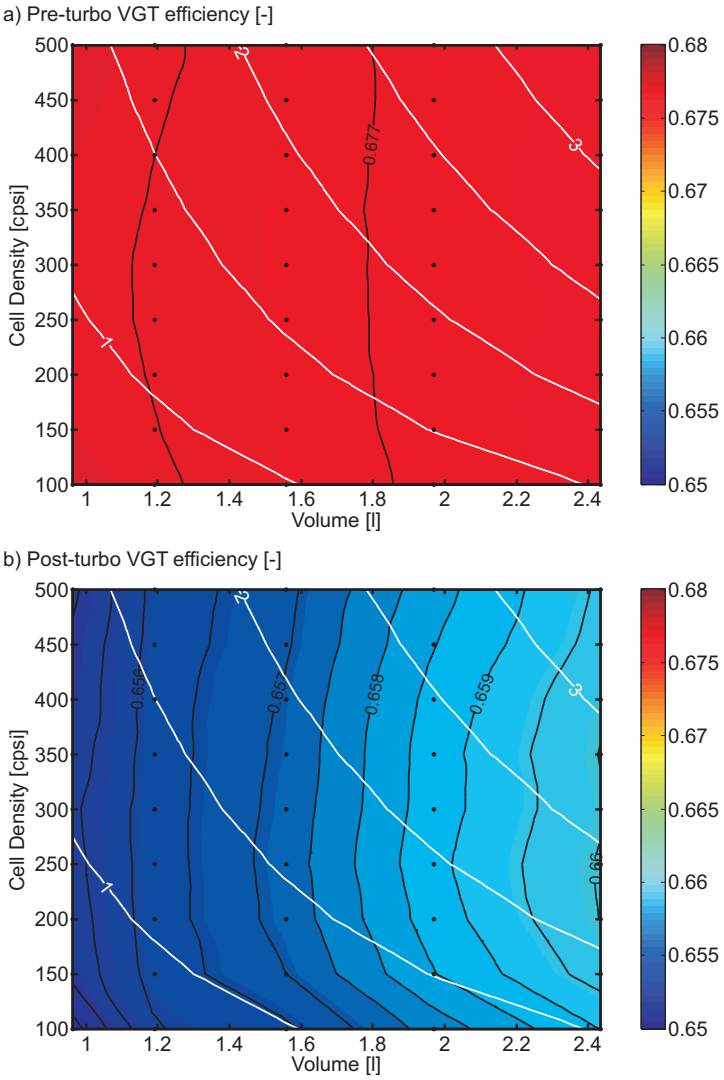

Figure 4.13: VGT efficiency as a function of DPF placement, monolith volume and cell density for reference TIF and clean DPF substrate.

4.4.1.2 Soot loaded substrate

As for the case of clean substrate some preliminary calculations were run in order to evaluate the difference between acting on the monolith diameter or on the effective length to achieve the desired volume downsizing. The considered geometries are the same detailed in Table 4.6 but this time a soot mass of 5 g has been imposed.

Results of these preliminary calculations are summarized in Figure 4.14. The same trend of the clean case (Figure 4.4) is observed, i.e. smaller volumes are associated with higher pressure drop and bsfc, both in pre- and post-turbo aftertreatment configuration. The clear difference is that the presence of soot makes the pressure drop, hence bsfc, dependent only on monolith volume. There is no distinction between diameter and effective length influence. It is due to the fact that the soot accumulation leads to the reduction of the porous wall permeability and to the particulate layer formation, whose thickness increases as the DPF volume reduces. As a consequence, the Darcy's law contribution to pressure drop becomes much more important than friction and inertial contributions. Other aspect to be highlighted under soot loading conditions is that the sensitivity of bsfc to DPF volume increases with respect to the case of clean substrate but is clearly lower when a pre-turbo DPF placement is selected. In case of post-turbo aftertreatment positioning, the penalty in bsfc is dramatic; bsfc increase reaches 10% between reference and minimum volume. It contrasts with the result provided by the pre-turbo DPF case in the same volume range; the bsfc penalty because of the DPF volume reduction would be only 3.75%. In fact, the DPF monolith could be reduced up to 1.26 l (-48.4% in volume) in pre-turbo placement providing the same bsfc as the reference volume in post-turbo location with 5 g of soot mass load, as shown in Figure 4.14(a).

These preliminary results allow extending the well-known low sensitivity of pre-turbo DPF placement to soot loading [120] also to volume reduction, with minimum effect on engine performance and no influence on control settings. Such a weak sensitivity can be also observed in Figure 4.15. This figure summarizes the trend of the bsfc as a function of the DPF pressure drop, placement and soot mass loading. Void symbols are used for soot and ash free substrate and full symbols to represent soot loading conditions (5 g). The lower slope of the pre-turbo plot compared with the post-turbo one is evident. It further underlines the potential of this kind of solution as a source of fuel economy improvement and aftertreatment cost saving with respect to current state of the art. Next, a detailed analysis of the effect of volume downsizing and cell density variation on the DPF pressure drop and bsfc will be performed. For the sake of coherence the case of acting on the monolith diameter will be considered.

Figure 4.16 represents the pressure drop when the DPF is loaded with 5 g of soot as a function of monolith volume and cell density. Despite the increase in

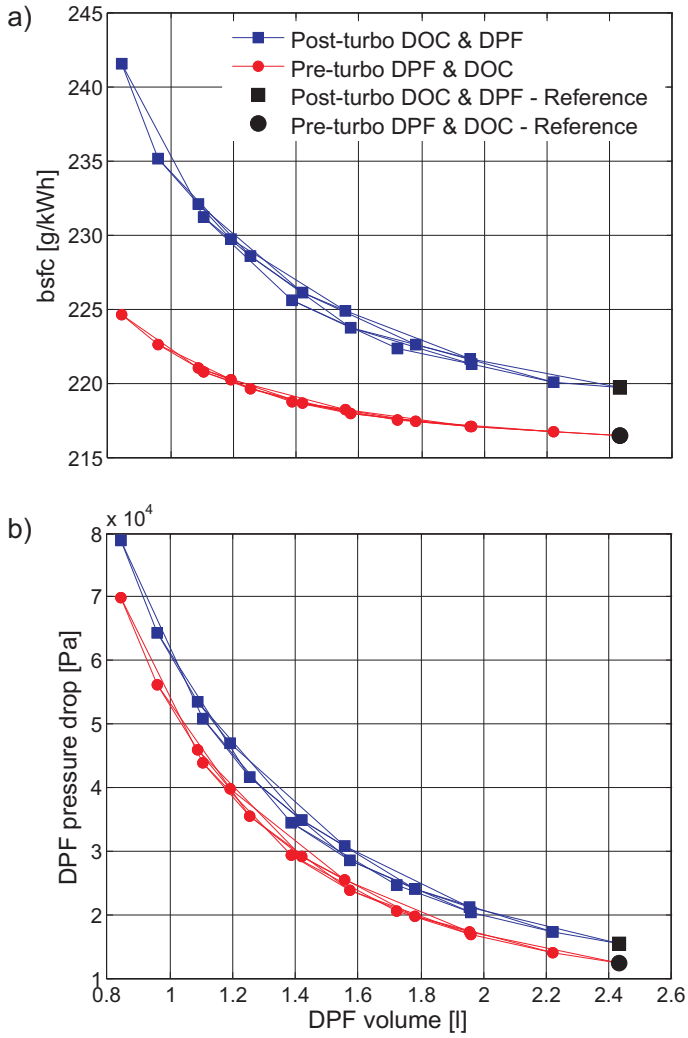

Figure 4.14: Comparison between pre- and post-turbo aftertreatment placement at 2500 rpm and 80% load as a function of the DPF macro-geometry for 5 g soot loading and reference cellular geometry: a) engine bsfc; b) DPF pressure drop.

pressure drop due to the soot loading the trend is the same as under clean DPF conditions. The only difference is the optimum cell density increase for every volume, which is falling out of the analysed range. It is due to the reduction of the permeability, as inferred from eq. 4.15.

The importance of the porous substrate contribution to pressure drop demands an increase in SFA (increase of cell density at constant TIF). At constant volume, it would produce the decrease of the filtration velocity because of the

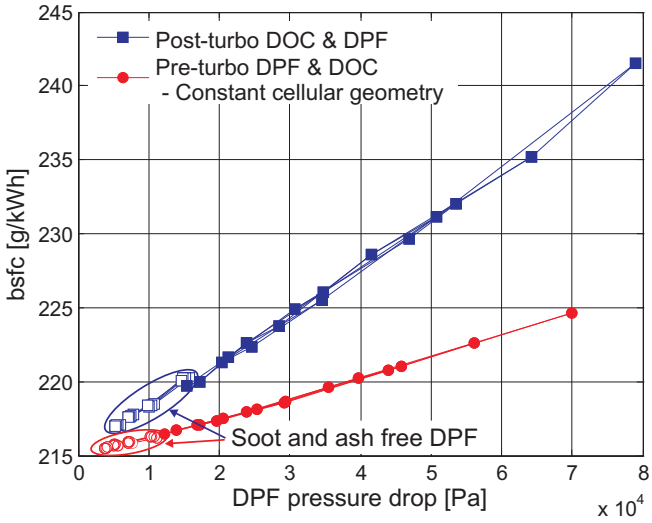

Figure 4.15: bsfc vs DPF pressure drop as a function of DPF placement and soot loading (soot and ash free vs. 5 g).

filtration area increase. The result would be the pressure drop reduction across the porous media compensating the friction losses increase.

Since too high cell densities may lead to plugging issues, this result emphasises the selection of high permeability substrates. It could further boost the interest in heterogeneous porous walls providing high filtration efficiency with low equivalent permeability [56] overcoming the passive regeneration issues of these substrates with pre-turbo placement. Longer monoliths keeping volume would be also positive to get lower optimum cell density. In this case, the diameter reduction has been shown not to be dramatically detrimental for pressure drop keeping constant OFA (constant TIF) since under soot loading conditions the macro-geometrical dependence is mainly in the volume, as shown in Figure 4.14. Other solutions concern asymmetrical cell designs increasing filtration area and providing higher ash loading capability [102].

The absolute pressure drop difference between post-turbo and pre-turbo DPF placement increases under soot loading conditions but the percentage difference decreases, as observed from the comparison between Figure 4.8 and Figure 4.17. When the DPF gets loaded, the pressure drop increases, but this increase is mainly governed by the increase of pressure drop across the porous media being the inertial contributions scarcely affected (only small inlet cross-section reduction due to particulate layer and minor velocity change due to density variation). In these conditions, the non-inertial contributions to pressure drop gain importance in percentage with respect to the inertial ones. Since the

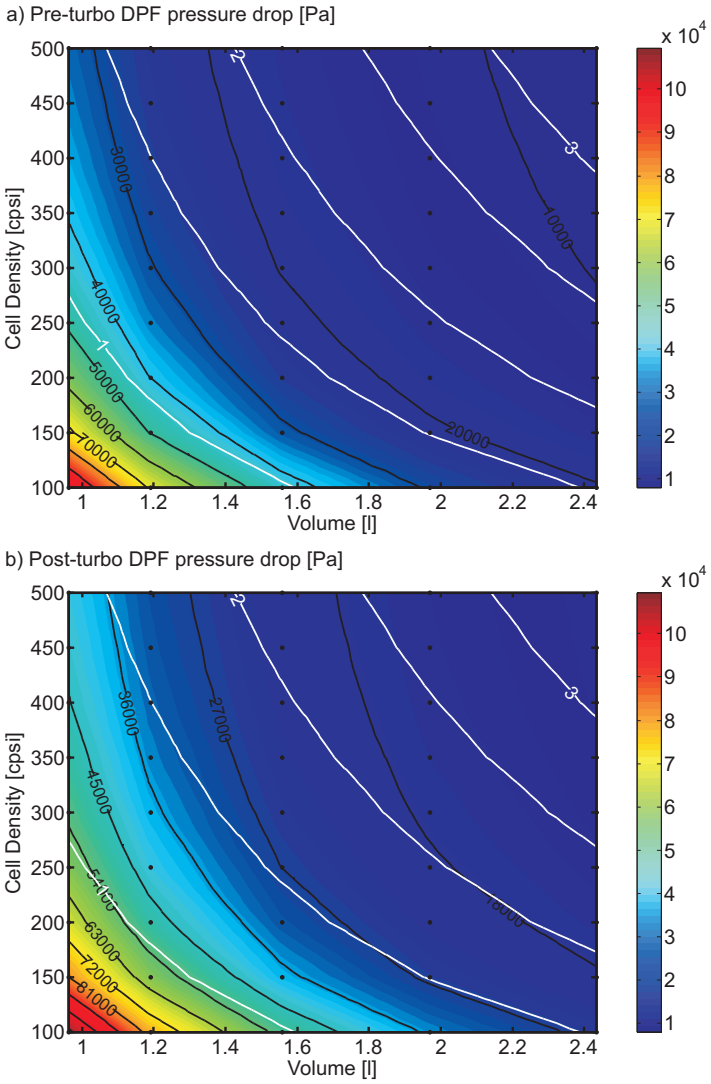

Figure 4.16: DPF pressure drop as a function of DPF placement, monolith volume and cell density for reference TIF and 5 g soot loading.

filtration velocity affects linearly the pressure drop, this magnitude makes that the difference between pre-turbo and post-turbo placement is not very much increased with respect to the difference shown for the same DPF volume and cell density under clean DPF conditions, which already includes the inertial effects on pressure drop.

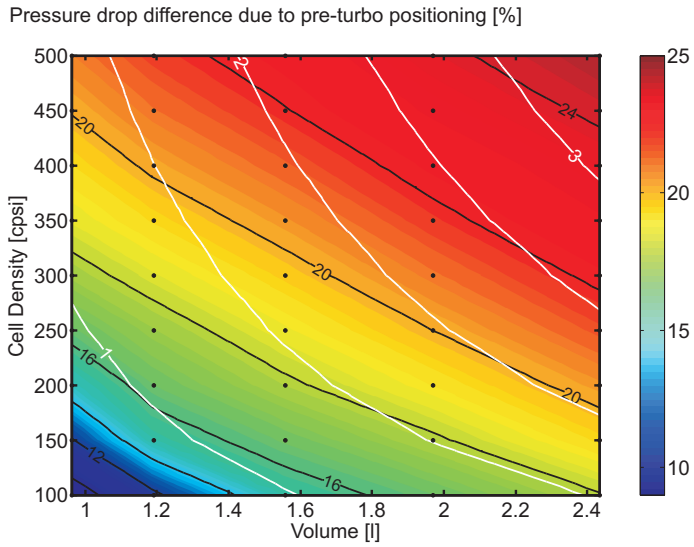

Figure 4.17: Percentage pressure drop difference between pre- and post-turbo DPF placement for reference TIF and 5 g soot loading.

The benefit in pressure drop across the porous media because of the lower filtration velocity in pre-turbo DPF placement may be partially offset by the negative effect on the permeability produced by the higher gas density in this placement. Even under clean conditions, the porous wall permeability is lower in the case of pre-turbo aftertreatment placement. When the DPF gets loaded with soot, besides the lower porous wall permeability in pre-turbo DPF configuration, it is necessary to add the lower particulate layer permeability. This effect is very marked since the difference is great because of the sensitivity of the SCF.

Figure 4.17 shows that the percentage reduction brought by the pre-turbo DPF placement is reduced as the volume and cell density decrease. It is due to the fact that the pressure drop across the particulate layer increases and contributes to the pressure drop damage in pre-turbo DPF placement. Besides the lower permeability of the porous media, imposing constant volume and decreasing cell density produces an increase of the filtration velocity and the particulate layer thickness due to the lower filtration area. It also happens at constant cell density when decreasing the monolith volume. One strategy to increase the pressure drop reduction produced by the pre-turbo DPF placement is to keep constant the filtration area. When moving on the plot at constant filtration area, the non-inertial pressure drop reduces its weight with respect to inertial contributions since the filtration velocity is not affected. Hence the

increase of the percentage reduction in pressure drop brought by the pre-turbo DPF placement.

Despite the trend in pressure drop difference increase, Figure 4.18 shows that the increase in bsfc penalty with post-turbo DPF placement is significantly higher. The pre-turbo DPF placement is insensitive to DPF soot loading [120] and the VGT can remain practically in the same position as shown in Figure 4.19(a). Only clear fuel damage is observed at very small volumes and cell densities. According to the results represented in Figure 4.18(a), a reduction of 42% in volume of the reference DPF (1.4 l) would provide only an increase of 1.2% in bsfc. This volume reduction in pre-turbo location provides lower bsfc than the reference geometry in post-turbo location with the same soot loading. If the comparison is performed against the reference DPF in post-turbo placement and clean substrate, the bsfc is the same despite the volume reduction and the soot loading condition in pre-turbo location.

As stated for clean DPF conditions, the difference in flow conditions at VGT inlet depending on the DPF placement has impact on the VGT control. It is a well-known effect that pre-turbo aftertreatment placement does not require VGT position modification because of the lower sensitivity to pressure drop change because of the soot loading [120] [114]. Such an effect is also evident as volume and cell density decrease, as Figure 4.19(a) shows. In comparison with the pre-turbo DPF placement, the increase of the engine back-pressure in post-turbo DPF placement due to pressure drop increase (soot, volume or cell density change) forces the VGT closing with respect to clean conditions and reference volume. Figure 4.19(b) clearly shows the VGT closing trend for the analysed operating point.

It is additionally feedback by an important resulting decrease of the VGT efficiency, which is shown in Figure 4.20(b). The consequence is a high penalty in fuel economy with this configuration. In this case the volume reduction up to 1.4 l (-42%) gives as a result a bsfc increase of 3.6% with respect to the reference DPF geometry.

4.4.2 Filtration efficiency analysis

Before analysing the response of the DPF filtration efficiency when the monolith volume and the cell density are modified it is important to underline that the simulations have been carried out computing the filtration efficiency but avoiding the soot deposition since it would modify the porous medium geometry. Thus the numerical stabilisation can be reached, properly assessing the filtration efficiency of the DPF for clean or given soot loading substrate condition. Therefore, inlet and outlet soot flow cannot be applied as usual to compute the in-cycle averaged filtration efficiency of the DPF. As alternative, an equivalent definition taking into account the mass flow profile along the inlet channel is

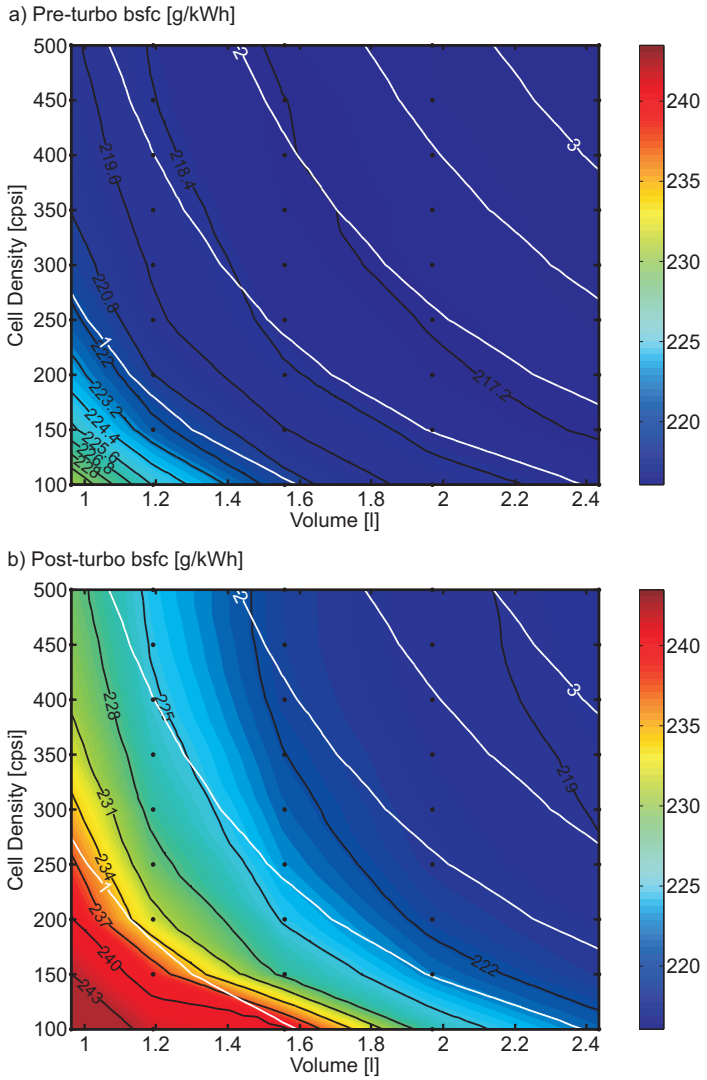

Figure 4.18: Brake specific fuel consumption as a function of DPF placement, monolith volume and cell density for reference TIF and 5 g soot loading.

proposed. Consequently, the in-cycle averaged filtration efficiency of the DPF is calculated based on the in-cycle averaged filtration efficiency in every control

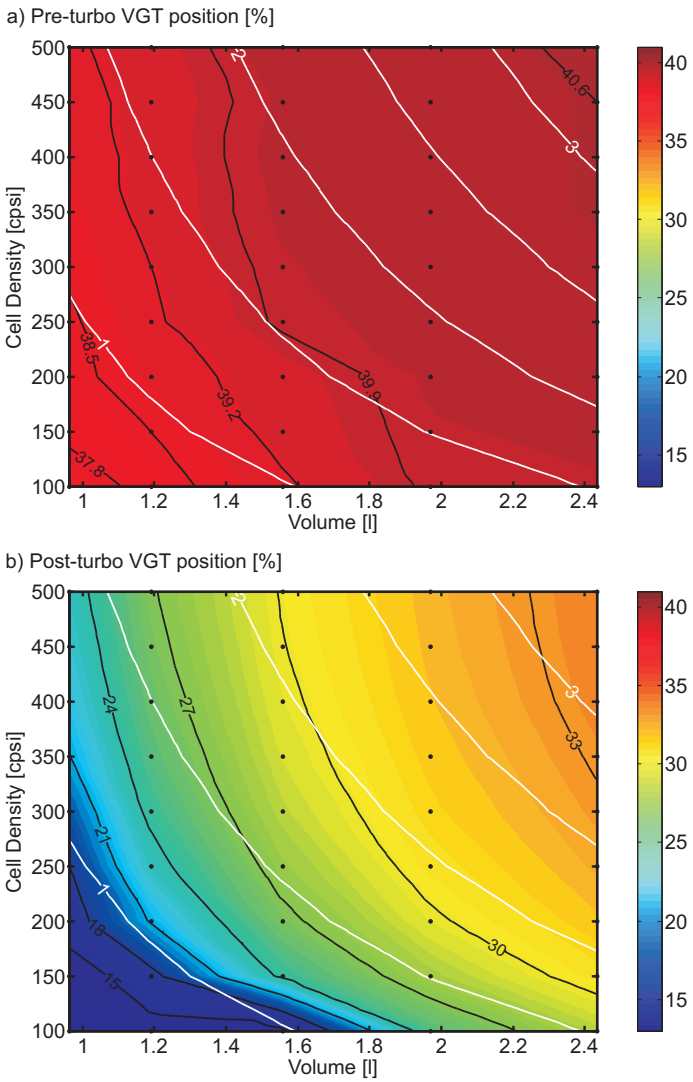

Figure 4.19: VGT position as a function of DPF placement, monolith volume and cell density for reference TIF and 5 g soot loading.

volume weighed by the in-cycle averaged mass flow across each control volume and the total mass flow across the DPF as:

$$\bar{E}_{f_{DPF}} = \frac{\sum_{k}^{n} \bar{E}_{f_{CV_k}} \dot{m}_{w_{CV_k}}}{\sum_{k}^{n} \dot{m}_{w_{CV_k}}}, \tag{4.18}$$

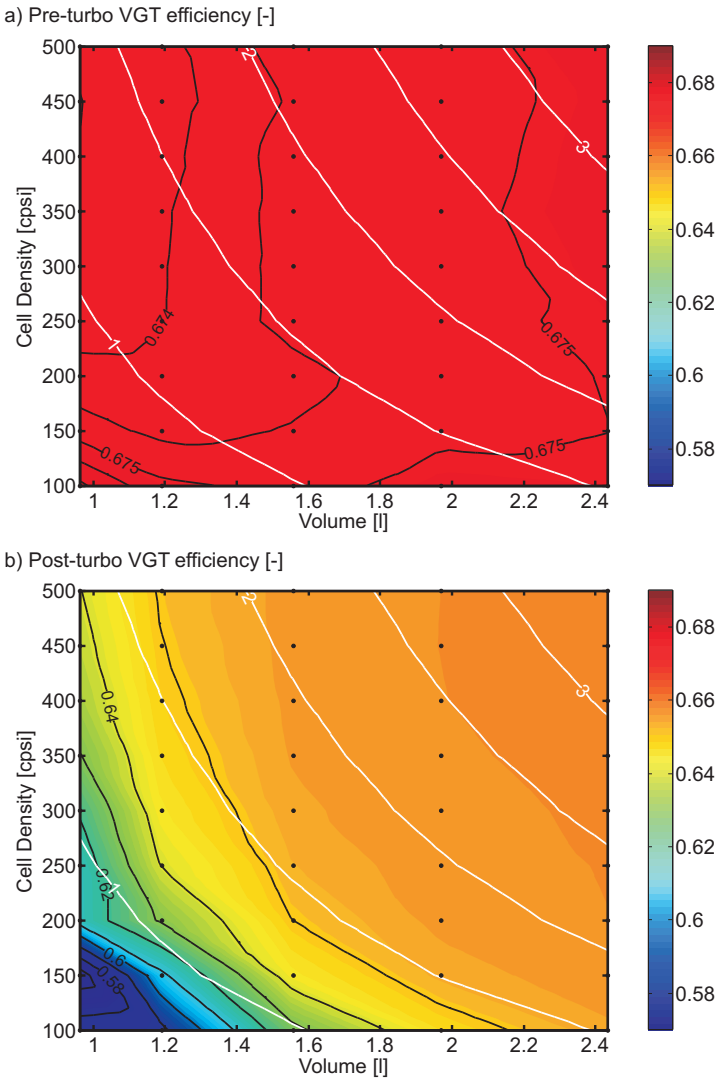

Figure 4.20: VGT efficiency as a function of DPF placement, monolith volume and cell density for reference TIF and 5 g soot loading.

where n is the number of control volumes along the DPF channels and $\bar{E}_{f_{CV_k}}$ is calculated according to eq. 3.28.

4.4.2.1 Clean substrate

As in the case of the pressure drop the first step of the filtration efficiency analysis has been a comparison between the effect of acting on the monolith

diameter or effective length. Figures 4.21(a) and (c) show the DPF filtration efficiency variation related with the length reduction in pre- and post-turbo placement. Alternatively Figures 4.21(b) and (d) refer to the case of diameter reduction.

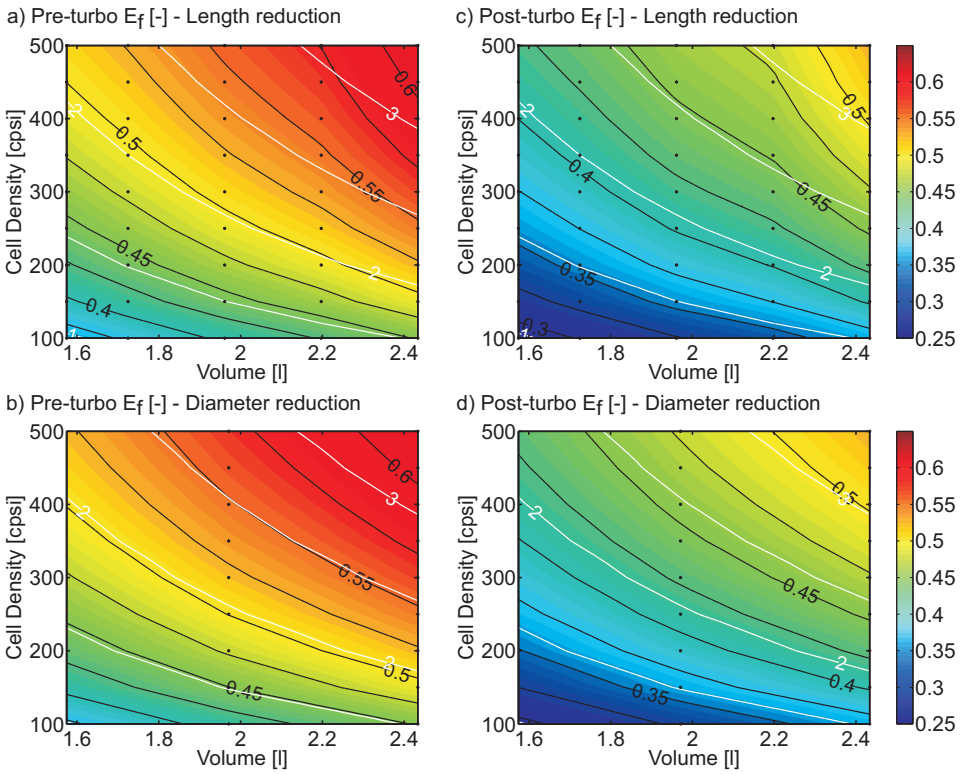

Figure 4.21: DPF filtration efficiency as a function of monolith volume and cell density for reference TIF and clean DPF substrate.

Both volume reduction strategies present DPF filtration efficiency profiles almost identical. Despite it, length reduction leads to slightly lower filtration efficiency (close to -1% in absolute reference). These small deviations are related to the different filtration velocity field. Figure 4.22(a) shows the filtration velocity along the inlet channels length for the minimum volume and baseline cell density both for diameter and length reduction. Most of the mass flow is subject to higher filtration velocity in the case of length reduction, what penalises the Brownian diffusion mechanism. However, in the diameter case the sharp filtration velocity in the rear part of the inlet channels produces a local penalty because of the high mass flow across the porous wall in this region. Consequently this region becomes very damaging in the calculation of

the average DPF filtration efficiency. As a result, the difference in DPF filtration efficiency is minimum between the two volume reduction strategies. Similar behaviour is found as the cell density is increased. Figure 4.22(b) shows how the increase of filtration area leads to very different trend in filtration velocity in comparison to Figure 4.22(a). Maximum local filtration velocity is similar to the 200 cpsi case for diameter or length reduction, but the minimum filtration velocity is clearly lower in a long region of the inlet channels. This behaviour explains the increase of the DPF filtration efficiency when the cell density does because of the higher weight of the low filtration velocity region. Nevertheless, the slight damage of the length against diameter reduction remains.

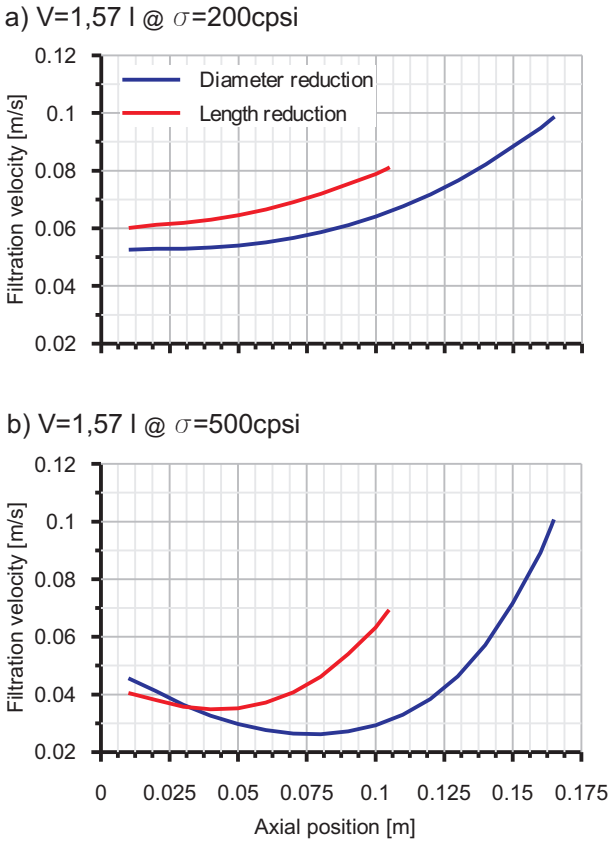

Figure 4.22: Impact of volume reduction strategy and cell density on filtration velocity with pre-turbine DPF configuration.

Once checked that the difference on the filtration efficiency behaviour between acting on the monolith length or diameter to achieve the desired DPF

volume reduction is negligible, it is possible to perform a deeper analysis based on diameter reduction for the sake of coherence with the pressure drop study.

Figure 4.23 represents the DPF filtration efficiency as a function of monolith volume and cell density for the reference TIF in the case of clean DPF substrate.

It is noticed that the ability of the filter to collect soot particles is directly related to the filtration area regardless the DPF placement: the higher the filtration area the higher the filtration efficiency. In absolute terms, pre-turbo DPF configuration provides higher DPF filtration efficiency than post-turbo. In the baseline case, i.e. monolith volume 2.43 l and cell density 200 cpsi, the pre-turbo DPF configuration leads to 0.52 in filtration efficiency, i.e. an increase of 21% with respect to the case of post-turbo DPF configuration. Approximately, pre-turbo DPF configuration provides an absolute increase of 10 percentage points in filtration efficiency in the analysed volume and cell density range. This difference brings the possibility of reducing the monolith volume in pre-turbo DPF configuration without any cell density variation up to 1.6 l getting to the same filtration efficiency in clean DPF conditions than the post-turbo placement.

The reason for such filtration efficiency increase with pre-turbo DPF placement lies on the different flow field across the DPF monolith. As proved in Chapter 3, under clean conditions the DPF filtration efficiency is mostly set by the Brownian diffusion contribution. This mechanism gets more efficient as the Peclet number decreases. Pre-turbo DPF placement contributes to such decrease because of the diffusion coefficient increase due to the higher gas temperature than in post-turbo case. In addition, the filtration velocity is also lower in most part of the cycle despite instantaneous fluctuations, as shown in Figure 3.5 (Section 3.5). Figure 4.24 confirms a relevant reduction of the Peclet number when the filter is placed upstream of the turbine thus justifying higher DPF filtration efficiency.

4.4.2.2 Soot loaded substrate

As for the previous cases, the first analysis has been aimed to check if there is any difference on the filtration efficiency behaviour related to the monolith dimension, i.e. diameter or length, reduced to get the desired filter volume downsizing. Figures 4.25(a) and (c) show the DPF filtration efficiency variation related with the length reduction while Figures 4.25(b) and (d) refer to the case of diameter reduction, both cases in pre- and post-turbo placement when 0.2 g of soot are deposited inside the filter. As in the clean substrate case (Figure 4.21) there is no significant variation between the case of length and diameter reduction. For both DPF placements the filtration efficiency trend with volume and cell density variations is exactly the same, being negligible the differences in absolute values. This result is consistent with the clean substrate case: a slight penalization of the same order for the two aftertreatment

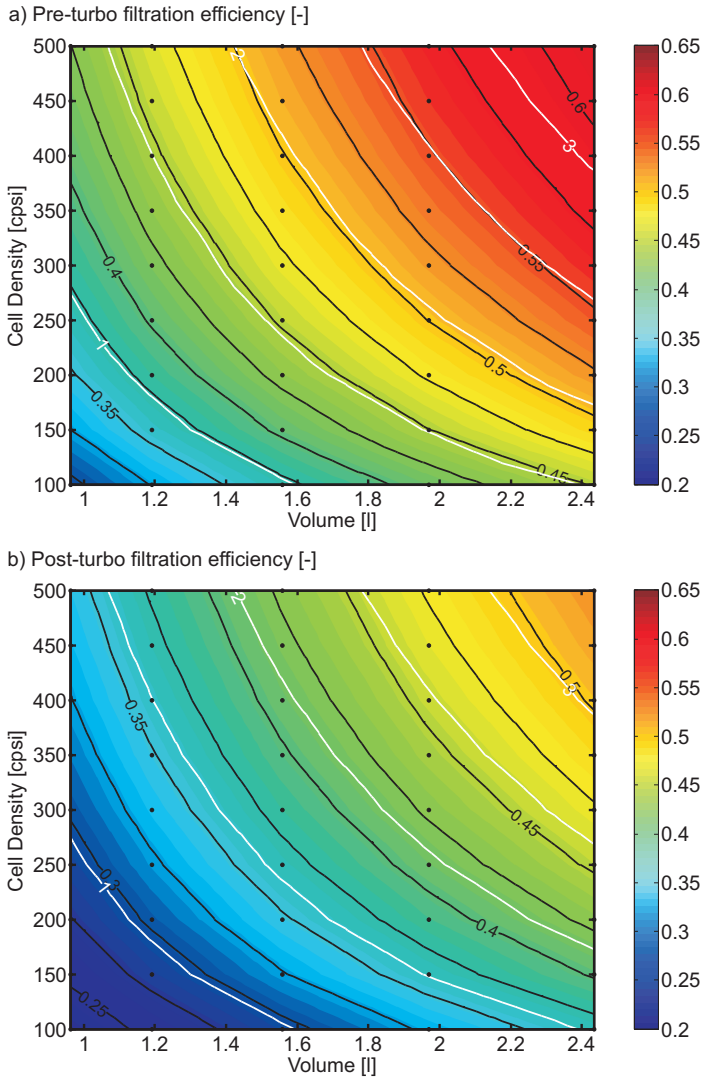

Figure 4.23: DPF filtration efficiency as a function of monolith volume and cell density for reference TIF and clean DPF substrate.

configurations is observed in the case of the length reduction. That is, the presence of soot inside the porous wall does not influence the filtration efficiency behaviour trend in front of the selected monolith dimension to achieve the volume downsizing. Therefore, analysis of diameter reduction will be considered in the following.

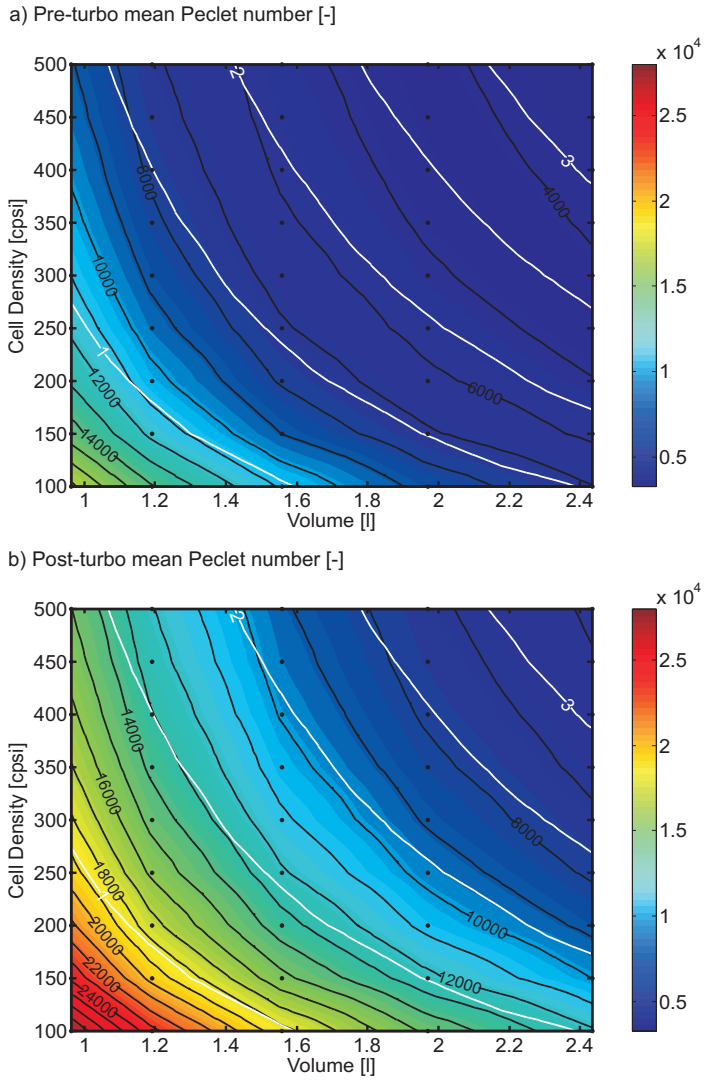

Figure 4.24: Peclet number across the porous wall as a function of monolith volume and cell density for reference TIF and clean DPF substrate.

Figure 4.26 shows the results in DPF filtration efficiency imposing a soot load equal to 0.2 g. This amount of soot avoids the saturation of the porous wall in every considered monolith geometry. As expected, the filtration efficiency is increased with respect to the clean filter. The main responsible of the filtration efficiency increase is found in the change of the porous wall microstructure. As a consequence of the soot accumulation the collector unit diameter increases

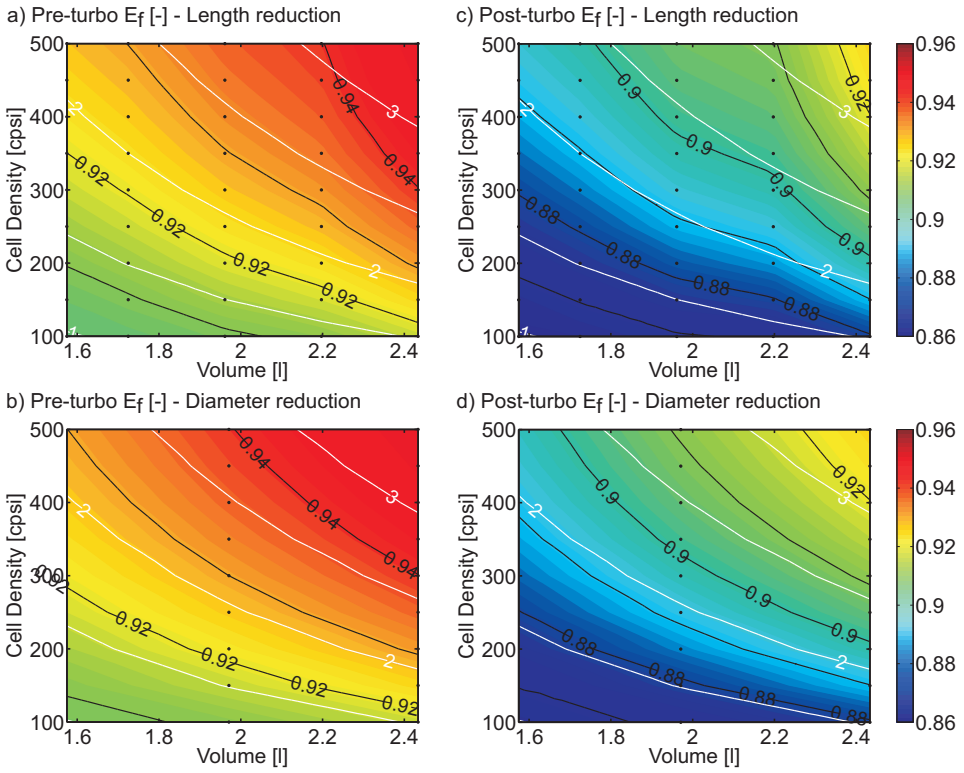

Figure 4.25: DPF filtration efficiency as a function of monolith volume and cell density for reference TIF and 0.2 g soot loading.

and the wall porosity decreases with respect to the clean case, as shown in Figure 4.27. This effect is independent on the DPF location so that no comparison between pre- and post-turbo configurations is shown.

The differences in collector unit diameter and porosity values as a function of the monolith geometry shown in Figure 4.27 are related to the variation of the soot amount per unit of filtration area mandated by changes of this last parameter. According to eqs. 4.19 and 4.20, at constant volume the cell density increment increases the filtration area by means of the specific filtration area increment:

$$SFA = \frac{2\alpha}{(\alpha + w_w)^2} = 2\alpha\sigma \tag{4.19}$$

$$A_f = SFA \frac{\pi D^2}{4} L_e \tag{4.20}$$

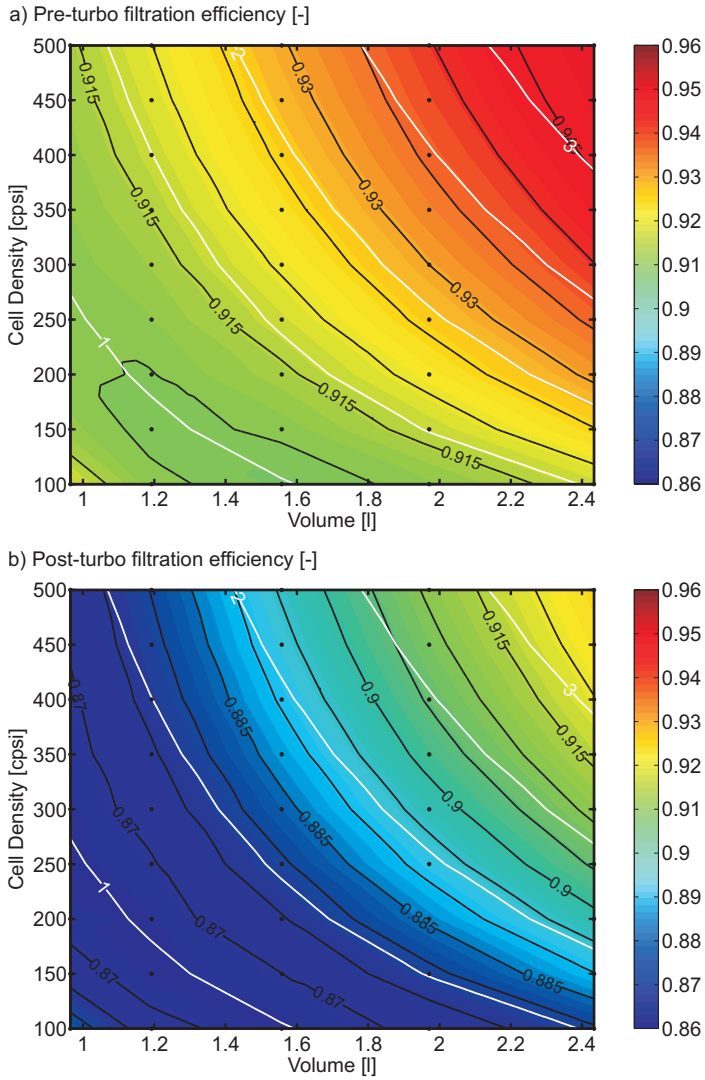

Figure 4.26: DPF filtration efficiency as a function of monolith volume and cell density for reference TIF and 0.2 g soot loading.

In turn, the volume increment at constant cell density, i.e constant SFA, also involves a linear increment of filtration area. Therefore, the higher cell density and volume the higher the filtration area and as a result the smaller the collector unit diameter and the higher the porosity. It is relevant to note how the soot capacity of the DPF porous wall is not only related to volume, as usually simplified. Figure 4.27 shows that the filtration area, i.e. the combi-

nation of volume and cellular geometry, is actually the governing parameter. Constant filtration area iso-lines coincide with constant collector unit diameter and porosity.

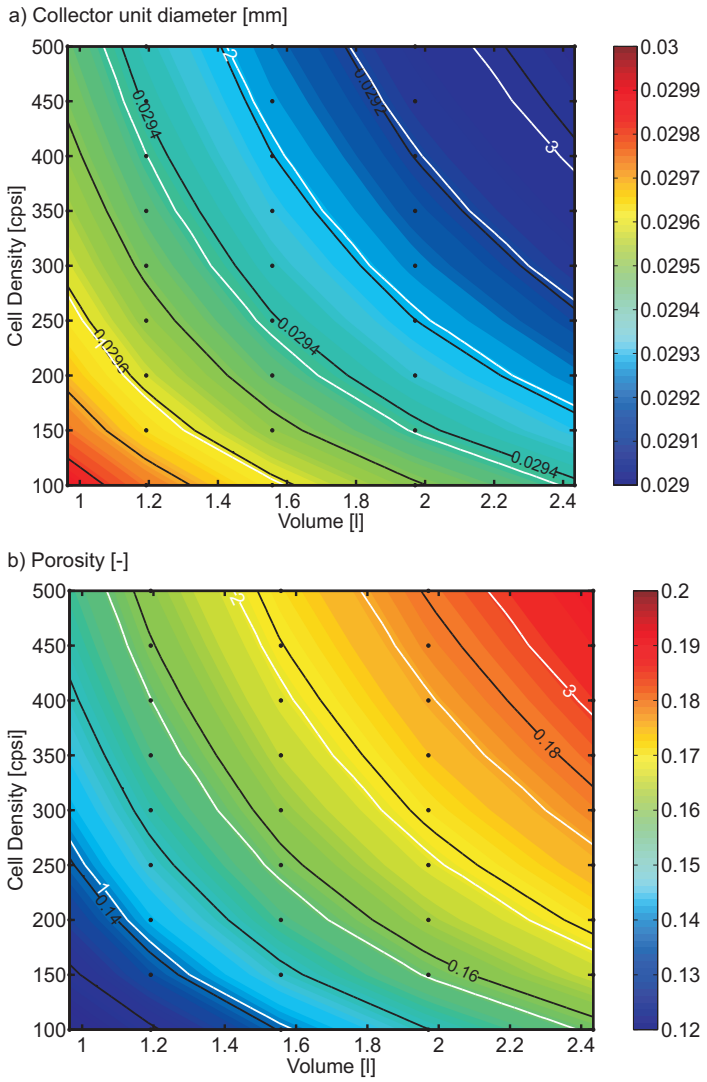

Figure 4.27: Porous wall microstructure as a function of monolith volume and cell density for reference TIF and 0.2 g soot loading.

As stated in equations 3.18 and 3.19, the porous wall microstructure directly impacts on the single sphere interception efficiency. In parallel, changes in microstructure also favour the increase of the packed bed efficiency according to

equation 3.23. Thus, the collector unit diameter increment and the porosity decrease produce the increment of the DPF interception efficiency, as represented in Figure 4.28. Such an increment is more marked as smaller volumes and cell densities are considered (bottom left corner of the contour plots). It permits the slight recover of the global filtration efficiency at very low volume and cell density values.

Also it can be noted how the order of magnitude of the interception contribution to the DPF filtration efficiency is similar to the DPF filtration efficiency in clean conditions. In addition, these effects are independent on the DPF location since the interception mechanism is only depending on the micro-geometry.

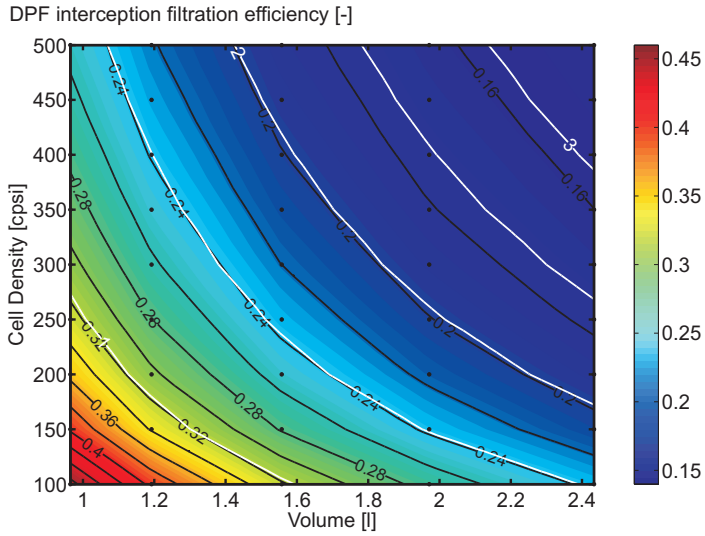

Figure 4.28: DPF interception filtration efficiency as a function of monolith volume and cell density for reference TIF and 0.2 g soot loading.

Figure 4.29 represents the effect of the soot loading on the Peclet number. Comparing with Figure 4.24, it is clearly noticed the increase of the Peclet number in the whole range. Such a Peclet number increase is governed by the microstructure variations despite the reduction in filtration velocity because of the DPF inlet pressure increment, i.e. gas density increment. In particular, the higher filtration velocity in post-turbo DPF placement makes the Peclet number in this location higher than the obtained by the pre-turbo configuration.

Despite the noticeable Peclet number increment, Figure 4.30 shows that the DPF filtration efficiency exclusively due to Brownian diffusion contribution increases because of the microstructure variation. In fact, the obtained values are higher than these of the DPF filtration efficiency in clean conditions shown in

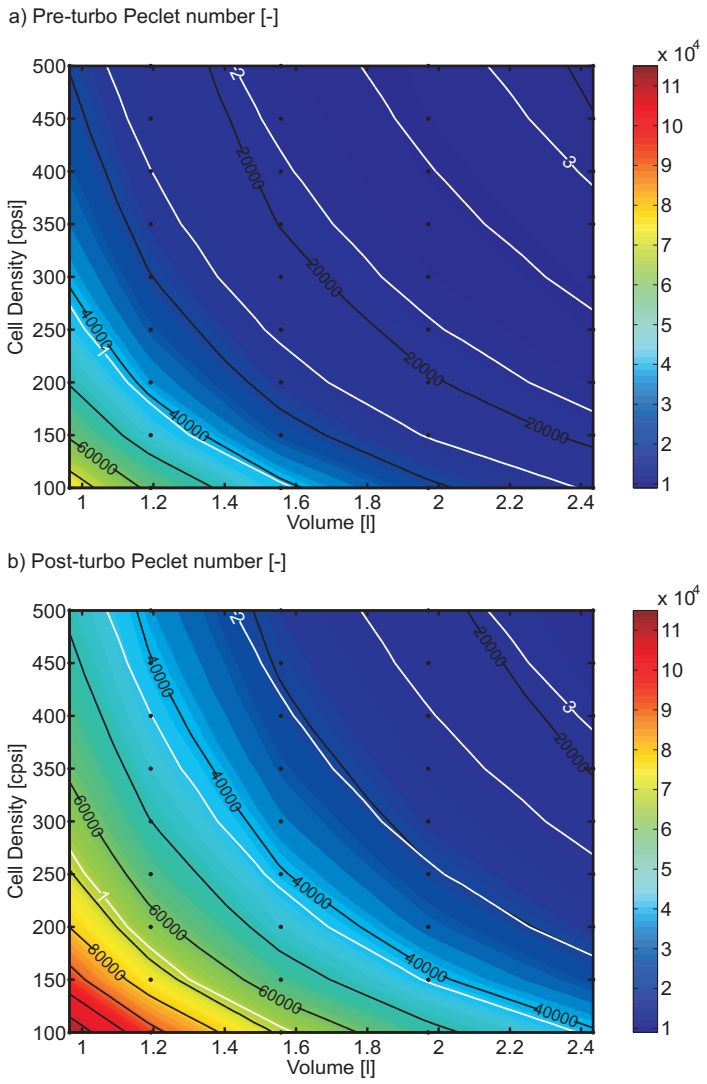

Figure 4.29: Peclet number across the porous wall as a function of monolith volume and cell density for reference TIF and 0.2 g soot loading.

Figure 4.23. In fact, the penalty related to the volume and cell density reduction results much more limited.

As expected, even very low soot loading produces a sharp increment of the DPF filtration efficiency. However, such an increment is particularly relevant in the small volume and low cell density range because of the maximum interception filtration efficiency together with the more homogeneous Brownian

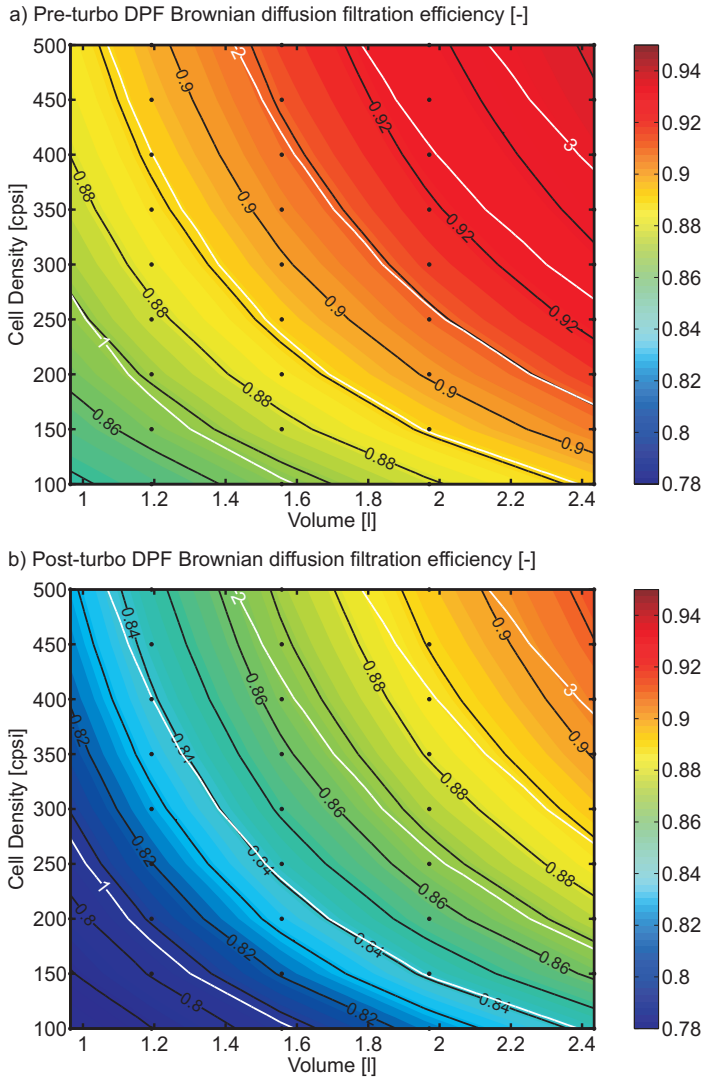

Figure 4.30: DPF Brownian diffusion filtration efficiency as a function of monolith volume and cell density for reference TIF and 0.2 g soot loading.

diffusion contribution with respect to clean conditions. As a result the DPF filtration efficiency becomes quite homogeneous in the whole range. The DPF filtration efficiency and its homogeneity as a function of the soot loading are to increase as the soot loading does.

4.4.3 Approach to volume reduction analysis

The trend shown in bsfc and filtration efficiency response suggests different approaches for DPF volume reduction as a function of its placement. While being very restrictive in post-turbo DPF placement because of the fast increase in fuel consumption, the pre-turbo DPF placement is more prone to discussion because of the low sensitivity of fuel consumption to pressure drop increase, hence to volume reduction. Additionally, lower soot loading levels are expected because of the higher temperature across the DPF [114]. Concerning the filtration efficiency, it presents the same trend independently of the DPF positioning. Nevertheless the filter presents a higher capacity of retaining particles when placed upstream of the turbine. Thanks to this filtration efficiency offset the pre-turbo DPF configuration presents an additional substantial room for DPF volume downsizing.

According to the sample of computed DPF macro-and meso-geometries, the range for the analysis of the DPF and engine performance is very broad. Therefore, given the baseline geometry, which is within the state of the art DPFs, the analysis of the potential for volume reduction can be approached considering the response of the DPF under two specific boundaries: constant specific filtration area and constant filtration area. A comprehensive analysis of the monolith volume reduction can be performed considering these constraints.

4.4.3.1 Constant specific filtration area

Within the monolith volume and cell density swept imposing constant TIF, the comparison at constant specific filtration area between two DPF geometries provides:

$$SFA_1 = SFA_2 \rightarrow \frac{2\alpha_1}{(\alpha_1 + w_{w1})^2} = \frac{2\alpha_2}{(\alpha_2 + w_{w2})^2} \tag{4.21}$$

Since TIF is constant, rearranging eq. 4.21 is obtained that:

$$\frac{2(TIF_1 - 1)}{w_{w1} TIF_1^2} = \frac{2(TIF_2 - 1)}{w_{w2} TIF_2^2} \rightarrow w_{w1} = w_{w2}, \tag{4.22}$$

so that the analysis at constant specific filtration area means that the honeycomb cell size and the porous wall thickness remain constant:

$$w_{w1} = w_{w2} \xrightarrow{\frac{\alpha}{w_w} = TIF - 1} \alpha_1 = \alpha_2 \tag{4.23}$$

Consequently, the cell unit geometric parameters (σ, OFA, LOF, HTP (without Nu influence), MIF and STP) are also kept constant under these analysis conditions. Therefore, the DPF performance is only affected by the macro-geometry change in volume and filtration area.

Constant specific filtration area means moving at constant cell density as volume reduces in the contour plots shown in previous sections. Figure 4.31 shows the effect of volume reduction on DPF pressure drop as a function of volume, TIF, DPF location and soot loading in the case of constant SFA, which has been chosen to be the same as that of the reference DPF for every TIF. Despite the selected cell density is pretty similar to the optimum value in clean conditions, the soot loading increase leads to an increasing pressure drop as volume reduces because of the induced filtration area decrease. It means the increase of the filtration velocity and the particulate layer thickness, which is shown in Figure 4.34(b). Consequently the Darcy's law contribution to pressure drop increases.

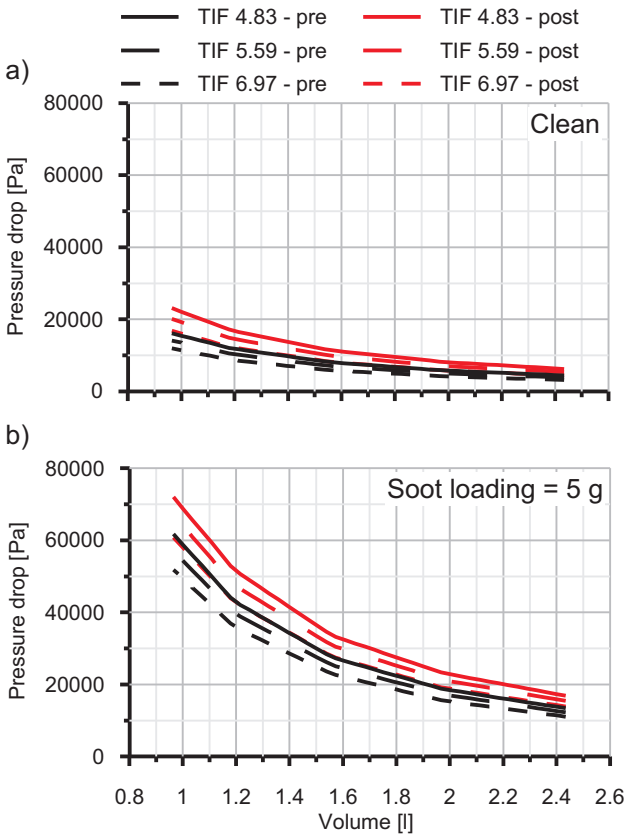

Figure 4.31: Effect of volume, TIF, placement and soot loading on DPF pressure drop in case of constant SFA.

As discussed in Section 4.4.1 the lower DPF pressure drop in pre-turbo aftertreatment placement is explained by the lower velocity across the DPF due to the higher gas density with respect to the post-turbo location. This result is obtained even with the negative effect of the higher gas pressure on the permeability of the porous medium. This penalty is caused by the slip flow correction, which is smaller as the pressure increases, like happens when changing the DPF placement from post- to pre-turbo. The slip flow effect is computed through the Stokes-Cunninham factor (SCF) [29], which multiplies the specific permeability to set the permeability of the porous medium at every operating condition. Figure 4.32 shows the porous wall permeability in clean (plot (a)) and soot loading (plot (b)) conditions as a function of volume, TIF and aftertreatment placement. In this case, the post-turbo permeability is only slightly higher than in pre-turbo placement because of the great difference between the mean free path of the gas molecules and the mean pore diameter. It provides very low Knudsen number, hence SCF values very close to 1.

However, the analysis of the particulate layer permeability, which is shown in Figure 4.33(a), reveals an important reduction of its value with respect to post-turbo DPF placement when the DPF is placed upstream of the turbine. The SCF in the particulate layer is higher than inside the porous wall. It is due to the fact that the mean pore diameter in this porous medium is lower than the gas mean free path and consequently the SCF gets over 1, as shown in Figure 4.33(b). Consequently the particulate layer permeability becomes very dependent on the SCF. The higher gas density in pre-turbo location leads to a reduction of the molecules mean free path. It makes the Knudsen number to decrease and in turns reduces the SCF and the particulate layer permeability with respect to the post-turbo DPF configuration. Nevertheless, its contribution to the pressure drop is not able to offset the pre-turbo pressure drop improvement due to other mechanisms.

Both the DPF placements suffer the same decreasing trend in SCF and permeability in the porous media as a function of the volume. This phenomenon is an additional contribution to damage the DPF pressure drop as volume reduces.

Concerning the influence of TIF on pressure drop, it is limited in comparison to the soot loading effect. Nevertheless its increase can offset part of the volume reduction damage. Higher TIF means higher α to w_w ratio. In order to keep the same cell density, the porous wall thickness must decrease and the cell size increase. Therefore an increase of SFA and filtration area is also obtained when TIF increases for the same volume and cell density. TIF increase is also involving higher OFA and STP but lower MIF and LOF.

Figure 4.34(a) shows the trend of w_w with TIF. It is independent of the monolith volume because the SFA is kept for each TIF (eq. 4.23). Similarly, Figure 4.34(b) shows that the particulate layer would be thicker with TIF and

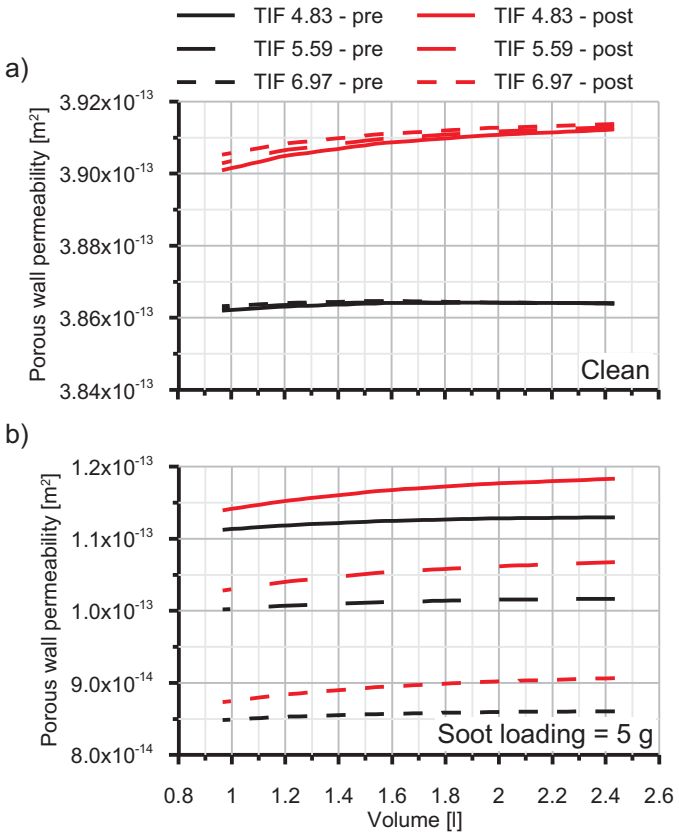

Figure 4.32: Effect of volume, TIF, placement and soot loading on porous wall permeability in case of constant SFA.

volume reduction because of the lower filtration area at constant SFA. Therefore, TIF increase provides smaller porous media thickness and lower filtration velocity leading to lower pressure drop.

The increment in pressure drop as volume decreases is reflected in bsfc, whose variation is shown in Figure 4.35. However, the incidence is clearly different between pre-turbo and post-turbo DPF placement. The monolith volume can be reduced up to 1.4 l (-42.5%) when the DPF is placed upstream of the turbine. With this volume, Figure 4.35(a) indicates that under clean conditions the bsfc would be kept almost unaffected. Under soot loading conditions (Figure 4.35(b)) the resulting specific fuel consumption would be equal to that of the reference volume in post-turbo placement.

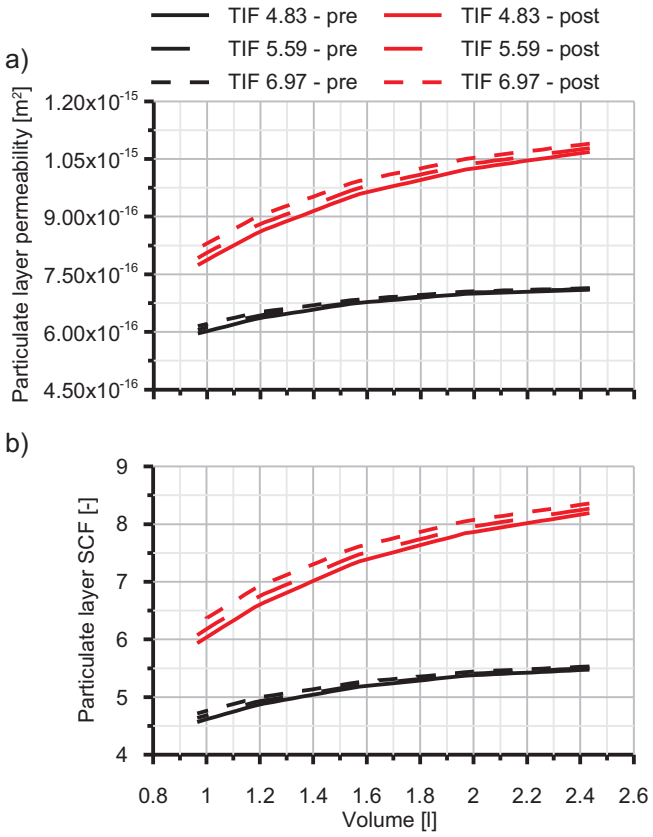

Figure 4.33: Effect of volume, TIF and placement on particulate layer permeability and SCF in case of constant SFA.

The low sensitivity of pre-turbo DPF placement to pressure drop increase underlines its potential for volume reduction and cost savings in aftertreatment even keeping the meso-structure. This result would be also useful regarding ash loading. Evidently, the DPF volume reduction affects negatively the ash loading capability. Nevertheless, the engine sensitivity to DPF loading in pre-turbo location is very low. It can be also understood as the capability to increase the quantity of the maximum ash mass able to be accumulated per unit of volume without negative effects on pressure drop and fuel penalty. Therefore, a margin for important DPF volume reduction can be still attainable preserving engine and DPF performance.

On the other hand, post-turbo DPF placement is not allowing volume reduction keeping state of the art meso-structure. The increase of pressure drop due to the filtration area reduction, which is fed back by the increasing VGT

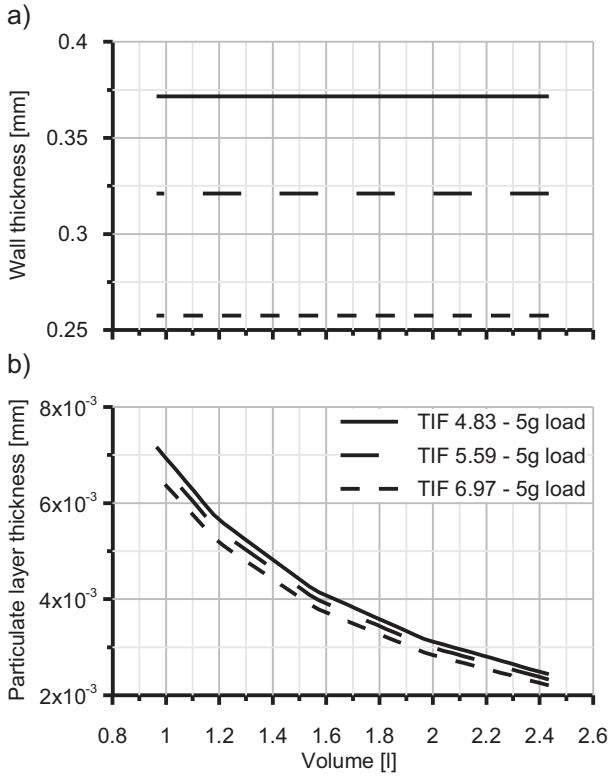

Figure 4.34: Effect of volume and TIF on porous media thickness in case of constant SFA.

closing and pressure ratio, leads to unacceptable fuel penalty even with low soot loading. Moreover, in this configuration the volume reduction results in loss of ash loading capability and higher pressure drop due to ash.

Concerning the DPF capability of collecting particles, Figure 4.36 shows the filtration efficiency trend as the monolith volume is reduced at constant SFA for the three considered TIF values. Constant SFA approach makes the DPF filtration efficiency very sensitive to volume, being damaged as volume is reduced. This is particularly relevant in clean conditions. In soot loading conditions (Figure 4.36(b)) it is possible to see the change in slope at low volumes marked by the interception mechanism increase. Reasons related to the fluid-dynamic field and micro-geometry (change from clean to soot loading conditions) have been already discussed in Section 4.4.2. However, it is interesting to note that at constant volume higher DPF filtration efficiency is always obtained by the pre-turbo DPF configuration. It ensures lower particulate matter emissions before the maximum DPF filtration efficiency is reached. In addition, constant

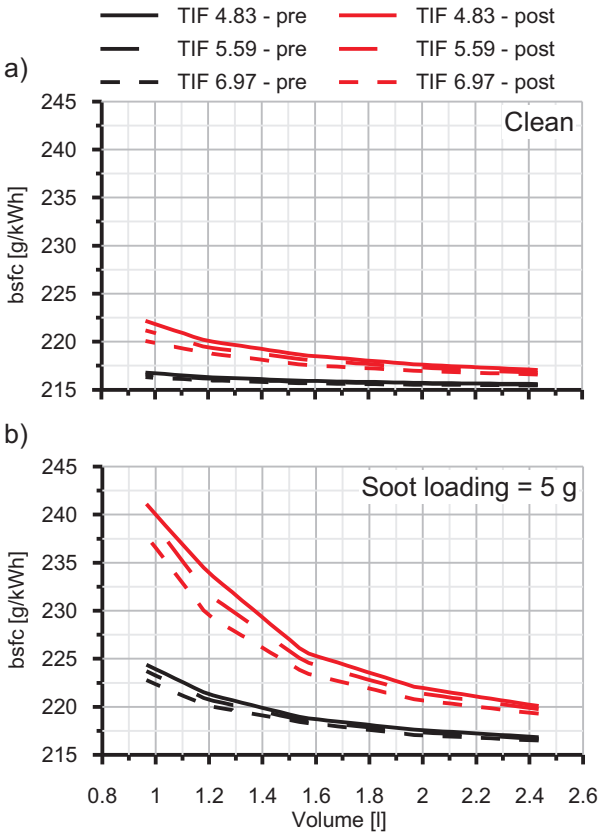

Figure 4.35: Effect of volume, TIF, placement and soot loading on brake specific fuel consumption in case of constant SFA.

SFA approach allows reaching a ~35% volume decrease (1.55 l) with pre-turbo DPF configuration providing the same filtration efficiency than the baseline volume in post-turbo DPF placement.

With respect to TIF, it is clearly observed that its influence within the whole range is again very slight. The variations are related to small change in filtration area. Keeping the baseline cell density and according to eq. 2.59, TIF increment is given by the same percentage of porous wall thickness decrease and cell size increment. As a consequence SFA is increased, i.e. wider channels at constant cell density means more contact surface between the gas and the porous substrate. Therefore, the filtration area is also increased thus leading to increase the Brownian diffusion contribution to particles collection because of the filtration velocity reduction.

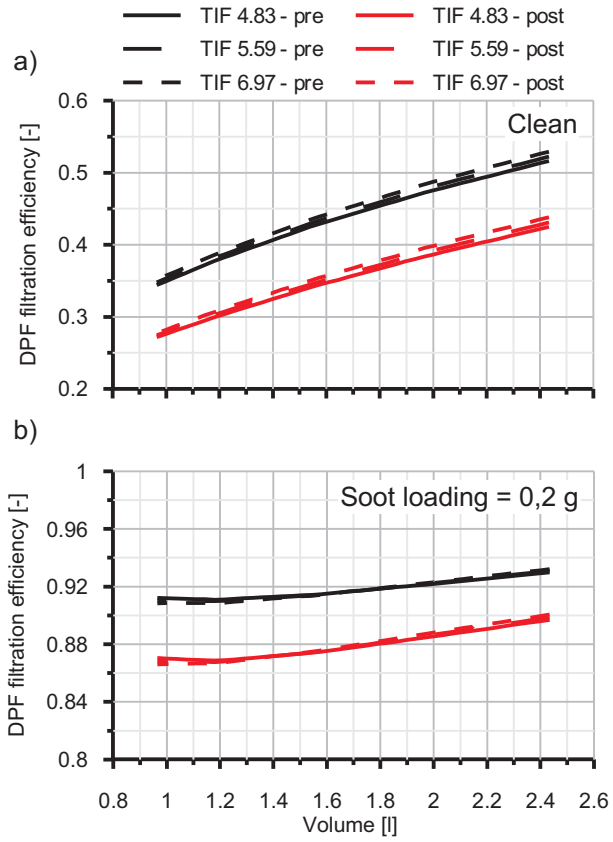

Figure 4.36: Effect of volume, TIF, placement and soot loading on the DPF filtration efficiency in case of constant SFA.

As the DPF is loaded the TIF effect becomes progressively negligible because of the growing importance of the microstructure. This result points out that TIF definition must be dependent on pressure drop performance, i.e. specific fuel consumption, together with other structural criteria such as MIF or STP.

4.4.3.2 Constant filtration area

Results in Section 4.4.1.1 and Section 4.4.1.2 have shown how low permeability substrates (i.e. low porous wall permeability and/or increasing soot & ash loading) find in high cell density a way to increase the filtration area and hence to reduce the damage on pressure drop and fuel consumption as monolith volume is reduced.

Figure 4.37 shows the brake specific fuel consumption as a function of volume, TIF, placement and soot loading when the filtration area is kept constant. Its value has been chosen equal to that of the reference DPF for every TIF. Since the maximum cell density in the study has been fixed to 500 cpsi, the minimum monolith volume that can be reached is 1.57 l (−35.4%). The bsfc with pre-turbo DPF placement becomes nearly constant in both clean (Figure 4.37(a)) and loaded conditions (Figure 4.37(b)). In the case of post-turbo DPF configuration an increasing penalty is found as volume reduces although it is lower than in the case of constant specific filtration area.

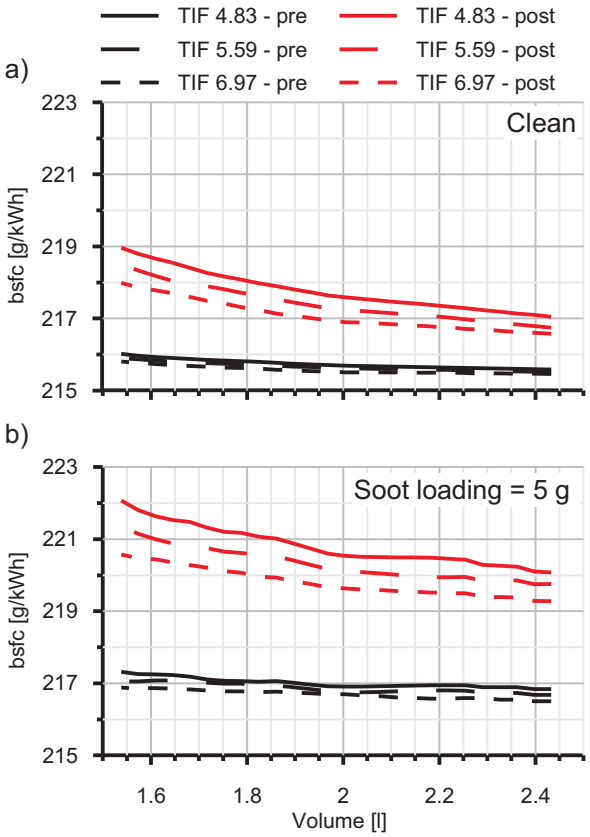

Figure 4.37: Effect of volume, TIF, placement and soot loading on brake specific fuel consumption in case of constant filtration area.

The disadvantages of this volume reduction strategy are issues related to channel plugging, mainly in post-turbo DPF placement. Hence the extended use of low cell density meso-structures in DPFs. Nevertheless, pre-turbo DPF

placement can better manage cell density increase due to the higher temperature providing better passive regeneration performance and lower engine sensitivity to pressure drop increase.

Figure 4.38 shows the pressure drop as a function of volume, TIF, placement and soot loading when the filtration area is kept constant. Comparing against Figure 4.31, both pre-turbo and post-turbo DPF architectures are clearly benefited in DPF pressure drop when the filtration area is kept despite the volume reduction.

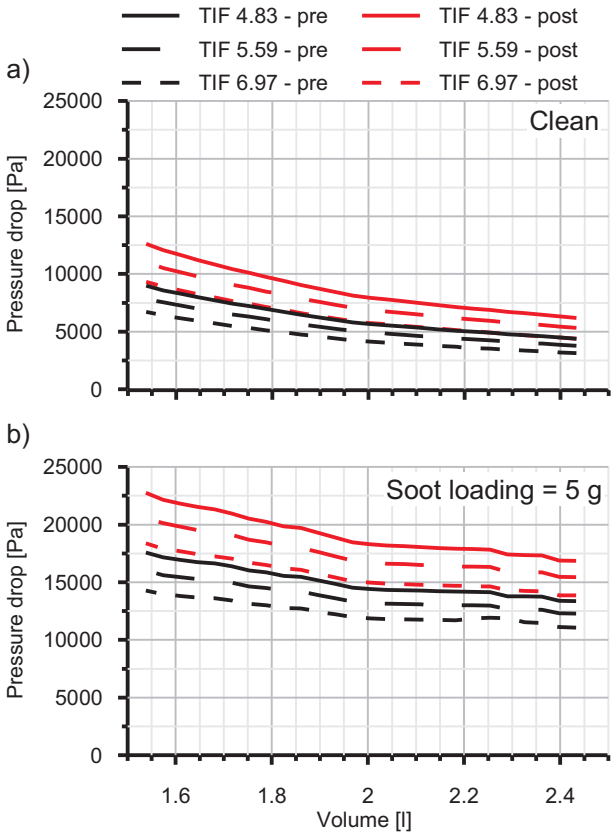

Figure 4.38: Effect of volume, TIF, placement and soot loading on DPF pressure drop in case of constant filtration area.

Although in this analysis the filtration area is the main parameter controlling the pressure drop change, these results come from a balance of different phenomena. Comparing against constant specific filtration area, to ensure a target filtration area as volume reduces leads to the following behaviour:

- Lower porous media pressure drop. According to the Darcy's law, it is produced by a reduction of filtration velocity and the porous media thickness. Figure 4.39(a) shows that the porous wall thickness decreases as volume does. In the case of the particulate layer thickness, which is shown in Figure 4.39(b), it is kept constant being is value imposed by the filtration area.

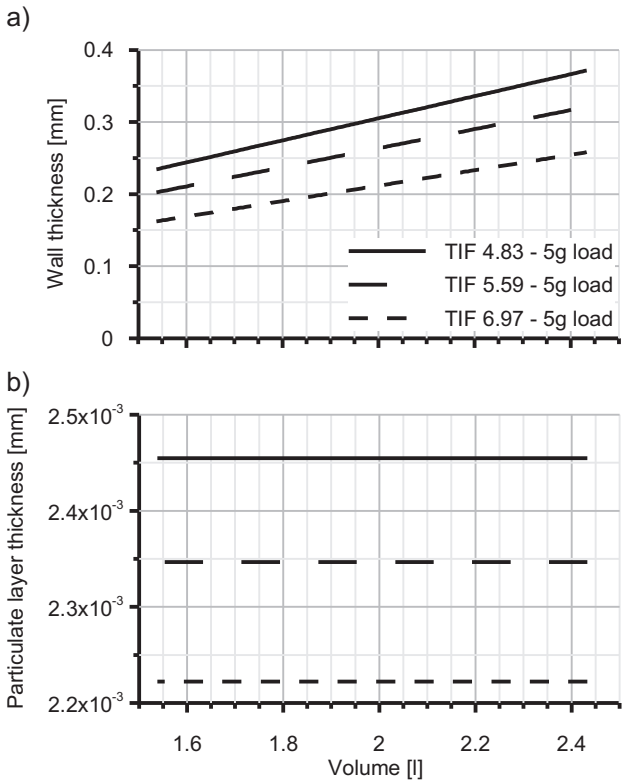

Figure 4.39: Effect of volume and TIF on porous media thickness in case of constant filtration area.

Concerning the porous wall permeability, when the porous wall is loaded it decreases with the DPF volume in the case of constant filtration area, as shown in Figure 4.40. However, this parameter remains almost constant when the specific filtration area is not modified (Figure 4.32). The reason lies in the balance between the fraction of porous wall with soot penetration and the fraction that is still kept clean. Assuming that the porous wall porosity and the mean pore diameter are not modified and that the soot properties are the same, the porous wall permeability is only

dependent on the fraction of porous wall thickness affected by soot penetration [10]. Considering as hypothesis that the soot penetration thickness does not change with the DPF geometry, the fraction of loaded porous wall thickness with soot penetration increases in the case of constant filtration area. It is due to the fact that the porous wall thickness is reduced as volume does. As a consequence, the porous wall permeability decreases for this design condition.

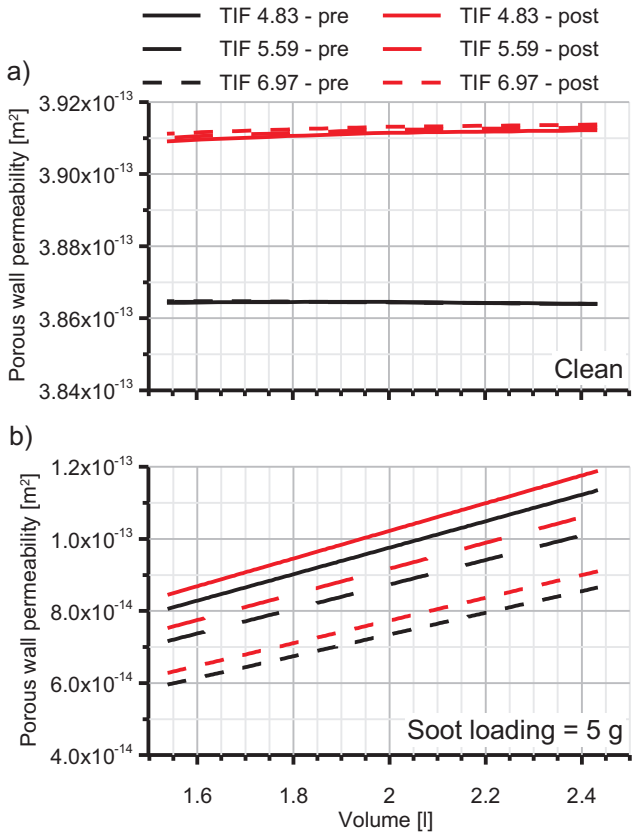

Figure 4.40: Effect of volume, TIF, placement and soot loading on porous wall permeability in case of constant filtration area.

Despite the trend in porous wall permeability, the particulate layer permeability is scarcely modified as volume reduces with constant filtration area, as Figure 4.41(a) shows, in contrast with constant specific filtration area case (Figure 4.33(a)). It brings very important benefits to pressure drop reduction. The reason explaining this response lies in the lower sensitivity of the Stokes-Cunningham factor to volume reduction when the filtration

area is kept constant, as represented in Figure 4.41(b). This result is the consequence of all contributions lowering the pressure drop. Hence lower change in gas density and in turn almost constant SCF favouring lower pressure drop (snowball effect).

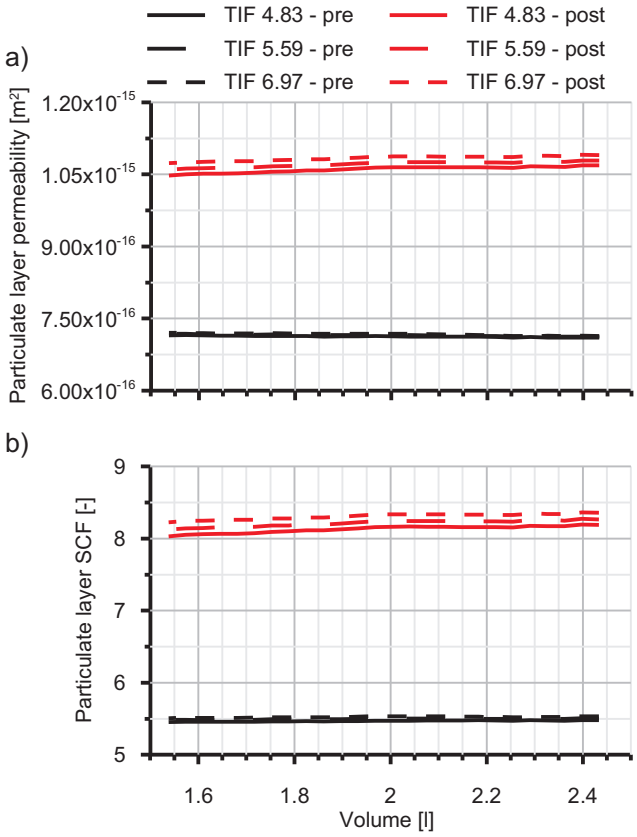

Figure 4.41: Effect of volume, TIF and placement particulate layer permeability in case of constant filtration area.

- Similar inertial pressure drop. Like constant specific filtration area case, the OFA is also constant with constant filtration area as volume reduces. To prove it the following reasoning can be done. Within the analysis boundaries (monolith volume and cell density swept at constant TIF), the comparison at constant filtration area between two DPF geometries

involves that the specific filtration area increases linearly as volume decreases:

$$A_f = cst \Rightarrow SFA_1 V_1 = SFA_2 V_2 \tag{4.24}$$

Expressing the specific filtration area as a function of TIF, it is obtained that:

$$\frac{2V_1(TIF_1 - 1)}{w_{w1} TIF_1^2} = \frac{2V_2(TIF_2 - 1)}{w_{w2} TIF_2^2} \tag{4.25}$$

and being TIF constant, then:

$$\frac{V_1}{w_{w1}} = \frac{V_2}{w_{w2}} \tag{4.26}$$

Consequently, the analysis under constant filtration area fulfils the following conditions:

$$w_{w2} = \frac{V_2}{V_1} w_{w1} \xrightarrow{\frac{\alpha}{w_w} = TIF - 1} \alpha_2 = \frac{V_2}{V_1} \alpha_1 \tag{4.27}$$

Applying these results to the definition of the OFA, it is found that this parameter remains constant:

$$\begin{aligned} OFA_2 &= \frac{\alpha_2^2}{2(\alpha_2 + w_{w2})^2} = \\ &= \frac{\left(\frac{V_2}{V_1}\alpha_1\right)^2}{2\left(\frac{V_2}{V_1}\alpha_1 + \frac{V_2}{V_1} w_{w1}\right)^2} = OFA_1 \end{aligned} \tag{4.28}$$

Under soot loading conditions, the case of constant filtration area provides higher inlet cross-section than the constant specific filtration area case for the same monolith diameter because of the lower particulate layer thickness. Therefore, a slight reduction of inertial pressure drop is expected at the monolith inlet.

- Pressure drop increase due to friction phenomena. The specific filtration area increases as volume reduces according to eq. 4.24. This determines a square increase of the friction factor with volume reduction for the constant filtration area case [93].

Considering the trend of the different mechanisms causing the pressure drop, the porous media contribution is controlling the overall response. The reduction in pressure drop given by the filtration area control strategy boosts its interest in sizing DPFs for pre-turbo use while preventing excessive cell density leading to channel plugging issues. From the results given in eq. 4.27, the cell density varies squarely with volume ratio:

$$\begin{aligned}\sigma_2 &= \frac{1}{(\alpha_2 + w_{w2})^2} = \frac{1}{\left(\frac{V_2}{V_1}\alpha_1 + \frac{V_2}{V_1}w_{w1}\right)^2} = \\ &= \frac{V_1^2}{V_2^2(\alpha_1 + w_{w1})^2} = \frac{V_1^2}{V_2^2}\sigma_1\end{aligned} \tag{4.29}$$

Furthermore, it can be demonstrated that the mechanical parameters MIF and STP are also kept constant:

$$\begin{aligned}MIF_2 &= \frac{w_{w2}^2}{(\alpha_2 + w_{w2})\,\alpha_2} = \\ &= \frac{\left(\frac{V_2}{V_1}w_{w1}\right)^2}{\left(\frac{V_2}{V_1}\alpha_1 + \frac{V_2}{V_1}w_{w1}\right)\frac{V_2}{V_1}\alpha_1} = MIF_1\end{aligned} \tag{4.30}$$

$$\begin{aligned}STP_2 &= TIF_2(1 - 2OFA_2) = \\ &= TIF_1(1 - 2OFA_1) = STP_1\end{aligned} \tag{4.31}$$

On the negative side, heat transfer parameters such as HPT and LOF suffer respectively a square and a linear increase as volume reduces:

$$\begin{aligned}HTP_2 &= \frac{1}{2}Nu\frac{SFA_2^2}{OFA_2} = \\ &= \frac{1}{2}Nu\frac{V_1^2}{V_2^2}\frac{SFA_1^2}{OFA_1} = \frac{V_1^2}{V_2^2}HTP_1\end{aligned} \tag{4.32}$$

$$\begin{aligned}LOF_2 &= \frac{1}{4}\left(\frac{SFA_2}{OFA_2} - 2SFA_2\right) = \\ &= \frac{1}{4}\frac{V_1}{V_2}\left(\frac{SFA_1}{OFA_1} - 2SFA_1\right) = \\ &= \frac{V_1}{V_2}LOF_1\end{aligned} \tag{4.33}$$

On one hand it means an increase of the heat losses that should be avoided by a proper packaging and insulation. However, the main problem comes from the effect of the higher heat transfer during transient operation. Although it is very positive for the substrate it also means the reduction of energy available at the turbine inlet with pre-turbo aftertreatment placement during transient accelerations. The trends in different parameters emphasise the need of a right balance for filtration area selection as volume reduces in order to find the best solution for the trade-off between pressure drop and thermal response.

With respect to the filtration efficiency Figure 4.42 shows that the constant A_f approach avoids any penalty on it related to DPF volume reduction. Remainder variables, i.e. TIF, DPF placement and loading show the same trends than in constant SFA approach.

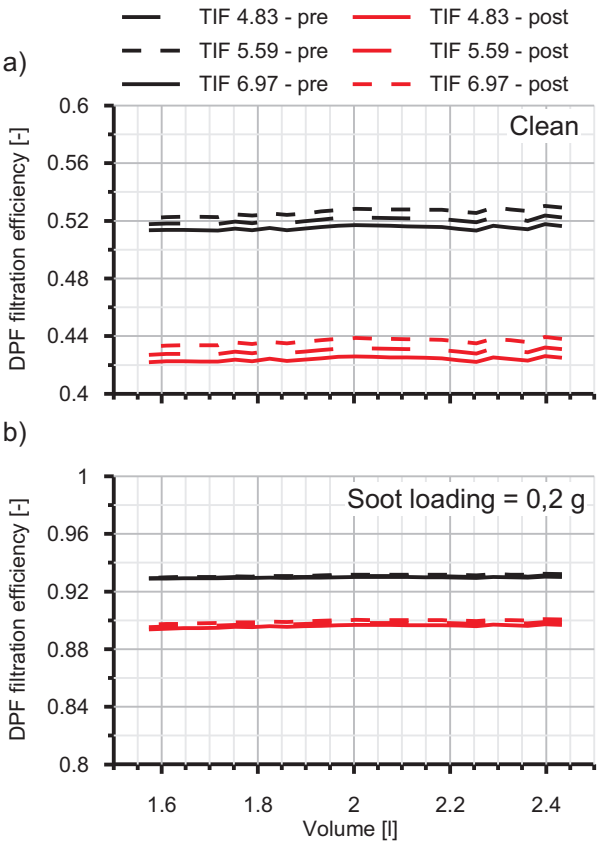

Figure 4.42: Effect of volume, TIF, placement and soot loading on the DPF filtration efficiency in case of constant filtration area.

4.5 Cost analysis

Besides fuel economy and aftertreatment performance improvement that a pre-turbo aftertreatment configuration can provide, the potential for monolith volume reduction may contribute to important cost savings in engine manufacturing. Taking as baseline the methodology for aftertreatment cost estimate proposed by Posada et al. [151], Figure 4.43 shows the DOC cost as a function of the volume. This cost estimate is including the cost of catalysts (Pt and Pd) with a representative concentration, substrate, washcoat, canning, accessories, overheads and long term productivity. The estimate cost for the reference geometry DOC is 86.5 $. It can be reduced up to 58.8 $ in a pre-turbo placement selecting the geometry providing the same dwell time than the reference geometry in post-turbo placement at medium-high load and the lowest pressure drop, i.e. D = 145 mm and L = 66 mm resulting in 1.09 litres monolith volume. It means that the DOC cost may be reduced around 33% in pre-turbo applications maintaining the dwell time of the reference post-turbo geometry.

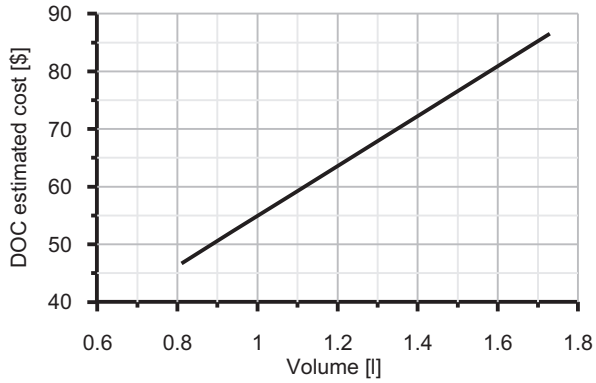

Figure 4.43: DOC cost estimate as a function of monolith volume.

Regarding the DPF cost, applying again the methodology proposed by Posada et al. [151], results similar to the DOC case are obtained, i.e. a linear decrease of the system cost as the monolith volume is reduced. Figure 4.44 shows the DPF cost estimate as a function of the monolith volume. For this aftertreatment system, the same cost items than in the DOC are considered. Apart, a constant cost for the regeneration system, fixed in 61$ according to Posada's proposal, is considered. Although the pre-turbo DPF placement brings advantage in terms of passive regeneration, that would contribute to lower the regeneration system and catalyst costs, these have been included in the cost estimate presented in Figure 4.44. Note that the here discussed cost analysis is based only on DPF monolith volume considerations in order to provide a rough idea of the

economic benefits related with the filter volume downsizing. Due to the lack of accurate information, the possible cost increase related, for example, to the production of higher cell density monoliths is not considered. With this in mind the analysis of Figure 4.44 permits calculating a cost reduction from 222.1 $ of the reference volume to 166.1 $ of a 1.57 l monolith, i.e. the minimum volume achievable keeping the reference filtration area. It corresponds to a 25% DPF cost reduction.

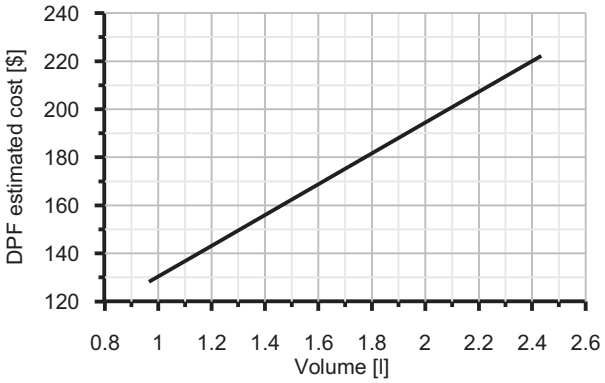

Figure 4.44: DPF cost estimate as a function of monolith volume.

Considering the above listed cost reductions, i.e. -33% for the DOC and -25% for the DPF, and the cost percentage of every aftertreatment system presented in Section 4.1, it is possible to conclude that placing the DPF and DOC in pre-turbo configuration permits a 13.3% cost saving on the whole Euro 6 aftertreatment price. Assuming that the aftertreatment represents around 30% of the engine cost, the above stated saving is reflected in a 4% lower engine cost.

4.6 Aftertreatment volume downsizing effect on engine transient operation

An additional advantage of the aftertreatment volume downsizing is the reduction of its thermal inertia, of particular interest in case of pre-turbo placement. Although the aftertreatment thermal inertia can contribute to remove the turbocharger lag during transient operation under hot wall operation, it turns into the most important disadvantage of the pre-turbo aftertreatment positioning during transient processes under cold wall operation [158]. It makes necessary a proper adaptation of the control strategies and the use of two-stage turbocharging or mechanical compressor to overcome satisfactorily the torque lag [117]. Even if the engine provides the target torque the aftertreatment

thermal transient can be very long. The consequence is negative on bsfc and pollutant conversion efficiency and/or passive regeneration because of the low substrate temperature. Nevertheless, it is worth highlighting that the pre-turbo location of the aftertreatment reduces the monolith warm-up if compared with post-turbo placement. It is mainly positive in the case of the aftertreatment monolith located just next to the exhaust manifold because this is the region of higher temperature. The warm-up of the aftertreatment system immediately after the first monolith will be subjected to the thermal inertia of such an element.

Anyway, the benefits of aftertreatment volume reduction in terms of faster thermal transient bring lower impact on transient bsfc and aftertreatment performance. Figure 4.45 shows the response of the engine during transient operation at constant engine speed (2000 rpm) from steady-state conditions at zero injected fuel to 80% in engine load. Blue series represents the experimental response of the engine with a single-stage turbocharger architecture and post-turbo placement of the DOC and DPF with reference geometry. In the same way, black series shows the experimental response of the engine under the same operating conditions but with pre-turbo DPF and DOC placement. As expected because of the single stage turbocharging, the comparison of engine torque, which is plotted in Figure 4.45(a), between both architectures clearly shows that the engine response is dramatically degraded by the pre-turbo aftertreatment placement. With this configuration, the DPF and DOC thermal inertia prevents the gas temperature from increasing at the inlet of the VGT, as plot (g) in Figure 4.45 shows. As a consequence the turbocharger lag lasts more and there is no increase of air mass flow (Figure 4.45(d)), hence of injected fuel mass (Figure 4.45(b)).

The engine model has been setup to reproduce the experimental response of the pre-turbo aftertreatment placement. It is represented by the green series in Figure 4.45. All the variables involved in the process are modeled with good precision. Only differences appear in the case of the DPF inlet temperature, which is represented in Figure 4.45(e). It is because of the fact that the measurement of the temperature at this location is affected by the thermal inertia of the thermocouple. The actual temperature trend should increase as fast as the model shows. The turbine inlet temperature in post-turbo placement (blue series in Figure 4.45(g)) is also affected by this phenomenon. Other experimental temperatures are not influenced by the thermocouple thermal inertia since their rate of increase is low due to the presence of previous elements in the exhaust line.

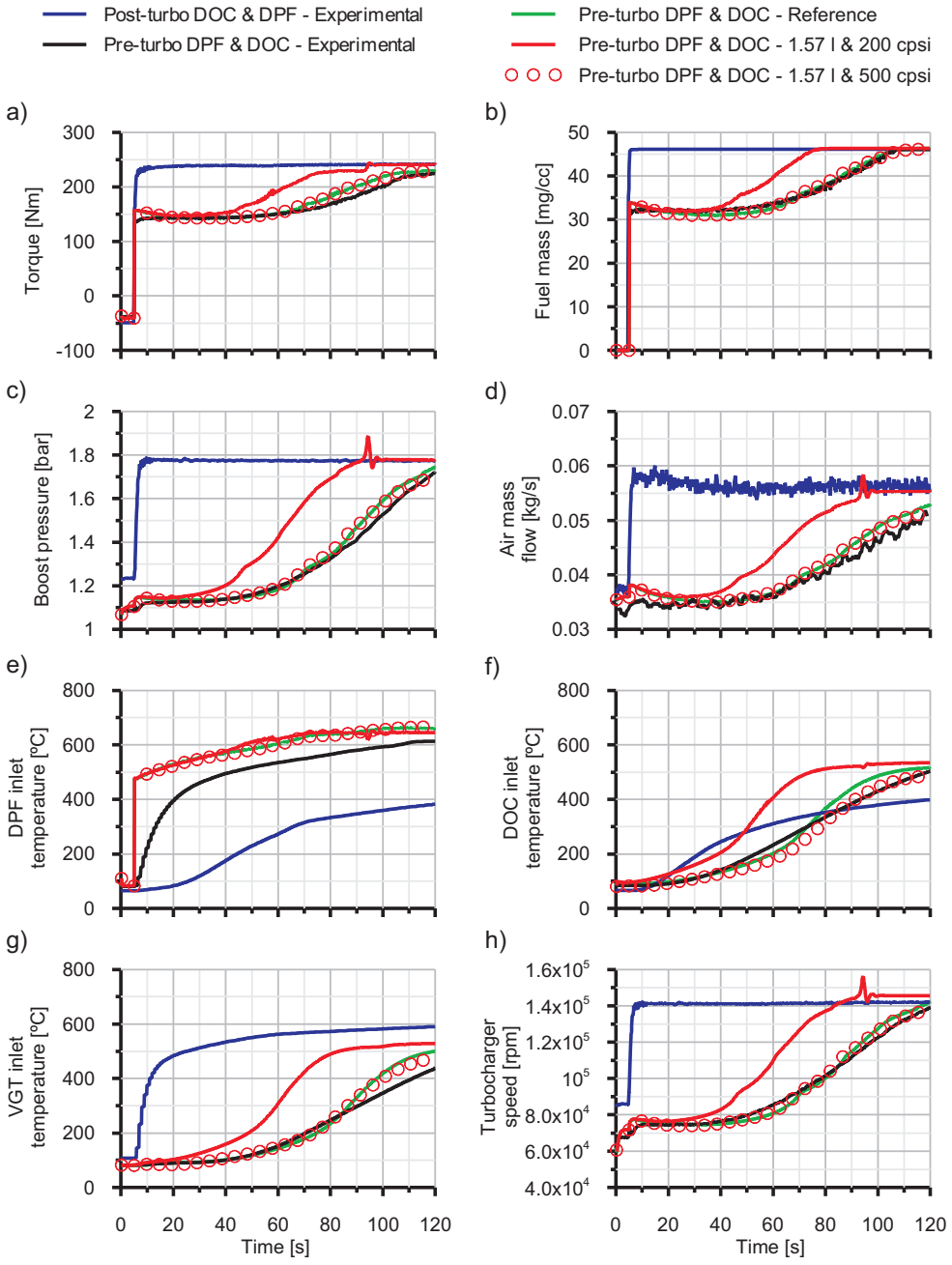

Figure 4.45: Effect of aftertreatment volume reduction in the transient response at 2000 rpm from zero to 80% engine load of a single stage turbocharged diesel engine with pre-turbo aftertreatment placement.

Once certified that the model behaves as the experimental response, the geometry of the aftertreatment systems has been modified according to the results obtained in the analysis under steady-state operating conditions. The DOC geometry has been selected to provide the minimum pressure drop and to ensure dwell time at medium-high load. According to the results shown in Figure 4.3 and Table 4.4, the DOC diameter has been kept at the reference value (145 mm) and the effective length reduced from 105 mm to 66 mm. As previously stated, it provides a volume reduction close to 40%. Regarding the DPF geometry, its volume has been reduced from 2.43 l to 1.57 l by means of diameter reduction. The value has been selected as the smallest volume able to maintain the reference filtration area with the maximum considered cell density. In this way it has been possible to compare the effect of the same DPF volume reduction at constant SFA with the case of constant filtration area.

The response of the pre-turbo aftertreatment configuration with reduced DPF and DOC volumes are represented by the red series: in continuous line the constant SFA case and in circles the constant filtration area case. The aftertreatment volume reduction leads to a noticeable thermal inertia reduction which improves the engine response. Nevertheless, the lag still remains. The target torque, which is represented in plot (a) of Figure 4.45, reaches the stabilization 80 s after the tip-in beginning once the VGT begins to regulate its position in the constant SFA case. In case of constant filtration area the lag is almost equal to the reference case. Although in the first case the response time is reduced with respect to the reference DPF and DOC volumes, it points out that the engine drivability cannot be recovered only with this solution, as proposed in [109]. However, there is an important acceleration of the thermal transient process at the aftertreatment that contributes to faster light-off and passive regeneration onset. Figure 4.45(f) shows that the aftertreatment volume reduction at constant specific filtration area (red line plot) increases the temperature level at the DOC, which is equal to that at the post-turbo placement up to 20 s after the tip-in beginning but clearly with greater rate of increase from this time. Stabilization around 525 °C is reached 80 s after the beginning of the transient process. As the DOC inlet coincides with the DPF outlet it also describes the temperature evolution at the DPF, which would ensure optimum conditions for passive regeneration. When the case of constant filtration area is considered (red circles plot) the sensible DPF HTP and LOF increase (eq. 4.32 and eq. 4.33) leads to a slower DOC inlet temperature increase. The higher heat transfer to the DPF walls slows down the DOC thermal transient resulting in a behaviour similar to the one of the reference case.

Figure 4.46 represents the change in engine dynamics when the engine incorporates a mechanical compressor assisting the turbocharger. Figure 4.46(a) shows that with this kind of architecture the target torque is reached instantaneously due to the fact that the mechanical compressor is able to provide a

sudden increase of the boost pressure. It is independent on the aftertreatment volume. The existence of this assistance, which as shown in Figure 4.46(d) requires an additional power supply of maximum 3 kW, also can contribute to improve the engine efficiency by managing the matching with the turbocharger. Figure 4.46(h) shows how the turbocharger speed stabilizes at low level controlling the VGT opening and dividing the compression ratio between the turbocompressor and the mechanical compressor supplying to it 2.5 kW. As a consequence, the VGT opening increases reducing the engine back-pressure and increasing the engine torque for the same injected fuel mass (Figure 4.46(a)).

As the transient process is faster and the maximum injected fuel mass and air mass flow are obtained from its beginning, the rate of increase of the gas temperature is also improved. Comparing plot (f) in Figure 4.45 and Figure 4.46 it is observed that the thermal steady conditions are reached with 20 s in advance at the DOC inlet when the aftertreatment volumes are reduced and the DPF specific filtration area is kept constant. Although this advance is higher for the reference aftertreatment size, aftertreatment volume reduction is still beneficial. As a consequence the gas temperature at the VGT inlet is closer to that experimentally obtained with the post-turbo aftertreatment placement, which is shown in Figure 4.46(g). The constant filtration area case benefit is similar to the reference volumes one. The DOC inlet temperature reaches 200 °C (a reasonable light-off temperature value) around 30 seconds after the tip in. On the negative side the higher heat losses related with the higher HTP lead to a slightly lower DOC inlet temperature, hence lower inlet VGT temperature, in stationary conditions. This is an additional constraint, together with the inlet channel plugging risk, to carefully take into account when selecting the cell density of the downsized DPF. An important advantage of the proposed architecture including a mechanical compressor is the possibility to match its control with the turbocharger in order to manage the temperature downstream of the turbine. It would allow controlling with flexibility the performance of other aftertreatment systems placed on this region such as the SCR.

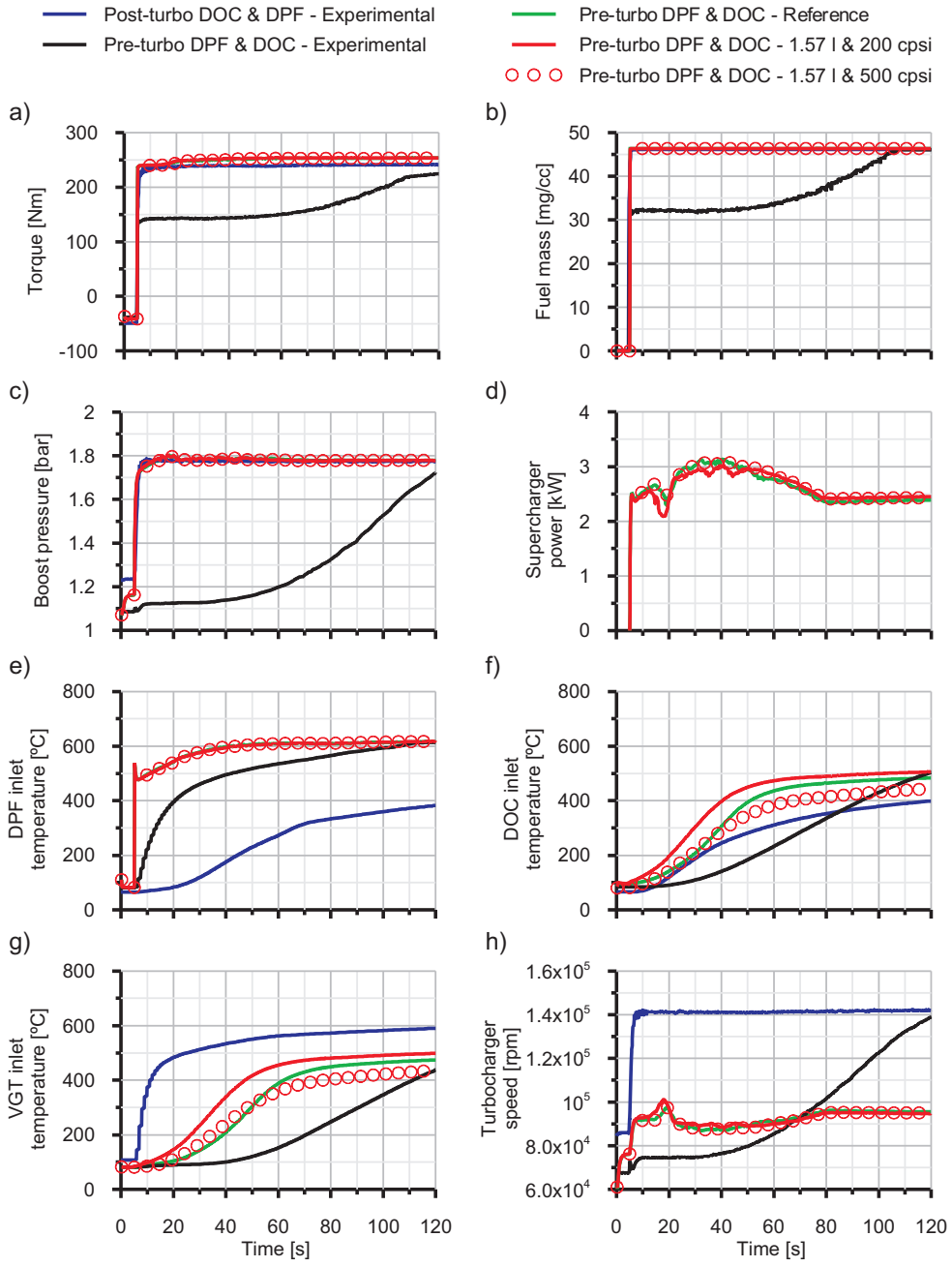

Figure 4.46: Effect of aftertreatment volume reduction in the transient response at 2000 rpm from zero to 80% engine load of a single stage turbocharged diesel engine with mechanical compressor and pre-turbo aftertreatment placement.

4.7 Summary

This chapter was aimed to the evaluation of the aftertreatment volume downsizing potential. The results and the analysis of the DOC and DPF volume reduction influence on engine fuel consumption, DOC dwell time and DPF filtration efficiency have been presented and compared between post- and pre-turbo aftertreatment positioning. The work is based on a computational study performed with a passenger car single stage turbocharged diesel engine, which has been previously setup to experimental data under steady-state and transient operation with post-turbo and pre-turbo aftertreatment configurations. The calculations have comprised volume variations based on monolith diameter and effective length. The substrate micro-structure has been kept constant.

Additionally the study of the DPF performance has also considered cellular geometry variations. The cell density has been modified imposing a cell size and porous wall thickness dependence given by constant TIF. This approach has allowed covering the influence of additional cell unit geometric parameters related to fluid-dynamic, thermal and mechanical performance. Furthermore the DPF analysis comprised both clean and soot loaded substrate conditions.

The results on DOC sizing have revealed that its volume can be reduced with barely effects on pressure drop and hence on engine fuel economy. Pressure drop can be reduced imposing length reduction at constant reference post-turbo diameter. Volume reductions close to 40% can be performed at medium-high load keeping constant dwell time between post- and pre-turbo DOC locations. However, the dwell time at low load can become lower in pre-turbo configuration with respect to the traditional placement. It is related to the lack of gas density increase in pre-turbo placement in this operating region. Nevertheless, the temperature increase and the flow conditions ensure fast light-off and high conversion efficiency.

On the DPF side, the post-turbo placement has shown a worse behaviour than the pre-turbo concerning engine fuel consumption penalty. This penalty is increasing as the monolith volume decreases being specially damaging under soot loading conditions. Results confirm theoretically that the general rule of DPF volume being at least equal to the engine displacement works right.

The analysis has revealed that as volume reduces the pressure drop performance can be recovered increasing the cell density, i.e. filtration area. Since in post-turbo DPF placement the average soot loading is expected to be high, problems regarding inlet channels plugging may also arise as the cell density is increased. Results on optimum cell density have shown that the value resulting in minimum pressure drop reduces as permeability and monolith length increase. Other approaches to reduce the optimum cell density could be devoted to increase the filtration area, for example through TIF increase. It also improves

the strain tolerance but may damage MIF. These solutions are also available for pre-turbo DPF placement.

The results obtained with pre-turbo DPF placement have confirmed the lower pressure drop caused by the DPF in this location and how the differences positively grow as the DPF gets loaded. The fuel consumption is scarcely sensitive to volume and soot loading changes because of the pressure drop location with respect to the turbine.

From a fluid-dynamic point of view, it has been shown that the DPF volume may be reduced more than 40% in pre-turbo placement. This reduction would not have effect on fuel economy under clean DPF conditions. Under soot loading operation the fuel consumption would be the same of the reference volume in post-turbo architecture. As in post-turbo DPF placement, if the cell geometry is modified to keep constant the filtration area the benefits in pressure drop reduction lead to almost constant fuel consumption independently of the monolith volume. Channel plugging issues due to high cell density could be the limit of this solution. Nevertheless, soot loading in pre-turbo DPF configuration is expected to be low because of the high temperature. Therefore, a balance solution between constant specific filtration area and constant filtration area should exist. It should provide safe DPF operation and lower pressure drop with minimum fuel consumption penalty. It is also important to consider that the increase of filtration area can be obtained keeping the mechanical performance of the monolith but increasing heat transfer and losses, i.e. LOF and HTP. These last items must be considered in pre-turbo aftertreatment applications because of the effect on the turbocharger lag under cold wall operating conditions.

Pre-turbo DPF configuration insensitivity to soot loading is also applicable to ash loading. The DPF volume reduction is also directly reducing the volume for ash accumulation. However, the lack of DPF loading influence on engine performance may result in the increase of the critical ash mass able to be accumulated per unit of volume. The advantages in pressure drop also highlight the interest in asymmetrical cell designs because of the additional ash loading capability benefits. Consequently, volume reduction and a suitable design of the cellular geometry may provide improved fluid-dynamic response with good thermal, mechanical and ash loading performance. Therefore, a margin for important DPF volume reduction can be still attainable preserving engine and DPF performance.

Concerning the DPF capacity of retaining particles the pre-turbo configuration provides higher filtration efficiency both for clean and low soot loading compared with post-turbo location. This is due to the lower Peclet number upstream of the turbine. As a consequence, tailpipe emitted particle mass and number before convergence to maximum filtration efficiency would be lower in pre-turbo DPF configurations.

The above described potential for DPF downsizing of pre-turbo DPF configuration based on fluid-dynamic criteria (engine fuel economy reduction) is strengthened by the fact that the monolith volume can be also reduced around 40% within a wide range of meso-geometry definitions improving the filtration performance with respect to post-turbo placement.

As for the pressure drop, volume reduction at constant specific filtration area, i.e. constant cell density, has revealed to be more prejudicial on the filtration efficiency than volume reduction at constant filtration area. Nevertheless the resulting value after a 33% monolith volume downsizing at constant SFA in pre-turbo case is still equal to the baseline one in post-turbo location. TIF is shown to be a second-order parameter on filtration efficiency and must be set based on pressure drop and thermo-mechanical resistance criteria. Consequently, this kind of strategy keeps the original DPF filtration performance with improvements in pressure drop (bsfc) and cost-savings in materials. The opposed strategy is to reduce the monolith volume keeping constant the filtration area at the same time TIF is also kept. The advantage is that the filtration efficiency keeps the same value as in baseline volume, both in pre- and post-turbo DPF placement. It is added to the benefits in pressure drop related to constant filtration area.

The above analysed possibility of reducing the aftertreatment systems volume in pre-turbo placement also has a strong influence on the final engine price. Considering a DOC volume downsizing close to 40% (from 1.73 to 1.09 litres) and a DPF one around 33% (from 2.43 to 1.57 litres) it was estimated a 13.3% cost saving on the whole Euro 6 aftertreatment price. In the final analysis this leads, assuming that the aftertreatment represents around 30% of the engine final price, to a 4% cheaper engine.

Although the reduction of the aftertreatment thermal inertia improves the DPF and DOC thermal transient, the engine response under transient operation with cold wall conditions has been shown to be extremely poor in single stage turbocharged engines. This is the main drawback concerning pre-turbo aftertreatment architectures, which demands two-stage turbocharged solutions or the use of superchargers combined with a proper boost control as strategy to keep engine drivability. It increases the packaging complexity of the exhaust line but would take out the advantages of this placement in terms of engine fuel economy and aftertreatment performance.

4.8 References

[10] J. R. Serrano, F. J. Arnau, P. Piqueras, and O. García-Afonso. “Packed bed of spherical particles approach for pressure drop prediction in wall-flow DPFs (diesel particulate filters) under soot loading conditions”. In: *Energy* 58 (2013), pp. 644–54 (cit. on pp. 3, 15, 17, 19, 63, 71, 73, 82, 87, 167).

[21] B. Carberry, G. Grasi, S. Guerin, F. Jayat, and R. Konieczny. “Pre-turbocharger Catalyst - Fast catalyst light-off evaluation”. In: *SAE Technical Paper 2005-01-2142*. 2005 (cit. on pp. 4, 121).

[27] *OpenWAM website, CMT - Motores Térmicos (Universitat Politécnica de Valéncia).* www.openwam.org. 2016 (cit. on pp. 16, 112).

[28] J. Galindo, J. R. Serrano, F. J. Arnau, and P. Piqueras. “Description and analysis of a one-dimensional gas-dynamic model with Independent Time Discretization”. In: *Proceedings of the ASME Internal Combustion Engine Division 2008 Spring Technical Conference ICES2008*. 2008 (cit. on pp. 16, 22, 67, 112).

[29] A. J. Torregrosa, J. R. Serrano, F. J. Arnau, and P. Piqueras. “A fluid dynamic model for unsteady compressible flow in wall-flow Diesel particulate filters”. In: *Energy* 36 (2011), pp. 671–684 (cit. on pp. 16, 17, 36, 62, 63, 72, 81, 158).

[32] F. Payri, A. Broatch, J. R. Serrano, and P. Piqueras. “Experimental-theoretical methodology for determination of inertial pressure drop distribution and pore structure properties in wall-flow diesel particulate filters (DPFs)”. In: *Energy* 36 (2011), pp. 6731–6744 (cit. on pp. 17, 18, 78, 125, 198).

[56] T. Bollerhoff, I. Markomanolakis, and G. Koltsakis. “Filtration and regeneration modeling for particulate filters with inhomogeneous wall structure”. In: *Catalysis Today* 188 (2012), pp. 24–31 (cit. on pp. 28, 138).

[75] G. Merkel, D. Beall, H. D.L., and V. M. J. “Effects of microstructure and cell geometry on performance of cordierite Diesel Particulate Filters”. In: *SAE Technical Paper 2001-01-0193*. 2001 (cit. on pp. 32, 34, 121, 124).

[80] C. D. Depcik and A. J. Hausmann. “Review and a methodology to investigate the effects of monolithic channel geometry”. In: *Journal of Engineering for Gas Turbine and Power* 135 (2013), pp. 032301 1–16 (cit. on pp. 34, 35, 38, 128).

[93] S. Gulati. “Cell design for ceramic monoliths for catalytic converter application”. In: *SAE Technical Paper 881685*. 1988 (cit. on pp. 35–37, 169).

[96] A. G. Konstandopoulos, E. Skaperdas, J. Warren, and R. Allansson. “Optimized filter design and selection criteria for continuously regenerating Diesel particulate traps”. In: *SAE Technical Paper 1999-01-0468*. 1999 (cit. on pp. 38, 128).

[97] A. G. Konstandopoulos and E. Kladopoulou. “The optimum cell density for wall-flow monolithic filters: effects of filter permeability, soot cake structure and ash loading”. In: *SAE Technical Paper 2004-01-1133*. 2004 (cit. on pp. 38, 128).

[98] S. J. Lee, S. J. Jeong, and W. S. Kim. “Numerical design of the diesel particulate filter for optimum thermal performances during regeneration”. In: *Applied Energy* 86 (2009), pp. 1124–1135 (cit. on pp. 38, 128).

[102] S. Bardon, B. Bouteiller, N. Bonnail, P. Girot, V. Gleize, L. Oxarango, P. Higelin, J. Michelin, S. Schuerholz, and F. Terres. “Asymmetrical channels to increase DPF lifetime”. In: *SAE Technical Paper 2004-01-950*. 2004 (cit. on pp. 38, 138).

[109] M. N. Subramaniam, V. Joergl, P. Keller, O. Weber, T. Toyoshima, and C. D. Vogt. “Feasibility assessment of a pre-turbo after-treatment system with a 1D modeling approach”. In: *SAE Technical Paper 2009-01-1276*. 2009 (cit. on pp. 40, 176).

[110] V. Joergl, P. Keller, O. Weber, K. Mueller-Hass, and R. Konieczny. “Influence of pre turbo catalyst design on diesel engine performance, emissions and fuel economy”. In: *SAE Technical Paper 2008-01-0071*. 2008 (cit. on pp. 40, 121).

[114] J. M. Lújan, V. Bermúdez, P. Piqueras, and O. García-Afonso. “Experimental assessment of pre-turbo aftertreatment configurations in a single stage turbocharged Diesel engine. Part 1: Steady-state operation”. In: *Energy* 80 (2015), pp. 599–613 (cit. on pp. 40, 113, 133, 135, 141, 156).

[116] J. M. Lújan, J. R. Serrano, P. Piqueras, and O. García-Afonso. “Experimental assessment of a pre-turbo aftertreatment configuration in a single stage turbocharged Diesel engine. Part 2: Transient operation”. In: *Energy* 80 (2015), pp. 614–627 (cit. on pp. 41, 113).

[117] V. Bermúdez, J. R. Serrano, P. Piqueras, and O. García-Afonso. “Analysis of heavy-duty turbocharged diesel engine response under cold transient operation with a pre-turbo aftertreatment exhaust manifold configuration”. In: *International Journal of Engine Research* 14.4 (2013), pp. 341–353 (cit. on pp. 41, 127, 173).

[120] V. Bermúdez, J. R. Serrano, P. Piqueras, and O. García-Afonso. "Influence of DPF soot loading on engine performance with a pre-turbo aftertreatment exhaust line". In: *SAE Technical Paper 2012-01-0362*. 2012 (cit. on pp. 42, 136, 141).

[128] J. M. Desantes, F. Payri, J. R. Serrano, and P. Piqueras. *Device for treating exhaust gases from diesel turbo-supercharged reciprocating internal combustion engines (RICE)*. Patent WO 2013/041747 A1. Priority date 23/09/2011. European Patent Office. 2013 (cit. on pp. 43, 44, 113).

[151] F. Posada, A. Bandivadekar, and J. German. "Estimated cost of emission control technologies for light-duty vehicles. Part 2 - Diesel". In: *SAE Technical Paper 2013-01-0539*. 2013 (cit. on pp. 112, 133, 172).

[152] *U.S. Environmental Protection Agency (EPA) and U.S. National Highway Traffic Safety Administration (NHTSA). Final rulemaking to establish standards and corporate average fuel economy standards, Joint technical support document. U.S. EPA - Office of International Policy, Fuel Economy and Consumer Programs.* 2010 (cit. on p. 112).

[153] *U.S. National Academy of Sciences (NAS), Assessment of fuel economy technologies for light-duty vehicles, The National Academic Press: Washington D.C.* 2011 (cit. on p. 112).

[154] F. Mallamo, S. Longhi, F. Millo, and L. Rolando. "Modeling of Diesel Oxidation Catalysts for calibration and control purpose". In: *International Journal of Engine Research* 15 (8) (2014), pp. 965–979 (cit. on p. 119).

[155] C. Seman. *http://www.wisegeek.com/what-is-space-velocity.htm*. 2016 (cit. on p. 119).

[156] E. Dawson and J. Kramer. "Faster is Better: The Effect of Internal Turbulence on DOC Efficiency". In: *SAE Technical Paper 2006-01-1525*. 2006 (cit. on p. 120).

[157] V. Bermúdez, J. R. Serrano, P. Piqueras, and O. García-Afonso. "Assessment by means of gas dynamic modelling of a pre-turbo diesel particulate filter configuration in a turbocharged HSDI diesel engine under full-load transient operation". In: *Proceedings of the Institution of Mechanical Engineers, Part D: Journal of Automobile Engineering* 225 (9) (2011), pp. 1134–1155 (cit. on p. 132).

[158] M. N. Subramaniam, C. Hayes, D. Tomazic, M. D. M., and C. Bruestle. "Pre-Turbo aftertreatment position for large bore Diesel engines - Compact and cost-effective aftertreatment with a fuel consumption advantage". In: *SAE International Journal of Engines* 4(1) (2011), pp. 106–116 (cit. on p. 173).

CHAPTER 5

Soot deposition analysis

Contents

Figures

Tables

5.1 Introduction

EXPERIMENTAL measurements of soot thickness at different DPF channel axial [159] and radial [160] positions evidenced a non-homogeneous soot deposition. It is known that this non-homogeneous spatial distribution of soot [11] and ash [12] [161] has strong influence on the filter performance. Also the microstructural properties, i.e. soot packing density and porosity, of the soot layer are considered to affect the generated pressure drop [13] [14]. Concerning the oxidation characteristics, Bagi *et al.* [162] found a correlation between the soot composition and the accumulated vehicle mileage and the ease of oxidation of the particle layer.

In the present chapter the effect of soot deposition variation inside the channels of a wall-flow DPF is analysed by means of experimental procedures and advanced optical techniques. Two different manners of modifying the particles deposition have been considered.

In one case the particle deposition has been altered by means of a water injection at the DPF inlet, i.e. it is an instantaneous action carried out once the particles have deposited. It has been shown in Section 2.6 that this technique leads to the reduction of the pressure drop generated by a soot loaded DPF. This behaviour is considered to be related with the capacity of the water droplets of dragging the soot towards the rear end of the inlet channels, generating regions of reduced particulate layer thickness. The result is the reduction of the engine back-pressure with the consequent bsfc decrease. In Chapter 4 it has been stated that the risk of inlet channels clogging at high soot or ash loadings could be increased when the DPF volume is reduced. Also, from Chapters 3 and 4 it resulted clear that placing the DPF upstream of the turbine leads to lower axial and filtration velocities, hence Peclet numbers. Konstandopoulos *et al.* [13] [163] stated that the Peclet number is a key parameter determining the resulting structure of the deposited particulate layer. It strongly affects the particle layer porosity, packing density and permeability. Authors found that the particulate layer porosity increases as the Peclet number decreases. As a result the soot packing density in the layer decreases. Similar results were found some years later by Koltsakis *et al.* [159] who investigated the parameters affecting the soot morphology by collecting real Diesel soot in single DPF channels. Authors obtained density values comprised between 25 and 100 kg/m^3 depending on flow velocity, pressure drop and soot loading. It corresponds to a porosity between 95% and 98.75% assuming the bulk soot density to be 2000 kg/m^3. It was observed a general trend of increasing porosity as the filtration velocity was lowered. In a more recent work Liu *et al.* [14] stated that the Peclet number can be a predictor of the porosity value for nanoparticles aggregate cakes. The lower particle layer density leads to thicker layer which in turn increases the risk of inlet channels clogging. The coupling of the pre-DPF water injection technique

with the filter volume downsizing would result very useful to limit the risk of inlet channels clogging.

The second analysed manner of modifying the particles deposition is by acting on the inlet DPF Peclet number. It has been reduced acting on the mass flow in the engine test bench. Contrarily to the water injection, it is a continuous action throughout the whole soot loading process. In this way it has been possible to evaluate the effect of a low Peclet number, characteristic of the pre-turbo DPF positioning as demonstrated in Chapters 3 and 4, on the soot particles deposition dynamics.

5.2 Methodology and experimental facilities

The same experimental facilities have been used in both the considered strategies aimed to the modification of the particles deposition. They are described in detail in the next sections.

The availability of 4 identical DPFs, whose main characteristics are summarized in Table 5.1, made possible to run several tests to evaluate the effects of the pre-DPF water injection technique and of the inlet DPF Peclet number variation on the filter performance.

Table 5.1: Characteristics of tested DPFs.

Diameter	[mm]	140
Length	[mm]	230
Plug length	[mm]	5
Volume	[l]	3.46
Cell width	[mm]	1.423
Wall thickness	[mm]	0.458
Cell density	[cpsi]	180
Porosity	[-]	0.41
Mean pore diameter	[μm]	18.55

The performed tests are summarized in Table 5.2.

First tests are related with the pre-DPF water injection technique. DPF #1 has been loaded up to 49.6 g of soot performing 22 consecutive pre-DPF water injections throughout the loading process. Then it has been regenerated in controlled conditions and loaded again up to 44.6 g of soot in reference conditions, i.e. without pre-DPF water injection events. In both the tests engine and filter interesting magnitudes have been recorded for comparison. After the second soot loading test, DPF #1 has been divided into 4 quarters. Every single quarter sample has been weighted and its pressure drop has been measured in a flow test bench. Then 3 of the 4 samples were subjected to a single water injection in different conditions, i.e. varying the injected water mass and the air

Table 5.2: Tests list.

Test	DPF	Collected soot mass	Optical analysis
Soot loading with pre-DPF water injection in engine test bench	#1	49.6 g	N
Reference soot loading in engine test bench	#1	44.6 g	N
Quarter samples pre-DPF water injection in flow test rig	#1	44.6 g	Y
Soot loading at $Pe_{w_0} = 2756$ (reference)	#2	6.8 g	Y
Soot loading at $Pe_{w_0} = 1643$	#3	7.4 g	Y
Soot loading at $Pe_{w_0} = 1218$	#4	7.5 g	Y

mass flow at the moment of the injection, in the same flow test bench. The other quarter sample was kept as a reference for the optical analysis. Quarter samples have been weighted again to confirm the lack of soot release during the injection and their pressure drop has been measured again in the flow test rig. Finally the quarter samples have been cut at different axial positions and optically analysed with an optical microscope and a scanning electron microscope (SEM).

Second session of tests is devoted to the characterization of the effect of the inlet DPF mean Peclet number variation on the filter performance, i.e. filtration efficiency and generated pressure drop. As commented in Section 5.1, positioning the DPF upstream of the turbine leads to lower filtration velocity, hence lower Peclet number at constant porous wall microstructure. DPF #2 has been loaded up to 6.8 grams of soot mass in reference Peclet conditions, i.e. 100% of the engine exhaust gas flow through the filter. DPF #3 and #4 have been loaded up to a soot mass similar to DPF #2, 7.4 and 7.5 g respectively, at a lower Peclet number. To decrease the Peclet number without affecting the engine raw emissions part of the exhaust gas flow was bled to a secondary line as it will be described in more detail in Section 5.2.1. Again the pressure drop generated by the 3 filters has been characterized in the flow test bench at different inlet temperature and air mass flow. Finally the DPFs have been cut at different axial positions and optically analysed with a scanning electron microscope (SEM) looking for differences in particle layer thickness and/or morphology.

5.2.1 Engine test bench

The exhaust line of a conventional engine test bench was adapted to provide the possibility of varying the Peclet number at the inlet of the DPF by means of filter inlet mass flow variations independently of the engine operating point. A scheme of the engine test bench is showed in Figure 5.1. Black circles in the scheme indicate the measurement location of the variables of interest. Focusing on the DPF, inlet and outlet temperature and pressure were measured. Also, soot particles concentration in both number and mass basis was measured upstream and downstream of the filter.

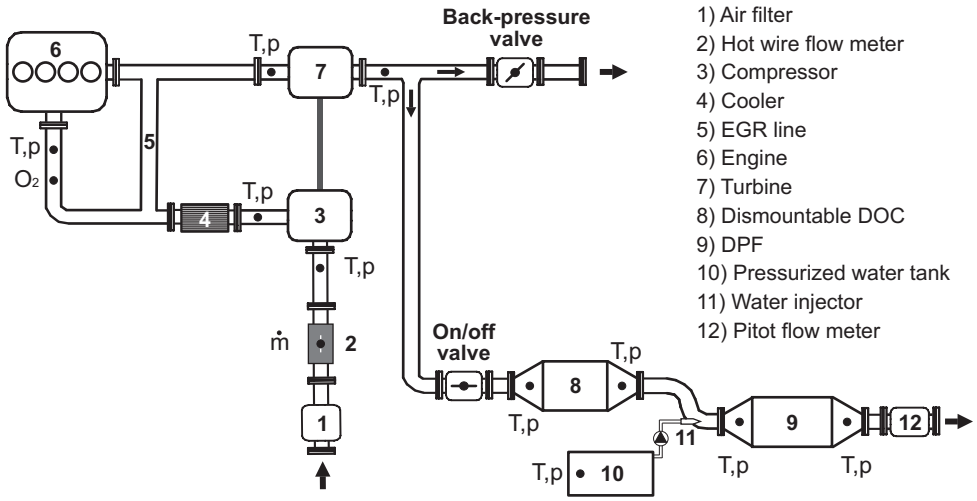

Figure 5.1: Scheme of the designed engine test bench.

As showed in Figure 5.1, the exhaust line is split in two parallel lines. In one a back-pressure valve is placed. Upstream the aftertreatment is mounted an on/off valve. By opening this valve and changing the position of the back-pressure valve different percentages of the engine exhaust gas are made to flow through the aftertreatment. The second line hosts the aftertreatment (DOC&DPF). Downstream of these systems is mounted the Pitot flow meter of the Horiba OBS-2200; in this way it was possible to monitor the engine exhaust gas flowing through the aftertreatment. Figure 5.2(a) shows the two valves: the back-pressure (vertical) and the on/off (horizontal). In the pictures in Figure 5.2(b) and (c) can be seen the aftertreatment line partially insulated to avoid heat losses downstream of the turbine and the void space where the DPF is placed. It can be also seen that the DOC was replaced by a bent duct. In all the soot loading processes the DOC was removed to avoid passive regeneration by NO_2. Every time the filter had to be regenerated the DOC was mounted again in

the aftertreatment line and a post injection was imposed. Finally, Figure 5.2(d) shows the intake with its filter and the extractor where the two exhaust lines converge.

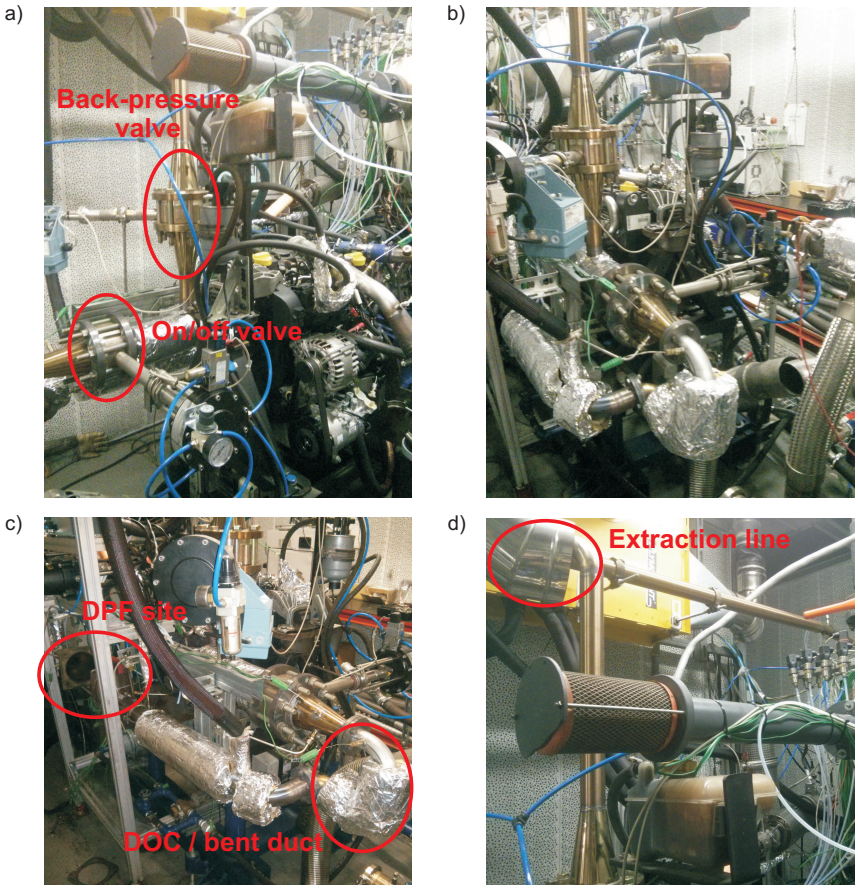

Figure 5.2: Pictures of the engine test bench.

Concerning the injected fuel mass, it was monitored in two manners. On one hand the ECU provided measures of the injection strategy, hence injected fuel mass in pilot, main and post injection (if any) in mg/cc. On the other hand the use of an AVL 733S fuel balance permitted the measure of the total injected mass in kg/h. The agreement between the two measures has been checked.

A SCHENCK W230 dynamometer, able to control engine speed and torque under steady-state and transient operating conditions, was coupled with the engine. In the specific a passenger car Diesel engine, whose characteristics are detailed in Table 5.3, was used to perform the tests. The engine was controlled

by a partially open electronic control unit (ECU). Consequently some of the engine settings maps could be recalibrated using the ETAS INCA software.

Table 5.3: Engine #3 specifications.

Type	dCi Diesel engine
Injection system	Common rail
Turbocharger	VGT
Displacement	1461 cm^3
Bore	76 mm
Stroke	80.5 mm
Cylinders number	4
Valves number	4 per cylinder
Compression ratio	1:15.3
Maximun power	77 kW at 4000 rpm
Maximun torque	240 Nm at 2000 rpm

In the scheme of Figure 5.1 the pressurized water tank used to perform the pre-DPF water injections is also showed. A 4 mm diameter simple calibrated orifice nozzle was placed in the inlet DPF cone. The nozzle was coupled with the water tank whose pressure was set by a pressure regulator connected with the facility pressurized line. Injected water mass is controlled by means of an electronic valve coupled with an analogical timer which control the injector opening time.

Concerning the particles concentration in the exhaust gas, it was measured with 2 different equipments: the TSI EEPS-3090 (engine exhaust particle sizer) spectrometer and the TSI DCS-100 (diffusion charging sensor) module of the Horiba 1230-PM (particle mass analyzer). The first provides fast response in particle concentration changes measuring the PSD in particles number per cubic meter within the range 5.6-560 nm with a frequency of 1 Hz [164]. The second equipment measures the particles length in real-time in mm/cm^3 and converts it in mg/m^3 with an inner calculation [165]. The above mentioned equipments were connected to a Dekati FPS-4000 dilution system [166]. The methodology used to measure the particles concentration is the one proposed by Desantes *et al.* [144]. Figure 5.3 shows the two stages of the exhaust dilution. At first is performed an isothermal dilution in the porous tube primary diluter (PTD). The aim is to reduce the volatile mass fraction avoiding the risk of nucleation at low temperature. In the second dilution the sample temperature is reduced in an ejector (ED). In this way the volatile mass fraction is further reduced and the evaporation at high temperature is avoided.

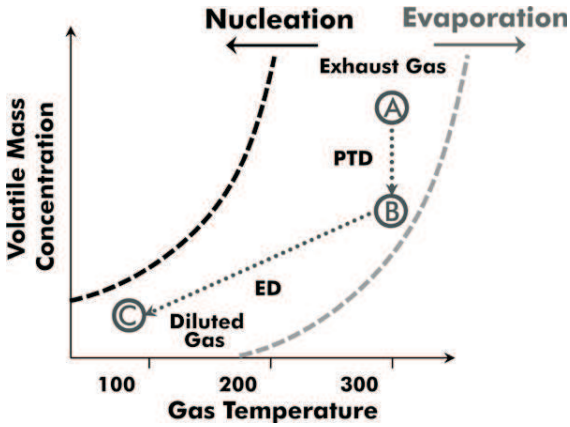

Figure 5.3: Particle evolution through the dilution system. Theoretical phase diagram used in the methodology for particle size distribution measuring [167].

As shown in Figure 5.4, the dilution system was connected to a pneumatic valve system allowing the measurement upstream and downstream of the DPF. The downstream exhaust gas particles concentration was continuously measured up to reach complete stabilization. Then the valves position was changed and the upstream exhaust gas particles concentration was measured for 120 seconds. The mean value through the 120 seconds was assumed to be representative of the raw emission at the DPF inlet during the whole test. Knowing the temperature and pressure, hence density, in the probing point it was possible to transform the measured values in soot particles mass flow in mg/s (from the TSI DCS-100 measure) and soot particles number flow in #/s (from the EEPS measure). Thus it has been possible to calculate the DPF filtration efficiency from the upstream / downstream difference on both number and mass basis.

As stated above the presence of the back-pressure valve and the Pitot flow meter provides the possibility of regulating the engine exhaust mass flow through the aftertreatment line.

The control of the mass flow through the aftertreatment makes possible to vary the filtration velocity, hence the Peclet number, without affecting the engine operating point and the particulate emission. On the other hand this technique makes possible to avoid undesired soot loading during the engine stabilization in the required operating point as during this phase no exhaust gas is made to flow through the aftertreatment line.

The selected engine operating point for the soot loading tests was 2250 rpm and 50 Nm torque. The original injection strategy of the selected engine point

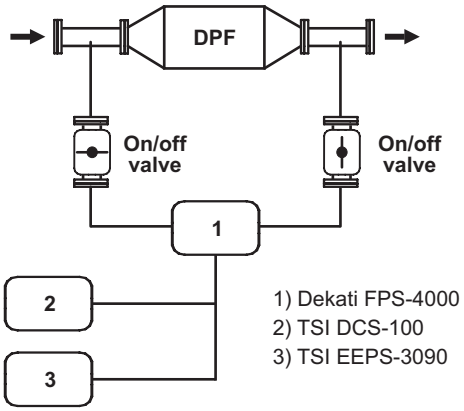

Figure 5.4: Scheme of the valves system for upstream/downstream DPF particles concentration measurement.

was a pilot injection of 1.3 mg/cc at -26.5 cad before top dead centre (BTDC) and a main injection of 8.7 mg/cc with a SoI (start of injection) of 8.55 cad after top dead centre (ATDC). A sweep in the SoI angle of the main injection was made looking for the increase of particles emission in order to achieve faster soot loading processes. Figure 5.5(a) and (b) show that as the SoI of the main injection is advanced, i.e. the main injection gets nearer to the pilot injection, particles emission in both number and mass basis increases. This trend has been measured with both the equipments used to evaluate the particle concentration, i.e. the EEPS-3090 spectrometer and the DCS-100. Only a slight difference can be observed between the values corresponding to 4.55 and 6.55 cad. Also, Figure 5.5(c) points out that a small decrease of the inlet DPF temperature takes place. It is of great interest as it reduces the risk of undesired passive filter regeneration. Finally, Figure 5.5(d) represents the engine exhaust mass flow which presents negligible variations when the SoI angle is changed.

The increase in soot emissions as the main injection gets nearer to the pilot injection is related with the reduction of the LOL (lift-off length), i.e. the location downstream of the fuel injector where the reaction zone of a diesel fuel jet stabilizes once the initial autoignition phase is over [168]. As a result the flame is initially developed in a richer zone, i.e. at higher fuel-air ratio, increasing the amount of soot precursor formation [169] [170]. Similar results were found by Desantes *et al.* [171] in the study of post-injections effects on combustion and emissions.

At the end of the sweeping process it was defined the engine operating point for all the soot loading processes considered in this chapter. Its main characteristics are summarized in Table 5.4. Highlight that all the soot loading

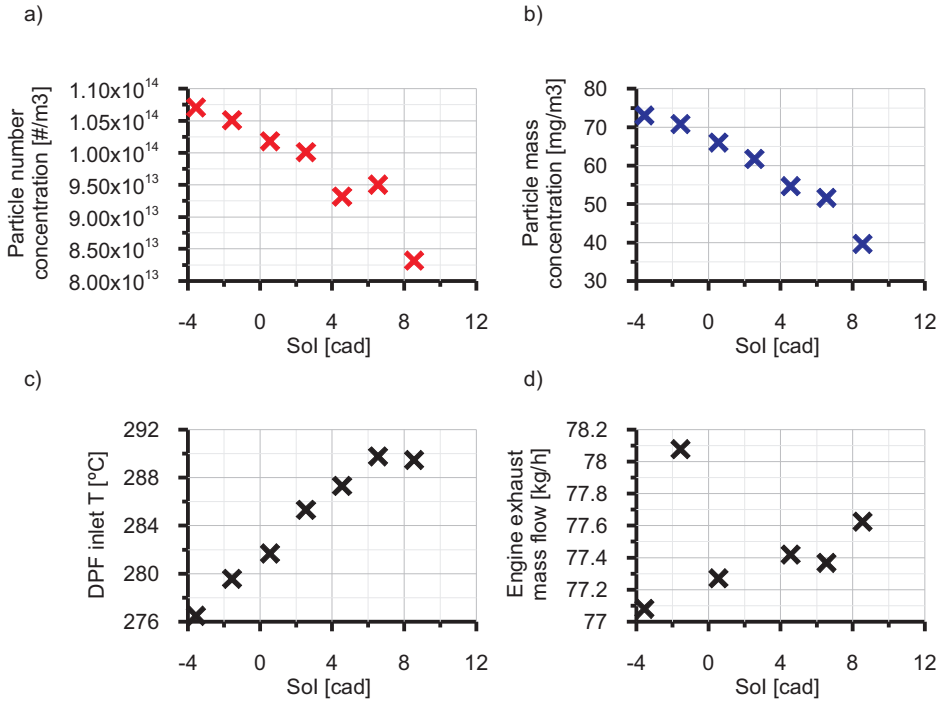

Figure 5.5: Effect of the SoI angle on particles emission and DPF inlet temperature.

tests have been performed at constant injected fuel mass. As a result the effect of the back-pressure increase, related with the DPF pressure drop increase, on the engine performance appears in terms of torque decrease rather than fuel injected mass increase.

Table 5.4: Engine operating point for soot loading tests.

Torque	[Nm]	50
Engine speed	[rpm]	2250
Air mass flow	[kg/h]	75
Total injected fuel mass	[kg/h]	2.7
Pilot injection fuel mass	[mg/cc]	1.3
Pilot injection SoI	[cad]	-26.5 BTDC
Main injection fuel mass	[mg/cc]	8.7
Main injection SoI	[cad]	-3.55 BTDC
DPF inlet T	[°C]	277

On the other hand the selected engine operating point to regenerate the filters was 2250 rpm and 65 Nm. As stated before when the filters had to be regenerated the DOC was mounted back in the aftertreatment line. In this operating conditions a post-injection of 10 mg/cc at 66 cad ATDC was manually imposed to the ECU to increase the DPF inlet temperature. Thus, the engine exhaust gas flow is 147 kg/h and the DPF outlet temperature 600°C, what guarantees complete soot oxidation in a reasonable time.

5.2.2 Flow test bench

As stated in the introduction of the present chapter, the pressure drop of the analysed filters and quarter filter samples has been characterized at different mass flow in a flow test bench available in the facilities of the CMT-Motores Termicos [32].

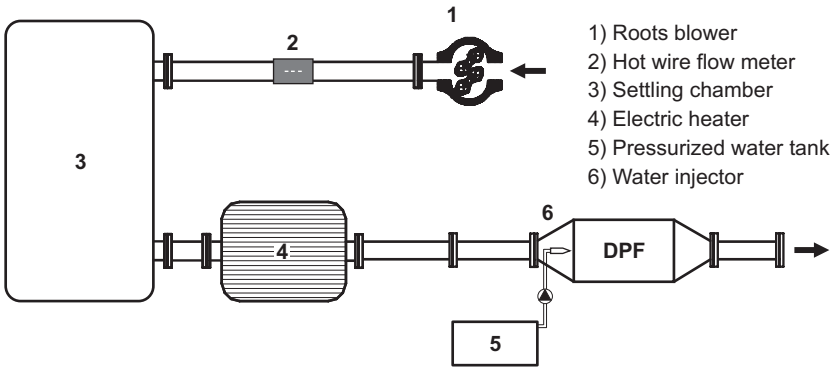

Figure 5.6: Scheme of the flow test bench.

Figure 5.6 shows a scheme of the set-up used for the tests. Ambient air at room temperature is made to flow through the filter by means of a roots blower. To take into account the effect of the temperature on the generated pressure drop and perform the tests in conditions similar to real engine ones, an electrical heater was placed upstream of the filter, providing the possibility of regulating the inlet DPF temperature. Thus the DPFs and quarter samples pressure drop was measured at temperature comprised between 20°C and 200°C. Temperature was not further increased to avoid the risk of undesired soot oxidation. The flow temperature is controlled with a PID controller connected to a thermocouple at the DPF inlet that regulates the electric heater power. The air mass flow is measured with an hot wire flow meter mounted upstream of a settling chamber. The differential pressure across the filter was measured with a water or mercury column in case or low/medium or high pressure drop

values respectively. In both the pre-DPF water injections (DPF #1 in Table 5.2) and inlet DPF mean Peclet variation tests (DPFs #2, #3 and #4 in Table 5.2) the pressure drop measures have been taken when the thermal transient of the monolith had ended, i.e. when the outlet DPF temperature reached a stationary value. This is of particular importance in the tests in which a water injection was performed at the DPF inlet. The injections were always performed with an air flow temperature of 200°C to simulate real in-engine conditions and achieve real evaporation conditions after the injection. The water at room temperature cools down the monolith that in turn cools the gas flow finally leading to a lower pressure drop measure. To avoid the effect of the cooling on the pressure drop, measures were taken after the monolith thermal transient was completed.

To conclude, testing the quarter filter samples in the flow rig required the design and construction of a special support. Figure 5.7(a) represents a scheme of the support, Figures 5.7(b) and (c) show a frontal view of the support and its installation in the flow test bench.

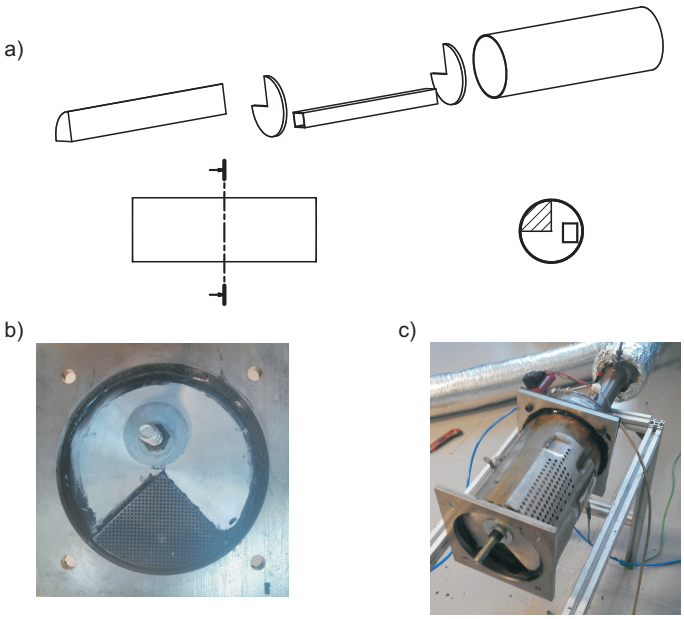

Figure 5.7: Scheme and pictures of the designed support for quarter filter samples testing in the flow test bench.

The monolith of DPF #1 was mechanically extracted from the canning with a press and divided into 4 quarters. Every quarter sample has been placed back into the canning, properly modified as shown in Figure 5.7. The support has

been sealed and mounted in the flow test bench to measure the pressure drop generated by every quarter sample.

5.2.3 Scanning Electron Microscope (SEM)

After the characterization of the DPFs and quarter samples pressure drop in the flow test bench, all the samples have been cut and optically analysed with a scanning electron microscope (SEM) available at the electron microscopy service of the UPV. A JEOL JSM-6300 SEM with an Oxford Instruments x-rays analyser, shown in Figure 5.8(a), coupled to the INCA software of Oxford Instruments for data acquisition and post-processing, has been used.

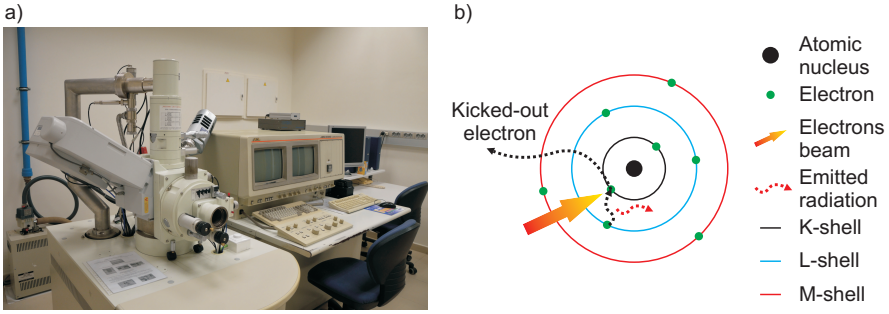

Figure 5.8: a) Picture of the SEM available at the UPV. b) Working principle scheme.

The scanning electron microscope is a type of electron microscope that permits the observation and characterization of heterogeneous organic and inorganic materials on a nanometer (nm) to micrometer (μm) scale [172]. According to McMullan [173] [174] the technique was developed by Manfred von Ardenne who invented a microscope with high magnification by scanning a very small raster with a demagnified and finely focused electron beam [175].

In the SEM, the area to be analysed is irradiated with a finely focused electron beam. The beam may be swept across the surface of the specimen in case an image is desired or may be static to obtain an analysis at a certain position. The interaction of the electrons beam and the sample produces several kind of signals including: secondary electrons (SE), backscattered electrons (BSE) and characteristics x-rays.

Secondary electrons are ejected from the k-shell, i.e. the innermost one closer to the nucleus, of the specimen atoms as a result of the interaction with beam electrons. They vary primarily as a result of differences in the sample surface topography. As a result, after proper detection and post-processing,

secondary electrons can provide images of the sample surface with resolution up to less than 0.5 nm.

On the contrary, backscattered electrons consist of high-energy electrons originating in the electron beam that are reflected or back-scattered out of the sample interaction volume by elastic scattering interactions with sample atoms. Heavy elements with high atomic number backscatter electrons more strongly than light elements, i.e. low atomic number, thus appearing brighter in the image. As a consequence, backscattered electrons are used to detect contrast between areas with different chemical compositions [176].

Finally, the emitted x-rays are a result of the electron bombardment. The external stimulation, i.e. the electron beam, excites an electron in an inner shell, kicking it out from the shell and creating an electron hole. Another electron from an outer, higher energy level fills this hole. The energy gap between the two shells is released in the form of an x-ray. The energy of the emitted x-ray is characteristic of the atomic structure of the emitting element and of the energy gap between the two shells. Thus electron replacement from shell L to K is named K-α peak, M to K is named K-β peak and M to L is named L-α peak. The analysis of the characteristics emitted x-radiation yield both qualitative identification and quantitative elemental information [172].

5.2.4 Digital microscope

In order to run a more macroscopical analysis to complement the information acquired with the SEM, a PCE-MM200 digital microscope has been used. This microscope provides the possibility of taking images and videos up to 200 magnification, i.e. of the order of magnitude corresponding to the monolith cell dimension. The microscope has been mounted on a guide system connected with two digitally controlled electric actuators that permit the precise motion of the microscope in 2 directions, covering the whole cross-section area of the monoliths and monolith quarters (Figure 5.9). The system was connected to a computer to control the actuators and take, store and post-process the images. In this way it has been possible to take a great number of monolith cells' pictures at different axial and radial positions.

Finally, additional pictures of the whole frontal sections of the quarter filter samples obtained from DPFs #1 and of the entire DPFs #2, #3 and #4 have been taken with a digital camera Nikon D3200.

5.3 Pre-DPF water injection analysis

The effect of the pre-DPF water injection has been assessed both in the engine test bench, i.e. performing several water injections throughout a soot loading process, and in the flow test rig, i.e. performing a single water injection on

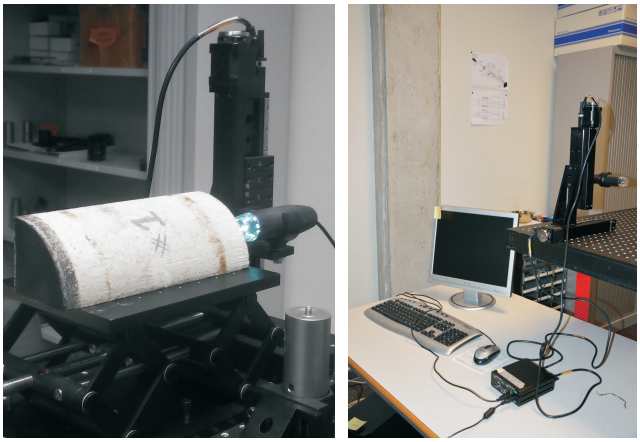

Figure 5.9: Pictures of the PCE-MM200 digital microscope mounted on the guide system.

quarter filter samples. In the first case the DPF has been loaded up to 49.6 g in the engine operating point described in Table 5.4. Throughout the soot loading process the filter was subjected to 22 water injections, starting when 12.6 soot grams were accumulated inside the filter. In the second case the DPF has been loaded up to 44.6 g in nominal conditions, i.e. without water injections, in the same engine operating point. The two soot loading processes are compared in the following sections to analyse the effect of the water injections. At the end of the reference soot loading process the filter was divided into 4 identical samples. One quarter sample was kept as reference and the others 3 were subjected to one single water injection varying the water mass flow and the air mass flow at the moment of the injection.

5.3.1 Assessment of pressure drop reduction

5.3.1.1 Engine test bench injections

Figure 5.10(a) shows a comparison of the evolution of the DPF pressure drop as soot is collected inside the filter between reference operating conditions (black line) and use of consecutive pre-DPF water injections (blue line). During both soot loading tests the engine was running in the operating conditions specified in Table 5.4. The first injection was performed when the collected soot mass was 12.6 g, corresponding to a pressure drop of 4000 Pa. The water tank pressure was set to 5 bar and the injection time was 2 seconds. As a result 152 grams of water per injection were used, that is, a water flow of 76 g/s. Considering the duration of the test and that 22 pre-DPF water injections with a mean time

span of 19 minutes have been performed, a mean water consumption of 366 g/h is calculated. As expected from [24] the DPF outlet temperature (red line in Figure 5.10) clearly shows that the pressure drop reduction is not related to the monolith cooling due to water injections. Indeed the thermal transient after every injection event lasts a negligible time compared with the time span between two consecutive injections. As the DPF outlet temperature recovers its nominal value, the pressure drop reduction is evident comparing to the reference soot loading test.

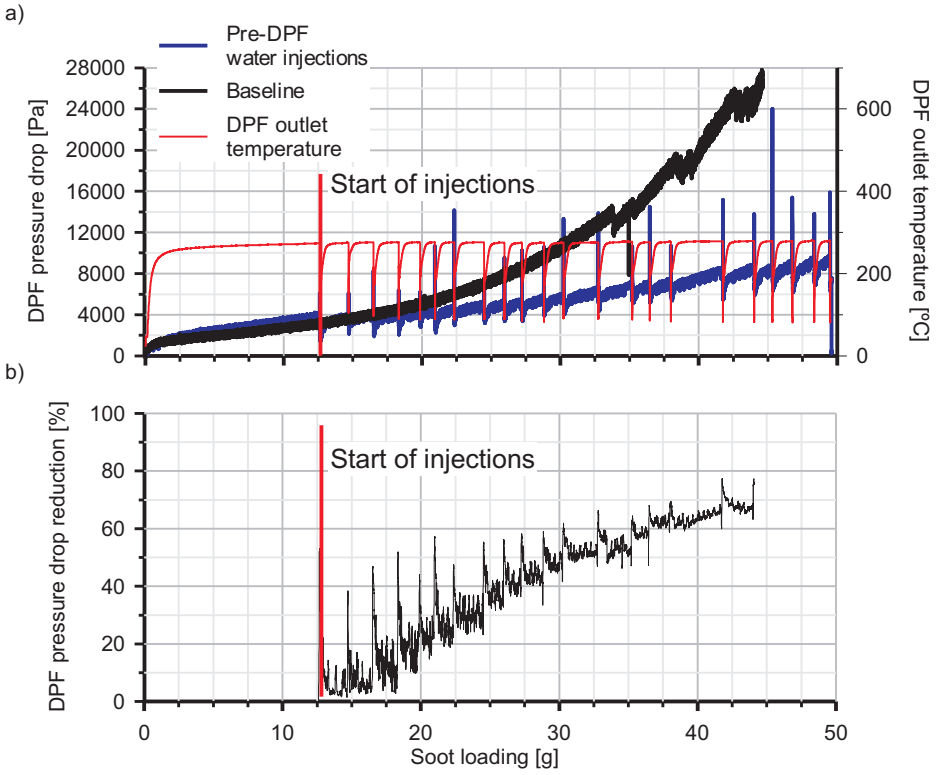

Figure 5.10: Comparison of DPF pressure drop with and without the pre-DPF water injection technique throughout the soot loading tests.

In Figure 5.10(b) the percentage pressure drop difference, calculated as:

$$\Delta p_{red} = \frac{\Delta p_{ref} - \Delta p_{wat}}{\Delta p_{ref}} 100 \tag{5.1}$$

is plotted. As soot is loaded, the percentage pressure drop difference between the two tests increases. It is due to the notable reference test pressure drop gain (black line) while in the case of consecutive pre-DPF water injections (blue line)

the pressure drop is way much less marked, increasing only 5000 Pa, i.e. from 4000 Pa to 9000 Pa, from the start of injections to the end of the soot loading process.

Comparing Figure 5.10 with Figure 2.14 it is possible to note that in this last case the pressure drop was maintained almost constant throughout the soot loading process. Despite this was not possible in the soot loading process showed in Figure 5.10, a notable DPF pressure drop reduction, on the order of 17000 Pa, was achieved at the end of the baseline soot loading process. The convex shape of the baseline test pressure drop curve showed in Figure 5.10 made impossible to precisely control the pressure drop despite the application of the pre-DPF water injection technique. Such a shape of the pressure drop curve can be confirmed by analysing Figure 5.11(b). It can be noted that the compressor inlet and outlet pressure are not affected by the increasing DPF pressure drop while in the case of the turbine the same convex shape showed in Figure 5.10 can be recognized. The turbine outlet pressure is directly set by the increasing DPF pressure drop. The turbine inlet pressure on the other hand is supposed to be set by the VGT closing governed by the electronic control unit. A similar pressure drop behaviour is also reported in the review of DPF design simulation performed by Yang *et al.* [177] in the case of a soot loading in g/l similar to the one considered in the present study, i.e. ≈ 13 g/l. Depcick and Assanis [145] hypothesized that the increase of the pressure drop curve slope with increasing soot loading is related to the effects of varying soot layer thickness on the flow area of the gases. The authors presented a pressure drop model that accounts for the effects of changing gaseous area in the inlet channel and varying cross-sectional area of flow through the soot layer. Thus the model calculates a velocity profile through the wall to account for the different surface areas in the inlet and outlet channels instead of using a one unique velocity value through either layer. According to the authors this effect becomes important starting from 8 g/l soot loading. In addition, the cross-sectional area reduction on one hand leads to higher axial velocity, what result in a linear increase of the friction pressure drop. On the other hand the smaller flow section leads to a square increase of the inertial pressure drop at the channel inlet (Section 2.2.2).

The effect of the DPF pressure drop increase on the engine is showed in Figure 5.12. Figure 5.12(a) shows that the back-pressure increase leads to a gradual penalization of the engine torque despite the same injected fuel mass. The result is the severe bsfc penalization showed in Figure 5.12(b). Despite the impossibility of keeping constant the DPF pressure drop to a desired value, the pre-DPF water injection technique leads to a considerable benefit in bsfc. Figure 5.12(b) shows a bsfc reduction close to 10% at the end of the baseline soot loading process. The reason lies in the notable decrease of the DPF pressure drop, hence engine back-pressure, resulting from the consecutive water injection. The application of the pre-DPF water injection technique reduces the filter

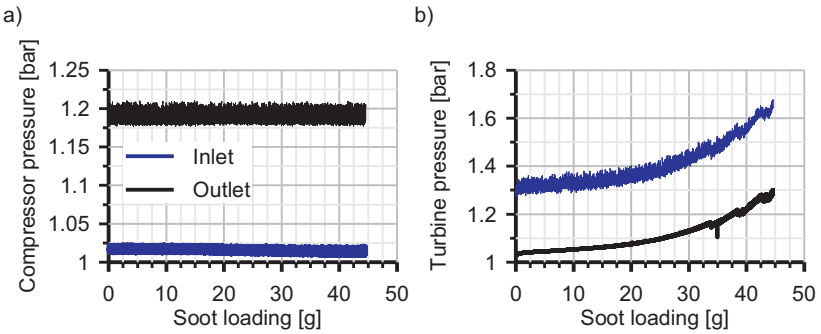

Figure 5.11: Turbo-compressor pressures evolution during the soot loading test without the pre-DPF water injection technique: a) compressor b) turbine.

pressure drop from 26000 Pa of the baseline test (black line in Figure 5.10) to 9000 Pa in the case of water injections (blue line in Figure 5.10) at the end of the soot loading process.

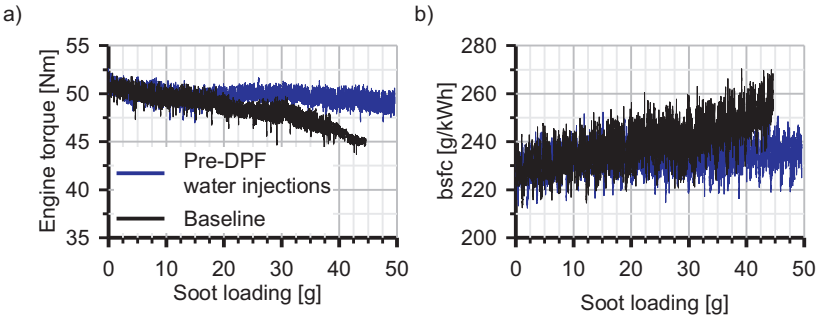

Figure 5.12: Comparison of engine torque and bsfc with and without the pre-DPF water injection technique during the soot loading tests.

5.3.1.2 Flow test bench injections

After the reference soot loading process, i.e. without water injections (black line in Figure 5.10), the monolith has been extracted from the canning and divided into 4 identical quarters. First of all every quarter sample has been weighted. Aim was to check the lack of soot release related to the water injection by comparing the quarters weight before and after the water injection. Then the generated pressure drop has been measured in the flow test bench described in Section 5.2.2. The pressure drop was measured at different air mass flows at

20°C and at 200°C inlet DPF temperature. For both the considered temperatures the roots blower power was gradually increased to raise the air mass flow and then decreased again to measure the pressure drop of every quarter sample twice. The repeatability of the pressure drop value guarantees that the increasing inlet pressure did not cause any particle layer detachment or compression (with the consequent density increase).

After these tests, three out of the four quarter samples have been subjected to a single pre-DPF water injection at different operating conditions, the last quarter has been kept as a reference for optical analysis. The operating conditions at the moment of every injection are detailed in Table 5.5. First injection (quarter #2) was performed at 35 kg/h air mass flow with an injector opening time of 2 seconds, what resulted in 168.6 g of injected water. In the case of the second injection (quarter #3) the air mass flow at the moment of the injection was lowered to 20 kg/h, keeping constant the injector opening time. The aim was to evaluate the influence of the swallowed air mass flow at the moment of the injection. In the last injection (quarter #4) both the air mass and the injector opening time were reduced to 20 kg/h and 1 s respectively. In this way it has been possible to evaluate also the influence of the injected water mass on the effectiveness of the pre-DPF water injection technique.

Table 5.5: Performed injections in flow test bench for every DPF quarter sample.

Quarter	Air mass flow [kg/h]	Inlet temperature [°C]	Injection pressure [bar]	Injector opening time [s]	Water mass flow [g/s]	Injected water mass [g]
#1 Ref	-	-	-	-	-	-
#2	35	200	5	2	84.3	168.6
#3	20	200	5	2	85.3	170.6
#4	20	200	5	1	83.2	83.2

Once the thermal transient related to the water flow has finished the pressure drop of every sample was measured again in the same conditions considered before the injection. Finally the samples were dismounted and weighted again to confirm the lack of soot release related to the injection.

Figure 5.13 shows the measured quarter samples pressure drop before and after the injection for different inlet air mass flow at 20 °C and 200 °C. Every couple of graphs is referred to a quarter sample: Figure 5.13(a) and (b) refer to quarter #1 of Table 5.5, Figure 5.13(c) and (d) refer to quarter #2 and so on. The repeatability of the pressure drop measure before and after reaching the maximum air mass flow can be observed in all the quarter samples. This is an interesting result that partially disagrees with the assumptions of Koltsakis *et al.* [159], Konstandopoulos *et al.* [13] [163] and Liu *et al.* [14] on the compressibility of the particulate layer. Indeed, in none of the measured case

the inlet pressure affected the particulate layer characteristics so to modify the generated pressure drop (Figure 5.13), neither in the most extreme case of ≈ 19000 Pa overpressure (Figure 5.13(d)). The same pressure drop was measured before and after reaching the maximum air mass flow, hence inlet pressure, value. This result indicates that once the particles are deposited and stuck on the porous wall, the inlet flow field does not affect the cake characteristics. Anyway, further investigation is needed to prove this assumption. Tests at more critical conditions than the considered here, i.e. ≈ 19000 Pa overpressure, 200°C inlet DPF temperature and 35 kg/h air mass flow, are to be performed to draw more reliable conclusions.

Note that due to root blower limitations it was not possible to reach the same maximum air mass flow in all the cases, especially in the case of 200 °C because of the pressure drop increase related to the air flow temperature increase. It is also important to note that the pressure drop of the quarter samples before the injection is not the same. Quarters #1 and #3 present the highest pressure drop, followed by quarter #4 and last by quarter #2. This behaviour is supposed to be related to a non-homogeneous soot distribution inside the filter, further promoted by the inlet DPF geometry, showed in Figure 5.14, that results in an asymmetric flow distribution.

Figure 5.15 shows the absolute and percentage pressure drop reduction after the application of the pre-DPF water injection technique. Again every couple of graphs is referred to a quarter sample at T = 20 °C and T = 200 °C. Quarter #1 is not showed as it was not subjected to water injection.

Important conclusions can be drawn from the analysis of Figures 5.13 and 5.15. The effect of the temperature is easily recognizable. As expected when the inlet DPF temperature is raised from 20 °C to 200 °C the pressure drop suffers a notable increase. This effect is related to the velocity increase due to the density decrease at constant air mass flow.

The water injection caused a notable pressure drop reduction in all the cases, comprised between 75% and 90% with respect to the value before the injection. In all the cases the percentage pressure drop reduction presents a lightly decreasing trend with increasing air mass flow, more marked as the temperature is increased from 20 °C to 200 °C. Such high values are on the same order of magnitude of the ones showed in Figure 5.10(b) for the maximum reached soot load, i.e. 44.6 g.

Quarter #2, i.e. 35 kg/h air mass flow and 168.6 g of injected water mass, presents a pressure drop reduction due to the water injection comprised between 80% and 87.5%. The highest measured pressure drop, corresponding to 35 kg/h at 200 °C, decreased from 19000 Pa to 4000 Pa, i.e. an absolute value of 15000 Pa. When the air mass flow at the moment of the injection is lowered to 20 kg/h keeping constant the injected water mass (quarter #3), a slightly higher percentage pressure drop reduction is observed, between 87.5% and

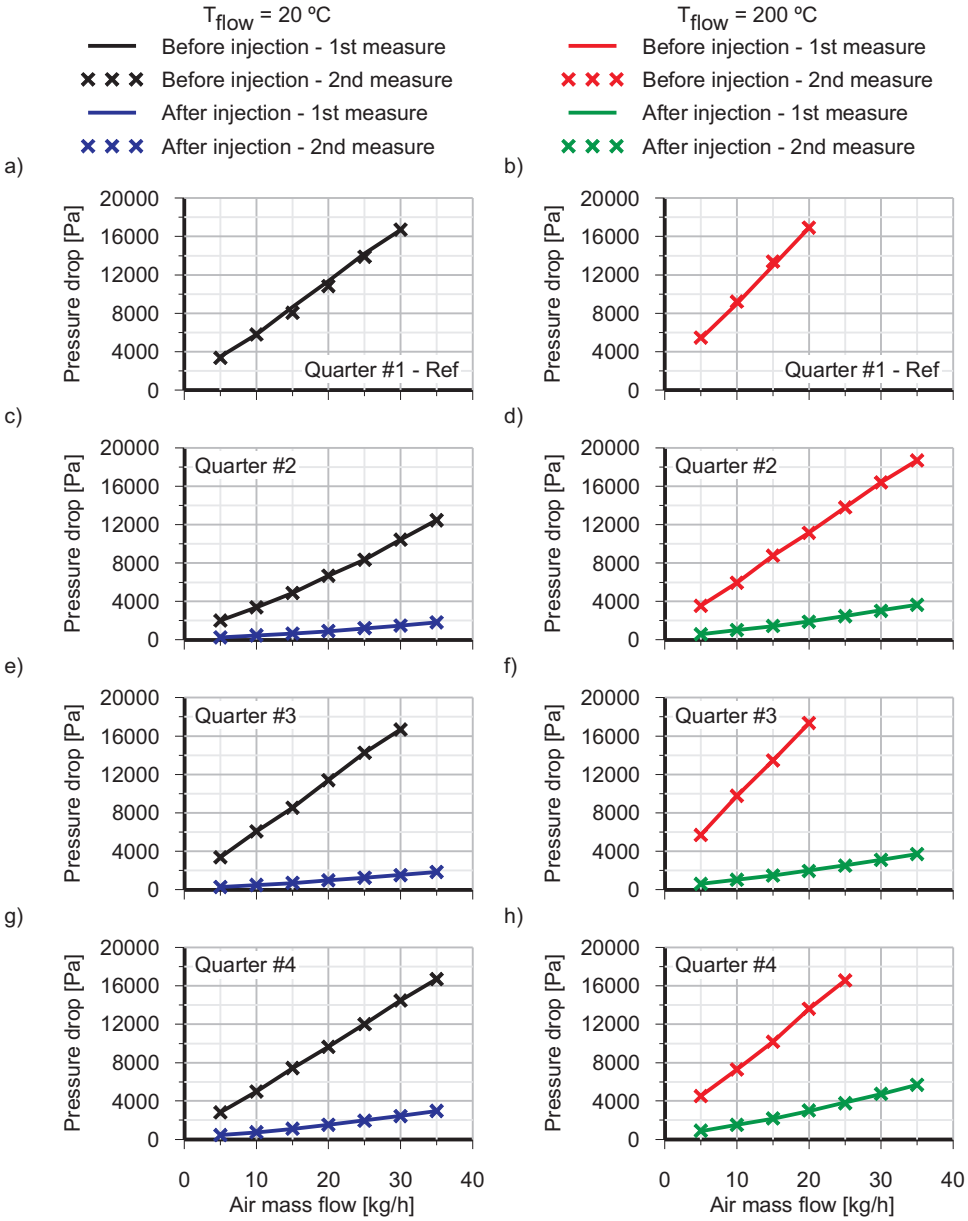

Figure 5.13: Pressure drop as a function of air mass flow and inlet temperature before and after the pre-DPF water injection in every DPF quarter sample.

92.5%. Anyway this result is considered to be related with the higher pressure drop before the injection of quarter #3 compared with quarter #2. Indeed, the

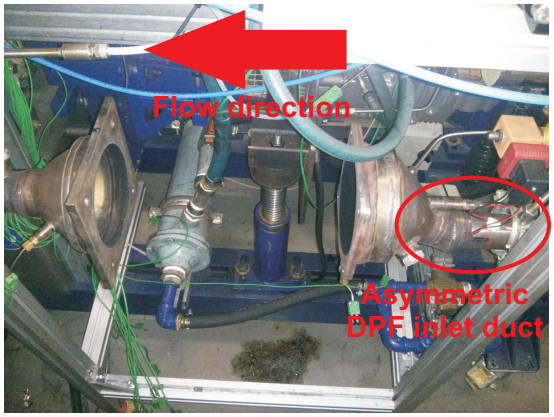

Figure 5.14: Picture of the inlet DPF geometry.

pressure drop value after the injection is about the same comparing quarter #3 with quarter #2. The performed optical analysis, described in next section, confirmed this hypothesis. It will be shown that the number of de-clogged channels is almost the same between quarter #3 and quarter #2 and that the most limiting parameter is the homogeneous distribution of the water jet throughout the quarter sample frontal section. Thus it is possible to state that the inlet air mass flow at the moment of the injection has a second order effect on the effectiveness of the pre-DPF water injection technique. This is certain in the 2 tested cases, i.e. 35 and 20 kg/h, the effect of further reduction of the air mass flow at the moment of the injection is worth to be investigated. Finally, quarter #4 has been subjected to an injection at low air mass flow and low injected water mass, i.e. 20 kg/h and 83.2 g respectively. The absolute pressure drop after the injection is the highest of the three tests, what results in a percentage pressure drop reduction comprised between 76% and 84%, i.e. the lowest of the three tests. The optical analysis will show that this result has to be attributed to the lower number of de-clogged channels comparing with quarter #3 and quarter #2. More details are given in Section 5.3.2. Anyway it is already possible to conclude that the injected water mass is the governing parameter of the effectiveness of the pre-DPF water injection technique.

5.3.2 Optical description of soot restructuring

Once verified in the flow test bench that the application of the pre-DPF water injection technique results in a notable reduction of the pressure drop of soot loaded filters, the quarter samples were cut at different axial positions and analysed with optical techniques looking for the reason explaining the measured

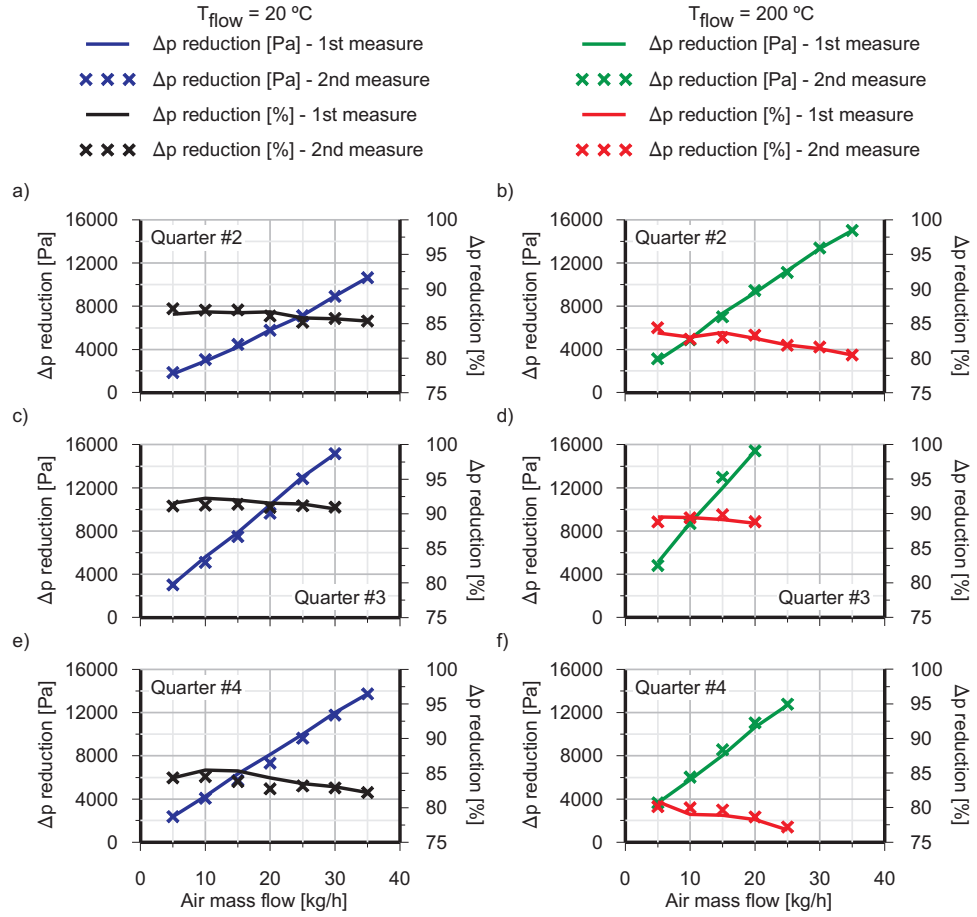

Figure 5.15: Quarter samples pressure drop reduction after the pre-DPF water injection.

pressure drop reduction. Every sample has been cut in 5 sections at 2.5, 8.5, 14.5 and 20.5 cm from the inlet section. Pictures of every whole section have been taken with a digital camera. The optical microscope has been used to take 17 pictures of every section at 5 radial and 4 angular different positions, giving a total of 170 pictures per quarter sample. A scheme of the obtained sections and the used numeration is sketched in Figure 5.16.

Figure 5.17 shows pictures of the whole frontal section of every quarter sample at the inlet of section #2 (following nomenclature of Figure 5.16), i.e. at 2.5 cm from the sample inlet. Below every picture, 3 images taken with the optical microscope, corresponding to positions 1, 11 and 13 according to nomenclature of Figure 5.16, are shown. The effect of the water injection is

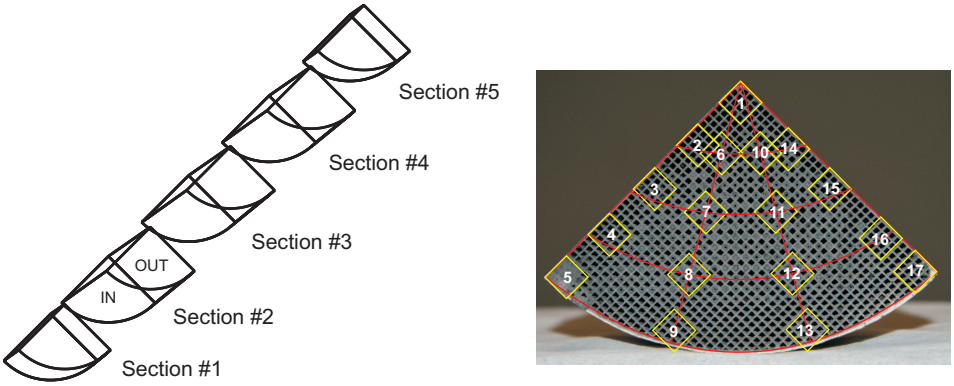

Figure 5.16: Scheme of the quarter samples cut sections and pictures numeration.

evident. In the reference sample, i.e. not subjected to water injection, all the inlet channels are almost completely clogged due to the high soot load reached at the end of the soot loading process. In the other samples there is a clear distinction between areas affected by the pre-DPF water injection and areas that have not been reached by the water droplets and remained essentially equal to the reference sample case (#1).

The observed non-homogeneity of the technique effectiveness throughout the samples frontal section is related to the injection setup. The water injection was performed using a simple 4 mm diameter duct, unable to generate a water spray homogeneously distributed throughout the quarter sample frontal section. To overcome this problem the injector was mounted so that the water stream firstly hits the metallic cover of the support for quarter filter samples (Figure 5.7). The generated water droplets fall down for gravity and are made to flow in the quarter sample inlet channels by the inlet air flow drag. This leads to the conclusion that optimizing the injector geometry to obtain a water flow affecting the whole sample frontal section, the pressure drop decrease related to the water injection technique would notably increase, and so the consequent bsfc saving.

As a first step a code was developed for the post-processing of the optical microscope images. The aim was to calculate the mean particle layer thickness distribution along the sample length in the reference quarter (#1). To obtain it the code transforms the picture from colour (Figure 5.18(a)) to black and white (Figure 5.18(b)), where white spaces identify the soot free regions. The area of the white spaces is calculated. Then, knowing the area of the reference clean cell and assuming that the layer is uniformly deposited leaving a square void space as shown in Figure 2.3, the particle layer thickness can be estimated. For every axial position, 4 images of the central part of the sample have been

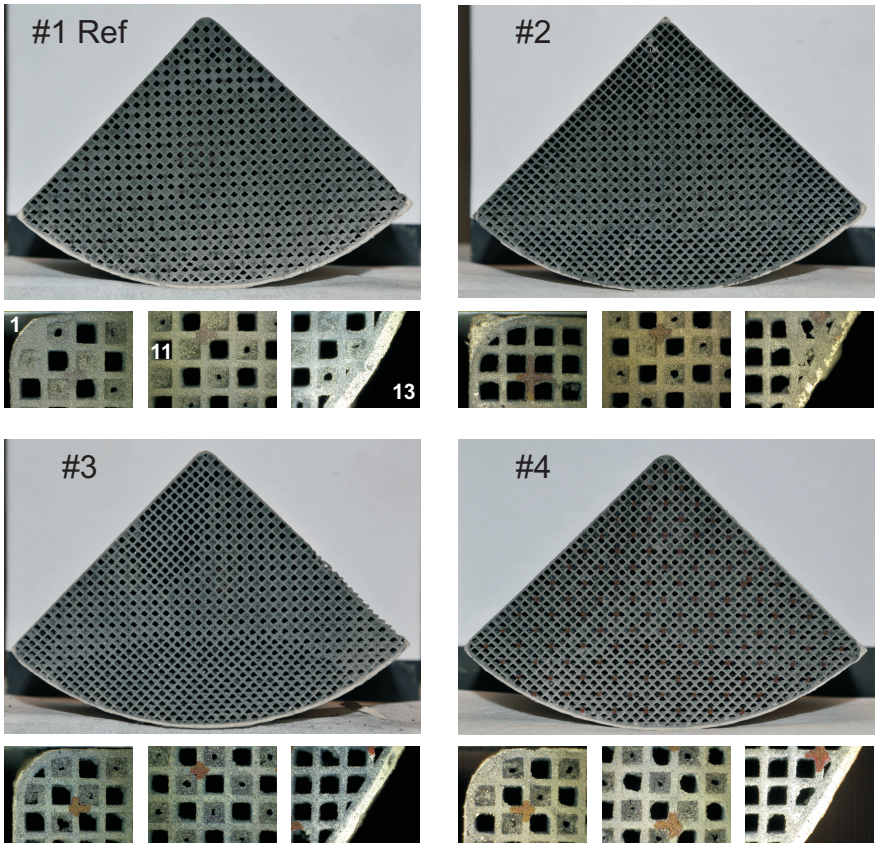

Figure 5.17: Camera and optical microscope pictures at Section #2 inlet of every quarter sample.

analysed, i.e. positions 7, 8, 11 and 12 according to the nomenclature defined in Figure 5.16. As shown in Figure 5.18, every picture contains 6 channels. As a result 48 channels per axial section (considering that the axial position of section i inlet and section $i-1$ outlet coincide) have been analysed in order to obtain the mean particle layer thickness value as a function of the axial position. Figure 5.18(c) shows the result of the post-processing for the baseline quarter sample (#1) at every cross-section position (7-8-11-12). For every axial position, coloured symbols represent the mean values while vertical bars represent the range between minimum and maximum observed particle layer thickness.

The calculated particulate layer thickness presents a notable dispersion, especially in cross-section position 12. This is confirmed also by the particulate layer thickness standard deviation shown in Figure 5.19. Considering the mean and standard deviation presented values it is possible to say that the particle

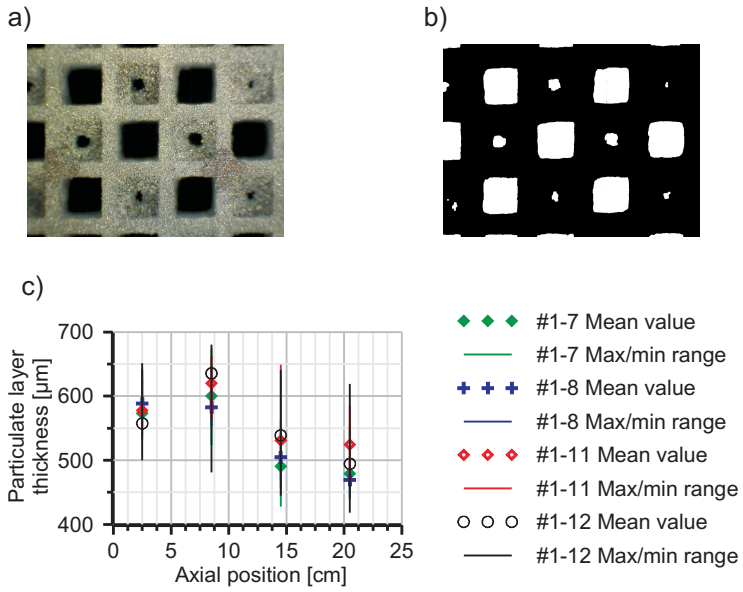

Figure 5.18: a) Original optical microscope picture. b) Black&white picture after post-processing. c) Particle layer thickness as a function of the axial position for quarter sample #1 (Reference).

layer thickness is almost constant along the filter length, with a value comprised between 500 and 600 μm. This conclusion is supported also by the filtration velocity field calculated with the developed model in Section 3.7.2. Despite this calculation is referred to a different soot loading process, Figure 3.13 shows that as soot is accumulated inside the filter, the filtration velocity profile is smoothed and gets to an almost uniform value along the filter length. Lupsea *et al.* [178] showed the same smoothing tendency of the filtration velocity as soot is accumulated inside the filter. As a result, particles tend to deposit uniformly along the filter length leading to an almost constant particle layer thickness profile. Also Koltsakis *et al.* [159] reported a uniform particle layer thickness along the filter length in case of a soot load of 8.2 g/l.

The developed post-processing code was not applied to the quarters subjected to pre-DPF water injection. It will be clearly shown later on with SEM images that after the injection there is no well-defined particle layer in the channels, only sparse cake layer fragments. Thus it makes no sense to calculate a mean particle layer thickness.

Knowing the particle layer thickness it was possible to estimate the particle layer density. It was done by assuming a constant mean layer thickness of 550 μm, i.e. the mean value of the estimated particle layer thickness along the

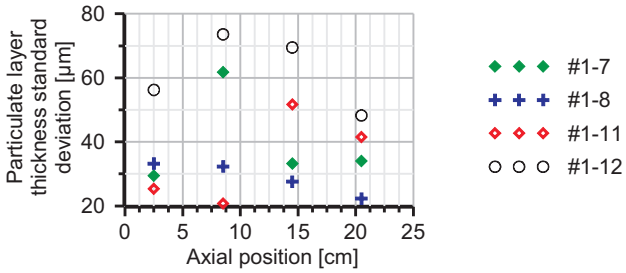

Figure 5.19: Particle layer thickness standard deviation as a function of the axial position for quarter sample #1 (Reference).

quarter sample length. From there, knowing the total collected soot mass and the filtration area, it was possible to calculate a mean particle layer density of 48 kg/m^3. This value is slightly lower than the one calculated by Koltsakis *et al.* [159] in the case of low filtration velocity, i.e. 1.4 cm/s. The mean filtration velocity value calculated throughout the reference soot loading process (black line in Figure 5.10(a)) performed in this work is 1.2 cm/s. Thus, the particle layer density value calculated in the present work follows the trend of decreasing particle layer density with decreasing filtration velocity shown by Koltsakis *et al.*.

Assuming the carbon density to be 2000 kg/m^3 a particle layer porosity of 0.976 is found. This value is in agreement with the one found by Liu *et al.* [14] in a recent work in which the authors collected diesel particles on a polytetrafluoroethylene (PTFE) filter. Also Elmoe *et al.* found similar particle layer porosity values in both the case of the simulation of nanoparticle cake formation on capillary filters [179] and the case of SEM analysis of nanoparticle deposits on a porous substrate [180].

The post-processing of the whole section pictures along the quarters length was proposed to evaluate the effectiveness of the pre-DPF water injection technique by means of a two-colours technique. It allowed evaluating the number of channels that were de-clogged by the water flow for every quarter sample. To do that first of all every picture is passed to black and white colours in which every white region represents an open channel, both inlet and outlet as the plugs are only visible from the extremities of the quarters. Very small white regions shown in Figure 5.20(a) represent extremely clogged inlet channels. Then the code compares the area of every white region with a threshold value above which the channel is considered to be clean. If this is the case, the code plots a red cross at the centroid of the white square (Figure 5.20(b)). The number of de-clogged channels is obtained by subtracting the known outlet channels number from the

counted clean channels. In the case of the inlet section, due to the presence of the inlet plug, the de-clogged channels number has been manually evaluated.

Figure 5.20(c) shows the obtained results applying the above described post-process at all the axial sections of the three quarter samples subjected to pre-DPF water injection. In all the cases it can be observed that the number of de-clogged channels decreases with the axial position, i.e. as the water droplets penetrates into the sample. Quarter #4 has the smaller number of de-clogged channels. This result agrees with the higher pressure drop after the water injection comparing with quarters #2 and #3, as shown in Figure 5.13. Quarters #2 and #3 present similar number of de-clogged channels as well as similar pressure drop after the injection. The slight differences between these two quarters are supposed to be related to the higher air mass flow at the moment of the injection, what results in higher droplets momentum, hence higher penetration and drag capacity.

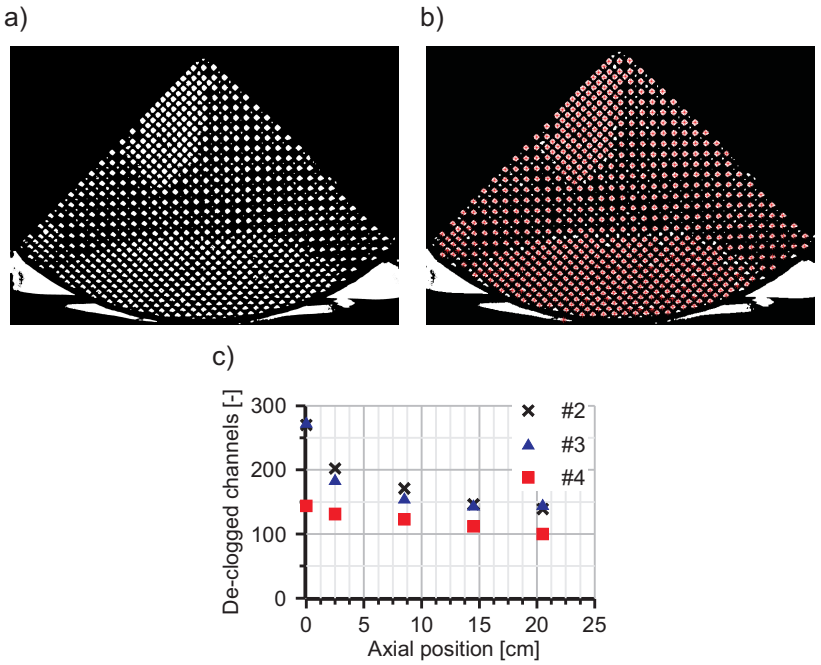

Figure 5.20: Example of the post-processing for open channels count and number of de-clogged channels as a function of the axial position for the three quarter samples subjected to pre-DPF water injection.

To integrate these results, the use of the SEM permitted to visualize with more detail the effect of the water flow on the particle layer and check if the water injection affected the soot deposited inside the porous wall. Also, the use of the

x-rays analyser allowed to precisely distinguish the monolith porous wall (SiC) from the soot particles (C). Because of the dimensions of the microscope sample chamber the sections showed in Figure 5.16 had to be further reduced. Smaller samples of 10 mm thickness, 35 mm length and 15 mm width were obtained from the inlet part of Sections 2 and 5 and from the outlet part of Section 3 of quarters #1 and #3 to get images at a low, medium and high distance from the filter inlet section. The samples for SEM analysis have been taken in the lower, external part of the quarters. As it resulted clear from the analysis of Figures 5.17 and 5.20 this is the area most affected by the water flow in all the 3 samples subjected to pre-DPF water injection.

Figure 5.21 shows a comparison between the reference quarter sample (#1 not subjected to water injection) and the quarter #3 at two different axial positions: 2.5 and 20.5 cm, i.e. the front and the rear sections of the samples. In the reference case (Figures 5.21(a) and (c)) a thick particle layer is observed, slightly thinner in the rear section as shown in Figure 5.18. On the contrary, in sample #3 (Figures 5.21(b) and (d)) the water flow strongly modified the particle layer. In the front section, i.e. at 2.5 cm, the thick particle layer has been replaced by a thin layer covering the channel surface with sparse, random presence of soot accumulation with a maximum thickness of only 130 μm in comparison with the values shown in Figure 5.18(c). Contrarily to what happens in the reference sample, Figure 5.21(d) shows that the presence of soot notably increases in the rear part of the channel. Also the maximum measured particle layer thickness increases from 130 μm at 2.5 cm to 180 μm at 20.5 cm from the sample inlet section. Anyway this value is still notably lower than the one of the reference quarter (#1) shown in Figure 5.18(c).

The presence of the particle layer can be observed with more detail in Figure 5.22, which shows a zoom of quarter sample #3 at axial position 2.5 cm. The elemental analysis of the sample presented in Figure 5.22(b) shows in green the presence of silicon, i.e. monolith porous wall grains, and in red the presence of carbon, i.e. soot. The presence of a thin particle layer on the whole channel surface is evident. This residual particle layer is believed to be responsible of the high filtration efficiency (> 99%) experimentally measured by Bermúdez *et al.* [25] after the pre-DPF water injections.

In order to deeper investigate the behaviour of the particle layer in the rear section of the samples subjected to water injection, an additional cut was performed at an axial position of 21.5 cm from the inlet sample section. Pictures from several channels taken with the optical microscope are showed in Figure 5.23. The accumulation of particle layer fragments (in dark color) in the rear part of the channel is evident. According to these results, it is believed that the water flow tends to detach big fragments of the particle layer and push them towards the end of the inlet channels. Figure 5.23(b) represents a sketch of the the hypothesized effect of the water droplets on the particle layer. The sparse

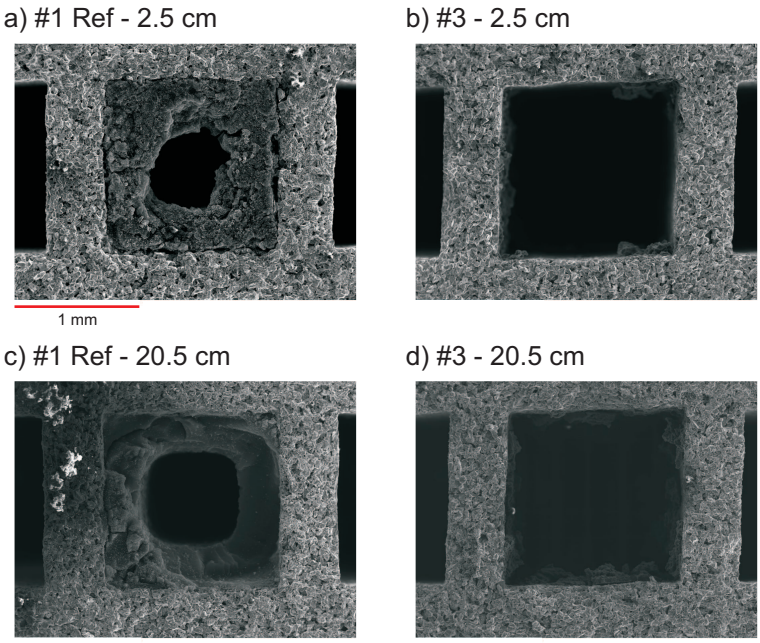

Figure 5.21: SEM images of reference and #3 quarter sample at 2.5 and 20.5 cm from the inlet section.

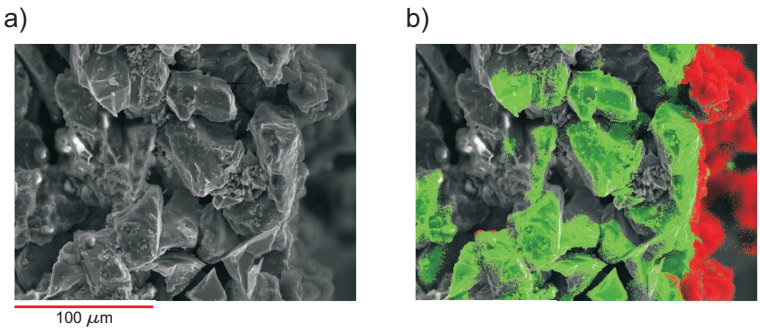

Figure 5.22: Porous wall-particle layer interface detail of #3 quarter sample at 2.5 cm from the inlet section. a) SEM image. b) Elemental analysis.

presence of small particle layer fragments has also been drawn. This hypothesis is further supported by the observed different adhesion of the particle layer in channels affected or not by the water injection. In the reference case and in the channels not affected by the water injection the particle layer was firmly stuck

on the porous wall. On the contrary, channels affected by the water injection process present a particle layer weakly stuck on the porous wall.

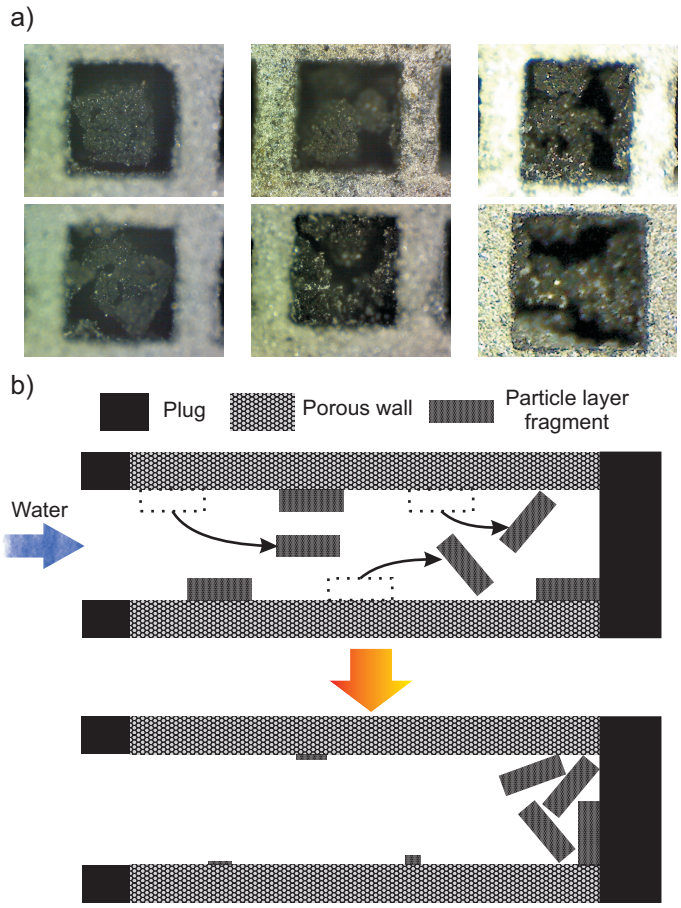

Figure 5.23: a) Optical microscope images of fragments of particle layer accumulated in the rear end part of the inlet channels. b) Scheme of the water effect on particle layer fragments.

Concerning the particles deposited in the inner of the porous wall during the deep bed filtration phase, the use of the SEM allowed to find out that the water injection does not affect them in an appreciable way. Applying the correlation to estimate the soot penetration thickness inside the porous wall as a function of the mean Peclet number described in Section 3.8, a value of 5.25 μm is obtained. This value agrees with the SEM images which show a very superficial deposition of the soot with negligible penetration inside the porous wall. Figure 5.24 shows that this behaviour was observed in both the analysed samples, i.e. subjected

(#3) or not (#1) to pre-DPF water injection. In both cases the pores of the porous wall have been observed to be clean. Thus it is possible to conclude that the water flow does not significantly affect the particles stored inside the porous wall.

In order to further verify the lack of any effect of the water flow on the particles deposited inside the porous wall the section showed in Figure 5.24(g) was further analysed. An elemental analysis of 4 specific sections of this picture, each marked with a green square, is showed in Figure 5.25. A superficial pore (Spectrum 1), a fragment of the particle layer stuck on the porous wall after the injection (Spectrum 2) and 2 deep pores (Spectrum 3 and 4) have been considered. The results of the elemental analysis is showed in the graphs around the SEM image. In this graphs the x axis represents the energy of the emitted x-rays in keV. As stated in Section 5.2.3 the energy of the emitted x-rays is a well defined characteristic of the emitting element, what makes possible to characterize the elemental composition of the specimen. On the y axis is represented the number of signals received by the equipment. In accordance with the coloured elemental map showed in Figure 5.24(h), Spectrum 1 ,i.e. a superficial pore at a depth of about 12μm, shows presence of both Si (representing the SiC porous wall) and C (representing soot). On the contrary, when the particle layer fragment is analysed (Spectrum2) the presence of soot (C) overcomes the Si one, proving the reliability of the technique. When deeper pores at about 100/125 μm are considered, negligible presence of soot (C) is showed. It confirms the above stated lack of effects of the water injection on the particles deposited inside the porous wall, i.e. soot is not pushed deeper inside the porous wall by the water droplets.

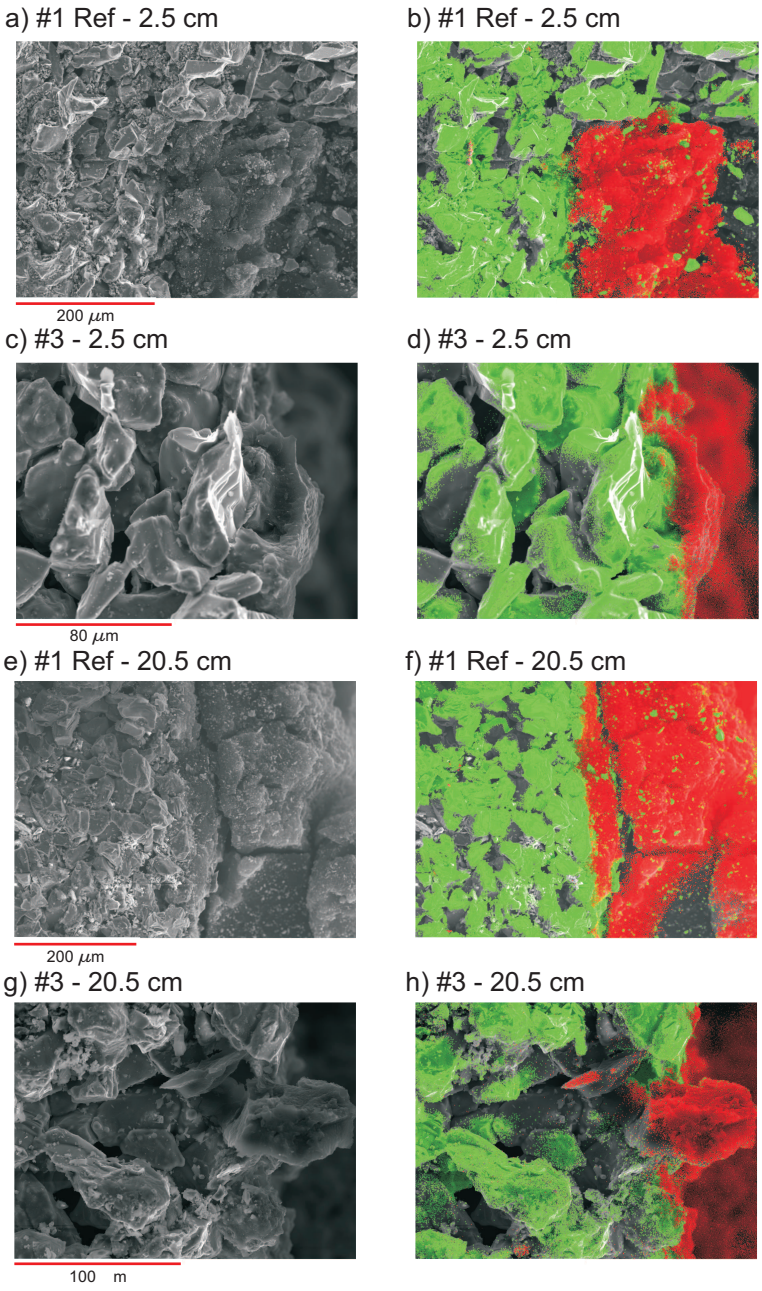

Figure 5.24: Examples of SEM images (left) and elemental map (rigth) from channels at different axial positions of quarter sample #1 (Ref) and #3.

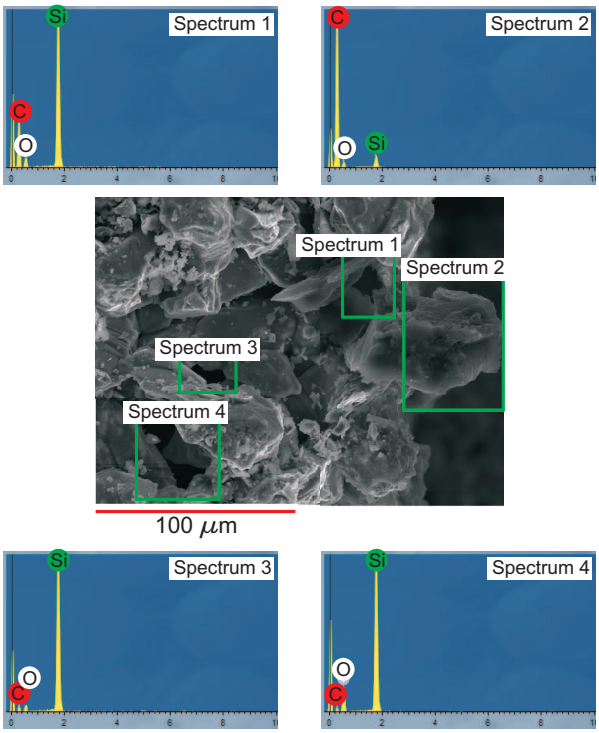

Figure 5.25: Examples of elemental analysis performed in different sections of Figure 5.24(g).

5.4 Peclet number effect on soot deposition

The test bench described in Section 5.2.1 was used to load 3 identical filters up to similar soot mass load varying the flow velocity, hence the Peclet number, without affecting the engine raw emission. The aim was to analyse the effect of the reduced Peclet number, characteristic of the pre-turbo DPF placement as discussed in Chapters 3 and 4, on the deposition characteristics of soot particles inside the inlet channels. Thus, the generated pressure drop and filtration efficiency corresponding to every Peclet number were measured in the engine test bench throughout the loading process. After the soot loading the three filters were tested in the flow test rig described in Section 5.2.2 in order to compare the generated pressure drop of every DPF against the same mass flow. Last, the advanced optical techniques described in Section 5.2.3 were also applied to analyse the differences in soot deposition characteristics.

5.4.1 Pressure drop and filtration analysis in engine test bench

All the soot loading processes were performed in the engine operating point defined in Table 5.4. The DPFs are named following the nomenclature defined in Table 5.2. According to Table 5.2, DPF #2 has been loaded in reference conditions, i.e. 100% of the engine exhaust gas mass was made to flow through the DPF (77.7 kg/h). In the case of DPF #3 and DPF #4 the exhaust gas mass flow through the filter was reduced to 39.97 kg/h and 29.85 kg/h respectively by acting on the back-pressure valve (Figure 5.1). Figure 5.26(a) shows the exhaust gas mass flow through the DPF in every soot loading test. The reduction of the exhaust gas mass flow through the DPF results in a mean filtration velocity decrease (Figure 5.26(b)) and a slower thermal transient (Figure 5.26(c)). Figure 5.26(d) shows the Peclet number for each soot loading test referred to clean porous wall conditions, i.e. 18.55 μm mean pore diameter and 41% porosity (Table 5.1).

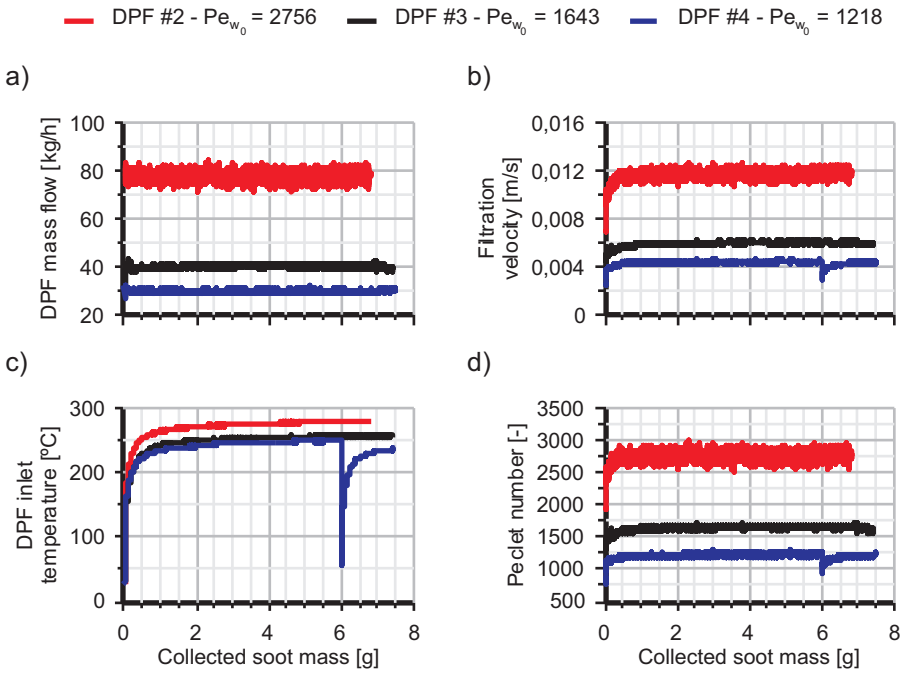

Figure 5.26: DPF parameters throughout the soot loading tests.

A discontinuity can be noted in the soot loading process of DPF #4. An issue in the engine test bench resulted in the necessity to stop the loading process and resume it a few minutes later. The transient behaviour of the Peclet number at the beginning of all the soot loading processes is related to the transient of

the filtration velocity, which directly affects the Pe value (eq. 3.10), and of the temperature, which affects the diffusion coefficient (eq. 3.11).

Figure 5.27 reports the measured pressure drop as soot is accumulated inside the filters. As it had to be expected, the pressure drop is lower at lower exhaust gas mass flow, i.e. lower Peclet number. Anyway this trend is not helpful for the characterization of the effect of the Peclet number on the particles deposition dynamics. The difference in the measured pressure drop is indeed due to the coupled effect of the reduced filtration velocity and of the different particles deposition characteristics. Therefore the filters were tested in controlled conditions in the flow test bench, as detailed in Section 5.4.2, in order to precisely analyse the effect of the reduction of the Peclet number on the generated pressure drop.

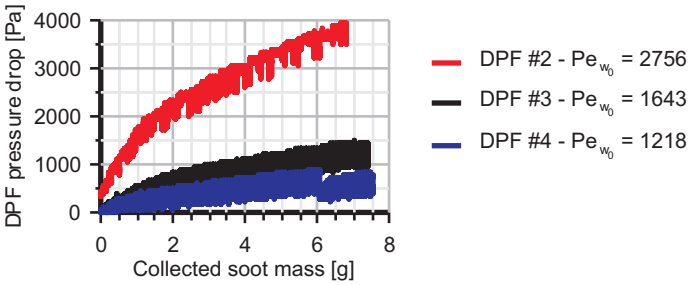

Figure 5.27: DPF pressure drop evolution as a function of the collected soot mass.

Figure 5.28 shows in plots (a) and (b) the calculated DPF filtration efficiency based on soot particles mass and number measurement respectively. Mass-based efficiency was calculated from the TSI DCS-100 measure whilst number-based was obtained from the TSI EEPS-3090 measure. As explained in Section 5.2.1 these equipments measure the volumetric mass and number soot particles concentration respectively. Thus, knowing the density and the exhaust gas mass flow at the inlet and outlet of the DPF it is possible to convert the measured volumetric mass and particle number concentrations to soot mass and particles number flow respectively as:

$$\dot{m}_s \left[\frac{kg}{s}\right] = \frac{\gamma_{s_{DCS}} \left[\frac{kg}{m^3}\right] \dot{m}_{exh} \left[\frac{kg}{s}\right]}{\rho_{exh} \left[\frac{kg}{m^3}\right]} \tag{5.2}$$

$$\dot{\#}_s \left[\frac{\#}{s}\right] = \frac{C_{s_{EEPS}} \left[\frac{\#}{m^3}\right] \dot{m}_{exh} \left[\frac{kg}{s}\right]}{\rho_{exh} \left[\frac{kg}{m^3}\right]} \tag{5.3}$$

Once this values are known upstream and downstream of the DPF it is possible to calculate the mass-based and number-based filtration efficiency respectively as:

$$E_{f_{mass}}[\%] = \frac{\left(\dot{m}_{s_{in}} - \dot{m}_{s_{out}}\right)}{\dot{m}_{s_{in}}} 100 \tag{5.4}$$

$$E_{f_{number}}[\%] = \frac{\left(\dot{\#}_{s_{in}} - \dot{\#}_{s_{out}}\right)}{\dot{\#}_{s_{in}}} 100 \tag{5.5}$$

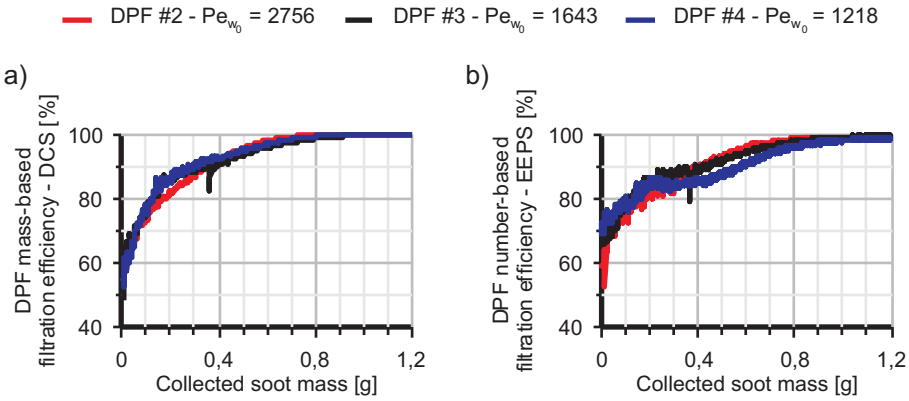

Figure 5.28: DPF filtration efficiency evolution with collected soot mass throughout the soot loading tests: a) mass-based efficiency from the TSI DCS-100 measure, b) number-based filtration efficiency from TSI EEPS-3090 measure.

The three filtration efficiency profiles are very similar in both mass- and number-basis. However, comparing the number-based collection efficiency of the clean porous wall between the highest Peclet number case and the lowest Peclet number case the difference is around 10 percentage points, i.e. 58% and 68% respectively. As stated in Section 3.3.1, the higher flow velocity of DPF #2 penalizes the Brownian collection mechanism (eq. 3.10). Anyway, the penalization induced by the filtration velocity increase is partially reduced because of the higher mean temperature throughout this soot loading process (Figure 5.26(c)), what increases the diffusion coefficient (eq. 3.11). This leads to a slight recover of the filtration efficiency and the reduction of the difference with respect to the lowest Peclet number soot loading process. This fact can also explain the small differences between DPF #3 and DPF #4.

The particles penetration thickness inside the porous wall affects the dynamics of both the filtration efficiency and the pressure drop as it sets the porous wall properties throughout the soot loading process. Also, it defines the soot

mass that is possible to accumulate inside the porous wall, hence the boundary between the deep bed and the cake layer filtration regime (Section 3.4). A correlation to estimate the particles penetration thickness inside the porous wall from the Peclet number in clean conditions was presented in Section 3.8. It was shown that the soot particles tend to penetrate deeply as the Peclet number increases, i.e. advection gets more important than diffusion. Applying this correlation to the performed soot loading processes the obtained soot penetration thickness is 5.23 μm, 3.12 μm and 2.31 μm for DPF #2, #3 and #4 respectively. As stated above the particles penetration thickness affects the filter saturation mass, which in turn marks the boundary between the deep bed and the cake layer filtration regime. The transition between the two regimes is characterized by the change in the pressure drop curve slope. Figure 5.29 shows the evolution of the pressure drop in the three tests separately.

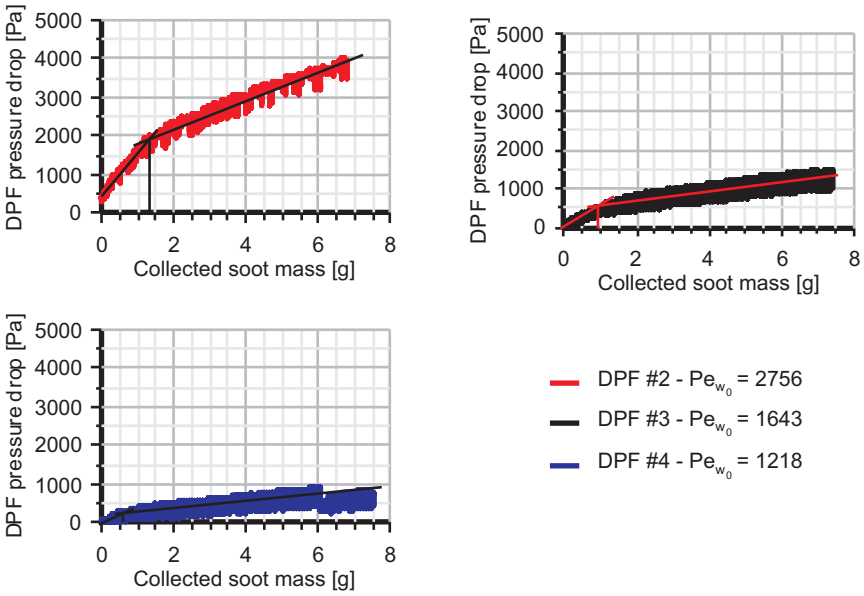

Figure 5.29: Effect of soot penetration thickness on the deep bed - cake layer filtration regime transition.

It can be seen that the slope change moves towards higher collected soot mass (from 0.62 g to 1.41 g) as the mean Peclet number throughout the loading process increases. This behaviour agrees with the prediction of the developed Peclet number - soot penetration thickness correlation, i.e. the higher the Peclet number the higher the soot penetration thickness, hence greater filter saturation mass. The estimation of the soot packing density inside the porous wall from the calculated soot penetration thickness and the observed saturation mass leads to

a value of 525 kg/m^3. This value falls inside the range observed by Lapuerta *et al.* [34].

5.4.2 Pressure drop analysis in flow test bench

After the soot loading processes in the engine test bench, the pressure drop generated by the 3 DPFs was measured in controlled conditions in the flow test bench described in Section 5.2.2. As in the case of Section 5.3.1.2, the pressure drop of every considered point was measured twice, i.e. firstly for increasing and then for decreasing air mass flow, to verify the repeatability of the measure. Figure 5.30 shows the measured pressure drop of each DPF for an inlet air mass flow comprised between 30 and 400 kg/h. The inlet DPF temperature is 100°C and 200°C in plots (a) and (b) respectively. As expected the pressure drop increases when increasing the air mass flow and temperature. Also, a clear trend of decreasing pressure drop with decreasing Peclet number throughout the soot loading process is observed. In the most extreme conditions, i.e. 400 kg/h and 200°C, the measured pressure drop values were 14790, 12400 and 10700 Pa for DPF#2, #3 and #4 respectively. Highlight that these results were obtained despite the slightly higher soot mass at the end of the loading processes in DPF #3 and #4 (7.4 and 7.5 grams respectively versus 6.8 g of DPF#2 as detailed in Table 5.2).

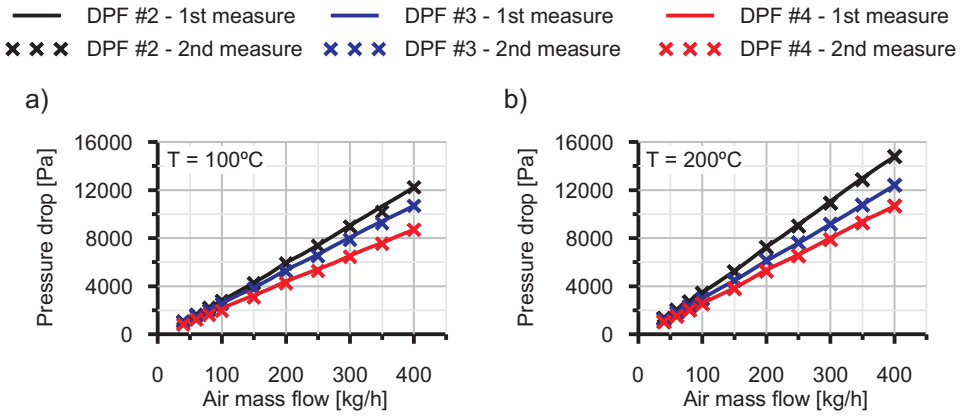

Figure 5.30: DPFs pressure drop as a function of the air mass flow and inlet DPF temperature.

In order to better figure out the measured pressure drop behaviour, Figure 5.31 shows the pressure drop percentage reduction between DPF #3 (blue line) and DPF #4 (red line) with respect to the reference Peclet number case (DPF #2). The pressure drop reduction of DPF #4 (Pe_{w_0} = 1218) is comprised

between 20% and 30%. The Peclet number increase to Pe_{w_0} = 1643 of DPF #3 leads to a smaller benefit in pressure drop, comprised between 5% and 15%. In both cases a slight trend of increasing pressure drop percentage reduction with increasing air mass flow and temperature is obtained.

As detailed in Section 2.2.2, the pressure drop of a soot loaded filter is related to four contributions: inertial, friction, Darcy's through the porous wall and Darcy's through the particulate layer. The firsts two contributions can be assumed to be almost identical between the 3 tested DPFs. The porous media contributions for both the porous wall and the particulate layer can be expressed in a simple way according to eq. 5.6:

$$\Delta p_{Darcy} = \frac{\mu u w}{k} \tag{5.6}$$

In eq. 5.6 μ is the flow viscosity, u is the velocity of the flow throughout the porous medium, w the porous medium thickness and k the porous medium permeability. The testing methodology in the flow test rig results in negligible differences in the firsts two parameters between the three tested DPFs. Thus, attention is to be focused on the porous media thickness and permeability. Focusing firstly on the porous wall, its thickness is the same in the three tested DPFs, i.e. 0.458 mm. The permeability on the other hand can be affected by the soot penetration thickness, i.e. the deeper the particles penetrate into the porous wall the lower the permeability because of the increased percentage of porous wall thickness interested by particles deposition. The calculated soot penetration thickness values correspond to the 1.14%, 0.68% and 0.5% respectively of the porous wall thickness. These values can partially justify the differences in the pressure drop measures by means of porous wall permeability variations. Anyway, the contribution of the particle layer has also to be taken into account.

As stated in Section 5.1, several authors reported a trend of decreasing particle layer density [13] [163], hence increasing porosity [14] and thickness, with decreasing Peclet number throughout the soot loading process. Consequently the permeability of the particle layer is believed to be affected by the particles deposition dynamics [159] [163]. As shown in eq. 5.6 these parameters affect the generated pressure drop. Concerning the particle layer thickness, it will be detailed in Section 5.4.3 that no notable differences between the three filters were noted from the optical analysis. Regarding the particle layer permeability, Konstandopoulos *et al.* [13] showed a trend of soot layer permeability increase with Peclet number decrease. In late works Konstandopoulos *et al.* [163] and Koltsakis *et al.* [159] define a hydrodynamic resistance factor H as in eq. 5.7:

$$\mathrm{H} = \rho_{pl} k_{pl} \tag{5.7}$$

Koltsakis *et al.* [159] show an increase in H from around $6\text{x}10^{-13}$ kg/m to around $8\text{x}10^{-13}$ kg/m when the filtration velocity is decreased. Unfortunately,

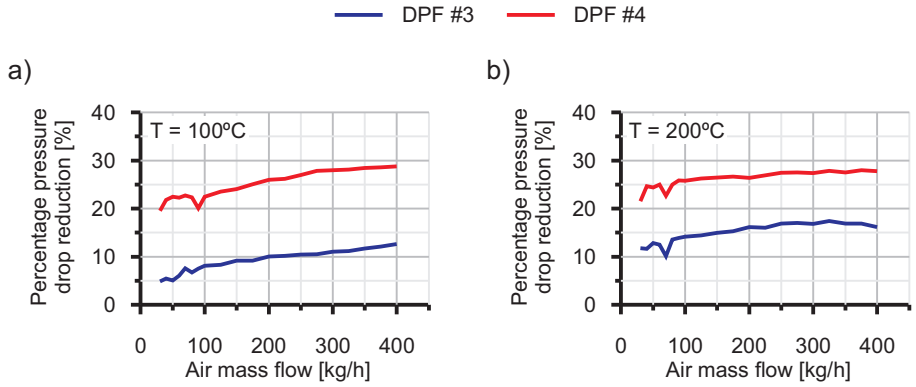

Figure 5.31: DPFs pressure drop percentage difference with respect to DPF #2 (Reference) as a function of the air mass flow and inlet DPF temperature.

no details on the filtration velocity values nor reduction are given. Anyway the ≈ 33% H increase could contribute to justify the percentage pressure drop difference between the three tests showed in Figure 5.31. Thus it is believed that the mean Peclet number variation throughout the soot loading process acts on the generated pressure drop by means of the combined action of the porous wall permeability variation related to the different soot penetration thickness and of the particle layer density and permeability variation.

5.4.3 Optical description of soot deposition

After the tests in the flow test bench the three DPFs were cut and optically analysed with the SEM. Aim was to check the influence of the Peclet number variation on the particles deposition inside the porous wall and in the particle layer. Cuts were performed following the same methodology than in the case of the characterization of the effect of the pre-DPF water injection (Figure 5.16). The selected axial position to perform the optical analysis was the outlet section of Section #3, corresponding to 14.5 cm from the filter inlet. As shown in Figure 5.32, four samples of 10 mm thickness, 35 mm length and 15 mm width were obtained from the outer part of DPF #2 (reference), #3 and #4.

The particle layer thickness in the four sections shown in Figure 5.32 of every DPF was measured using the caliper of the SEM. The measures were performed in different channels and different positions of the same channel. As a result almost 200 measures per DPF were taken, around 50 for any section. Figure 5.33 shows an example of SEM images of the whole channel for every DPF and a plot of the performed measures.

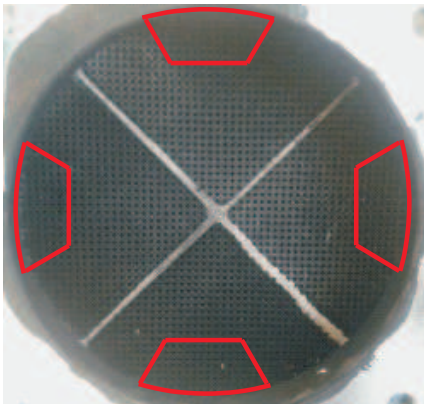

Figure 5.32: Positions of the cut to obtain SEM samples.

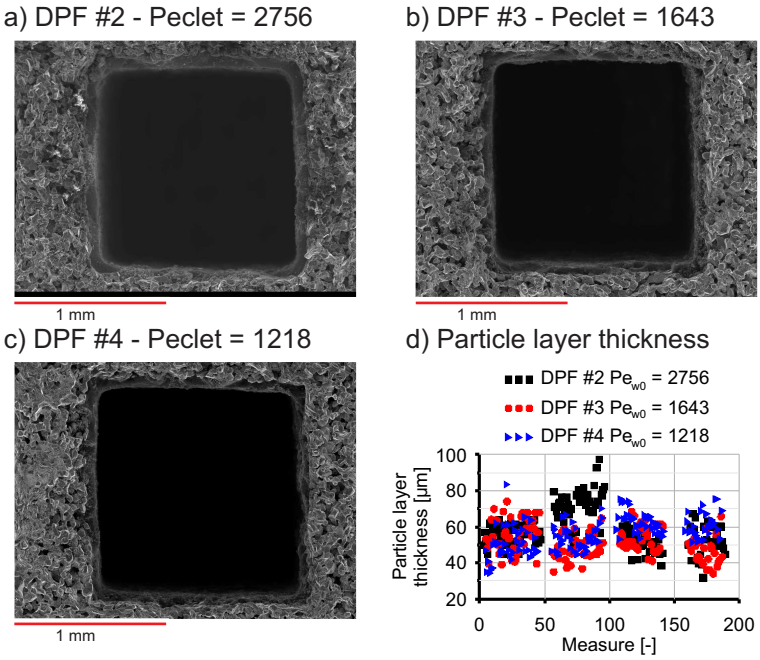

Figure 5.33: Examples of SEM images of the whole channel and measured particle layer thickness of DPF #2 (reference), #3 and #4.

SEM images in Figure 5.33 show very similar particle layer thickness independently of the DPF. This result is confirmed by the caliper measurements shown in Figure 5.33(d). The calculated mean particle layer thickness values

are 58.6, 51.4 and 56.3 μm for DPF #2, #3 and #4 respectively. To deeper analyse the collected data, the frequency density of any measured value was calculated considering 5 μm width intervals, i.e. the frequency of a value comprised between 0 and 5 μm, 5 and 10 μm, 10 and 15 μm and so on up to 120 μm was calculated. Figure 5.34 shows the result of the calculation. DPF #2 and #4 present a peak of frequency density at 55 μm whilst in the case of DPF #3 the value is slightly lower, i.e. 50 μm. Also, DPF #2 shows a non-negligible frequency density for high particle layer thickness values, in the range 75-85 μm. This trend contrasts with the literature in which decreasing particle layer density with decreasing mean Peclet number is shown. Considering that the collected soot mass is similar in the three performed soot loading tests, a thinner particle layer was expected when moving from DPF #4 to DPF #2, i.e. for increasing mean Peclet number. Anyway a notable dispersion in the measured values was observed, contributing to the uncertainty of the results. Minimum and maximum measured values were 31.6-97.4 μm with a standard deviation of 11.5 μm for DPF #2, 34-74 μm with a standard deviation of 8.75 μm for DPF #3 and 34.3-83.3 μm with a standard deviation of 9 μm for DPF #4.

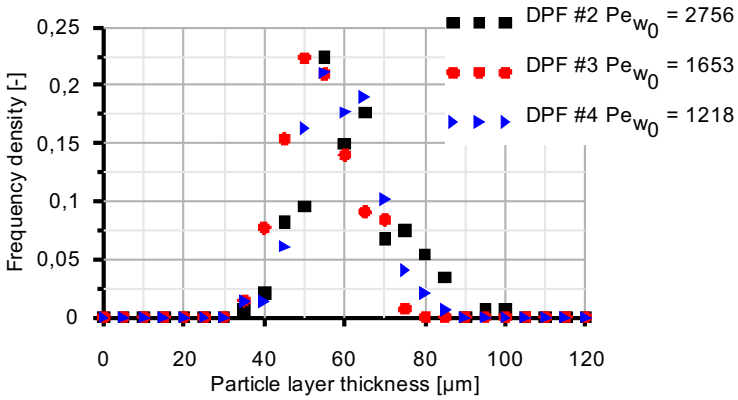

Figure 5.34: Frequency density plot of the measured particle layer thickness of DPF #2 (reference), #3 and #4.

This dispersion in the data is mainly related to three reasons. The irregularity of the porous wall surface makes difficult to establish the boundary between porous wall and particle layer, thus making impossible to establish a reference line to take as 0 for the measure of the particle layer thickness. On the other hand the reduced particle layer thickness, coupled with the previous mentioned issue, results in a marked absolute and percentage deviation between the measures. Last, despite the high magnification number at which the measures were taken, the SEM caliper showed to be very sensible to small variations,

i.e. a small difference in pixels when taking the measure results in a notable difference in microns. Therefore, to get more reliable results about the particle layer thickness, tests with higher soot load, hence thicker cake layer, should be analysed as this would contribute to reduce the impact of the measurement error on the thickness evaluation.

To analyse the effect of the mean Peclet number variation throughout the soot loading process on the particles deposition inside the porous wall, several SEM images at high magnification of the pores of the sections shown in Figure 5.32 have been analysed for every DPF. Figure 5.35 shows an example of images taken in different sections of the studied DPFs.

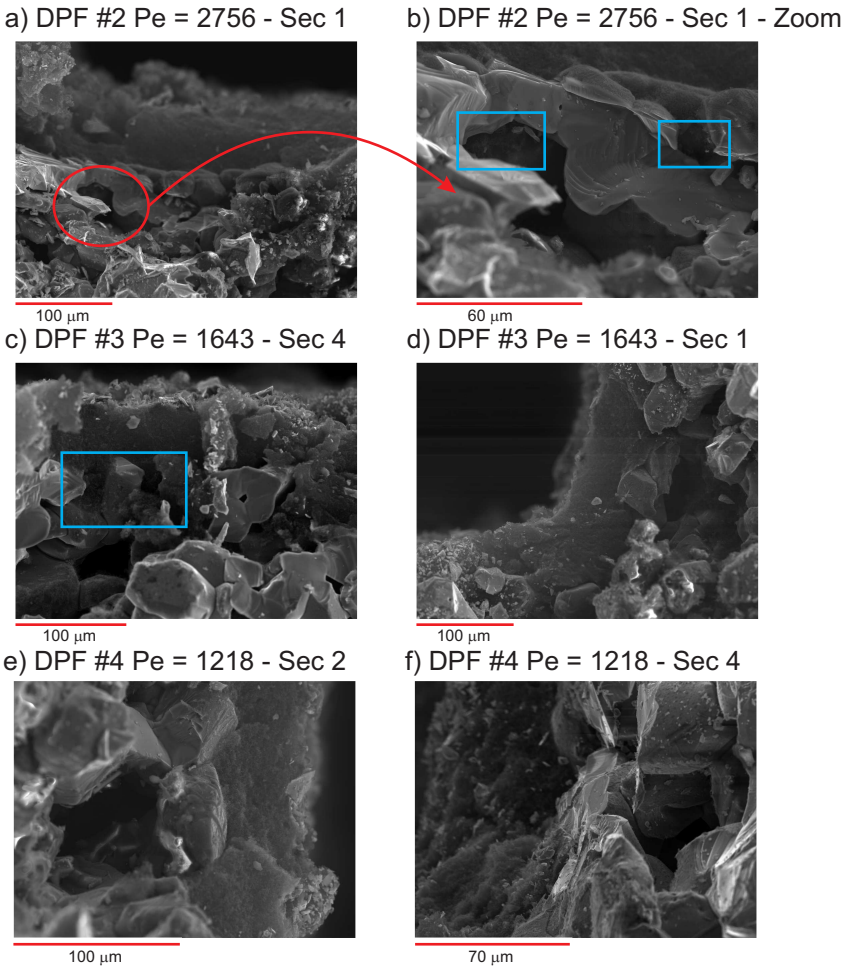

Figure 5.35: Examples of SEM images (left) and elemental map (rigth) at axial position 14.5 cm of DPF #2, #3 and #4.

As in the case of the soot loading process analysed in Section 5.3.2 for the characterization of the pre-DPF water injection technique, no deep penetration of soot inside the porous wall has been observed in none of the cases, as claimed in this work. Occasionally some sparse presence of particles in the form of a misty, dispersed structure has been noted in superficial pores, as marked by blue squares in Figures 5.35(b) and (c). The observed behaviour, with higher presence of soot inside the porous wall as the Peclet number increases, agrees with the calculated soot penetration thickness, i.e. 5.23 μm, 3.12 μm and 2.31 μm for DPF #2, #3 and #4 respectively, which predict very superficial particles deposition in all the considered DPFs. Again, as in the case of the characterization of the pre-DPF water injection technique, the calculated soot penetration thickness is of the order of magnitude of the porous wall rugosity in all the tested Peclet number case.

Despite the impossibility of drawing reliable conclusions on the effect of the mean Peclet number on the particle layer density from optical analysis because of the low reached soot mass, the measured pressure drop behaviour does not leave any space for uncertainties. Concerning general conclusions, soot loading processes at reduced mean Peclet number exhibit lower pressure drop. The reason lies in the coupling of lower soot particles penetration inside the porous wall and higher cake layer porosity. As a result the permeabilities of the porous media are increased. Thus it is possible to conclude that the inlet DPF flow dynamic field characteristic of the pre-turbo positioning, corresponding to reduced filtration velocity and Peclet number comparing with the post-turbo positioning, results in favourable particles deposition characteristics that finally leads to a reduction of the generated pressure drop.

5.5 Summary

In the present chapter the effect of the modification of the particles deposition characteristics inside the DPF has been experimentally analysed. Two different manners of modifying the particles deposition were taken into account. On one hand, the effect of the pre-DPF water injection technique was analysed. It involves the variation of the already deposited soot particles. On the other hand, the impact of the Peclet number defining the soot loading process was also analysed.

The aim of the pre-DPF water injection technique is to limit and/or control the pressure drop generated by a loaded DPF. The application of consecutive pre-DPF water injections throughout the soot loading process led to a maximum 70% pressure drop and 10% bsfc reduction at the end of the soot loading process (44.6 soot grams) comparing with the case of the reference test. The DPF loaded up to 44.6 g in reference conditions has been divided into four quarters. Three of

them were subjected to a single water injection event in different conditions in a flow test bench, i.e. varying the injected water mass and the air mass flow at the moment of the injection. A pressure drop reduction around 85% was measured after the single injections performed in the flow test bench with no sample mass variation. The optical analysis of the reference sample at different axial positions evidenced a mean particulate layer thickness of 550 μm, i.e. almost completely clogged inlet channels. The analysis of the quarter samples subjected to pre-DPF water injection allowed finding out that the water flow physically clean the channels de-clogging them. The number of de-clogged channels is mainly affected by the injected water mass and the axial position. It was observed a reduction of de-clogged channels, i.e. a reduction of the technique effectiveness, when reducing the injected water mass from 168.6 g to 83.2 g. Also, the number of de-clogged channels was observed to decrease moving towards the rear end of the inlet channels. The analysis of the de-clogged channels revealed that the technique effectiveness can be strongly improved by optimizing the injection strategy. It was observed indeed that the water flow only affected a limited portion of the inlet sample cross-section area, in particular the lower part. The optimization of the injection strategy in order to obtain a water flow affecting the whole sample frontal section could lead to a notable increase of the pressure drop reduction and bsfc saving related to the pre-DPF water injection technique. The channels affected by the water injections have been shown to present a thin soot layer covering the channel surface with sparse, random presence of particle layer fragments of variable thickness. An accumulation of particles layer fragments has been found in the rear end part of the inlet channels. It is believed that the water flow tends to detach big fragments of the particle layer and push them towards the end of the inlet channels leaving almost clean the overwhelming majority of the channel length. About the particles deposited inside the porous wall, the pre-DPF water injection technique has been showed to have none effect on them. Comparing SEM images of the reference sample with images of samples subjected to water injection, focusing on the inner part of the porous wall no remarkable differences were observed. A very superficial penetration was observed in all cases, in agreement with the soot penetration thickness estimated with the correlation developed in the present work. The lack of difference in the particles deposited inside the porous wall together with the observed residual thin soot layer is believed to be responsible of the high filtration efficiency (> 99%) experimentally measured by Bermúdez *et al.* [25] after the pre-DPF water injections.

With respect to the Peclet number variation, three soot loading processes were performed in identical DPFs up to similar soot load mass (≈ 7 g) varying the Peclet number by controlling the mass flow through the DPF. Experimental results from the engine test bench evidenced that the change from deep bed to cake layer filtration regime takes place at higher collected soot mass as the Peclet

number increases. It indicates an increasing particles penetration thickness inside the porous wall as the Peclet number increase, in accordance with the proposed Peclet number - soot penetration thickness correlation (Section 3.8). To deeply analyse the influence of the Peclet number decrease on the generated pressure drop the DPFs were also tested in a flow test bench. A sweep in inlet air mass flow at 100°C and 200°C was performed. The measured pressure drop has been shown to decrease as the Peclet number throughout the soot loading does. It is believed to be due to the coupling of the reduced particles penetration thickness inside the porous wall, which leads to higher porous wall permeability, and increased particulate layer porosity, which in turn sets a higher particulate layer permeability. Although related to the porosity, no reliable conclusions could be drawn about the particle layer thickness, hence density. The layer thickness values obtained applying the SEM technique resulted to be almost identical in the three DPFs. Anyway, issues related with the porous wall rugosity and the reduced particle layer thickness resulted in a great dispersion of the data. On the other hand the analysis of SEM images of the porous wall permitted to state that no deep penetration of soot particles inside the porous wall occurred, as predicted by the Peclet number - soot penetration thickness correlation proposed in Section 3.8. Some sparse presence of particles in the form of a misty, dispersed structure was only observed in superficial pores.

5.6 References

[11] S. Nishina, K. Takeuchi, M. Shinohara, M. Imamura, M. Shibata, Y. Hashimoto, and F. Watanabe. “Novel nondestructive imaging analysis for catalyst washcoat loading and DPF soot distribution using terahertz wave computed tomography”. In: *SAE International Journal of Fuels and Lubricants* 5(1) (2011), pp. 343–351 (cit. on pp. 3, 189).

[12] Y. Liu, C. Su, A. Clerc J.and Harinath, and L. Rogoski. “Experimental and modeling study of ash impact on DPF backpressure and regeneration behaviors”. In: *SAE International Journal of Engines* 8(3) (2015), pp. 1313–1321. (Cit. on pp. 3, 189, 249).

[13] A. G. Konstandopoulos, E. Skaperdas, and M. Masoudi. “Microstructural properties of soot deposits in Diesel particulate traps”. In: *SAE Technical Paper 2002-01-1015*. 2002 (cit. on pp. 3, 27, 189, 206, 227).

[14] J. Liu, J. J. Swanson, D. B. Kittelson, D. Y. H. Pui, and J. Wang. “Microstructural and loading characteristics of diesel aggregate cakes”. In: *Powder Technology* 241 (2013), pp. 244–251 (cit. on pp. 3, 189, 206, 214, 227).

[24] V. Bermúdez, J. R. Serrano, P. Piqueras, and O. García-Afonso. “Pre-DPF water injection technique for loaded DPF pressure drop reduction and control”. In: *Applied Energy* 140 (2015), pp. 234–245 (cit. on pp. 5, 8, 43, 44, 48, 80, 203).

[25] V. Bermúdez, J. R. Serrano, P. Piqueras, and D. Campos. “Analysis of the influence of pre-DPF water injection technique on pollutants emission”. In: *Energy* 89 (2015), pp. 778–792 (cit. on pp. 5, 45–47, 65, 216, 233).

[32] F. Payri, A. Broatch, J. R. Serrano, and P. Piqueras. “Experimental-theoretical methodology for determination of inertial pressure drop distribution and pore structure properties in wall-flow diesel particulate filters (DPFs)”. In: *Energy* 36 (2011), pp. 6731–6744 (cit. on pp. 17, 18, 78, 125, 198).

[34] M. Lapuerta, R. Ballesteros, and F. Martos. “A method to determine the fractal dimension of diesel soot agglomerates”. In: *Journal of Colloid and Interface Science* 303 (2006), pp. 149–158 (cit. on pp. 20, 226).

[144] J. M. Desantes, V. Bermúdez, S. Molina, and W. G. Linares. “Methodology for measuring exhaust aerosol size distributions using an engine test under transient operating conditions”. In: *Measurement Science and Technology* 22(11) (2011), p. 115101 (cit. on pp. 80, 194).

[145] C. D. Depcik and D. Assanis. “Simulating area conservation and the gas-wall interface for one-Dimensional based Diesel particulate filter models”. In: *Journal of Engineering for Gas Turbines and Power* 130(6) (2008), p. 062807 (cit. on pp. 80, 81, 204).

[159] G. C. Koltsakis, A. Konstantinou, O. A. Haralampous, and Z. C. Samaras. “Measurement and intra-layer modelling of soot density and permeability in wall-flow filters”. In: *SAE Technical Paper 2006-01-0261*. 2006 (cit. on pp. 189, 206, 213, 214, 227).

[160] S. Bensaid, D. Marchisio, N. Russo, and D. Fino. “Experimental investigation of soot deposition in diesel particulate filters”. In: *Catalysis Today* 147S (2009), S295–S300 (cit. on p. 189).

[161] Y. Wang, V. Wong, A. Sappok, and S. Munnis. “The sensitivity of DPF performance to the spatial distribution of ash inside DPF inlet channels”. In: *SAE Technical Paper 2013-01-1584*. 2013 (cit. on p. 189).

[162] S. Bagi, V. Sharma, M. Patel, and P. B. Aswath. “Effects of Diesel soot composition and accumulated vehicle mileage on soot oxidation characteristics”. In: *Energy & Fuels* 30(10) (2016), pp. 8479–8490 (cit. on p. 189).

[163] A. G. Konstandopoulos, M. Kostuglou, N. Vlachos, and E. Kladopoulo. “Progress in Diesel particulate filter simulation”. In: *SAE Technical Paper 2005-01-0946*. 2005 (cit. on pp. 189, 206, 227).

[164] *TSI. Model 3090. Engine exhaust particle sizer spectrometer. Operation and service manual.* (Cit. on p. 194).

[165] R. Montajir, T. Kusaka, Y. Bamba, and M. Adachi. “A New Concept for Real-Time Measurement of Particulate Matter (Soot and SOF)”. In: *SAE Technical Paper 2005-01-3605*. 2005 (cit. on p. 194).

[166] *Dekati. Fine smart particle sampler FPS-4000. Operation and service manual.* (Cit. on p. 194).

[167] V. Bermúdez, J. V. Pastor, J. J. López, and D. Campos. “Experimental correlations for transient soot measurement in diesel exhaust aerosol with light extinction, electrical mobility and diffusion charger sensor techniques”. In: *Measurement Science and Technology* 25 (2014), p. 065204 (cit. on p. 195).

[168] L. Pickett, D. Siebers, and C. Idicheria. “Relationship between ignition processes and thelift-off length of Diesel fuel jets”. In: *SAE Technical Paper 2005-01-3843*. 2005 (cit. on p. 196).

[169] J. Dec. “A conceptual model of DI Diesel combustion based on laser-sheet imaging”. In: *SAE Technical Paper 970873*. 1997 (cit. on p. 196).

[170] D. Tree and K. Svensson. “Soot processes in compression ignition engines”. In: *Progress in Energy and Combustion Science* 33 (2007), pp. 372–309 (cit. on p. 196).

[171] J. M. Desantes, J. J. Arrégle J..and López, and A. García. “A comprehensive study of Diesel combustion and emissions with post-injection”. In: *SAE Technical Paper 2007-01-0915*. 2007 (cit. on p. 196).

[172] I. J. Goldstein, D. E. Newbury, D. C. Joy, C. E. Lyman, P. Echlin, E. Lifshin, L. Sawyer, and J. Michael. *Scanning electron microscopy and X-ray microanalysis. Third edition.* Kluwer academic / Plenum, 2012 (cit. on pp. 200, 201).

[173] D. McMullan. “Von Ardenne and the scanning electron microscope”. In: *Proceedings of the Royal Microscopical Society* 23 (1988), pp. 283–288 (cit. on p. 200).

[174] D. McMullan. “Scanning electron microscopy 1928–1965”. In: *Scanning* 17 (3) (1995), pp. 175–185 (cit. on p. 200).

[175] M. Von Ardenne. *Improvements in electron microscopes*. GB 511204. 1937 (cit. on p. 200).

[176] I. J. Goldstein, D. E. Newbury, P. Echlin, D. C. Joy, C. Fiori, and E. Lifshin. *Scanning electron microscopy and x-ray microanalysis*. Plenum Press, 1981 (cit. on p. 201).

[177] S. Yang, C. Deng, Y. Gao, and Y. He. “Diesel particulate filter design simulation: a review”. In: *Advances in Mechanical Engineering* 8(3) (2016), pp. 1–14 (cit. on p. 204).

[178] J. Lupsea, M. Campoloa, and A. Soldati. “Modelling soot deposition and monolith regeneration for optimal design of automotive DPFs”. In: *Chemical Engineering Science* 151 (2016), pp. 36–50 (cit. on p. 213).

[179] T. D. Elmoe, A. Tricoli, J. D. Grunwaldt, and S. E. Pratsinis. “Filtration of nanoparticles: evolution of cake structure and pressure-drop”. In: *Journal of Aerosol Science* 40 (2009), pp. 965–981 (cit. on p. 214).

[180] T. D. Elmoe, A. Tricoli, and J. D. Grunwaldt. “Characterization of highly porous nanoparticle deposits by permeance measurements”. In: *Powder Technology* 207 (2011), pp. 279–289 (cit. on p. 214).

CHAPTER 6

Conclusions and future works

Contents

6.1 Introduction

AN analysis of the filtration and pressure drop phenomena happening in a wall-flow DPF has been performed in the present work. The problem has been approached from a computational and an experimental point of view. Thus, the first part of this thesis has been dedicated to the development, coding and implementation in OpenWAM™ of a wall-flow PF filtration model. The developed code has been firstly validated versus several experimental soot loading processes, both in-house and from the literature. Its capacity of predicting the pressure drop and the filtration efficiency dynamics of wall-flow DPFs has been proven. Concerning the filtration efficiency, the model has been shown to be able to deal with the effect of the particle size distribution. The capability of the filter of retaining particles of different size within the range of Diesel engines emission has been modelled with good accuracy. In the mark of the developed model has also been proposed a correlation to estimate the soot penetration thickness inside the porous wall from the Peclet number.

Later, the developed model has been used to evaluate the potential for aftertreatment (DOC&DPF) volume downsizing considering the conventional post-turbo aftertreatment configuration, i.e. downstream of the turbine, and the pre-turbo configuration, i.e. upstream of the turbine. On the DOC side, the effect of the volume downsizing on the generated pressure drop and the Dwell time, as an index of the HC and CO conversion efficiency, has been evaluated. On the DPF side on the other hand an accurate analysis of the monolith volume reduction effect on the generated pressure drop and filtration efficiency, both in clean and soot loaded substrate conditions, has been performed. The volume reduction analysis has been approached considering two extreme cases: keeping constant the specific filtration area, hence the cell density, and keeping constant the filtration area. Also, the effect of the DOC&DPF monoliths volume downsizing on the cost of these systems has been analysed. Last, the variation of the engine response during transient operation related to the aftertreatment volume reduction has been evaluated.

It has been stated that the cell density increase to keep constant the filtration area in downsized DPF could lead to an increased risk of inlet channels clogging. In case the high passive regeneration rate of the pre-turbo positioning is put aside, this proneness of channels clogging could be further increased in this aftertreatment positioning due to the characteristics of the flow field upstream of the turbine, i.e. lower Peclet number comparing with the post-turbo positioning. Bibliographic evidences indeed showed a particulate layer density reduction as the Peclet number throughout the soot loading process is reduced. Such a reduced density leads to a thicker particulate layer comparing at same soot load. To reduce or completely avoid the risk of inlet channels clogging the pre-DPF water injection technique has been experimentally evaluated by

coupling advanced optical techniques and pressure drop measurements in a flow test bench. On the other hand the above mentioned density reduction, characteristic of low Peclet number soot loading processes, is associated with an increase of the particulate layer permeability, what results in a reduction of the generated pressure drop with the resulting benefits for the engine fuel economy. Thus the effect of the Peclet number variation on the soot particles deposition dynamics has been evaluated. Again, the effects of the Peclet number reduction have been analysed by coupling advanced optical techniques and pressure drop measurements in a flow test bench.

6.2 Main contributions

The main contributions of this PhD thesis are summarized in the following sections. For the sake of clarity they are separated per topic.

6.2.1 PF filtration model

A 1D PF filtration model has been developed, described and validated within the framework of this PhD thesis. The model has been implemented in OpenWAM™. It is based on the packed bed of spherical particles approach to describe the properties of the porous medium. As a consequence the filtration efficiency of the porous substrate can be referred to the response of a single collector unit. To assess it the Brownian diffusion, interception and inertial deposition mechanisms are considered. According to experimental and computational evidences the main hypothesis of the model is the partial soot penetration into the porous wall. Therefore, the porous wall is divided into two layers: an inner one, i.e. facing the inlet channel, and an outer one, i.e. facing the outlet channel. The former is assumed to be the only one in which soot deposition takes place. Its microstructure is modified because of the soot accumulation in its interior. The outer slab is considered to be kept always clean, i.e. it is not subjected to particles accumulation.

The model includes a sticking coefficient in the filtration efficiency calculation. Such a parameter has to be included in order to properly predict the filtration efficiency in clean conditions but does not affect its evolution with the soot load.

The filtration efficiency and pressure drop dynamics have been shown to be governed by the soot penetration inside the porous wall. Their correct modelling relies on the proper estimate of the porous wall fraction affected by particles deposition. Thus, a correlation for the estimation of soot penetration thickness inside the porous wall has been proposed. It has been shown that soot penetration is linearly proportional to the Peclet number referred to the characteristics of the clean porous wall, i.e. porosity and collector unit diameter.

The application of the proposed correlation resulted in the precise modelling of the pressure drop and filtration efficiency dynamics measured in in-house and literature soot loading tests. On the other hand, the comparison of the calculated penetration thickness with SEM images of 3 different soot loaded DPFs samples has showed that the use of the representative aggregate particles diameter provides soot penetration values that comprise the overwhelming majority of the collected soot mass.

The analysis of the modelled results indicates that the transition between deep bed and cake filtration regime depends on the flow field prediction, which causes the saturation of the porous wall along the inlet channel length. Therefore, transition in pressure drop, i.e. the reduction of its increasing rate up to be governed by the particulate layer properties, is essentially dependent on macroscale properties. Consequently 1D modelling is required for its correct prediction in order to avoid mismatch in the evolution of microscale properties such as porosity or mean pore diameter change. The capability to model the local transition, which depends on microgeometry properties of the loaded porous wall, is very limited in lumped quasi-steady porous medium models. It is based on criteria related to cell loading and effective filtration area for particulate layer initial growth. Nevertheless, the influence of these phenomena on the filter response has been shown to be of second order. The interest for these approaches lies in the need to avoid non-physical discontinuities thus providing a smooth variation of the involved porous media properties.

Last, very good accuracy to predict the filtration efficiency as a function of the particle size has been obtained. It has been computed within the range of aerosol size in internal combustion engines, i.e. covering from primary to aggregate particles. It has been shown that the governing parameters for the right modelling of the DPF filtration efficiency as a function of the particle size are the Brownian diffusion and interception deposition mechanisms.

6.2.2 Aftertreatment volume downsizing in pre- and post-turbo configuration

The benefits, in terms of aftertreatment (DOC&DPF) volume downsizing, related to the pre-turbo aftertreatment architecture have been computationally evaluated. The calculations have comprised volume, i.e. monolith diameter and effective length, variations keeping constant the substrate micro-structure. Additionally, the study of the DPF performance also considered cellular geometry variations: for every volume the cell density has been modified imposing a cell size and porous wall thickness dependence given by constant TIF. This approach has allowed covering the influence of additional cell unit geometric parameters related to fluid-dynamic, thermal and mechanical performance. Furthermore the DPF analysis comprised both clean and soot loaded substrate conditions.

On the DOC side, it has been demonstrated that its volume can be reduced with barely effects on pressure drop, hence on engine fuel economy. Pressure drop can be reduced imposing length reduction at constant reference post-turbo diameter. Concerning dwell time, volume reductions close to 40% can be performed at medium-high load keeping constant dwell time between post- and pre-turbo DOC locations. At low load the dwell time can become lower in pre-turbo configuration with respect to the traditional placement. It is related to the lack of gas density increase in pre-turbo placement in this operating region due to the low pressure increase in comparison with the temperature raise. Nevertheless, such a temperature increase and the flow conditions ensure fast light-off and high conversion efficiency despite the volume reduction.

On the DPF side, the post-turbo placement has shown a worse behaviour than the pre-turbo concerning engine fuel consumption penalty. This penalty is increasing as the monolith volume decreases being specially damaging under soot loading conditions. The analysis has revealed that as volume reduces the pressure drop performance can be recovered increasing the cell density, i.e. the filtration area. However, the lower capability for ash accumulation can become a critical constraint. In addition, inlet channels plugging problems may arise as the cell density is increased since in post-turbo DPF placement the average soot loading is expected to be high. On the contrary, results obtained with pre-turbo DPF placement have confirmed the lower pressure drop generated by the DPF in this location and how the differences positively grow as the DPF gets loaded. The fuel consumption is scarcely sensitive to volume and soot loading changes because of the pressure drop location with respect to the turbine. Consequently the VGT control calibration becomes less sensitive to these variables. From a fluid-dynamic point of view, it has been shown that the DPF volume may be reduced more than 40% in pre-turbo placement. This reduction would not have effect on fuel economy under clean DPF conditions. Under soot loading operation the fuel consumption would be the same of the reference volume in post-turbo architecture. If the cell geometry is modified to keep constant the filtration area, the benefits in pressure drop reduction lead to almost constant fuel consumption independently of the monolith volume. The lower capability for ash accumulation related to the cell density increase is believed to be less problematic in pre-turbo aftertreatment configuration. The low sensitivity to soot loading of the bsfc in this configuration is also applicable to ash loading. This solution has as limit channel plugging issues due to high cell density. Nevertheless, soot loading in pre-turbo DPF configuration is expected to be low because of the high temperature. Therefore, a balance solution between constant specific filtration area and constant filtration area should exist. It should provide safe DPF operation and lower pressure drop with minimum fuel consumption penalty. It is also important to consider that the increase of filtration area can be obtained keeping the mechanical performance of the

monolith but increasing heat transfer and losses, i.e. LOF and HTP. These last items must be considered in pre-turbo aftertreatment applications because of the effect on the turbocharger lag under cold wall operating conditions.

Concerning the DPF capacity of retaining particles, the pre-turbo configuration provides higher filtration efficiency both for clean and low soot loading compared with post-turbo location. This is due to the lower Peclet number upstream of the turbine. As a consequence, tailpipe emitted particle mass and number before convergence to maximum filtration efficiency would be lower in pre-turbo DPF configurations. The above described potential for DPF downsizing of pre-turbo DPF configuration based on fluid-dynamic criteria (engine fuel economy reduction) is strengthened by the fact that the monolith volume can be reduced around 40% within a wide range of meso-geometry definitions improving the filtration performance with respect to post-turbo placement. As for the pressure drop, volume reduction at constant specific filtration area, i.e. constant cell density, has revealed to be more prejudicial on the filtration efficiency than volume reduction at constant filtration area. Nevertheless the resulting value after a 33% monolith volume downsizing at constant SFA in pre-turbo case is still equal to the baseline one in post-turbo location. TIF is shown to be a second-order parameter on filtration efficiency and might be set based on pressure drop and thermo-mechanical resistance criteria. Consequently, this kind of strategy keeps the original DPF filtration performance with improvements in pressure drop (bsfc) and cost-savings in materials. The opposed strategy is to reduce the monolith volume keeping constant the filtration area at the same time TIF is also kept. The advantage is that the filtration efficiency keeps the same value as in baseline volume, both in pre- and post-turbo DPF placement (differences between these configuration remain). It is added to the benefits in pressure drop related to constant filtration area. The analysed possibility of reducing the aftertreatment systems volume in pre-turbo placement also has a strong influence on the final engine price. Considering a DOC volume downsizing close to 40% (from 1.73 to 1.09 litres) and a DPF one around 33% (from 2.43 to 1.57 litres) it was estimated a 13.3% cost saving on the whole Euro 6 aftertreatment price. In the final analysis this leads, assuming that the aftertreatment represents around 30% of the engine final price, to a 4% cheaper engine. Although the reduction of the aftertreatment thermal inertia improves the DPF and DOC thermal transient, the engine response under transient operation with cold wall conditions has been shown to be extremely poor in single stage turbocharged engines. This is the main drawback concerning pre-turbo aftertreatment architectures, which demands two-stage turbocharged solutions or the use of superchargers combined with a proper boost control as a strategy to keep engine drivability. It increases the packaging complexity of the exhaust line but would take out the advantages of this placement in terms of engine fuel economy and aftertreatment performance.

6.2.3 Pre-DPF water injection effect

The pre-DPF water injection is a relatively new technique patented by CMT - Motores Térmicos aimed to reduce and control the pressure drop generated by a soot and/or ash loaded DPF. It modifies the particulate layer distribution in the inlet channels generating a pressure drop reduction. In the mark of this thesis the interest in this technique relies in its potential for limiting or completely avoiding the risk of inlet channels clogging at high soot loadings related to the filter volume downsizing. The effectiveness of this technique has been experimentally proven in the present work by means of tests in the engine test bench, i.e. performing several water injections throughout a soot loading process, and in the flow test rig, i.e. performing a single water injection on quarter filter samples.

In the first case the effect of the pre-DPF water injections has been analysed by comparing two soot loading tests up to similar soot load in the same engine operating point. In the first test 22 water injections were performed while the second test was run in reference conditions, i.e. no water injections. The comparison showed a maximum 70% pressure drop and 10% bsfc reduction at the end of the reference soot loading process.

After these tests, the DPF loaded in reference conditions was divided into four quarters. Three of these quarters were subjected to a single water injection event in different conditions in a flow test bench, i.e. varying the injected water mass and the air mass flow at the moment of the injection, the last one was kept as a reference. The pressure drop and the weight of any quarter was compared before and after the injection to characterize the effect of the water injection and prove that the pressure drop reduction is not due to soot release related to the injection. A pressure drop reduction comprised between 75% and 95% was measured after the three single injections performed in the flow test bench with no sample mass variation. The optical analysis of the reference sample at different axial positions evidenced that the high achieved soot mass inside the filter (12.9 g/l) resulted in a mean particulate layer thickness of 550 μm, i.e. almost completely clogged inlet channels. The analysis of the quarter samples subjected to single pre-DPF water injection allowed to find out that the water flow physically clean the channels de-clogging them. The number of de-clogged channels is mainly affected by the injected water mass and the axial position. It was observed a reduction of de-clogged channels, i.e. a reduction of the technique effectiveness, when reducing the injected water mass. The air mass flow at the moment of the injection has been shown to have minor importance on the technique effectiveness within the analysed range. In all the three cases the number of de-clogged channels was observed to decrease moving towards the rear end of the inlet channels. The analysis of the number of de-clogged channels revealed that the technique effectiveness can be strongly

improved by optimizing the injection strategy in order to homogeneously affect the whole cross-section area. It was observed indeed that the water flow only affected a limited portion of the inlet sample cross-section area. The channels affected by the water injections were shown to present a thin soot layer covering the channel surface with sparse, random presence of particulate layer fragments of variable thickness. An accumulation of particles layer fragments has been found in the rear end part of the inlet channels at axial position 21.5 cm, i.e. 1.5 cm from the filter end. It is believed that the water flow tends to detach big fragments of the particulate layer and push them towards the end of the inlet channels leaving almost clean the overwhelming majority of the channel length. About the particles deposited inside the porous wall, the comparison of SEM images of the reference sample with images of samples subjected to water injection has not evidenced any influence due to the water drag. A very superficial penetration has been observed in all cases, in agreement with the soot penetration thickness estimated with the correlation developed in the present work. The lack of difference in the particles deposited inside the porous wall together with the observed residual thin soot layer is believed to be responsible of the high filtration efficiency after the pre-DPF water injections ($> 99\%$) experimentally measured in previous tests at CMT - Motores Térmicos.

6.2.4 Peclet variation effect

The interest in the Peclet number variation effect on the particles deposition dynamics in the present work is related to its importance on the analysis of the pre-turbo DPF positioning. It has been showed in this work that when the DPF is placed upstream of the turbine it works at a lower Peclet number. Literature evidences state that the decrease of the Peclet number throughout a soot loading process leads to the increase of the particulate layer porosity. As a consequence, the density of the particulate layer is lowered whilst its permeability increases.

The analysis of the Peclet number variation effect was experimentally assessed by performing three soot loading processes in identical DPFs up to similar soot load mass but varying the exhaust gas mass flow across the DPF with a by-pass system. As a result, the soot loading tests were performed at three different Peclet numbers. Experimental results from the engine test bench evidenced that the change from deep bed to cake layer filtration regime takes place at higher collected soot mass as the Peclet number increase. It indicates an increasing soot penetration thickness inside the porous wall as the Peclet number increase, in accordance with the proposed Peclet number - soot penetration thickness correlation.

To deeply analyse the effect of the Peclet number variation, the pressure drop of the DPFs was also measured in a flow test bench at different temperature and air mass flow. The measured pressure drop has been shown to decrease with

the Peclet number throughout the soot loading, a reduction comprised between $\approx 15\%$ and $\approx 25\%$ has been calculated. It is believed to be due to the coupling of the reduced particles penetration thickness inside the porous wall, which leads to higher porous wall permeability, and increased particulate layer porosity, which in turn sets a higher particulate layer permeability. Although related to the porosity, no reliable conclusions could be drawn about the particulate layer thickness, hence density. The SEM caliper has been used to take a high number of measures of the particulate layer thickness for each DPF. Both the calculated mean and more probable particulate layer thickness values resulted to be almost identical in the three DPFs. Anyway, issues related with the porous wall rugosity and the reduced particulate layer thickness resulted in a great dispersion of the data. On the other hand the analysis of SEM images of the porous wall permitted to state that no deep penetration of soot particles inside the porous wall occurred, as predicted by the Peclet number - soot penetration thickness correlation developed in Section 3.8. Some sparse presence of particles in the form of a misty, dispersed structure was only observed in superficial pores.

6.3 Future works

Several topics treated in the present work are worth of further investigation, either because of the interest in making the model more predictive or because of the possibility of their on-engine application.

In Chapter 3 it has been stated that a sticking coefficient appears in the evaluation of the porous wall filtration efficiency. Currently this parameter needs to be adjusted from experimental data in order to precisely reproduce the filtration efficiency value in clean porous wall conditions. The analysis and the modelling of a large number of soot loading processes with different DPF microstructure and fluid dynamic conditions, either in-house or from the literature, could be useful in the definition of a correlation for this parameter, making the developed model more predictive.

About the DPF model of OpenWAM™, the implementation of a 1D regeneration sub-model is required to achieve a complete computational tool able to precisely calculate the global filter behaviour during real driving conditions functioning. It will provide the possibility of simulating standard driving cycles like the NEDC or the WHTC as well as predicting the DPF behaviour during on-road emission testing as provided for by the RDE legislation. On the other hand, the development and the implementation in OpenWAM™ of DOC, LNT and SCR models are required to completely simulate the tail pipe emissions and the engine behaviour. Two PhD thesis are currently being developed at CMT - Motores Térmicos on these themes.

About modelling, the extensive use of models to predict the engine and aftertreatment performance makes of great interest the developing of a lumped DPF model able to quickly calculate the pressure drop, filtration, regeneration and heat transfer phenomena taking place in this system. The loss of information implied by the use of lumped models would be compensated by the velocity of the calculation, making this tool very useful for preliminary design calculations or parametric studies. Such a tool could also be implemented in the engine control system, enhancing the regeneration control and the DPF diagnosis based on physical insights.

Regarding the aftertreatment downsizing, an experimental validation of the computationally obtained results would be of great interest. On the DOC side, the absence of channels plug results in the ease of physically reduce the monolith length and evaluate its effect on the CO and HC conversion efficiency in different engine operating conditions. On the DPF side, the presence of the channel plug makes the experimental evaluation of the diameter reduction effect viable in the current facilities of CMT - Motores Térmicos. On the other hand, the support of a DPF manufacturer would be probably necessary to experimentally evaluate the effect of the monolith length reduction. Also, a parametric study of the effect of the microstructure variation on a downsized DPF would be of interest, aimed to explore the possibility of further DPF performance improvements. Simulations of downsized monoliths considering the two proposed strategies, i.e. constant specific filtration area and constant filtration area, performing a sweep in porous wall porosity and mean pore diameter would add two degrees of freedom to the system. Thus, on one hand it will be possible to analyse microstructural solutions aimed to the optimization of the DPF back-pressure and filtration efficiency. On the other hand, the effect of the porosity on the tensile strength (eq. 2.48 [81]) and the modulus of elasticity (eq.2.49 [82]) of the porous wall would permit considering the structural and mechanical performance, i.e. TIF, MIF, LOF and HPT, in the optimization of the DPF. Also in this case the experimental evaluation of this study would require the support of a ceramic monolith manufacturer.

The pre-DPF water injection technique is probably the most innovative on-engine application studied in this PhD thesis. It could be applied either to downsized or to reference volume filters. On one hand in Section 3.6 it was stated that the developed filtration model has been provided with a feature that gives the possibility of simulating the water injection process. The availability of this computational tool could be very effective in the optimization of the pre-DPF water injection technique. In fact, the simulation of the experimental tests run in the present work would be helpful to achieve a deeper understanding of the phenomena related to the water injection and their effect on the flow field and the particles deposition inside the filter. On the other hand it has been stated in Section 5.3 that the performed pre-DPF water injection only affected a limited

portion of the monolit cross-section area, resulting in a limited number of de-clogged channels. The possibility of affecting the whole section of the DPF with the water injection would probably increase the number of de-clogged channels and could lead to a notable increase of the pressure drop reduction and bsfc saving related to the pre-DPF water injection technique. The time span between consecutive injections could be also increased because of the higher cleaned filtration area, hence more available surface for inlet particles deposition. An experimental validation of this hypothesis would be of great interest. Also on the experimental side, the characterization of the pre-DPF water injection on ash loaded, rather than soot loaded, DPFs would be worth of being performed. Experimental and computational studies of ash impact on DPF back-pressure [12] [65] showed that the presence of a thin ash membrane prevents deep bed filtration, hence reducing the pressure drop of soot loaded filters. As the ash load increases this benefit is reduced until the appearance of a rapid back-pressure increase due to the combined effect of the filter effective length reduction related to the ash plug and of the significant inlet channel hydraulic diameter reduction. The pre-DPF water injection has been shown in the present work to leave a thin particulate layer inside the affected channels. If the ash layer presents the same behaviour, i.e. a thin ash membrane is left after the pre-DPF water injection, the advantages related to it would be maintained. On the other hand, if the water injection resulted in the removal of the thick ash layer and the compaction of the ash plug some inlet channel hydraulic diameter and filter effective length would be recovered with the related back-pressure benefit. These hypothesis are considered worth of being experimentally validated.

To conclude, in Section 5.4 it has been impossible to draw reliable conclusions on the effect of the Peclet number variation on the particulate layer density due to the limited particulate layer thickness of the performed tests. The availability of a testing, cutting and imaging methodology, together with post-processing codes to estimate the particulate layer thickness from optical microscope images makes worth to plan a test campaign similar to the one performed in this work and described in Section 5.4. Though, in this case the ultimate collected soot mass should be such that the developed particulate layer presents a notable thickness in order to minimize the uncertainties in its measure. On the other hand the Peclet number range should be way much wider than the one considered in this study so to make the effect of the soot particles penetration inside the porous wall and its variation related with the Peclet number more evident.

The effect of the soot deposition variation, whether related to pre-DPF water injection or to inlet DPF Peclet number variation, on the regeneration dynamics is worth to be investigated. The characterization of the oxidation rate variations related to the water injection or the particulate layer characteristics defined by the Peclet number is of interest. The analysis of a large number of regenerations processes of DPFs loaded in known and controlled conditions, i.e. known Peclet

number, could lead to the identification of a correlation between this parameter and the oxidation rate. Such a correlation would be a powerful tool to implement in a DPF regeneration model. Also, the possible generation of hot-spots inside the filter and its effect on the monolith integrity has to be evaluated.

6.4 References

[12] Y. Liu, C. Su, A. Clerc J.and Harinath, and L. Rogoski. “Experimental and modeling study of ash impact on DPF backpressure and regeneration behaviors”. In: *SAE International Journal of Engines* 8(3) (2015), pp. 1313–1321. (Cit. on pp. 3, 189, 249).

[65] A. Sappok, Y. Wang, R. Wang, C. Kamp, and V. Wong. “Theoretical and experimental analysis of ash accumulation and mobility in ceramic exhaust particulate filters and potential for improved ash management”. In: *SAE International Journal of Fuels and Lubricants* 7(2) (2014), pp. 511–524 (cit. on pp. 32, 249).

[81] R. H. Heck, J. Wei, and J. R. Katzer. “Mathematical modeling of monolithic catalysts”. In: *Aiche journal* 22(3) (1976), pp. 477–484 (cit. on pp. 34, 248).

[82] G. Groppi, A. Belloli, E. Tronconi, and P. Forzatti. “A comparison of lumped and distributed models of monolith catalytic combustors”. In: *Chemical Engineering Science* 50(17) (1995), pp. 2705–2715 (cit. on pp. 34, 248).

Bibliography

[1] **Payri, F. and Desantes, J.**
Motores de combustión interna alternativos
ed. by Reverté, E. 2015 (cit. on p. 3)

[2] **Okui, N. and Kobayashi, M.**
"A study on hybrid control method for improvement of fuel economy and exhaust-gas emission of hybrid trucks"
in: *SAE Technical Paper 2015-01-1780* 2015 (cit. on p. 3)

[3] **Bond, T. C., Doherty, S. J., Fahey, D. W., Forster, P. M., and al., et**
"Bounding the role of black carbon in the climate system: A scientific assessment"
in: *Journal of Geophysical Research: Atmospheres* 118(11) (2013), pp. 5380–5552 (cit. on p. 3)

[4] **Oberdster, G. and Utell, M. J.**
"Ultrafine particles in the urban air: to the respiratory track and beyond"
in: *Environmental Health Perspectives* 110(8) (2002), A440–A441 (cit. on p. 3)

[5] **Pope, C. A. and Dockery, D. W.**
"Health effects of fine particulate air pollution: lines that connect"
in: *Journal of the Air and Waste Management Association* 56(6) (2006), pp. 709–742 (cit. on p. 3)

[6] **Gupta, A., Kartik, V., and Ramanarayanan, C.**
"Experimental study on performance of a parallel Diesel hybrid vehicle retrofitted with a single planetary gear train as an add-onn transmission"
in: *SAE Technical Paper 2016-28-0154* 2016 (cit. on p. 3)

[7] **Lajunen, A.**
"Energy efficiency of conventional, hybrid electric, and fuel cell hybrid powertrains in heavy machinery"
in: *SAE Technical Paper 2015-01-2829* 2015 (cit. on p. 3)

[8] **Burke, A.**
"Saving petroleum with cost-effective hybrids"
in: *SAE Technical Paper 2003-01-3279* 2003 (cit. on p. 3)

[9] *Regulation (EC) No 715/2007 of the European Parliament and of the Council of 20 June 2007 on type approval of motor vehicles with respect to emissions from light passenger and commercial vehicles (Euro 5 and Euro 6) and on access to vehicle repair and maintenance information*
Official Journal of the European Union 2007 (cit. on pp. 3, 62)

[10] **Serrano, J. R., Arnau, F. J., Piqueras, P., and García-Afonso, O.**
"Packed bed of spherical particles approach for pressure drop prediction in wall-flow DPFs (diesel particulate filters) under soot loading conditions"
in: *Energy* 58 (2013), pp. 644–54
(cit. on pp. 3, 15, 17, 19, 63, 71, 73, 82, 87, 167)

[11] **Nishina, S., Takeuchi, K., Shinohara, M., Imamura, M., Shibata, M., Hashimoto, Y., and Watanabe, F.**
"Novel nondestructive imaging analysis for catalyst washcoat loading and DPF soot distribution using terahertz wave computed tomography"
in: *SAE International Journal of Fuels and Lubricants* 5(1) (2011), pp. 343–351 (cit. on pp. 3, 189)

[12] **Liu, Y., Su, C., Clerc J.and Harinath, A., and Rogoski, L.**
"Experimental and modeling study of ash impact on DPF backpressure and regeneration behaviors"
in: *SAE International Journal of Engines* 8(3) (2015), pp. 1313–1321.
(Cit. on pp. 3, 189, 249)

[13] **Konstandopoulos, A. G., Skaperdas, E., and Masoudi, M.**
"Microstructural properties of soot deposits in Diesel particulate traps"
in: *SAE Technical Paper 2002-01-1015* 2002
(cit. on pp. 3, 27, 189, 206, 227)

[14] **Liu, J., Swanson, J. J., Kittelson, D. B., Pui, D. Y. H., and Wang, J.**
"Microstructural and loading characteristics of diesel aggregate cakes"
in: *Powder Technology* 241 (2013), pp. 244–251
(cit. on pp. 3, 189, 206, 214, 227)

[15] **Hiereth, H.**
"Daimler-Benz AG car test with a free-running pressure-wave charger - A study for an advanced supercharging system"
in: *SAE Technical Paper 890453* 1989 (cit. on pp. 4, 40)

[16] **Jenny, E., Hansel, J., and Mayer, A.**
"The transient behaviour of supercharged passenger car diesel engines fitted with particulate traps"
in: *SAE Technical Paper 890453* 1989 (cit. on pp. 4, 40)

[17] **Moya, D.**
"Contribución a la predición del ruido pulsante de admisión y escape en motores de combustión interna alternativos"
PhD thesis. Universitat Politécnica de Valéncia 2005 (cit. on p. 4)

[18] **Piqueras, P.**
"Contribution to thermo-and fluid dynamic modelling of wall-flow Diesel particulate filters (text in spanish)"
PhD thesis. Universitat Politécnica de Valéncia 2010
(cit. on pp. 4, 16)

[19] **García-Afonso, O.**
"Analisis teorico-experimental de la arquitectura pre-turbo de sistemas de post-tratamiento en MCIA"
PhD thesis. Universitat Politécnica de Valéncia 2013
(cit. on pp. 4, 42)

[20] **Reizig, M., Brück, R., Konieczny, R., and Treiber, P.**
"New Approaches to Catalyst Substrate Application for Diesel Engines"
in: *SAE Technical Paper 2001-01-0189* 2001 (cit. on p. 4)

[21] **Carberry, B., Grasi, G., Guerin, S., Jayat, F., and Konieczny, R.**
"Pre-turbocharger Catalyst - Fast catalyst light-off evaluation"
in: *SAE Technical Paper 2005-01-2142* 2005 (cit. on pp. 4, 121)

[22] *SCR system for 2-Stroke MAN Diesel Engines*
Johnson Matthey webpage: www.jmcatalysts.com 2009 (cit. on p. 4)

[23] **Desantes, J. M., Payri, F., Piqueras, P., and Serrano, J. R.**
Sistema de filtro
Spanish Patent ES2408243(B1) 2013 (cit. on pp. 5, 8, 16, 43)

[24] **Bermúdez, V., Serrano, J. R., Piqueras, P., and García-Afonso, O.**
"Pre-DPF water injection technique for loaded DPF pressure drop reduction and control"
in: *Applied Energy* 140 (2015), pp. 234–245
(cit. on pp. 5, 8, 43, 44, 48, 80, 203)

[25] **Bermúdez, V., Serrano, J. R., Piqueras, P., and Campos, D.**
"Analysis of the influence of pre-DPF water injection technique on pollutants emission"
in: *Energy* 89 (2015), pp. 778–792 (cit. on pp. 5, 45–47, 65, 216, 233)

[26] **Johnson, T.**
"Review of Vehicular Emissions Trends"
in: *SAE International Journal of Engines* 8(3):2015 (2015), pp. 1152–1167 (cit. on p. 15)

[27] *OpenWAM website, CMT - Motores Térmicos (Universitat Politécnica de Valéncia).*
www.openwam.org 2016 (cit. on pp. 16, 112)

[28] **Galindo, J., Serrano, J. R., Arnau, F. J., and Piqueras, P.**
"Description and analysis of a one-dimensional gas-dynamic model with Independent Time Discretization"
in: *Proceedings of the ASME Internal Combustion Engine Division 2008 Spring Technical Conference ICES2008* 2008
(cit. on pp. 16, 22, 67, 112)

[29] **Torregrosa, A. J., Serrano, J. R., Arnau, F. J., and Piqueras, P.**
"A fluid dynamic model for unsteady compressible flow in wall-flow Diesel particulate filters"
in: *Energy* 36 (2011), pp. 671–684
(cit. on pp. 16, 17, 36, 62, 63, 72, 81, 158)

[30] **Bisset, E. J.**
"Mathematical model of the thermal regeneration of a wall-flow monolith Diesel particulate filter"
in: *Chemical Engineering Science* 39.7-8 (1984), pp. 1233–1244
(cit. on p. 16)

[31] **Dullien, F.**
Porous Media. Fluid Transport and Pore Structure
Academic Press, New York 1992 (cit. on pp. 17, 33, 75)

[32] **Payri, F., Broatch, A., Serrano, J. R., and Piqueras, P.**
"Experimental-theoretical methodology for determination of inertial pressure drop distribution and pore structure properties in wall-flow diesel particulate filters (DPFs)"
in: *Energy* 36 (2011), pp. 6731–6744 (cit. on pp. 17, 18, 78, 125, 198)

[33] **Kuwabara, S.**
"The forces experienced by randomly distributed parallel circular cylinders or spheres in a viscous fluid at small Reynolds numbers"
in: *Journal of the Physical Society of Japan* 14 (1959), pp. 527–532
(cit. on pp. 17, 24, 30, 63)

[34] **Lapuerta, M., Ballesteros, R., and Martos, F.**
"A method to determine the fractal dimension of diesel soot agglomerates"
in: *Journal of Colloid and Interface Science* 303 (2006), pp. 149–158 (cit. on pp. 20, 226)

[35] **Heywood, J. B.**
Internal Combustion Engine Fundamentals
McGraw-Hill 1988 (cit. on p. 20)

[36] **Dobbins, R. A.**
"Soot inception temperature and the carbonization rate of precursor particles"
in: *Combustion and Flame* 130(3) (2002), pp. 204–214 (cit. on p. 20)

[37] **Kondo, K., Aizawa, T., Kook, S., and Pickett, L.**
"Uncertainty in Sampling and TEM Analysis of Soot Particles in Diesel Spray Flame"
in: *SAE Technical Paper 2013-01-0908* 2013 (cit. on p. 20)

[38] **Konstandopoulos, A. G., Kostuglou, M., Skaperdas, E., Papaioannou, E., Zarvalis, D., and Kladopoulou, E.**
"Fundamental studies of Diesel particulate filters: transient loading, regeneration and aging"
in: *SAE Technical Paper 2000-01-1016* 2000 (cit. on pp. 21, 25)

[39] **Winterbone, D. and Pearson, R.**
Theory of engine manifold design: wave action methods for IC engines
Professional Engineering Publishing 2000 (cit. on pp. 22, 67)

[40] **Galindo, J., Serrano, J. R., Piqueras, P., and García-Afonso, O.**
"Heat transfer modelling in honeycomb wall-flow diesel particulate filters"
in: *Energy* 43 (2012), pp. 201–213 (cit. on pp. 22–24)

[41] **Fuchs, N. A.**
The mechanics of aerosols
ed. by Davies, C. N. Pergamon press 1964 (cit. on pp. 24, 70)

[42] **Friedlander, S. K.**
"Mass and heat transfer to single spheres and cylinders at low Reynolds numbers"
in: *AIChE Journal* 3(1) (1957), pp. 43–48 (cit. on p. 24)

[43] **Stokes, G. G.**
"On the effect of the internal friction of fluids on the motion of a pendulum"
in: *Transactions of the Cambridge Philosophical Society* 9 Part 2 (1851), pp. 8–106 (cit. on p. 24)

[44] **Tomotika, S and Aoi, T**
"The steady flow of viscous fluid past a sphere and circular cylinder at small Reynolds numbers"
in: *Quarterly Journal of Mechanics and Applied Mathematics* 3 (1950), pp. 140–161 (cit. on p. 24)

[45] **Lee, K. and Gieseke, J.**
"Collection of aerosol particles by packed beds"
in: *Environmental Science and Technology* 13.4 (1979), pp. 466–470 (cit. on pp. 24, 27, 68, 70)

[46] **Happel, J.**
"Viscous flow in multiparticle systems: Slow motion of fluids relative to beds of spherical particles"
in: *American Institute of Chemical Engineers Journal* 4 (1958), pp. 197–201 (cit. on p. 24)

[47] **Lee, K. W., Reed, L. D., and Gieseke, J. A.**
"Pressure drop across packed beds in the low Knudsen number regime"
in: *Journal of Aerosol Science* 9 (1978), pp. 557–565 (cit. on p. 24)

[48] **Kirsh, A. A. and Fuchs, N. A.**
"Studies on fibrous aerosols filters - II. Pressure drop in systems of parallel cylinders"
in: *Annals of Occupational Hygiene* 10 (1967), pp. 23–30 (cit. on p. 24)

[49] **Yeh, H. and Liu, B.**
"Aerosol filtration by fibrous filtersI. Theoretical"
in: *Journal of Aerosol Science* 5 (1974), pp. 191–204 (cit. on p. 24)

[50] **Konstandopoulos, A. G. and Johnson, J. H.**
"Wall-flow Diesel particulate filters - Their pressure drop and collection efficiency"
in: *SAE Technical Paper 890405* 1989 (cit. on pp. 27, 39, 63)

[51] **Mohammed, H., Triana, A. P., Yang, S. L., and Johnson, J. H.**
"An advanced 1D 2-layer catalized Diesel particulate filter model to simulate: filtration by the wall and particulate cake, oxidation in the wall and particulate cake by NO2 and O2 and regeneration by heat addition"
in: *SAE Technical Paper 2006-01-0467* 2006 (cit. on p. 27)

[52] **Stanmore, B., Brilhac, J., and Gilot, P.**
"The oxidation of soot: a review of experiments, mechanisms and models"
in: *Carbon* 39 (2001), pp. 2247–2268 (cit. on p. 27)

[53] **Huinh, T. C., Johnson, J. H., Yang, S. L., Bagley, S. T., and Warner, J. R.**
"A one dimensional computational model for studying the filtration and regeneration characteristics of a catalyzed wall flow Diesel particulate filter"
in: *SAE Technical Paper 2003-01-0841* 2003 (cit. on p. 27)

[54] **Tandon, P., Heibel, A., Whitmore, J., Kekre, N., and Chithapragada, K.**
"Measurement and prediction of filtration efficiency evolution of soot loaded diesel particulate filters"
in: *Chemical Engineering Science* 65 (2010), pp. 4751–4760
(cit. on pp. 28, 65, 70)

[55] **Langmuir, I.**
"The production of rain by a chain reaction in Cumulus clouds of temperatures above freezing"
in: *Journal of the Atmospheric Sciences* 5 (1948), pp. 175–192
(cit. on p. 28)

[56] **Bollerhoff, T., Markomanolakis, I., and Koltsakis, G.**
"Filtration and regeneration modeling for particulate filters with inhomogeneous wall structure"
in: *Catalysis Today* 188 (2012), pp. 24–31 (cit. on pp. 28, 138)

[57] *Axisuite user's manual*
www.exothermia.com. Exothermia S.A. 2010 (cit. on p. 28)

[58] **Gong, J. and Rutland, C. J.**
"PDF-based heterogeneous multiscale filtration model"
in: *Environmental Science and Technology* 49(8) (2015), pp. 4963–4970
(cit. on pp. 29, 96, 97)

[59] **Fukushima, S. and Ohno, K.**
"New approach for pore structure and filtration efficiency characterization"
in: *SAE Technical Paper 2007-01-1918* 2007 (cit. on pp. 29, 34)

[60] **Mizuno, Y., Miyairi, Y., Katsube, F., Ohara, E., Takahashi, A., Makino, M., Mizutani, T., Yuki, K., and Kurachi, H.**
"Study on wall pore structure for next generation diesel particulate filter"
in: *SAE Technical Paper 2008-01-0618* 2008 (cit. on p. 29)

[61] **Ogyu, K., Ogasawara, T., Sato, H., Yamada, K., and Ohno, K.**
"Development of high porosity SiC-DPF which is compatible with high robustness and catalyst coating capability for SCR coated DPF applica-

tion"
in: *SAE Technical Paper 2013-01-0840* 2013 (cit. on p. 29)

[62] **Guan, B., Zhan, R., Lin, H., and Huang, Z.**
"Review of the state-of-the-art of particulate filter technology"
in: *Journal of Environmental Management* 154 (2015), pp. 225–258
(cit. on pp. 31, 33, 34, 38, 95)

[63] **Briot, A., Carranza, F., Girot, P., and Bardon, S.**
"Minimizing filter volume by design optimization"
in: *SAE Technical Paper 2007-01-0657* 2007 (cit. on p. 31)

[64] **Aravelli, K. and Heibel, A.**
"Improved lifetime pressure drop management for Robust Cordierite (RC) filters with Asymmetric Cell Technology (ACT)"
in: *SAE Technical Paper 2007-01-0920* 2007 (cit. on pp. 32, 38)

[65] **Sappok, A., Wang, Y., Wang, R., Kamp, C., and Wong, V.**
"Theoretical and experimental analysis of ash accumulation and mobility in ceramic exhaust particulate filters and potential for improved ash management"
in: *SAE International Journal of Fuels and Lubricants* 7(2) (2014), pp. 511–524 (cit. on pp. 32, 249)

[66] **Fujii, S. and Asako, T.**
"Design optimization of non-catalyzed DPF from viewpoint of back pressure in ash loading state"
in: *SAE Technical Paper 2011-01-2091* 2011 (cit. on p. 32)

[67] **Fujii, S. and Asako, T.**
"Development of artificial ash accelerated accumulation test method"
in: *SAE Technical Paper 2010-01-2171* 2010 (cit. on p. 32)

[68] **Sappok, A., Govani, I., Kamp, C., Wang, Y., and Wong, V.**
"In-situ optical analysis of ash formation and transport in Diesel Particulate Filters during active and passive DPF regeneration processes"
in: *SAE International Journal of Fuels and Lubricants* 6(2) (2013), pp. 336–349 (cit. on p. 32)

[69] **Johnson, T.**
"Diesel emission control in review"
in: *International Journal of Engine Research* 10 (2009), pp. 275–285
(cit. on p. 32)

[70] **Benaqqa, C., Gomina, M., Beurotte, A., Boussuge, M., Delattre, B., Pajot, K., Pawlak, E., and Rodrigues, F.**
"Morphology, physical, thermal and mechanical properties of the constitutive materials of Diesel Particulate Filters"
in: *Applied Thermal Engineering* 62 (2014), pp. 599–606
(cit. on p. 32)

[71] **Ogunwumi, R. S., Dong, Q., Murrin, T. A., Bhargava, R. Y., Warkins, J. L., and Heibel, A. K.**
"Performance evaluations of aluminum titanate Diesel Particulate Filters"
in: *SAE Technical Paper 2007-01-0656* 2007 (cit. on p. 32)

[72] **Li, J. and Mital, R.**
"Effect of DPF design parameters on fuel economy and thermal durability"
in: *SAE Technical Paper 2012-01-0847* 2012 (cit. on p. 32)

[73] **Dimou, I., Sappok, A., Wong, V., Fujii, S., Sakamoto, H., Yuuki, K., and Vogt, C.**
"Influence of material properties and pore design parameters on non-catalyzed Diesel Particulate Filter performance with ash accumulation"
in: *SAE Technical Paper 2012-01-1728* 2012 (cit. on pp. 32, 34)

[74] **Mizutani, T. et al.**
"The study for structural design of the segmented SiC-DPF"
in: *SAE Technical Paper 2006-01-1527* 2006 (cit. on pp. 32, 39)

[75] **Merkel, G., Beall, D., D.L., H., and J., V. M.**
"Effects of microstructure and cell geometry on performance of cordierite Diesel Particulate Filters"
in: *SAE Technical Paper 2001-01-0193* 2001
(cit. on pp. 32, 34, 121, 124)

[76] **Boger, T., Jamison, J., Warkins, J., Golomb, N., C., W., and Heibel, A.**
"Next generation Aluminum Titanate filter for light-duty Diesel applications"
in: *SAE Technical Paper 2011-01-0816* 2011 (cit. on p. 32)

[77] **Johnson, T. V.**
"Vehicular emissions in review"
in: *SAE International Journal of Engines* 5 (2012), pp. 216–234
(cit. on p. 32)

[78] **Li, C., Mao, F., Swartzmiller, S., Wallin, S., and Ziebarth, R.**
"Properties and performance of Diesel Particulate Filters of an advanced ceramic material"
in: *SAE Technical Paper 2004-01-0955* 2004 (cit. on p. 33)

[79] **Li, C., Koelman, H., Ramanathan, R., Baretzky, U., Forbriger, G., and Meunier, T.**
"Particulate Filter design for high performance Diesel engine application"
in: *SAE Technical Paper 2008-01-1747* 2008 (cit. on p. 33)

[80] **Depcik, C. D. and Hausmann, A. J.**
"Review and a methodology to investigate the effects of monolithic channel geometry"
in: *Journal of Engineering for Gas Turbine and Power* 135 (2013), pp. 032301 1–16 (cit. on pp. 34, 35, 38, 128)

[81] **Heck, R. H., Wei, J., and Katzer, J. R.**
"Mathematical modeling of monolithic catalysts"
in: *Aiche journal* 22(3) (1976), pp. 477–484 (cit. on pp. 34, 248)

[82] **Groppi, G., Belloli, A., Tronconi, E., and Forzatti, P.**
"A comparison of lumped and distributed models of monolith catalytic combustors"
in: *Chemical Engineering Science* 50(17) (1995), pp. 2705–2715 (cit. on pp. 34, 248)

[83] **Yuuki, K., Ito, T., Sakamoto, H., Matsubara, R., Hashimoto, S., and Hamanaka, T.**
"The effect of SiC properties on the performance of catalyzed Diesel particulate filter (DPF)"
in: *SAE Technical Paper 2003-01-0383* 2003 (cit. on pp. 34, 35)

[84] **Khair, M.**
"A review of Diesel particulate filter technologies"
in: *SAE Technical Paper 2003-01-2303* 2003 (cit. on p. 34)

[85] **Rose, D., Jamison, J., Boger, T., and Kataria, R.**
"Light duty Diesel exhaust gas after treatment challenges and technologies for post BS-IV regulations"
in: *SAE Technical Paper 2013-26-0051* 2013 (cit. on p. 34)

[86] **Murtagh, M., Sherwood, D., and Socha, L.**
"Development of a diesel particulate filter composition and its effect on thermal durability and filtration performance"
in: *SAE Technical Paper 940235* 1994 (cit. on pp. 34, 35, 63, 78, 84)

[87] **Howitt, J. and Montierth, M.**
"Cellular ceramic Diesel particulate filter"
in: *SAE Technical Paper 81104* 1981 (cit. on p. 34)

[88] **Ogyu, K., Oya, T., Ohno, K., and Konstandopoulos, A. G.**
"Improving of the filtration and regeneration performance by the Sic-DPF with the layer coating of PM oxidation catalyst"
in: *SAE Technical Paper 2008-01-0621* 2008 (cit. on p. 35)

[89] **Cavataio, G., Girard, J., and Lambert, C.**
"Cu/Zeolite SCR on high porosity filters: laboratory and engine performance evaluations"
in: *SAE Technical Paper 2009-01-0897* 2009 (cit. on p. 35)

[90] **Tan, J., Solbrig, C., and Schmieg, S.**
"The development of advanced 2-Way SCR/DPF systems to meet future Heavy-duty Diesel emissions"
in: *SAE Technical Paper 2011-01-1140* 2011 (cit. on p. 35)

[91] **Kawakami, A., Mizutani, T., Shibagaki, Y., Yuuki, K., Sakamoto, H., Vogt, C., Tatsuyuki Kuki, T., Heuss, W., Kattouah, P., and Makino, M.**
"High porosity DPF design for integrated SCR functions"
in: *SAE Technical Paper 2012-01-0843* 2012 (cit. on p. 35)

[92] **Nakamura, K., Vlachos, N., Konstandopoulos, A., Iwata, H., and Kazushige, O.**
"Performance Improvement of Diesel Particulate Filter by Layer Coating"
in: *SAE Technical Paper 2012-01-0842* 2012 (cit. on p. 35)

[93] **Gulati, S.**
"Cell design for ceramic monoliths for catalytic converter application"
in: *SAE Technical Paper 881685* 1988 (cit. on pp. 35–37, 169)

[94] **Heck, R., Robert, J., and Gulati, S. T.**
Catalytic air pollution control. Commercial Technology.
Wiley, New York 2009 (cit. on p. 36)

[95] **Gulati, S.**
"Performance parameters for advanced ceramic catalyst supports"
in: *SAE Technical Paper 1999-01-0269* 1999 (cit. on p. 37)

[96] **Konstandopoulos, A. G., Skaperdas, E., Warren, J., and Allansson, R.**
"Optimized filter design and selection criteria for continuously regenerating Diesel particulate traps"
in: *SAE Technical Paper 1999-01-0468* 1999 (cit. on pp. 38, 128)

[97] **Konstandopoulos, A. G. and Kladopoulou, E.**
"The optimum cell density for wall-flow monolithic filters: effects of filter permeability, soot cake structure and ash loading"
in: *SAE Technical Paper 2004-01-1133* 2004 (cit. on pp. 38, 128)

[98] **Lee, S. J., Jeong, S. J., and Kim, W. S.**
"Numerical design of the diesel particulate filter for optimum thermal performances during regeneration"
in: *Applied Energy* 86 (2009), pp. 1124–1135 (cit. on pp. 38, 128)

[99] **Konstandopoulos, A. and Kostoglou, M.**
"Analysis of asymmetric and variable cell geometry wall-flow particulate filters."
in: *SAE Technical Paper 2014-01-1510* 2014 (cit. on p. 38)

[100] **Nakamura, K., Konstandopoulos, A., Kostoglou, M., Shibata, T., and Hashizume, Y.**
"New asymmetric plugging layout of Diesel Particulate Filters for the pressure drop reduction"
in: *SAE Technical Paper 2014-01-1512* 2014 (cit. on p. 38)

[101] **Heibel, A. and Bhargava, R.**
"Advanced Diesel Particulate Filter design for lifetime pressure drop solution in light duty applications"
in: *SAE Technical Paper 2007-01-0042* 2007 (cit. on p. 38)

[102] **Bardon, S., Bouteiller, B., Bonnail, N., Girot, P., Gleize, V., Oxarango, L., Higelin, P., Michelin, J., Schuerholz, S., and Terres, F.**
"Asymmetrical channels to increase DPF lifetime"
in: *SAE Technical Paper 2004-01-950* 2004 (cit. on pp. 38, 138)

[103] *U.S. Environmental Protection Agency (EPA), regulatory impact analysis: control of emissions of air pollution from highway Heavy-Duty engines, 2000, U.S. Environmental Protection Agency - Office of Transportation and Air Quality.*
2000 (cit. on p. 39)

[104] **Blanchard, G., Colignon, C., Griard, C., Rigaudeau, C., Salvat, O., and Seguelong, T.**
"Passenger car series application of a new Diesel Particulate Filter system using a new Ceria-based fuel-borne catalyst: from the engine test bench to european vehicle certification"
in: *SAE Technical Paper 2002-01-2781* 2002 (cit. on p. 39)

[105] **Kai, R., Sekiya, T., Ogawa, M., Saiki, K., Matsubara, R., Kurachi, H., Brayer, M., Warner, E., Fujii, S., and Ren, S.**
"Thermal-mechanical durability of DOC and DPF aftertreatment system for light heavy pickup truck application"
in: *SAE Technical Paper 2009-01-2707* 2009 (cit. on p. 39)

[106] **Schuster, H. D.**
"Verminderung der Partikelemission amb PKW-Motor"
in: *VDI-Bericht* 559 (1985) (cit. on p. 39)

[107] **Mayer, A., Buck, A., and Bressler, H.**
"The knitted Particulate Trap: field experience and development progress"
in: *SAE Technical Paper 930362* 1993 (cit. on p. 40)

[108] **Mayer, A., Schmidt, R. M., Sudmanns, H., Mattes, P., and Buck, A.**
"Pre-turbo application of the knitted fiber diesel particulate trap"
in: *SAE Technical Paper 940459* 1994 (cit. on p. 40)

[109] **Subramaniam, M. N., Joergl, V., Keller, P., Weber, O., Toyoshima, T., and Vogt, C. D.**
"Feasibility assessment of a pre-turbo after-treatment system with a 1D modeling approach"
in: *SAE Technical Paper 2009-01-1276* 2009 (cit. on pp. 40, 176)

[110] **Joergl, V., Keller, P., Weber, O., Mueller-Hass, K., and Konieczny, R.**
"Influence of pre turbo catalyst design on diesel engine performance, emissions and fuel economy"
in: *SAE Technical Paper 2008-01-0071* 2008 (cit. on pp. 40, 121)

[111] **Brüstle, C., Downey, M., Subramaniam, M. N., Birckett, A., and Tomazic, D.**
"Aftertreatment in a pre-turbo position: size and fuel consumption advantage for Tier 4 large-bore Diesel engines"
in: *Aachen Colloquium Automobile and Engine Technology 2011* 2011 (cit. on p. 40)

[112] **Osborne, D. T., Fritz, S. G., and Iden, M.**
"Exhaust emissions from a 2,850 kW EMD SD60M locomotive equipped with a Diesel Oxidation Catalyst"
in: *ASME/IEEE Joint Rail Conference and Internal Combustion Engine Division Spring Technical Conference* 2007 (cit. on p. 40)

[113] **Blanchet, S., Richmond, R., and Vaneman, G.**
"Implementation of the effectiveness-Ntu methodology for catalytic converter design"
in: *SAE Technical Paper 980673* 1998 (cit. on p. 40)

[114] **Lújan, J. M., Bermúdez, V., Piqueras, P., and García-Afonso, O.**
"Experimental assessment of pre-turbo aftertreatment configurations in a single stage turbocharged Diesel engine. Part 1: Steady-state operation"
in: *Energy* 80 (2015), pp. 599–613
(cit. on pp. 40, 113, 133, 135, 141, 156)

[115] **Bermúdez, V., Lujan, J. M., Piqueras, P., and Campos, D.**
"Pollutants emission and particle behavior in a pre-turbo aftertreatment light-duty diesel engine"
in: *Energy* 66 (2014), pp. 509–522 (cit. on p. 41)

[116] **Lújan, J. M., Serrano, J. R., Piqueras, P., and García-Afonso, O.**
"Experimental assessment of a pre-turbo aftertreatment configuration in a single stage turbocharged Diesel engine. Part 2: Transient operation"
in: *Energy* 80 (2015), pp. 614–627 (cit. on pp. 41, 113)

[117] **Bermúdez, V., Serrano, J. R., Piqueras, P., and García-Afonso, O.**
"Analysis of heavy-duty turbocharged diesel engine response under cold transient operation with a pre-turbo aftertreatment exhaust manifold configuration"
in: *International Journal of Engine Research* 14.4 (2013), pp. 341–353
(cit. on pp. 41, 127, 173)

[118] *WHTC emission test cycles*
https://dieselnet.com/standards/cycles/whtc.php 2016 (cit. on p. 41)

[119] **Payri, F., Serrano, J. R., Piqueras, P., and García-Afonso, O.**
"Performance Analysis of a Turbocharged Heavy Duty Diesel Engine with a Pre-turbo Diesel Particulate Filter Configuration"
in: *SAE Technical Paper 2011-37-0004* 2011 (cit. on p. 42)

[120] **Bermúdez, V., Serrano, J. R., Piqueras, P., and García-Afonso, O.**
"Influence of DPF soot loading on engine performance with a pre-turbo aftertreatment exhaust line"
in: *SAE Technical Paper 2012-01-0362* 2012 (cit. on pp. 42, 136, 141)

[121] **Watanabe, Y., Araki, Y., Kobashi, K., and Henda, Y.**
An exhaust gas purification device for a compression-ignition combustion engines
Patent Application EP 0823545 (B1) 2002 (cit. on p. 42)

[122] **ElringKlinger**
Seal for combustion engine has catalysis element or particulate filter element connected to the seal with sealing plate whereby sealing plate has exhasut gas passage through which exhaust gas of combustion engine ows
Patent Application DE 202006004489 (U1) 2006 (cit. on p. 42)

[123] **Winsor, R. and Baumgard, K.**
Internal combustion engine with a dual particulate traps ahead of turbocharger
Patent Application US/2009 0151328 (A1) 2009 (cit. on p. 42)

[124] **Toshihisa, S., Hiromichi, Y., Yoshimitsu, H., Yoshio, Y., and Zenichiro, K.**
Exhaust emission control device
Patent Application JP2002364335 (A) 2005 (cit. on p. 43)

[125] **Sludder, C., Storey, J., Lewis, S., Styles, D., Giulano, J., and Hoard, J.**
"Hydrocarbons and particulate matter in EGR cooler deposits: Effects of gas flow rate, coolant temperature and oxidation catalyst"
in: *SAE Technical Paper 2008-01-2467* 2008 (cit. on p. 43)

[126] **Takashi, M., Hideo, N., Toshio, I., Kazuya, O., and Seiji, I.**
Exhaust gas recirculating system
Patent Application JP2005232996 (A) 2005 (cit. on p. 43)

[127] **Payri, F., Desantes, J. M., Galindo, J., and Serrano, J. R.**
Exhaust manifold of a turbo-supercharged reciprocating engine
Patent WO2010092201A1. Priority date 13/02/2009. European Patent Office. 2010 (cit. on p. 43)

[128] **Desantes, J. M., Payri, F., Serrano, J. R., and Piqueras, P.**
Device for treating exhaust gases from diesel turbo-supercharged reciprocating internal combustion engines (RICE)
Patent WO 2013/041747 A1. Priority date 23/09/2011. European Patent Office. 2013 (cit. on pp. 43, 44, 113)

[129] *Regulation (EC) No 595/2009 of the European Parliament and of the Council of 18 June 2009 on type-approval of motor vehicles and engines with respect to emissions from heavy duty vehicles (Euro VI) and on access to vehicle repair and maintenance information and amending Regulation (EC) No 715/2007 and Directive 2007/46/EC and repealing Directives 80/1269/EEC, 2005/55/EC and 2005/78/EC*
Official Journal of the European Union 2009 (cit. on p. 62)

[130] *Official website of the European Union.*
2015 (cit. on p. 62)

[131] **Somiya, S., Adler, J., Petasch, U., and al., et**
Handbook of Advanced Ceramics: Materials, Applications, Processing, and Properties. Chapter 8.1
Academic Press 2013 (cit. on p. 63)

[132] **Yapaulo, R., Wirojsakunchai, E., Orita, T., Foster, D., Akard, M., Walker, L., and Lance, M.**
"Impact of filtration velocities and particulate matter characteristics on diesel particulate filter wall loading"
in: *International Journal of Engine Research* 10.5 (2009), pp. 287–304 (cit. on p. 63)

[133] **Fino, D., Russo, N., Millo, F., Vezza, D., Ferrero, F., and Chianale, A.**
"New tool for experimental analysis of diesel particulate filter loading"
in: *Top Catalysis* 52 (2009), pp. 13–20 (cit. on pp. 63, 71)

[134] **Kamp, C., Sappok, A., and Wong, V.**
"Soot and ash deposition characteristics at the catalyst-substrate interface and intra-layer interactions in aged diesel particulate filters illustrated using Focused Ion Beam (FIB) milling"
in: *SAE Technical Paper 2012-01-0836* 2012 (cit. on p. 63)

[135] **Stewart, M., Gallant, T., Kim, D., Maupin, G., and Zelenyuk, A.**
"Fuel efficient diesel particulate filter (DPF) modeling and development"
in: *Pacific Northwest National Laboratory, PNNL-19476* 2010 (cit. on p. 63)

[136] **Yamamoto, K., Oohori, A., Yamashita, H., and Daido, S.**
"Simulation on soot deposition and combustion in diesel particulate filter"
in: *Proceedings of the Combustion Institute* 32 (2009), pp. 1965–1972 (cit. on p. 63)

[137] **Choi, S. and Lee, K.**
"Detailed Investigation of Soot Deposition and Oxidation Characteristics in a Diesel Particulate Filter Using Optical Visualization"
in: *SAE Technical Paper 2013-01-0528* 2013 (cit. on pp. 63, 73)

[138] **Piscaglia, F., Rutland, C., and Foster, D.**
"Development of a CFD model to study the hydrodynamic characteristics and the soot deposition mechanism on the porous wall of a Diesel particulate filter"
in: *SAE Technical Paper 2005-01-0963* 2005 (cit. on p. 64)

[139] **Serrano, J. R., Arnau, F. J., Piqueras, P., and García-Afonso, O.**
"Application of the two-step Lax&Wendroff-FCT and the CE-SE method to flow transport in wall-flow monoliths"
in: *International Journal of Computer Mathematics* 91(1) (2014), pp. 71–84 (cit. on pp. 66, 67)

[140] **Desantes, J. M., Serrano, J. R., Arnau, F. J., and Piqueras, P.**
"Derivation of the method of characteristics for the fluid dynamic solution of flow advection along porous wall channels"
in: *Applied Mathematical Modelling* 36 (2012), pp. 3144–3152
(cit. on p. 67)

[141] **Ferrel, W.**
An Introduction to Probability Theory and Its Applications
Wiley, New York 1971 (cit. on p. 71)

[142] **Logan, B. E., Jewett, D. G., Arnold, R. G., Bouwer E., J., and O'Melia, C. R.**
"Clarification of clean-bed filtration models"
in: *Journal of Environmental Engineering* 121 (1995), pp. 869–873
(cit. on p. 71)

[143] **Rief, S., Kehrwald, D., Schmidt, K., and Wiegmann, A.**
"Simulation of ceramic DPF media, soot deposition filtration efficiency and pressure drop evolution"
in: *Proceedings of the 10th World Filtration Congress 2008;3:318-22*
2008 (cit. on p. 74)

[144] **Desantes, J. M., Bermúdez, V., Molina, S., and Linares, W. G.**
"Methodology for measuring exhaust aerosol size distributions using an engine test under transient operating conditions"
in: *Measurement Science and Technology* 22(11) (2011), p. 115101
(cit. on pp. 80, 194)

[145] **Depcik, C. D. and Assanis, D.**
"Simulating area conservation and the gas-wall interface for one-Dimensional based Diesel particulate filter models"
in: *Journal of Engineering for Gas Turbines and Power* 130(6) (2008), p. 062807 (cit. on pp. 80, 81, 204)

[146] **Liu, Y., Gong, J., Fu, J., Cai, H., and Long, G.**
"Nanoparticle motion trajectories and deposition in an inlet channel of wall-flow diesel particulate filter"
in: *Journal of Aerosol Science* 40 (2009), pp. 307–323
(cit. on pp. 80, 81)

[147] **Karin, P., Cui, L., Rubio, P., Tsuruta, T., and Hanamura, K.**
"Microscopic visualization of PM trapping and regeneration in micro-structural pores of a DPF wall"
in: *SAE International Journal of Fuels and Lubricants* 2(1) (2009), pp. 661–669 (cit. on pp. 91, 92, 94, 95)

[148] **Sanui, R. and Hanamura, K.**
"Scanning Electron Microscopic visualization of transition from surface pore filtration to cake filtration inside Diesel Particulate Filter walls"
in: *SAE Technical Paper 2015-01-1018* 2015 (cit. on pp. 91, 92)

[149] **Karin, P.**
"Microscopic visualization and characterization of particulate matter trapping and oxidation in diesel particulate filters and membrane filters"
PhD thesis. Tokyo Institute of Technology 2010 (cit. on p. 93)

[150] **Marre, S., Palmeri, J., Larbot, A., and Bertrand, M.**
"Modeling of submicrometer aerosol penetration through sintered granular membrane filters"
in: *J. Colloid Interface Sci.* 274 (2004), pp. 167–182 (cit. on pp. 95, 96)

[151] **Posada, F., Bandivadekar, A., and German, J.**
"Estimated cost of emission control technologies for light-duty vehicles. Part 2 - Diesel"
in: *SAE Technical Paper 2013-01-0539* 2013
(cit. on pp. 112, 133, 172)

[152] *U.S. Environmental Protection Agency (EPA) and U.S. National Highway Traffic Safety Administration (NHTSA). Final rulemaking to establish standards and corporate average fuel economy standards, Joint technical support document. U.S. EPA - Office of International Policy, Fuel Economy and Consumer Programs.*
2010 (cit. on p. 112)

[153] *U.S. National Academy of Sciences (NAS), Assessment of fuel economy technologies for light-duty vehicles, The National Academic Press: Washington D.C.*
2011 (cit. on p. 112)

[154] **Mallamo, F., Longhi, S., Millo, F., and Rolando, L.**
"Modeling of Diesel Oxidation Catalysts for calibration and control purpose"
in: *International Journal of Engine Research* 15 (8) (2014), pp. 965–979
(cit. on p. 119)

[155] **Seman, C.**
http://www.wisegeek.com/what-is-space-velocity.htm
2016 (cit. on p. 119)

[156] **Dawson, E. and Kramer, J.**
"Faster is Better: The Effect of Internal Turbulence on DOC Efficiency"
in: *SAE Technical Paper 2006-01-1525* 2006 (cit. on p. 120)

[157] **Bermúdez, V., Serrano, J. R., Piqueras, P., and García-Afonso, O.**
"Assessment by means of gas dynamic modelling of a pre-turbo diesel particulate filter configuration in a turbocharged HSDI diesel engine under full-load transient operation"
in: *Proceedings of the Institution of Mechanical Engineers, Part D: Journal of Automobile Engineering* 225 (9) (2011), pp. 1134–1155
(cit. on p. 132)

[158] **Subramaniam, M. N., Hayes, C., Tomazic, D., M., M. D., and Bruestle, C.**
"Pre-Turbo aftertreatment position for large bore Diesel engines - Compact and cost-effective aftertreatment with a fuel consumption advantage"
in: *SAE International Journal of Engines* 4(1) (2011), pp. 106–116
(cit. on p. 173)

[159] **Koltsakis, G. C., Konstantinou, A., Haralampous, O. A., and Samaras, Z. C.**
"Measurement and intra-layer modelling of soot density and permeability in wall-flow filters"
in: *SAE Technical Paper 2006-01-0261* 2006
(cit. on pp. 189, 206, 213, 214, 227)

[160] **Bensaid, S., Marchisio, D., Russo, N., and Fino, D.**
"Experimental investigation of soot deposition in diesel particulate filters"
in: *Catalysis Today* 147S (2009), S295–S300 (cit. on p. 189)

[161] **Wang, Y., Wong, V., Sappok, A., and Munnis, S.**
"The sensitivity of DPF performance to the spatial distribution of ash inside DPF inlet channels"
in: *SAE Technical Paper 2013-01-1584* 2013 (cit. on p. 189)

[162] **Bagi, S., Sharma, V., Patel, M., and Aswath, P. B.**
"Effects of Diesel soot composition and accumulated vehicle mileage on soot oxidation characteristics"
in: *Energy & Fuels* 30(10) (2016), pp. 8479–8490 (cit. on p. 189)

[163] **Konstandopoulos, A. G., Kostuglou, M., Vlachos, N., and Kladopoulo, E.**
"Progress in Diesel particulate filter simulation"
in: *SAE Technical Paper 2005-01-0946* 2005
(cit. on pp. 189, 206, 227)

[164] *TSI. Model 3090. Engine exhaust particle sizer spectrometer. Operation and service manual.*
(cit. on p. 194)

[165] **Montajir, R., Kusaka, T., Bamba, Y., and Adachi, M.**
"A New Concept for Real-Time Measurement of Particulate Matter (Soot and SOF)"
in: *SAE Technical Paper 2005-01-3605* 2005 (cit. on p. 194)

[166] *Dekati. Fine smart particle sampler FPS-4000. Operation and service manual.*
(cit. on p. 194)

[167] **Bermúdez, V., Pastor, J. V., López, J. J., and Campos, D.**
"Experimental correlations for transient soot measurement in diesel exhaust aerosol with light extinction, electrical mobility and diffusion charger sensor techniques"
in: *Measurement Science and Technology* 25 (2014), p. 065204
(cit. on p. 195)

[168] **Pickett, L., Siebers, D., and Idicheria, C.**
"Relationship between ignition processes and thelift-off length of Diesel fuel jets"
in: *SAE Technical Paper 2005-01-3843* 2005 (cit. on p. 196)

[169] **Dec, J.**
"A conceptual model of DI Diesel combustion based on laser-sheet imaging"
in: *SAE Technical Paper 970873* 1997 (cit. on p. 196)

[170] **Tree, D. and Svensson, K.**
"Soot processes in compression ignition engines"
in: *Progress in Energy and Combustion Science* 33 (2007), pp. 372–309
(cit. on p. 196)

[171] **Desantes, J. M., Arrégle J..and López, J. J., and García, A.**
"A comprehensive study of Diesel combustion and emissions with post-injection"
in: *SAE Technical Paper 2007-01-0915* 2007 (cit. on p. 196)

[172] **Goldstein, I. J., Newbury, D. E., Joy, D. C., Lyman, C. E., Echlin, P., Lifshin, E., Sawyer, L., and Michael, J.**
Scanning electron microscopy and X-ray microanalysis. Third edition.
Kluwer academic / Plenum 2012 (cit. on pp. 200, 201)

[173] **McMullan, D.**
"Von Ardenne and the scanning electron microscope"
in: *Proceedings of the Royal Microscopical Society* 23 (1988), pp. 283–288
(cit. on p. 200)

[174] **McMullan, D.**
"Scanning electron microscopy 1928–1965"
in: *Scanning* 17 (3) (1995), pp. 175–185 (cit. on p. 200)

[175] **Von Ardenne, M.**
Improvements in electron microscopes
GB 511204 1937 (cit. on p. 200)

[176] **Goldstein, I. J., Newbury, D. E., Echlin, P., Joy, D. C., Fiori, C., and Lifshin, E.**
Scanning electron microscopy and x-ray microanalysis
Plenum Press 1981 (cit. on p. 201)

[177] **Yang, S., Deng, C., Gao, Y., and He, Y.**
"Diesel particulate filter design simulation: a review"
in: *Advances in Mechanical Engineering* 8(3) (2016), pp. 1–14
(cit. on p. 204)

[178] **Lupsea, J., Campoloa, M., and Soldati, A.**
"Modelling soot deposition and monolith regeneration for optimal design of automotive DPFs"
in: *Chemical Engineering Science* 151 (2016), pp. 36–50
(cit. on p. 213)

[179] **Elmoe, T. D., Tricoli, A., Grunwaldt, J. D., and Pratsinis, S. E.**
"Filtration of nanoparticles: evolution of cake structure and pressure-drop"
in: *Journal of Aerosol Science* 40 (2009), pp. 965–981 (cit. on p. 214)

[180] **Elmoe, T. D., Tricoli, A., and Grunwaldt, J. D.**
"Characterization of highly porous nanoparticle deposits by permeance measurements"
in: *Powder Technology* 207 (2011), pp. 279–289 (cit. on p. 214)